Western Graduate&PostdoctoralStudies

Western University
Scholarship@Western

Electronic Thesis and Dissertation Repository

12-10-2014 12:00 AM

A New Generation of Polymer/Ceramic Composite Biomaterials for Bone Regeneration

Mehrnaz Salarian
The University of Western Ontario

Supervisor
Prof. Paul A. Charpentier
The University of Western Ontario

Graduate Program in Biomedical Engineering
A thesis submitted in partial fulfillment of the requirements for the degree in Doctor of Philosophy
© Mehrnaz Salarian 2014

Follow this and additional works at: https://ir.lib.uwo.ca/etd

Part of the Biomaterials Commons

Recommended Citation

Salarian, Mehrnaz, "A New Generation of Polymer/Ceramic Composite Biomaterials for Bone Regeneration" (2014). *Electronic Thesis and Dissertation Repository*. 2562.
https://ir.lib.uwo.ca/etd/2562

This Dissertation/Thesis is brought to you for free and open access by Scholarship@Western. It has been accepted for inclusion in Electronic Thesis and Dissertation Repository by an authorized administrator of Scholarship@Western. For more information, please contact wlswadmin@uwo.ca.

www.manaraa.com

A NEW GENERATION OF POLYMER/CERAMIC COMPOSITE BIOMATERIALS FOR BONE REGENERATION

(Thesis format: Integrated Article)

by

Mehrnaz Salarian

Graduate Program in Biomedical Engineering

A thesis submitted in partial fulfillment
of the requirements for the degree of
Doctor of Philosophy

The School of Graduate and Postdoctoral Studies
The University of Western Ontario
London, Ontario, Canada

© Mehrnaz Salarian 2014

www.manaraa.com

Abstract

There is a substantial emerging interest for fundamental and applied research on the reinforcement of polymeric materials using nanotechnology. In the biomedical industry, development of novel bone cement composite materials with enhanced mechanical properties is of tremendous potential importance. The most universally used injectable bone cement is made of poly(methyl methacrylate) (PMMA); however, the major disadvantage of PMMA is its non-biodegradability. Polymers such as poly(propylene fumarate) (PPF) and polycaprolactone (PCL) are biodegradable, but suffer from a lack of mechanical properties. The aim of this research was to test the efficacy of these biodegradable polymers integrating nanotechnology for the development of composite biomaterials with improved mechanical properties sufficient for bone cements.

This goal was investigated through a range of different studies. Focusing on nanostructured titania (n-TiO_2) initially, titania nanofibers (n-TiO_2 fibers) and nanowires (n-TiO_2 wires) were introduced into a PPF matrix for potential use as an orthopaedic biomaterial to treat skeletal bone defects and diseases such as osteonecrosis. PPF was modified with maleic anhydride to provide functionality for the coordination of PPF to the surface of TiO_2 nanofibers through a ring-opening reaction. The synthesis and modification of PPF were confirmed by NMR (^{1}H and ^{13}C) and XPS. The reaction chemistry of the functionalized PPF and nano-TiO_2 was also investigated by XPS and FTIR analyses. The PPF-grafted nano-TiO_2 was further employed in the development of bone cement composites by crosslinking/polymerization in the presence of N-vinyl pyrrolidone. Mechanical testing of the resulting bone cement composites demonstrated a significant enhancement of the tensile and flexural properties attributed to the chemical bonding between the PPF matrix and TiO_2 nanofibers. On the basis of the determined mechanical properties, an optimum composition was found at 5 wt% loading of n-TiO_2 fiber (0.5% in the starting composition) which provided a significant increase in Young's modulus (153%), tensile strength (113%), flexural modulus (196%), and flexural strength (126%) when compared with the unfilled PPF. These improvements were attributed to the chemical linkage of the filler to the polymer matrix which enhances the transfer of a

www.manaraa.com

mechanical load to the n-TiO_2 fiber, leading to an increase in the mechanical properties of the bone cement composite.

Secondly, bone formation is an angiogenesis-dependent process, and the need for treatment modalities that enhance neovascularization is especially important for bone regeneration in necrotic bone. A bone cement system capable of delivering an angiogenic modulator in a controlled manner may have the ability to boost the angiogenic response when injected to an osteonecrotic lesion. Therefore, an angiogenic agent, ginsenoside Rg_1, was incorporated into an orthopedic PPF-based cement. Additionally, Sr-doped TiO_2 nanofibers synthesized in supercritical CO_2 were added to the cement formulation as an alternative radiopacifier to enable visualization of the bone cement composites and potential monitoring of the healing and loosening processes. XPS analysis showed that Sr^{2+} was doped in the crystalline matrix of anatase with the formation of $SrTiO_3$. The strong interfacial adhesion between PPF and nanofibers were characterized by SEM, FTIR, XPS, and thermal analyses and mechanical testing. The Sr-doped n-TiO_2 fibers were shown to provide reasonably higher radiopacity to the PPF matrix, which is 0.32 ± 0.03 mm Al, than the unmodified fibers at the same loading level (0.20 ± 0.01 mm Al). In addition, bone cement composites loaded with ginsenoside Rg_1 were found to provide a high drug release without sacrificing the mechanical properties of the bone cement. Furthermore, tube formation bioassays suggested that human umbilical vein endothelial cell lines would rearrange and align into a tubular structure in the presence of ginsenoside Rg_1. Consequently, the proposed cement combines the immediate mechanical support given by the chemical bonding between the filler/polymer and optimum radiopacity (0.30 ± 0.12 mm Al) due to the incorporation of the Sr-doped TiO_2 nanofibers to PPF matrix.

Thirdly, because of the unique biological activities of ginsenoside Rg_1, upregulating *in vitro* proliferation, migration, chemo-invasion, and tube formation in human umbilical vein endothelial cells (HUVECs), Rg_1 can be incorporated into scaffold materials for bone tissue engineering applications. This incorporation could be achieved by encapsulation of ginsenoside Rg_1 in biodegradable microspheres of PPF. Rg_1-loaded PPF microspheres were prepared by both a double emulsion and a microfluidic technique for the first time in this research. The size and morphology of the Rg_1-loaded PPF

www.manaraa.com

microspheres were characterized by SEM, showing unimodal 50-65 μm size diameters using the microfluidic technique, ideal for easy flowing powders required in commercial formulations. The PPF microspheres produced from the microfluidic technique gave high encapsulation efficiencies of up to 95.35 ± 0.82%, while those obtained from a conventional double emulsion method gave a much broader size distribution in the range of 2-45 μm with lower encapsulation efficiencies of 78.48 ± 1.68%. Release profiles were studied and quantified by UV-Vis spectrophotometry, with the results showing a lower initial burst in the release of Rg_1 from the unimodal microspheres prepared by the microfluidic technique than from the double emulsion method. The burst effect was followed by a slow release profile which can be used for long term drug delivery applications to maintain the ginsenoside Rg_1 concentration for an extended time period. Moreover, the released Rg_1 showed a significant stimulatory effect on angiogenesis behavior and tube formation in human umbilical vein endothelial cells (HUVECs). Therefore, PPF microspheres developed in this study have potential for next-generation biomedical agents in drug-release devices for bone tissue engineering.

Finally, the use of hydroxyapatite HAp is rather limited for heavy load-bearing applications due to low mechanical reliability and poor processability. Therefore, immobilization of a biocompatible metal/metal oxide on the surface of HAp has been receiving increased attention for applications involving the enhancement of mechanical properties of biocompatible prostheses. A novel nanostructured HAp and a composite of HAp and TiO_2 with ultrafine structure and significantly improved mechanical properties were prepared using combined co-precipitation and sol-gel method in the green solvent, $scCO_2$, and incorporated into poly(ε-caprolactone) (PCL) matrix to develop scaffolds with enhanced physical and mechanical properties for bone regeneration. SEM and TEM analyses were employed to examine the morphology of the HAp nanoplates and HAp-TiO_2 nanocomposites. The presence of Ti, O, Ca, and P in the HAp-TiO_2 nanocomposites was detected by EDX. In addition, the effect of metal alkoxide concentration, reaction temperature, and pressure on the morphology, crystallinity, and surface area of the resulting nanostructured composites was examined using SEM, XRD, and the BET method. Chemical composition of the products were characterized using FTIR, XPS, and XANES analyses. TGA analysis was performed to investigate thermal behavior of the

www.manaraa.com

synthesized nanomaterials. Mechanical testing revealed a significant increase in the Young's modulus (88.6%), tensile strength (122%), flexural modulus (47%), and flexural strength (59.6%) of PCL/HAp-TiO_2 composites containing 20 wt % HAp-TiO_2 compared to PCL/HAp composites.

Keywords

TiO_2 nanofibers, Poly(propylene fumarate), Functionalization, Maleic anhydride, Nanocomposite, Mechanical enhancement, Bone cement, Sr-doped TiO_2 nanofibers, Radiopacity, Angiogenesis, Ginsenosied Rg_1, Hydroxyapatite-Titania nanocomposite, Morphology, Super critical carbon dioxide, Sol-gel method, Biodegradable microsphere, Drug delivery, Microfluidics, Monodispersity.

www.manaraa.com

Co-Authorship Statement

This dissertation is prepared in the integrated article format. Manuscripts that have been previously published, or submitted for publication, or finalized for submission form the body of this dissertation which are presented with some adjustments in Chapters 2 through 6.

Title: Synthesis and characterization of novel TiO_2-poly(propylene fumarate) nanocomposites for bone cementation (Chapter 2). **Authors:** Mehrnaz Salarian, William Z. Xu, Mark C. Biesinger, Paul A. Charpentier. The experimental work was conducted by Mehrnaz Salarian under the guidance of advisor Dr. Paul A. Charpentier. XPS analyses were performed by Dr. Mark Biesinger. NMR measurements and help with interpretation were done with Dr. William Z. Xu. The draft of this manuscript was written by Mehrnaz Salarian with the great help of Dr. Mark C. Biesinger in the discussion. Modifications were carried out under the close supervision of Dr. Paul A. Charpentier. The final version of this article was published by the Journal of Materials Chemistry B 2 (2014) 5145-5156.

Title: Delivery of an angiogenic mediator for bone regeneration in a radiopaque Sr^{2+}-modified TiO_2/poly(propylene fumarate) based bone cement (Chapter 3). **Authors:** Mehrnaz Salarian, William Z. Xu, Richard Bohay, Edmund M. K. Lui, and Paul A. Charpentier. The experimental works were conducted by Mehrnaz Salarian under the guidance of advisor Dr. Paul A. Charpentier. Radiopacity measurements set up and calculations were performed under the direct guidance of Dr. Richard Bohay. The biological works were done by Mehrnaz Salarian under the guidance of Dr. Edmund M. K Lui. The draft of this manuscript was written by Mehrnaz Salarian and corrected by Dr. Paul A. Charpentier and William Z. Xu This manuscript is manuscript is under preparation for publication.

Title: Fabrication of monodisperse ginsenoside Rg1-loaded PPF microspheres using a microfluidic device for bone regeneration (Chapter 4). **Authors:** Mehrnaz Salarian, Raziye Samimi, Zhiqiang Wang, Tsun-Kong Sham, Edmund M.K Lui, and Paul A.

www.manaraa.com

Charpentier. The experimental works were conducted by Mehrnaz Salarian under the guidance of advisor Dr. Paul A. Charpentier. Dr. Raziye Samimi helped in the experimental set up and design. XANES data measurements facilities were provided by Dr. Tsun-Kong Sham and interpretations were done Dr. Zhiqiang Wang. The biological works were done by Mehrnaz Salarian under the guidance of Dr. Edmund M. K Lui. The draft of this manuscript was written by Mehrnaz Salarian and corrected by Dr. Paul A. Charpentier. This manuscript is under preparation for publication.

Title: Hydroxapatite-TiO_2-based nanocomposites synthesized in supercritical CO_2 for bone tissue engineering: physical and mechanical properties (Chapter 5). **Authors:** Mehrnaz Salarian, William Z. Xu, Zhiqiang Wang, Tsun-Kong Sham, and Paul A. Charpentier. The experimental works were conducted by Mehrnaz Salarian under the guidance of advisor Dr. Paul A. Charpentier. XANES data measurements facilities were provided by Dr. Tsun-Kong Sham and interpretations were done Dr. Zhiqiang Wang. The draft of this manuscript was written by Mehrnaz Salarian with the great help of Dr. Zhiqiang Wang and Dr. William Z. Xu. Modifications were carried out under the close supervision of Dr. Paul A. Charpentier. The final version of this article was published by the ACS Applied Materials and Interfaces 86 (2014) 115-123.

www.manaraa.com

Dedication

To Mina and Mohammadreza

www.manaraa.com

Acknowledgments

I would like to express my grateful appreciation to my advisor Professor Paul A. Charpentier for for his supervision, insight, advice, and guidance throughout all stages of this research. The completion of this dissertation would not have been possible without his incomparable support and encouragement.

I gratefully thank Dr. Edmund M. K. Lui and Dr. Hua Pei for their impressive advice and helps in biological studies of ginsenoside Rg_1. I would like to express my sincere gratitude to Dr. Richard Bohay of Dentistry department, UWO for X-ray Radiography, Dr. Mark Besigner of the Surface Science Western, UWO for his expert work on the XPS analyses, Dr. Todd Simpson of Nanofabrication laboratory, UWO for SEM, Dr. Carmen Andrei of Brockhouse Institute, McMaster University, for HRTEM, Ms. Aneta Borecki of the Department of Chemistry, UWO for the powder XRD, and Mr. Ross Davidson of the Surface Science Western, UWO for SEM work. Many thanks go to Ms. Dong Zhao of the University of Saskatchewan for the XANES data measurements.

I have been indebted to Dr. William Xu, the postdoctoral fellow of the research group, for his invaluable advice, constructive comments, and scientific discussions. I gratefully thank Dr. Tsun-Kong Sham and Dr. Zhiqiang Wang for providing us with XANES measurements facilities and interpretations. I also would like to appreciate the assistance of Dr. Jun Yang and Dr. Tingjie Li in microfluidic studies design and preparation.

I would also thank all my colleagues in Charpentier's Lab, Dr. Nasrin Farhangi, Dr. Lijuan Yang, Dr. serge ayissi, Chao Chen, Qasem Alsharari, and Koosha Azhie for their cooperation, friendship, and help.

Words are not enough to express my gratitude towards my family. I wish to thank my parents, Mina and Mohammadreza, to whom this thesis is dedicated. Without their dedication, unconditional love, emotional support, guidance, and encouragement I would not have been able to accomplish my academic pursuits. I thank my lovely sister, Mehrnoush, whose love, support, and endless patience have been truly inspirational throughout all my endeavors. I also owe my true friends, Alireza and Sahar, for their support, patience, and love.

www.manaraa.com

Finally, I would like to mention that this work has been carried out with support from The Ontario Ginseng Innovation & Research Consortium (OGIRC).

www.manaraa.com

Table of Contents

Abstract ii

Co-Authorship Statement vi

Dedication viii

Acknowledgments ix

Table of Contents xi

List of Tables xvi

List of Figures xvii

List of Appendices xxiii

List of Abbreviations, Symbols, Nomenclature xxiv

Chapter 1 1

1 General Introduction and Literature Review 1

1.1 Vascular necrosis of femoral head 1

1.2 Cementation 5

1.2.1 PMMA-based bone cements 6

1.2.2 Poly(propylene fumarate)-based bone cements and properties 8

1.3 Angiostimulating activity of ginsenoside Rg_1 16

1.4 Inorganic reinforcing agents 18

1.4.1 Hydroxyapatite 18

1.4.2 Hydroxyapatite/titania nanocomposites 20

1.4.3 Titania 21

1.4.4 Synthesis of nanostructured materials in supercritical CO_2 22

1.5 Microencapsulation of bioactive molecules into a polymer matrix 23

1.5.1 Techniques for bioactive molecules-loaded microspheres preparation 25

www.manaraa.com

1.6 Scope of the research 25

1.7 References 27

Chapter 2 40

2 Synthesis and Characterization of Novel TiO_2-Poly(propylene fumarate) Nanocomposites for Bone Cementation 40

2.1 Introduction 41

2.2 Experimental details 43

2.2.1 Materials 43

2.2.2 Characterization 44

2.2.3 Preparation of materials 45

2.3 Results and Discussion 50

2.3.1 Synthesis of poly(propylene fumarate) (PPF) 50

2.3.2 Preparation of TiO_2-PPF nanocomposites and bone cement composites . 54

2.3.3 Mechanical properties of crosslinked PPF and bone cement composites. 62

2.4 Conclusions 66

2.5 References 68

Chapter 3 72

3 Delivery of an angiogenic mediator for bone regeneration in a radiopaque Sr-doped TiO_2/poly(propylene fumarate) based bone cement 72

3.1 Introduction 73

3.2 Experimental details 76

3.2.1 Materials 76

3.2.2 Characterization 77

3.2.3 Preparation of materials 81

3.3 Results and Discussion 88

www.manaraa.com

3.3.1 X-ray diffraction analysis of Sr-doped TiO_2 nanoparticles synthesized in supercritical CO_2 88

3.3.2 Scanning electron microscopy (SEM) and energy-dispersive X-ray spectroscopy (EDX) analyses of Sr-doped TiO_2 nanoparticles synthesized in supercritical CO_2 90

3.3.3 X-ray photoelectron spectroscopy (XPS) measurement of Sr-doped TiO_2 and Sr^{2+}-TiO_2/PPF nanocomposites nanocomposites 91

3.3.4 Fourier transform infrared (FTIR) spectroscopy of Sr^{2+}-TiO_2/PPF nanocomposites 94

3.3.5 TGA 95

3.3.6 Mechanical testing (tensile and flexural strength and modulus) 96

3.3.7 Radiopacity 100

3.3.8 Angiogenesis effect/tube formation of HUVEC cell line 101

3.3.9 *In vitro* drug release behavior of Rg_1 103

3.4 Conclusions 106

3.5 References 107

Chapter 4 113

4 Encapsulation of ginsenoside Rg_1 within PPF Microspheres using Microfluidic Technique 113

4.1 Introduction 114

4.2 Experimental details 117

4.2.1 Materials 117

4.2.2 Characterization of PPF microspheres encapsulating ginsenoside Rg_1 .. 118

4.2.3 Preparation of materials 119

4.2.4 Determination of encapsulation efficiency (EE) of Rg_1-loaded PPF microspheres 122

4.2.5 *In vitro* release of ginsenoside Rg_1 123

4.2.6 Angiogenic activity of ginsenoside Rg_1 before encapsulation into and after release from the PPF microspheres 123

www.manaraa.com

4.3 Results and Discussion 124

4.3.1 Surface morphology and particle size analysis of the Rg_1-loaded PPF microspheres 124

4.3.2 Encapsulation efficiency of Rg_1 in the PPF microspheres 126

4.3.3 Fourier transform infrared (FTIR) spectroscopy of Rg_1, PPF, and Rg_1-loaded PPF microspheres 127

4.3.4 X-ray diffraction analysis of Rg_1, placebo PPF microspheres, and Rg_1-loaded PPF microspheres 128

4.3.5 XANES spectroscopy of Rg_1, PPF, and Rg_1-loaded PPF microspheres. 129

4.3.6 Release of ginsenoside Rg_1 from delivery system *in vitro* 131

4.3.7 Angiogenesis effect/tube formation of HUVEC cell line 133

4.4 Conclusions 136

4.5 References 138

Chapter 5 142

5 Hydroxapatite-TiO_2-based Nanocomposites Synthesized in Supercritical CO_2 for Bone Tissue Engineering: Physical and Mechanical Properties 142

5.1 Introduction 143

5.2 Experimental details 145

5.2.1 Materials 145

5.2.2 Characterization 145

5.2.3 Preparation of materials 147

5.3 Results and Discussion 150

5.3.1 SEM and TEM characterization of the as-synthesized HAp and calcined HAp-TiO_2 composites powders 150

5.3.2 EDS analysis of HAp and HAp-TiO_2 nanocomposites 154

5.3.3 XRD analysis of HAp and HAp-TiO_2 nanocomposites 156

5.3.4 FTIR spectroscopy of HAp and HAp-TiO_2 nanocomposites 158

www.manaraa.com

5.3.5 BET analysis of HAp and HAp-TiO_2 nanocomposites synthesized in supercritical CO_2 159

5.3.6 XPS measurements of HAp and HAp-TiO_2 nanocomposites synthesized in supercritical CO_2 161

5.3.7 XANES spectroscopies of TiO_2, HAp, and HAp-TiO_2 nanocomposites synthesized in supercritical CO_2 164

5.3.8 TGA of HAp and HAp-TiO_2 nanocomposites 167

5.3.9 Mechanical properties of PCL/HAp and PCL/HAp-TiO_2 composites 169

5.4 Conclusions 172

5.5 References 174

Chapter 6 179

6 Conclusions and Recommendations 179

6.1 Conclusions 179

6.2 Recommendations 182

Appendices 185

Appendix A. Calibration curve of Rg_1 185

Appendix B. Copyright releases. 186

Curriculum Vitae 192

www.manaraa.com

List of Tables

Table 1.1. ARCO international classification of osteonecrosis.[24] 4

Table 2.1. Formulation of the TiO_2-PPF nanocomposites. 48

Table 2.2. Formulation of the bone cement composites. 49

Table 2.3. Mechanical Properties of the crosslinked PPF and the synthesized bone cement composites. 64

Table 3.1. Formulation of the Sr^{2+}-TiO_2/PPF nanocomposites. 85

Table 3.2. The different compositions for the bone cement composites in each system. 87

Table 3.3. Elemental composition of Sr-doped TiO_2 nanofibers (n = 3, mean ± SD). 91

Table 3.4. Radiopacity values (mm Al) of bone cement composites of equivalent Al thickness (means ± SD). 100

Table 5.1. Synthesis conditions of HAp and HAp-TiO_2 nanostructures in $scCO_2$ and characterization results (morphology and BET surface area). 151

Table 5.2. Ca/P atomic ratio of HAp powders and HAp-TiO_2 nanocomposites. 156

Table 5.3. Atomic percentage of the elements detected in the HAp-2 and HAp-TiO_2-2 samples. 162

Table 5.4. Mechanical Properties of PCL/HAp and PCL/HAp-TiO_2 composites. 171

www.manaraa.com

List of Figures

Figure 1.1. The lack of normal blood supply to the femoral head causes the bone to die. 2

Figure 1.2. The operative procedure of cementation for osteonecrosis of femoral head... 6

Figure 1.3. Cross-linking reaction of PPF and PPF-DA to synthesize PPF/PPF-DA polymer networks.[45] 9

Figure 1.4. Degradation scheme of PPF/PPF-DA networks.[57] 10

Figure 1.5. Multi-step process of blood vessels formation. 15

Figure 1.6. The schematic overview of ginsenoside Rg_1-mediated angiogenic action in HUVEC. 17

Figure 1.7. Crystal structure of stoichiometric hydroxyapatite. 20

Figure 2.1. Crosslinking and degradation scheme of PPF-PPF-PVP networks. 42

Figure 2.2. Synthetic Scheme for the Preparation and Functionalization of PPF. 51

Figure 2.3. A comparison of ^{1}H NMR spectra of (a) propylene glycol, (b) the synthesized PPF, and (c) MA-PPF in $CDCl_3$. 52

Figure 2.4. ^{1}H NMR spectrum of the synthesized PPF in $CDCl_3$ showing integrals of the peaks. 53

Figure 2.5. A comparison of ^{13}C NMR spectra of (a) propylene glycol, (b) the synthesized PPF, and (c) MA-PPF in $CDCl_3$ 54

Figure 2.6. (a) SEM and (b) TEM images and the distribution of (c) diameter and (d) aspect ratio of the synthesized TiO_2 nanofibers. 55

Figure 2.7. Synthetic Scheme for the preparation of (4) TiO_2-PPF nanocomposites and (5) bone cement composites. 56

www.manaraa.com

Figure 2.8. ATR-FTIR spectra of (a) TiO_2, (b) PPF, (c) TiO_2-PPF nanocomposite, and (d) crosslinked bone cement composite. 57

Figure 2.9. Binding modes of RCOO- with TiO_2 surface (R= H or CH_3). 58

Figure 2.10. High resolution XPS record of C 1s region of (a) PPF and (b) MA-PPF, high resolution XPS record of O 1s region of (c) PPF and (d) MA-PPF, (e) XPS full-scan spectrum of the TiO_2-PPF nanocomposite, high resolution XPS scan of the C 1s region of (f) the TiO_2-PPF nanocomposite and (g) the mechanically mixed TiO_2-PPF nanocomposite, high resolution XPS scan of the O 1s region of (h) the TiO_2-PPF nanocomposite, and high resolution XPS scan of the Ti 2p region of (i) the TiO_2-PPF nanocomposite. 60

Figure 2.11. TGA curves of: (a) TiO_2, (b) PPF, (c) crosslinked PPF, (d) TiO_2-PPF nanocomposite (synthesized using 1 g of MA-PPF and 0.0250 g of TiO_2) and (e) crosslinked bone cement composite (made of 1 g of TiO_2-PPF synthesized using 0.0250 g of TiO_2). 61

Figure 2.12. Derivative thermogravimetric (DTG) curves of: (a) PPF, (b) crosslinked PPF, (c) (d) TiO_2-PPF nanocomposite (synthesized using 1 g of MA-PPF and 0.0250 g of TiO_2) and (e) crosslinked bone cement composite (made of 1 g of TiO_2-PPF synthesized using 0.0250 g of TiO_2). 62

Figure 2.13. SEM images of the fracture planes of (a) crosslinked unmodified PPF, (b) bone cement composite-1, (c) crack bridging within the bone cement composite-1, and (d) bone cement composite-2. 66

Figure 3.1. Synthetic scheme for the preparation and functionalization of PPF and the synthesis of Sr^{2+}-TiO_2/PPF nanocomposite and bone cement composite. 84

Figure 3.2. Powder XRD spectra of (a) TiO_2, (b) Sr-doped TiO_2 synthesized using 20 wt% of $Sr(NO_3)_2$, and (c) ZrO_2-modified TiO_2 nanofibers..... 89

www.manaraa.com

Figure 3.3. SEM images of (a) the 5 wt% Sr-doped TiO_2 and (b) the 20 wt% Sr-doped TiO_2 and EDX Spectra of (c) the 5 wt% Sr-doped TiO_2 and (d) the 20 wt% Sr-doped TiO_2. 91

Figure 3.4. (a) XPS full-scan spectrum of the Sr-doped TiO_2 nanoparticles, high resolution XPS record of O 1s region (b), high resolution XPS scan of the Ti 2p region (c), and high resolution XPS scan of the Sr 3d region (d) of the Sr-doped TiO_2 nanoparticles and high resolution XPS record of the C 1s region (e), high resolution XPS record of the O 1s region (f), high resolution XPS scan of the Ti 2p region (g), and high resolution XPS scan of the Sr 3d region (h) of the Sr^{2+}-TiO_2/PPF nanocomposite-3. 93

Figure 3.5. ATR-FTIR spectra of (a) PPF, (b) Sr^{2+}-TiO_2/PPF nanocomposite-3, and (c) crosslinked bone cement composite-3. 95

Figure 3.6. (A) TGA curves of: (a) TiO_2, (b) PPF, (c) crosslinked PPF, (d) Sr^{2+}-TiO_2/PPF nanocomposite-3 (synthesized using 1 g of MA-PPF and 0.015 g of Sr-doped TiO_2), and (e) crosslinked bone cement composite-3 (made of 1 g of Sr^{2+}-TiO_2/PPF synthesized using 0.015 g of Sr-doped TiO_2). (B) Derivative thermogravimetric (DTG) curves of: (a) PPF, (b) crosslinked PPF, (c) Sr^{2+}-TiO_2/PPF nanocomposite-3 (synthesized using 1 g of MA-PPF and 0.015 g of Sr-doped TiO_2), and (d) crosslinked bone cement composite-3 (made of 1 g of Sr^{2+}-TiO_2/PPF synthesized using 0.015 g of Sr-doped TiO_2). 96

Figure 3.7. Mechanical properties of cross-linked bone cement composites as a function of the Sr-doped TiO_2 nanofibers concentration..... 98

Figure 3.8. SEM images of the fracture planes of: (a) crosslinked unmodified PPF, (b-d) bone cement composite-2, and (e) bone cement composite-3 (the arrows show Sr-doped TiO_2 nanofibers are agglomerating at higher concentrations within the polymer matrix).99

Figure 3.9. Tube formation of HUVECs cell line cultured in different extract-contained media from bone cements. 103

www.manaraa.com

Figure 3.10. The cumulative amount of released ginsenoside Rg_1 from Rg_1-loaded bone cement composite-1, Rg_1-loaded bone cement composite-2, and Rg_1-loaded bone cement composite-3. 105

Figure 4.1. Chemical structure of (a) ginsenoside Rg_1 and (b) PPF 117

Figure 4.2. Schematic of the double emulsion method. 120

Figure 4.3. Schematic of the microfluidic system. 122

Figure 4.4. SEM images of Rg_1-loaded PPF microspheres from (a, b) double emulsion method and (c, d) microfluidic method where the continuous phase flow rate and disperse phase flow rate was 0.1 and 0.01 ml/min, respectively, and (e, f) microfluidic method where the continuous phase flow rate and disperse phase flow rate was 0.2 and 0.01 ml/min, respectively. 125

Figure 4.5. Image J number of size distributions for Rg_1-loaded PPF microspheres. ... 126

Figure 4.6. FTIR spectra of (a) ginsenoside Rg_1, (b) PPF, and (c) Rg_1-loaded PPF microspheres prepared using microfluidic method. 128

Figure 4.7. XRD patterns of (a) background, (b) placebo PPF microspheres prepared using microfluidic method, (c) ginsenoside Rg_1, and (d) Rg_1-loaded PPF microspheres prepared using microfluidic method. 129

Figure 4.8. (a) C K-edge XANES spectra of pure PPF microspheres, ginsenoside Rg_1, and Rg_1-loaded PPF microspheres prepared using microfluidic method. (b) Linear fitting of the Rg_1-loaded PPF microspheres prepared using microfluidic method. Inset shows the π^* resonance. 131

Figure 4.9. Release profiles of ginsenoside Rg_1 from monodisperse PPF microspheres. 133

Figure 4.10. Tube formation of HUVECs cell line cultured in different extract-contained media from PPF microspheres. 136

www.manaraa.com

Figure 5.1. Schematic representation of the preparation of HAp precursor. 149

Figure 5.2. Schematic representation of sol-gel process for producing HAp-TiO_2 composites..... 149

Figure 5.3. SEM images of the (a) TiO_2 nanotubes calcined at 450 °C, (b) as-prepared HAp-1 nanoplates, (c) as-prepared HAp-2 nanoplates, (d) HAp-TiO_2-1 nanocomposites calcined at 500 °C, (e) HAp-TiO_2-2 nanocomposites calcined at 500 °C, and (f) HAp-TiO_2-h nanocomposites and TEM images of (g) HAp-TiO_2-2 nanocomposites calcined at 500 °C and (h) HAp-TiO_2-h nanocomposites. Arrows in Figure 5.3c indicate the voids between aggregates of plate-like HAp secondary particles. 154

Figure 5.4. EDS elemental mapping of HAp-TiO_2-2 nanocomposites: (a) selected area on the sample, (b) O mapping, (c) Ti mapping, (d) P mapping, and (e) Ca mapping. 154

Figure 5.5. EDS elemental mapping of HAp-TiO_2-h nanocomposites: (a) selected area on the sample, (b) O mapping, (c) Ti mapping, (d) P mapping, and (e) Ca mapping. 155

Figure 5.6. EDX spectra of the (a) HAp-2 and (b) HAp-TiO_2-2 nanocomposites. 156

Figure 5.7. XRD patterns of the (a) HAp-2, (b) HAp-TiO_2-2, and (c) HAp-TiO_2-h nanocomposites. In Figure 5.7b&c, filled triangles are representing the prominent characteristic peaks of anatase TiO_2. 158

Figure 5.8. Fourier transform infrared (FTIR) spectroscopy of the (a) HAp-2, (b) HAp-TiO_2-2, and (c) HAp-TiO_2-h nanocomposites. 159

Figure 5.9. N_2 adsorption/desorption isotherm of the (a) HAp-2 and (b) HAp-TiO_2-2 nanocomposites..... 160

Figure 5.10. (a) XPS survey spectrum of the HAp-2 and core level spectra of (b) Ca 2p, (c) P 2p, and (d) O 1s recorded from the HAp-2 and (e) XPS survey spectrum of the HAp-TiO_2-2 and core level spectra of (f) Ca 2p, (g) P 2p, (h) O 1s, and (i) Ti 2p recorded from the HAp-TiO_2-2..... 164

www.manaraa.com

Figure 5.11. Ti $L_{3,2}$-edge XANES spectra of the (a) TiO_2 nanoparticles calcined at 450 °C, (b) TiO_2 nanoparticles calcined at 750 °C, and (c) HAp-TiO_2-2 nanocomposite. ... 165

Figure 5.12. Ca $L_{3,2}$-edge XANES spectra of the (a) HAp and (b) HAp-TiO_2-2 nanocomposite powders. ... 166

Figure 5.13. (I) O K-edge XANES spectra of the (b) HAp-TiO_2-2 nanocomposites in comparison with (b) HAp-2, (c) TiO_2 nanoparticles calcined at 450 °C, and (d) TiO_2 nanoparticles calcined at 750 °C. **(II)** O K-edge linear fitting of the HAp-TiO_2-2 nanocomposites. ... 167

Figure 5.14. TGA spectrum of (a) HAp-2, (b) HAp-TiO_2-2 nanocomposites, and (c) HAp-TiO_2-h nanocomposites ... 169

Figure 5.15. SEM images of the fracture surfaces of (a) PCL/HAp and (b-d) PCL/HAp-TiO_2 containing 20 wt% HAp and HAp-TiO_2, respectively. Short arrows indicate nanorods pullout and the long arrows indicate crack bridging by the TiO_2 nanorods. ... 171

www.manaraa.com

List of Appendices

Appendix A. Calibration curve of Rg_1 185

Appendix B. Copyright releases. 186

www.manaraa.com

List of Abbreviations, Symbols, Nomenclature

Abbreviations

AcOH	Acetic acid
ARCO	Association Research Circulation Osseous
AL	Actual drug loading
Al_2O_3	Alumina
BET method	Brunauer-Emmet-Teller method
bFGF	Basic fibroblast growth factor
BMSCs	Bone marrow stromal cells
BMP-2	Bone morphogenic protein-2
BPO	Benzoyl peroxide
CaP	Calcium phosphate
CT	Computed tomography
DCM	Dichloromethane
1D	One dimensional
3D	Three-dimensional
DMA	Dynamic mechanical analyzer
DMAP	4-dimethylaminopyridine
DMT	N-dimethyl-p-toluidine
DTG	Derivative thermogravimetric
EDX	Energy-dispersive x-ray spectroscopy
EE	Encapsulation efficiency
eNOS	Endothelial nitric oxide synthase
FGFR-1	Fibroblast growth factor receptor-1
FTIR	Fourier transform infrared spectroscopy
FS	Flexural strength
FM	Flexural modulus
GR	Glucocorticoid receptor
HAp	Hydroxyapatite

www.manaraa.com

HUVEC	Human umbilical vein endothelial cells
MA	Maleic anhydride
NMR	Nuclear magnetic resonance
NO	Nitric Oxide
N-VP	N-vinyl-2-pyrrolidinone
PBS	Phosphate buffered solution
PCL	Poly(ε-caprolactone)
PDMS	Poly(dimethylsiloxane)
PLGA	Poly(lactic-co-glycolic acid)
PLLA	Poly(L-lactic acid) (PLLA)
PMMA	Poly(methyl methacrylate)
PPF	Poly(propylene fumarate)
PPF-DA	poly(propylene fumarate)-diacrylate
PVA	Poly (vinyl alcohol)
PVP	Poly(N-vinyl pyrrolidone)
$scCO_2$	Supercritical CO_2
SCF	Supercritical fluids
SEM	Scanning electron microscope
SWNTs	Single-walled carbon nanotubes
SFE	Supercritical fluid extraction
TCP	Tricalcium phosphate
TEM	Transmission electron microscopy
TGA	Thermogravimetric analysis
THF	Tetrahydrofuran
THR	Total hip replacement
n-TiO_2 fibers	Titania nanofibers
TIP	Titanium isopropoxide
TRD	Texas red dextran
TTCP	Tetracalcium phosphate
UV-Vis	Ultraviolet-visible
VEGF	Vascular endothelial growth factor
XANES	X-ray absorption near edge structure
XPS	X-ray Photoelectron Spectroscopy

www.manaraa.com

XRD	X-ray diffraction
ZrO_2	Zirconium dioxide

Symbols

P	Pressure (psi)
P_c	Critical pressure (psi)
T_c	Critical temperature (°C)
T	Temperature (°C)

www.manaraa.com

Chapter 1

1 General Introduction and Literature Review

1.1 Vascular necrosis of femoral head

Blood circulation is a key factor to have healthy bone tissue, since it transports oxygen, nutrition, carbon dioxide, waste, and other materials to and from bone cells.[1] However, there are many risk factors which can cause the temporary or permanent loss of blood supply to bone. Reduced blood flow to bones will result in osteonecrosis, which mainly occurs in the weight-bearing parts of the body, for example the anterosuperior aspect of the femoral head, as shown in Figure 1.1.[2] Osteonecrosis is a disease with a wide ranging etiology and poorly understood pathogenesis,[3] being most common in adults between the ages of 20 and 50 years.[4] Regardless of what causes the death of the bone cell, the cellular events and therefore the tissue responses constituting the repair are the same whether the cells are killed by interfering with their blood supply, by freezing them, or killing them with cytotoxic chemical agents.[5] Because of this common path for repair and the fact that the actual cause of cell death is unknown in most cases, the term “osteonecrosis” is used rather than “avascular necrosis”, which indicates a distinct etiology for cell death.[5]

www.manaraa.com

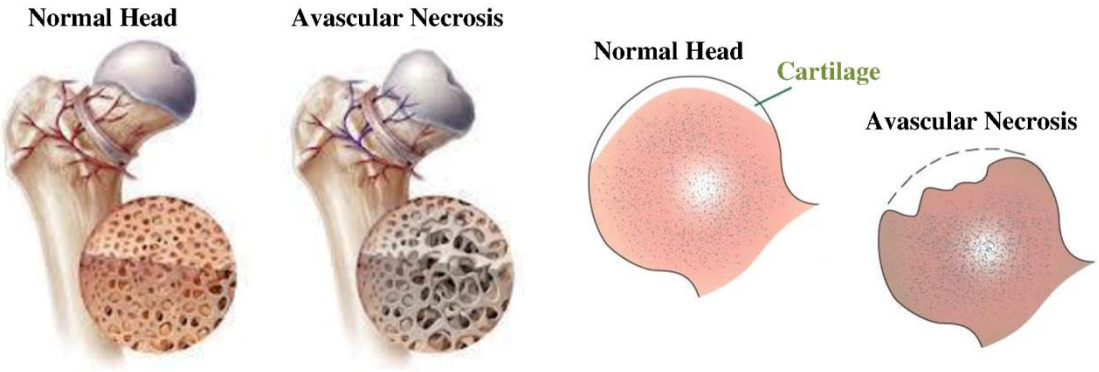

Figure 1.1. The lack of normal blood supply to the femoral head causes the bone to die.

Etiology is the study of the factors that cause a disease. Trauma-induced avascular necrosis of the femoral head represents the most common type of aseptic osteonecrosis.[6] With the stress of weight-bearing, the necrotic segment of bone is likely to collapse leading to painful degenerative arthritis of the hip.[7] Therefore, the term "avascular necrosis" is exclusively used for this post-traumatic group, as they originate in ischemia resulting from blood flow interruption.[6] When the mechanism of necrosis is not clearly understood, the etiology is often presumed on the basis of an association with a particular risk factor.[2] For example, obesity and gout are considered to be frequent as noted by R. Merle d'Aubigne, but their role is uncertain.[8] Moreover, alcoholism is implicated as a risk factor for avascular necrosis as Ono and Sugioka identified an increased risk for avascular necrosis in people who drank as little as 400 milliliters of alcohol per week.[9] In addition, steroid therapy in which corticosteroids were dministered before pain appeared in the hip accounts for a rising incidence of necrosis of the femoral head.[10, 11] Exposure to corticosteroids and alcohol consumption are responsible for approximately 90% of all reported causes of avascular necrosis.[2] Age is also considered to be a modulating factor having an influence on the development of avascular necrosis, although the reported data are contradictory.[12] According to Brown there is a strong relationship between older age and higher incidence of avascular necrosis;[13] however, Barnes et al. reported a decrease in the avascular necrosis incidence beyond the age of 75.[14] Furthermore, women have shown a higher tendency

www.manaraa.com

towards avascular necrosis than men.[12] Besides, there is a higher number of avascular necrosis incidence among patients with a higher level of activity before fracture.[6]

Pathogenesis deals with the cellular events, reactions, and other pathological mechanisms happening in the progression and development of a disease.[2] Multiple theories about the mechanism of interruption of the blood supply to the femoral head have been formulated.[2, 8] Some of these theories comprise thromboemboli in the blood supply to bone resulting from circulating fat or nitrogen bubbles,[15] abnormally shaped red blood cells causing sickle-cell anaemia,[16] infection and vasculitis leading to vessel wall injury,[2] and radiation damage or release of vasoactive factors as in Gaucher disease.[17]

Osteonecrosis of the femoral head leads to end-stage degenerative arthritis, which is responsible for approximately 10% of the primary total hip arthroplasties performed in the United States.[18] If no treatment is applied, more than 70% of osteonecrotic femoral heads will collapse and require prosthetic replacement within three to four years of diagnosis.[19] In early stages of osteonecrosis, the goal is to avoid collapse.[20] Present surgical treatments such as core decompression and bone grafting have been the most effective treatments for necrosis of the femoral head at an early stage.[4] However, these methods consume time for biologic incorporation of bone graft, revascularization, or replacement of dead bone by creeping substitution, and are less efficacious in Stages III and IV.[20] When lesions are large and collapse has already occurred, the goal is to halt additional collapse and to restore femoral head sphericity.[21] Bone grafting techniques are less successful at joint restoration once collapse occurs (Stage III osteonecrosis), so the open reduction and cement fixation (cementation) can be more efficacious;[4, 20] total hip arthroplasty is the most successful treatment for Stage IV.[22]

The Association Research Circulation Osseous (ARCO) international classification system classifies osteonecrosis into five stages (0-IV) using computer tomography (CT) scanning, magnetic resonance imaging (MRI), and bone scanning findings summarized in Table 1.1.[23] Stage 0 includes at-risk patients, who have shown no positive radiographic, MRI, or scintigraphic findings. Patients with Stage I osteonecrosis have

www.manaraa.com

normal radiographs and CT scans with positive MRI or scintigraphic findings or both, and they are treated by core decompression. In Stage II osteonecrosis, a mottled and sclerotic rim around the area of necrosis is evident in radiographs and CT scans in addition to the MRI changes diagnostic for osteonecrosis. These patients are treated with vascularized free fibular grafts. Based on the location and extent of infarct size, Stages I and II are subcategorized into three types (A, B, and C). Patients with Stage III osteonecrosis show a crescent sign, flattening, or both in radiographs and CT scan, and they are treated by open reduction and cementation. Stage III is also subdivided (A, B, and C) using the quantification of collapse.[20] In Stage IV osteonecrosis, arthritic findings become evident, and total hip arthroplasty is the most successful treatment for Stage IV.[20]

Table 1.1. ARCO international classification of osteonecrosis.[24]

Stage	**0**	**I**	**II**	**III**	**IV**
Findings	All present diagnostic techniques are normal or non-diagnostic	X-ray and CT-scan are normal. At least one of the below mentioned techniques is positive	NO subchondral fracture (Crescent Sign). X-ray shows abnormalities: a mottled aspect , sclerosis, osteolysis, and focal porosis	Crescent Sign on the X-ray and/or flattening of articular surface of femoral head	Osteoarthritis joint space narrowing, acetabular changes, joint destruction
Techniques	X-ray and CT Scintigraph MRI	Scintigraph MRI *Quantitate on MRI	X-ray, CT Scintigraph MRI *Quantitate on MRI & X-ray	X-ray, CT Only *Quantitate on X-ray	X-ray Only
Subclassification	NO	LOCATION 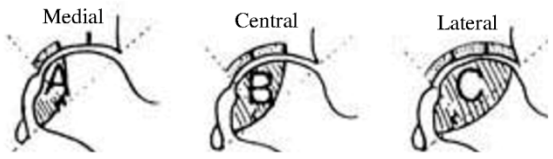			NO
Quantitation	NO	QUANTITATION **% area of femoral head involvement** minimal A < 15 % moderate B 15-30% extensive C > 30% **length of crescent** A < 15 % B 15-30% C > 30% **% surface collapse & dome depression** 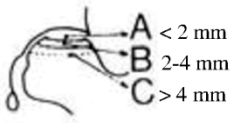			NO

www.manaraa.com

1.2 Cementation

Cement fixation is a recently introduced method for treating stage III osteonecrosis of femoral heads. Bone cementation involves the injection of fluid material, which instantly hardens in the defect, and provides mechanical support to prevent collapse.[20] Bone cement is considered to make the treatment of irregular defects easier. It is also easier to use for clinical practice, providing immediate symptomatic relief and faster recovery of the patient, while allowing improvement in mobility.[23, 25] Cement augmentation has the potential to maintain reduction and restore femoral head sphericity and prevent further collapse before progression to stage IV disease.[21, 25] However, the long term results in regard to progression of disease and secondary arthritis is unknown. The possible indication for this procedure is a young patient with stage III osteonecrosis who has active, unresolved disease.[4, 20]

The procedure is performed with the patient in the lateral decubitus position. A 20-cm incision is made centered over the greater trochanter, and a T-shaped capsulotomy is made at the base of the femoral neck. Using a skeletal traction device, subluxation and distraction of the femoral head and observation of the pathologic area of articular cartilage is performed. Then, a 6-mm hole is drilled in the neck (Figure 1.2(A)), which allows access for debridement of dead bone and insertion of cement. A joker is used to elevate the necrotic bone and reduce the collapse. Next, the high or low viscosity cement is pressurized by injection with a cement gun into the femoral head, and the injection is completed when the shape of the femoral head is restored. Reduction of the collapsed segment is performed under direct observation, and the cement is allowed to harden with contouring and molding of the femoral head by the acetabulum. A small bone dowel graft from the greater trochanter is used to plug the hole (Figure 1.2(B)). After the operation, the patient is encouraged to mobilize the hip, while weight-bearing is only permitted after 3 weeks with the assistance of crutches for as many as 6 months.[4, 20]

www.manaraa.com

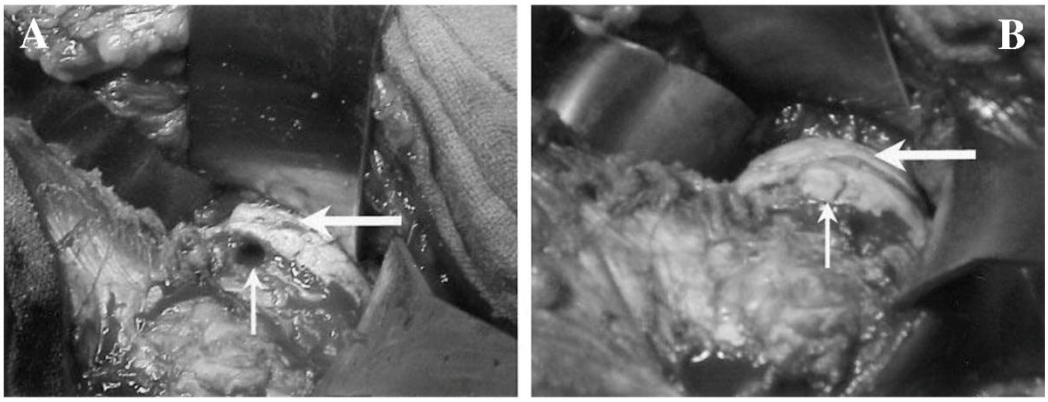

Figure 1.2. The operative procedure of cementation for osteonecrosis of femoral head.

A small burr hole is created at the base of the cartilage allowing for debridement of necrotic bone and access for the cement (small arrow). Cartilage deformity is shown (large arrow) (A). A small bone dowel taken from the greater trochanter is placed in the entry hole (small arrow). The cartilage deformity has been reduced (large arrow) (B).[20]

1.2.1 PMMA-based bone cements

The history of bone cements goes back more than 100 years ago. Gluck et al. reported the use of ivory ball-and-socket joints in the treatment of hip joint diseases.[26] They used a cement composed of colophony, pumice powder, and plaster to stabilize these joints in the bone.[27] The most universally used injectable bone cement is made of poly(methyl methacrylate) (PMMA).[28] Haboush presented a self-curing acrylic dental cement to secure a total hip replacement.[26, 29] At this time, PMMA cements were mostly used in dentistry to produce partial dentures, artificial teeth, orthodontic retainers, denture repair resins, and so forth. However, Charnley pioneered the use of PMMA in total hip replacement (THR) in 1964 to secure fixation of the acetabular and femoral components and to transfer loads to bone.[30, 31] Nowadays, several million joint replacements are performed worldwide each year with more than half of them using bone cements, with an increasing trend.[32] In 1982 Ewald et al. performed hip arthroplasties that preserved a normal articular surface, whereby the trabecular bone of the femoral head was replaced with PMMA in experimental animals.[33] In addition, Wood et al. first practiced the use

www.manaraa.com

of PMMA in cement augmentation for the treatment of stage III vascular necrosis of the femoral head in 2000, and found that the use of this procedure should be restricted to symptomatic, young patients (less than 40 years), preferably with mild to moderate Stage III osteonecrosis.[4]

1.2.1.1 Drawbacks associated with PMMA

PMMA is reportedly bioinert and shows good biocompatibility over long-term follow-up.[34] Several inherent advantages to PMMA include familiarity for operating physicians, ease of handling, good biomechanical strength and stiffness, and cost-effectiveness.[35] However, there are several disadvantages associated with PMMA bone cements.[26] Firstly, PMMA is nonbiodegradabile; thus, it cannot be replaced with new bone formation.[36, 37] Secondly, the high exothermic reaction during polymerization, ranging between 67 and 124 °C at the center of the cement mantle *in vivo* results in impaired local blood circulation and thermal necrosis of the surrounding bone at the cement-bone interface.[38] Thirdly, the release or leakage of unreacted monomer liquid before polymerization of the cement in the bone bed may cause chemical necrosis of the bone.[38] Forthly, the foreign body reaction at the cement-bone interface indicates that PMMA cement is not bioinert and biocompatible. The cellular responses or tissue reactions might be associated with the chemical effects from unreacted MMA monomer produced during the setting process, and may be involved as the possible cause of junctional tissue damage and cement loosening.[36] According to Herman et al., PMMA cement particles evoke inflammatory periprosthetic tissue responses directly affecting the bone resorption at the cement-bone interface.[39] Fifthly, PMMA bone cements suffer from shrinkage during polymerization.[38] In addition, toxic substances or unreacted monomers released during the setting process may jeopardize the repairing process such as cell proliferation, neovascularization, and the dead bone resorption by osteoclasts or new woven bone formation by osteoblasts.[36, 37] Therefore, it is of great necessity to develop a bioactive bone cement which is nontoxic, isothermic curing, mechanically capable, and has osteoconductive and osteoinductive properties.

www.manaraa.com

1.2.2 Poly(propylene fumarate)-based bone cements and properties

Recently, poly(propylene fumarate) (PPF) has attracted considerable interest as a promising degradable material for treating skeletal defects.[40] PPF is a linear and unsaturated polyester made of repeating units, which contain one unsaturated carbon-carbon double bond allowing for cross-linking of the polymer into a covalent polymer network and two ester linkages for hydrolysis of the polymer into biocompatible products fumaric acid and propylene glycol, both of which can be absorbed by the body.[41, 42] Cross-linked PPF is often incorporated with calcium phosphates found to provide comparable mechanical properties to those of human trabecular bone.[43] Although the double bonds of PPF can cross-link with itself to form cross-linked polymer networks,[44] a variety of cross-linking agents such as N-vinyl pyrrolidinone (N-VP), poly(propylene fumarate)-diacrylate (PPF-DA), poly(ethylene glycol)-dimethacrylate (PEG-DMA), diethyl fumarate, and methylmethacrylate (MMA) have been explored in combination with PPF.[45] When combined with an appropriate initiator system, it may be cross-linked *in situ* during surgery to form a solid biodegradable bone cement via an addition polymerization reaction between PPF and cross-linking reagents.[46] The chemical structure of PPF and PPF-DA and cross-linking reaction of PPF and PPF-DA are shown in Figure 1.3. As the cross-linking reaction proceeds, the viscous polymer is transformed to a putty-like state before solidifying. During this transition, the material may be injected or molded into a bone defect. It is particularly interesting for orthopaedic applications in filling irregularly shaped bone defects, which are relatively inaccessible, with minimal surgical intervention.[41] Addition polymerization reactions are generally exothermic as in the case of PMMA bone cements, which may cause some local tissue necrosis. In the case of PPF with N-VP used as a cross-linker, the generated heat by the addition polymerization reaction between PPF and N-VP is milder with no local tissue necrosis noted *in vivo* after implantation compared to the curing temperature measured for PMMA bone cement.[47] For example, the maximum cross-linking temperature reported for a range of formulations based on PPF, N-VP, benzoyl peroxide, and tricalcium phosphate (TCP) varied from 38 to about 48 °C.[48, 49] Besides, the curing times varied between 1 and 121 min allowing the composites to be tailored to specific applications.[49]

www.manaraa.com

The properties of cross-linked PPF networks, including mechanical strength, degradation kinetics, and handling of the polymer are dependent on the molecular characteristics of the constituent polymer, including the molecular weight and polydispersity of PPF.[46] It has been reported that achieving high molecular weight PPF is difficult. Typically PPF molecular weights vary from 500 to 4,000 Da, and polydispersities are generally below 1.4.[46] The major disadvantage of PPF is that it is a viscous liquid at room temperature, which makes handling of the polymer somewhat cumbersome.[50] As PPF molecular weight increases, its viscosity also increases, which often impacts the handling of the polymer and the intended applications.[46] Furthermore, a higher molecular weight PPF and a more viscous polymer solution may cause greater autoacceleration of the polymerization, leading to rapid release of heat.[48] However, the total heat released upon crosslinking decreased by an increase in PPF molecular weight.[51]

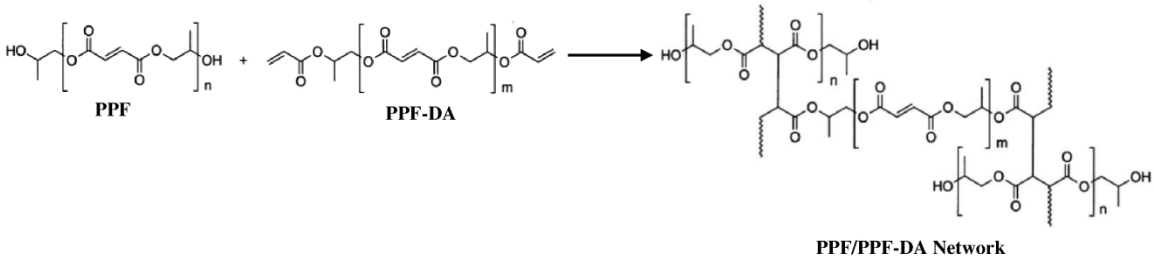

Figure 1.3. Cross-linking reaction of PPF and PPF-DA to synthesize PPF/PPF-DA polymer networks.[45]

PPF-based materials undergo only bulk degradation by hydrolysis of the ester linkages within its chemical structure.[52] PPF degrades to fumaric acid, a naturally occurring substance, found in the tri-carboxylic acid cycle (Krebs cycle), and propylene glycol, which is a commonly used diluent in drug formulations.[53, 54] Degradation time is dependent upon polymer structure as well as other factors.[54, 55] According to Timmer et al., PPF/PPF-DA systems represent a fairly slow *in vitro* degradation over 52 weeks in buffered saline solution at 37 °C.[56] They also demonstrated that low quantities of acrylic acid and poly(acrylic acid-co-fumaric acid) along with fumaric acid and propylene glycol were obtained upon degradation of PPF/PPF-DA via ester hydrolysis as illustrated in Figure 1.4.[45] According to Peter et al. PPF-based materials do not exhibit

www.manaraa.com

a deleterious long-term inflammatory response when implanted subcutaneously in rats and rabbits.[54] In addition, *in vitro* cytotoxicity studies by Timmer et al. demonstrated favorable cell viability in the presence of the water-soluble extracts of PPF/PPF-DA.[45] Consequently, PPF-based polymers have been widely explored for a number of biomedical applications, such as the fabrication of orthopedic implants, scaffolds for tissue engineering, controlled bioactive factor delivery systems, and cell transplantation vehicles owing to their injectability, biocompatibility, and biodegradability.

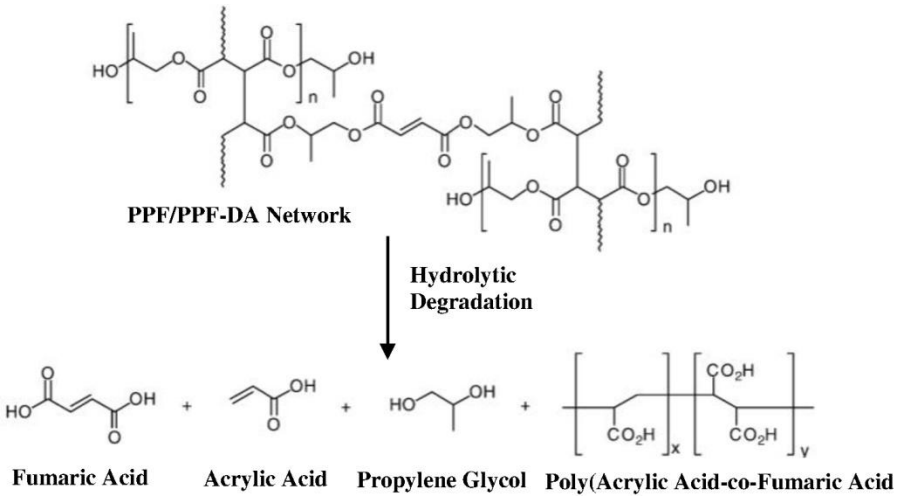

Figure 1.4. Degradation scheme of PPF/PPF-DA networks.[57]

1.2.2.1 Mechanical properties

The mechanical properties of PPF networks differ greatly depending on the synthesis method and the cross-linking agent.[58] Mechanical properties of PPF polymeric networks can be tailored by varying the molecular weight of PPF, the molecular weight of the cross-linking agent used for the formation of PPF-based network, and the ratio of the cross-linking agent to PPF.[56] Yaszemski et al. showed that PPF-based scaffolds have a greater degradation from the surface region compared to the interior of the scaffold specimen. When this material was used as a temporary replacement, it was able to provide the reconstructed skeletal region with adequate mechanical strength from the time of surgery, through the time that the material degraded and the region reconstituted itself with new bone, until the new bone provided the required mechanical properties.[59] As the PPF-based scaffold degrades from its surface and has new bone continually

www.manaraa.com

advance against that surface, it may allow the remaining bulk of nondegraded material farther from the surface to retain its mechanical properties and provide strength to the reconstructed region.[59] He et al. prepared PPF-based polymer networks by radical polymerization using PPF and PPF-DA macromers, and demonstrated a dramatic increase in the compressive strength of PPF/PPF-DA polymer networks as the double bond ratio of PPF/PPF-DA decreased.[60] Additionally, incorporation of ceramic filler materials such as hydroxyapatite (HAp),[42] tricalcium phosphate (TCP),[51] dicalcium phosphate dehydrate,[61] calcium carbonate,[54, 62] calcium sulfate,[54] or bioactive glasses[63] could be used to enhance the mechanical strength. Particularly β-TCP has been shown to be useful for reinforcement, and compositions without TCP reinforcement disintegrated very early in the implant.[54, 64] However, the development of composite materials combining PPF and inorganic particles has not been investigated to a large extent, in comparison with the extensive research efforts dedicated to PMMA-based composites.

Shi et al. investigated the effects of the dispersion of single-walled carbon nanotubes (SWNTs) and functionalized SWNTs (F-SWNTs) in unsaturated PPF, and examined the rheological properties of un-cross-linked nanocomposite formulations as well as the electrical and mechanical properties of cross-linked nanocomposites.[65, 66] F-SWNTs were produced from individual SWNTs by a diazonium-based method, and showed better dispersion than unmodified SWNTs in both un-cross-linked and cross-linked PPF matrixes. Mechanical testing demonstrated a 3-fold increase in both compressive modulus and flexural modulus and a 2-fold increase in both compressive offset yield strength and flexural strength of crosslinked nanocomposites compared to the pure PPF networks. Low SWNT concentrations of the order of 0.05 wt% gave the best properties.[65] In another attempt, Sitharaman et al. studied the effects of size and surface area of the carbon nanostructures on the rheological properties of un-cross-linked PPF nanocomposites and the mechanical properties of cross-linked nanocomposites as a function of the nanostructure loading. It was found that the rheological properties of un-cross-linked nanocomposites depend mainly on the carbon nanostructure size, while the mechanical properties of the cross-linked nanocomposites are dependent on the carbon nanostructure surface area.[67] However, there is a sustained debate regarding the

www.manaraa.com

biocompatibility of carbon nanotubes, and bone cement reinforced with carbon nanotubes may have adverse effects on the surrounding living cells.[68] Horch et al. studied the mechanical enhancement of cross-linked PPF using surface-modified carboxylate alumoxane nanoparticles.[69] They investigated various surface-modified nanoparticles, including a surfactant alumoxane, an activated alumoxane, a mixed alumoxane containing both activated and surfactant groups, and a hybrid alumoxane containing both groups within the same substituent. They found that hybrid alumoxane nanoparticles dispersed in PPF/PPF-DA exhibited over a 3-fold increase in flexural modulus at 1 wt % loading compared to the polymer resin alone. This dramatic improvement in flexural properties is attributed to the fine dispersion of nanoparticles into the polymer and the increased covalent interaction between the polymer chains and the surface-modified nanoparticles.[69]

1.2.2.2 Radiopacity

Radiopacity refers to the relative inability of electromagnetic radiation, specifically X-rays, to pass through a particular material. Radiopaque substances do not allow X-rays or similar radiation to pass through, and exhibit a white appearance in radiographic imaging using X-rays.[70, 71] Radiopacity is a desirable property in bone cements allowing post-operative assessment using X-radiography.[72] It is important that the orthopaedic surgeon can easily monitor healing and loosening processes to differentiate between bone, bone cement, and osteolysis after a joint replacement surgery.[73]

PMMA itself is a radiolucent material, and PMMA cement did not contain any radiopaque materials until 1972; therefore, it was impossible to directly determine the boundaries of bone cement of pure PMMA matrix during the surgery by ordinary X-ray imaging techniques.[73] For this reason, 8-15 wt% X-ray radiopaque media, barium sulphate ($BaSO_4$) or zirconium dioxide (ZrO_2), have been added to all commercially available PMMA bone cements.[74] Poor wetting and weak interfacial interactions between the inorganic particulates and the non-polar polymer matrix often result in detrimental effects on the mechanical properties of the cement.[72] According to Lewis et al. incorporation of strontium oxide (SrO) particles as an alternative radiopacifier in an acrylic cement matrix provided a radiopacity as high as that exhibited by a cement

www.manaraa.com

containing $BaSO_4$. It also gave improved biocompatibility while inhibiting bacterial growth. However, SrO fillers did not provide a significant increase in fracture toughness and fatigue properties compared to a $BaSO_4$-containing cement.[75] Hernandez et al. used radiopaque strontium hydroxyapatite (SrHA) treated with MMA as filler particles in a PMMA based cement to enhance the compressive properties of the composites by improving the integration between the filler particles and the acrylic matrix.[76] Abboud et al. incorporated alumina (Al_2O_3) particles treated with the coupling agent 3-(trimethoxysilyl)propyl methacrylate (c-MPS) into a PMMA matrix in an attempt to produce reinforced radiopaque cements. This coupling agent enhanced the reinforcement effect, while the formulations required high processability because of poor wetting of the filler surface with liquid monomer.[77] Gomoll et al. achieved a significant enhancement in tensile strength of an acrylic bone cement by incorporating nanosized radiopaque $BaSO_4$ particles.[78] Ricker et al. investigated the effect of nano MgO and nano $BaSO_4$ on the PMMA matrix in an attempt to improve the cytocompatibility and radiopacity of the PMMA based bone cements. They found that poor osteoblast function of PMMA could be improved by incorporation of MgO or $BaSO_4$ nanoparticles.[79] In another attempt, Goto et al. incorporated silanized n-TiO_2 particles (60 wt%, average diameter 200 nm) into a cement matrix, but did not obtained a composite with improved flexural modulus.[80] Khaled et al. added functionalized n-SrO-TiO_2 tubes to a PMMA matrix presenting significantly enhanced mechanical properties, radiopacity, and biocompatibility.[72]

On the contrary, a very limited number of studies have been performed to improve the radiopacity of PPF-based bone cements. Kim et al. introduced PPF biopolymer containing 30% barium sulfate as a suitable alternative for kyphoplasty.[81] However, a major drawback associated with the presence of barium sulphate is poor dispersion of these radiopacifiers through the polymer resin, which can affect both crack initiation and crack propagation in the hardened cement.[75, 82] In another study, Wu et al. attempted to improve radiopacity and visual control of PPF cement using a newly developed bone filler, a-TCP/HAp, and sought to quantify the radiopacity by CT scan.[83] Therefore, there is a sustained interest and need for innovative development of PPF-based bone cements exhibiting sufficient mechanical properties, radiopacity, improved

www.manaraa.com

biocompatibility, and reasonable handling properties in order to overcome the prevailing limitations of the current commercial bone cements.

1.2.2.3 Angiogenesity

It is also believed that delivery of bioactive molecules from the PPF-based composite or delivery of osteoblasts and osteoid cultured on the material may promote bone growth in a surgical site where it would otherwise not occur.[84] However, without a sufficient vascular support, these approaches are not considered to be effective in a necrotic environment. The need for treatment modalities that enhance neovascularization in necrotic femoral head is especially important for bone regeneration, because bone formation is an angiogenesis-dependent process.[85, 86] Therefore, a system capable of delivering an angiogenic growth factor in a controlled and localized manner may have the ability to boost the angiogenic response when implanted subcutaneously.

Angiogenesis is a complex multi-step process which consists of activation, chemotactic invasion and migration, morphological alteration, proliferation, and capillary tube formation of endothelial cells (ECs) from preexisting vasculature (shown in Figure 1.5.);[87]. Angiogenesis is a key step in many physiological and pathological situations including development, wound healing, and tumor growth. There is a dynamic balance between inhibitors and stimulators of angiogenesis in the mature organism. Stimulators include an adequate matrix such as fibrin or collagen, and angiogenic growth factors.[86] A variety of growth factors that direct angiogenesis have been identified. The most important angiogenesis inducer is vascular endothelial growth factor (VEGF) owing to its potency, selectivity for endothelial cells, and ability to regulate key steps in angiogenesis, including proliferation and migration of endothelial cells.[88] Nitric oxide (NO) is also considered to be a critical angiogenesis stimulator. Kaigler et al. showed that by delivering VEGF from a biodegradable polymeric scaffold made of PLGA, blood vessel formation and vascular perfusion could be sufficiently enhanced in osseous defects where the blood supply had been compromised by radiation therapy.[89] It is believed that localized VEGF delivery may be acting not only on the vasculature, but also directly on osteoprogenitor cells, osteoblasts, osteoclasts, and conjunctively with osteoinductive factors resident in the osseous defects. Other studies have investigated the use of large

www.manaraa.com

quantities of osteoinductive protein, BMPs, in the repair of irradiated osseous defects. Leach et al. hypothesized that the addition of an osteoconductive surface to VEGF-releasing scaffolds would enhance bone regeneration through improved vascularization and integration with native tissues. They incorporated VEGF into three-dimensional, porous scaffolds made from PLGA for localized protein delivery, then coated the surface with bioactive glass to enhance the osteoconductivity and potentially the osteoinductivity of the construct.[90] Similarly, Murphy et al. synthesized a biomineral coating on the surface of three-dimensional, porous PLGA scaffold via a biomimetic approach to serve as an osteogenic substrate, and VEGF was incorporated into the scaffolds for localized delivery to direct simultaneous regeneration of bone and vascular tissue.[91]

It is important to note that promoting bone regeneration via induced angiogenesis could be particularly important in larger-sized defects, in which the presence of a vascular supply is perhaps more vital.[91] In addition, it is noteworthy that the clinical delivery of VEGF in patients undergoing reconstruction can potentially be harmful, particularly if the defect area was originally created by resection of a malignancy as it is well documented that VEGF contributes to the growth of tumors.[89]

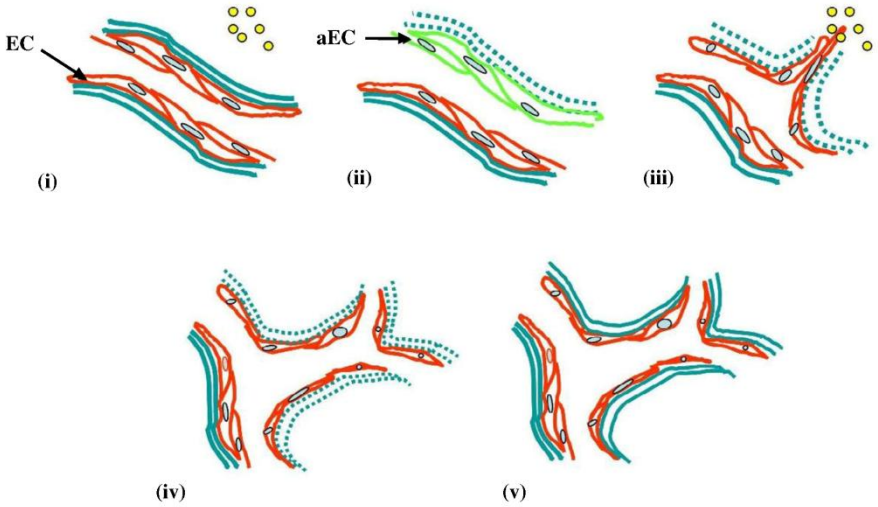

Figure 1.5. Multi-step process of blood vessels formation.
(i) reception of angiogenic signals (yellow spot) from the surrounding by endothelial cells (EC); (ii) retraction of pericytes from the abluminal surface of capillary and secretion of protease from activated endothelial cells (aEC) and proteolytic degradation

www.manaraa.com

of extracellular membrane (green dash-line); (iii) chemotactic migration of EC under the induction of angiogenic stimulators; (iv) proliferation of EC and formation of lumen/canalisation by fusion of formed vessels with formation of tight junctions; (v) recruitment of pericytes and deposition of new basement membrane and initiation of blood flow.[87]

1.3 Angiostimulating activity of ginsenoside Rg_1

Ginsenoside Rg_1, the most prevalent active constituent of ginseng, has been demonstrated to be a highly stable proangiogenic compound by upregulating *in vitro* proliferation, migration, chemo-invasion, and tube formation in human umbilical vein endothelial cells (HUVECs) as well as ex vivo aortic sprouting and *in vivo* neovascularization.[92] Rg_1 is a functional ligand of the glucocorticoid receptor. Leung et al. suggested that Rg_1 can activate the glucocorticoid receptor triggering non-transcriptional pathways to produce NO production.[92] Basically, Rg_1 increases the phosphorylation of GR and endothelial nitric oxide synthase (eNOS) leading to an increase in NO production in human umbilical vein endothelial cell.[92] NO is an important transcellular signaling molecule contributing to anti-tumor, anti-microbial, anti-inflammatory, anti-oxidative, and immunosuppressive activity of macrophages. Thus, NO-related endothelial proliferation and angiogenesis has been shown to be part of the activities of Rg_1.[92] In addition, Cheung reported that Rg_1 increases interaction between the glucocorticoid receptor and the fibroblast growth factor receptor-1 (FGFR-1) and mediates its ligand-independent transactivation, resulting in eNOS phosphorylation, ultimately enhancing angiogenesis.[93] Leung et al. showed for the first time that Rg_1 is a potent stimulator of vascular endothelial growth factor (VEGF) expression in human umbilical vein endothelial cells.[94] VEGF can upregulate the expression of endothelial NO synthase (eNOS), thereby inducing the release of NO and subsequent activation of endothelial cells and smooth muscle cells in vessels, keratinocytes and macrophages in wounds, and tumor cells.[87] Furthermore, NO can increase VEGF synthesis in a positive feedback manner. In other words, VEGF and nitric oxide (NO) are critical angiogenic stimulators, closely related to ginsenoside-mediated angiomodulation.[87] VEGF and NO work

www.manaraa.com

closely with one another in the modulation of angiogenesis. The schematic overview of ginsenoside Rg_1-mediated angiogenic action in HUVEC is shown in Figure 1.6.

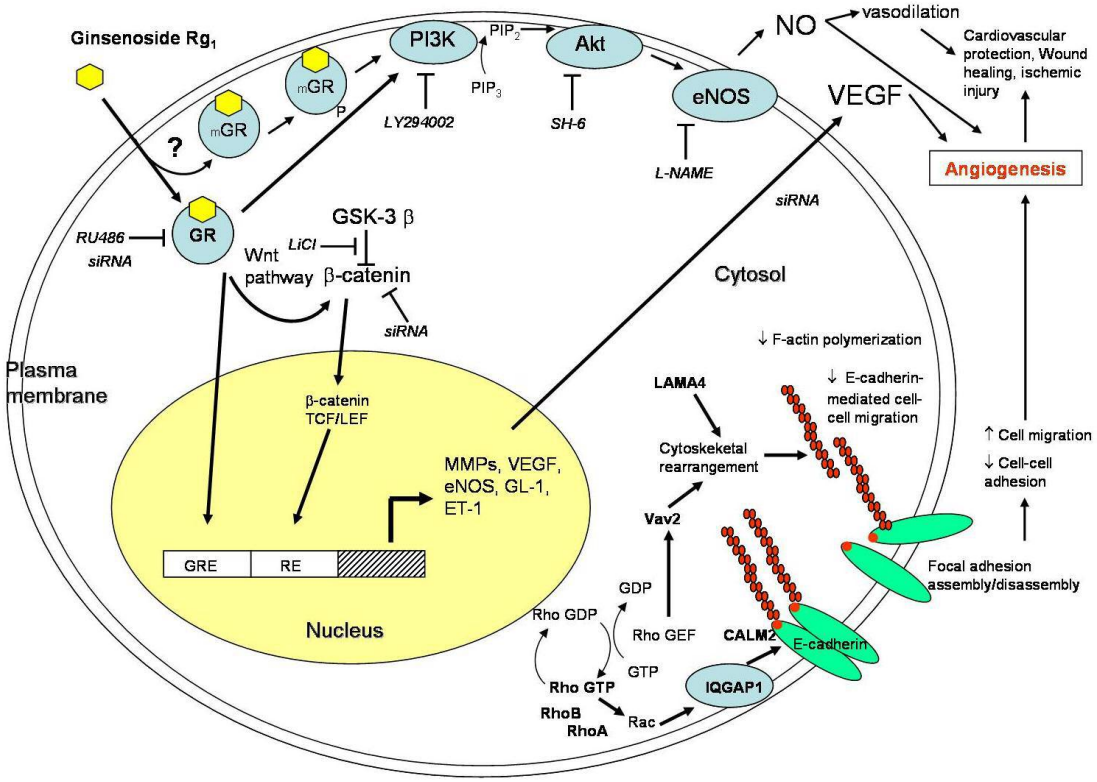

Figure 1.6. The schematic overview of ginsenoside Rg_1-mediated angiogenic action in HUVEC.

Ginsenoside Rg_1 acts as a functional ligand of glucocorticoid receptor (GR). It increases nitric oxide (NO) production via the PI3K-Akt pathway: GR → phosphatidylinositol-3 kinase (PI3K)/Akt pathway → endothelial nitric oxide synthase (eNOS) pathway. Rg_1 also increases vascular endothelial growth factor (VEGF) production through the GR → PI3K/Akt → GSK3β → β-catenin/TCF pathway. Gene expression profiling data indicated that Rg_1 could increase the expression of a group of genes, which are related to cell-cell adhesion, migration and cytoskeletal remodeling.[87]

www.manaraa.com

1.4 Inorganic reinforcing agents

1.4.1 Hydroxyapatite

Calcium phosphates [95], in particular hydroxyapatite (HAp), has attracted a great deal of attention for dental and orthopedic applications owing to its excellent biocompatibility, remarkable ability to bond directly to bone (bioactivity), high osteoconductivity, and close chemical and crystallographic structure with the mineral phase of human hard tissues, bone and teeth.[96, 97] Stoichiometric HAp, with the chemical formula $Ca_{10}(PO_4)_6(OH)_2$, has a hexagonal crystal structure (Figure 1.7).[98] The mineral constituent of bone, enamel, and dentin consists of one phase known as B-type HAp having phosphate groups in the HAp crystal lattice substituted with a carbonate ion. HAp crystals grow along the *c-axis* when nucleated on collagen fibers in mineralized tissue (Figure 1.7).[99, 100]

HAp can be synthesized by many chemical processing routes such as solid state reaction,[101] co-precipitation,[102] sol-gel method,[103] pyrolysis of aerosols,[104] microemulsion,[105] hydrothermal, sol-gel hydrothermal,[106] and surfactant-assisted hydrothermal techniques.[107, 108] Solid state reactions usually give stoichiometric and well-crystallized products but they require relatively high temperatures and long heat-treatment times.[107] Wet precipitation represents a common commercial route for the preparation of nanometer size HAp. Here, the drop-wise addition of phosphoric acid to a suspension of calcium hydroxide, or reactions between calcium nitrate and ammonium phosphate results in a calcium-deficient apatite precipitate.[102] Sol-gel chemistry involves the hydrolysis of phosphorous containing alkoxides and calcium salt and subsequent polycondensation providing molecular level mixing leading to excellent control over the composition and chemical homogeneity of the product. However, to produce crystalline HAp powders using this method, calcination at elevated temperature is required, which may cause the formation of secondary phases such as β-TCP and granular particle shapes.[109] Hydrolysis methods are also used to prepare HAp using acid calcium phosphates such as dicalcium phosphate dihydrate (DCPD), octacalcium phosphate (OCP), or anhydrous dicalcium phosphate.[110] The hydrothermal technique usually results in HAp powders with a high degree of crystallinity and the Ca/P ratio

www.manaraa.com

close to the stoichiometric value, 1.67. However, the obtained powders have typical agglomeration with very poor control on morphology, and their size distribution is relatively wide.[111] Surfactant-assisted hydrothermal method has been used to synthesize HAp nanopowders, nanorods, and nanoneedles.[112] This method inhibits the excess agglomeration of the particles, since the surfactants can adsorb onto the surface of the particles. In addition, the surfactants can serve as a versatile "soft" template for the synthesis of 1 D nanostructured materials.[107, 113] Furthermore, the hydrothermal treatment can effectively improve the crystallinity of the HAp product.[113]

The principal limitation of HAp in its clinical use as load bearing implants, such as artificial bones or teeth, is its poor mechanical properties, especially in a wet environment. Therefore, regardless of its favorable biological properties, the poor mechanical properties of HAp can lead to instability and unsatisfactory performance of the implant or scaffold in the presence of body fluids and under local loading.[114, 115] The diameter and aspect ratio of the HAp powders are important characteristics for biomedical applications. Studies have shown that diameters in the nano-scale are desirable for optimal biological and mechanical performances. Mechanical properties, such as fracture strength and fracture toughness, of the ceramic materials could be improved remarkably by making one dimensional (1-D) nanoscale building blocks such as nanorods, nanofibers, nanowires, and nanotubes.[113, 116] Nanomaterials have also shown superior osteoconductive and bioactive properties as compared to their micron-sized counterparts.[117, 118] In addition, according to Chung et al. the nano-sized HAp provided nanocomposites with superior stiffness and strength, and induced greater trabecular bone formation at the tissue-implant interface.[119]

www.manaraa.com

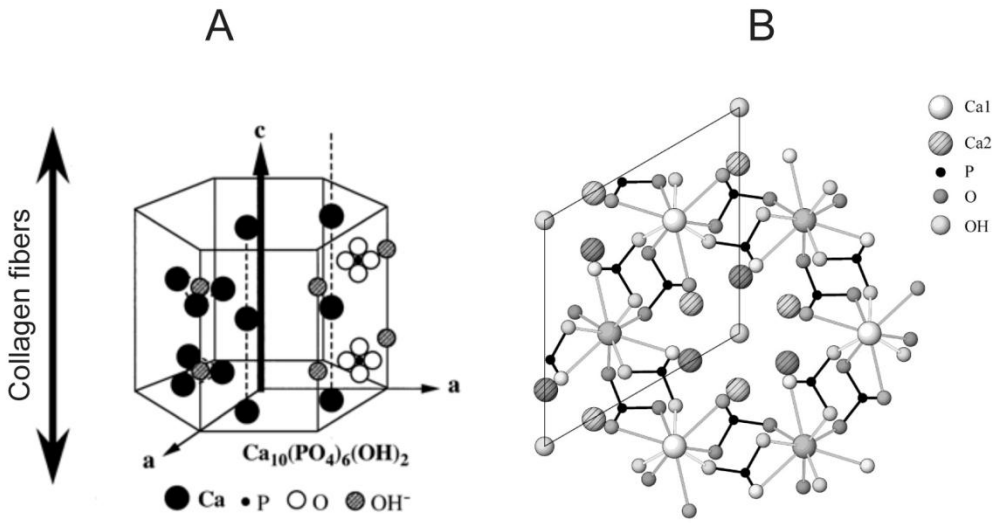

Figure 1.7. Crystal structure of stoichiometric hydroxyapatite.

In mineralized tissues, apatite develops primarily along the c-axis of the hexagonal structure, and is oriented along the extended collagen microfibril (A).[99] Hexagonal crystal structure of hydroxyapatite projected onto the 001 plane (as visualized down the c-axis) (B).[100]

1.4.2 Hydroxyapatite/titania nanocomposites

The artificial HAp suffers from its intrinsic low mechanical reliability; thus, the use of HAp is still rather limited for heavy load-bearing applications.[114] Immobilization of a biocompatible metal/metal oxide on the surface of HAp will enhance the mechanical properties of HAp along with improved cellular responses and biocompatibility.[120] Li et al. studied the reinforcement effect of alumina in Al_2O_3-HAp composites showing that the mechanical strength of HAp ceramics increased with increasing the alumina content, with 30 wt% alumina ($70Al_2O_3$-HAp) exhibiting a 2-fold increase in strength compared with pure HAp.[121] In another attempt, Sung et al. successfully synthesized homogeneous mixtures of hydroxyapatite (HAp) and yttria-stabilized zirconia (YSZ) nanoparticles using chemical co-precipitation and subsequent calcination. The prepared nanocomposites showed improved mechanical properties, such as flexural strength of ~155 MPa and fracture toughness of ~2.1 MPa $m^{1/2}$ owing to the YSZ contribution to the HAp matrix.[122] Furthermore, Santos et al. reported the preparation of bioglass-hydroxyapatite composite samples by a liquid phase sintering process, using a 2.5 wt %

www.manaraa.com

addition of Bioglass to HAp. The addition of Bioglass to hydroxyapatite helped the rapid formation of the Ca, P-layer, as the time required for nucleation to start was much shorter for the composite than for HAp alone. This behavior is attributed to the presence of a highly soluble tricalcium phosphate phase formed from the reaction between Bioglass and the HAp matrix during the liquid phase sintering process.[123]

Among the different HAp-based composites, HAp-TiO_2 composites have attracted considerable attention, due to the combined advantages of both materials, namely HAp providing bioactivity and TiO_2 overcoming the poor adhesion to the implant.[124] Such composites are expected to have improved mechanical properties, better structural integrity, and flexibility than pure HAp ceramics.[125, 126] In addition, HAp-TiO_2 composites have the ability to adsorb and decompose bacteria and organic materials, and it is beneficial in antibacterial applications, environmental purifications, and also for photocatalytic decomposition of biomaterials, such as proteins and lipids.[127]

Various processing techniques such as sol-gel,[128] hydrolysis of Ti-bearing dicalcium phosphate powders,[129] hydrothermal method,[130] combined high gravity and hydrothermal process,[115] electropinning method,[126] and microwave-assisted co-precipitation process[131] have been utilized to synthesize HAp-TiO_2 nanocomposites. Even though all the aforementioned techniques involve simplified preparation procedures, obtaining a crystalline powder in most of these cases requires costly heat treatments at a high temperature or for a long reaction period. Besides, they are not environmentally friendly, and suffer scale-up problems.[125] Therefore, it is necessary to develop more efficient methodology of synthesis to prepare HAp-TiO_2 composites.

1.4.3 Titania

Titanium is a common clinically used biomaterial exhibiting corrosion resistance, biocompatibility, and excellent mechanical performance.[132] A TiO_2 coating on the surface of titanium provides a passive surface layer to the implant increasing its corrosion resistance and impeding the passage of metal ions (Ti^{4+}) into the body.[133] Furthermore, the TiO_2 coating displays high external hardness. Therefore, titanium alloy implants coated with TiO_2 exhibit excellent biocompatibility as well as high mechanical

www.manaraa.com

strength.[132] The high biocompatibility of titanium is beneficial in load-bearing implants, implants intended to stimulate metabolic responses, and also cell-culture substrate for *in vitro* culture and tissue engineering.[134]

TiO_2 particles (>100 nm) have been shown to be biologically inert in both humans and animals.[135] With the development of nanotechnology, it has been considered that nanoparticles might be more toxic than larger particles of the same substance because of their larger surface area, enhanced chemical reactivity, and easier penetration into cells.[136] However, several studies have shown that the cytotoxicity of nano-sized titania was negligible as compared to other nanoparticles.[74] Besides, without UV irradiation, titania nanoparticles have shown no inflammatory effect or genotoxicity in rats, and induced no DNA damage in human cells. Moreover, high photocatalytic efficiency of nanophase titania results in potential phototoxic effects on bacteria, cancer cells, and tumors. This is because of the reactions between the oxidizing agents produced from the redox reaction of the photogenerated holes and electrons and the biomolecules leading to the damage of the biomolecular structure. Therefore, due to the low cytotoxicity and fair biocompatibility, this material is overwhelmingly used as a replacement for teeth and bones. Moreover, titania nanotubes/fibers have high aspect ratios and high surface area to volume ratios, which may lead to significantly enhanced physical and mechanical properties. In addition, biocompatible and radiopaque SrO or ZrO_2 components can be incorporated into the titania nanotube/fibers to provide higher radiopacity compared to the nonmodified nanoparticles.

1.4.4 Synthesis of nanostructured materials in supercritical CO_2

Supercritical fluids exhibit a range of unusual properties that can be exploited for new reactions and new routes to process materials beneficial for the fine chemical and pharmaceutical industries.[137, 138]

In the past decade, it has been shown that a sol-gel process in $scCO_2$ is a promising technique for synthesizing metal oxide nanomaterials. However, due to the low solubility of precursors in CO_2, various surfactants have been examined in the sol-gel process in CO_2 affecting the morphology of the nanomaterials. For example, Tadros et al. studied

www.manaraa.com

the synthesis if TiO_2 nanoparticles in $scCO_2$ by hydrolysis and condensation of titanium alkoxides using the anionic fluorinated surfactant, $[F(CF_2CF_2)_zCH_2CH_2O]_xP(O)(ONH_4)_y$ (where x=1 or 2, y=2 or 1, z=1–7).[139] In another attempt, Tatsuda et al. prepared TiO_2-coated activated carbon by the penetration of titanium (IV) isopropoxide (TIP) dissolved in supercritical CO_2 into the nano-spaces of activated carbon.[140] In the past decade, it has been shown that sol-gel processes using a green solvent such as supercritical carbon dioxide ($scCO_2$) are attractive to synthesize metal oxide nanomaterials. Reverchon et al. synthesized amorphous TiO_2 nanoparticles on the pilot scale in $scCO_2$ without the assistance of surfactant.[95] Also, Sun et al. prepared titania-silica binary oxides using the inorganic precursors, tetraethyl orthosilicate (TEOS) and TIP, simultaneously or sequentially impregnated into a polypropylene (PP) matrix using $scCO_2$ as a swelling agent and carrier.[141] Recently, Sui et al. synthesized TiO_2 nanofibers with a typical diameter ranged from 9 to 100 nm by esterification and condensation of titanium alkoxides using acetic acid as the polymerization agent in $scCO_2$.[142] The Charpentier lab also synthesized porous ZrO_2 aerogels,[143] ZrO_2-modified TiO_2 nanotubes,[144] and N-doped ZrO_2/TiO_2 bimetallic materials,[145] nano TiO_2/graphene composites,[146] and Fe-doped TiO_2 nanowires grown on the surface of graphene sheets[147] using a similar approach in supercritical CO_2.

1.5 Microencapsulation of bioactive molecules into a polymer matrix

Controlled-release drug-delivery systems are becoming increasingly important in biomedicine, showing several advantages compared to the conventional approaches. One of the most important limitations of conventional dosage forms is that partial degradation of the drug happens before it reaches the intended target in the body. However, controlled drug delivery systems preserve the active agent from spoilage caused by enzyme attack. A drug delivery system increases the penetration of the drug into the diseased tissue, so bioavailability of the drug is enhanced along with an increase in the efficacy and toxicity reduction.[148] The delivery system acts as a reservoir of the drug, with specific time-release profiles of the drug, and it leads to a partial control of the pharmacokinetics.[149] Also, a better compliance and convenience for the patient is provided.[149]

www.manaraa.com

Microencapsulation of bioactive molecules into a polymer matrix has been developed as a method for local delivery of the active pharmaceutical ingredient (API) in a controlled manner, over a prolonged period of time.[149] The polymer protects the API, thus reducing the need for multiple doses during a prolonged therapy.[150] A variety of systems based on natural or synthetic polymers have been examined to deliver API's in a sustained manner.[151] Haesslein et al. designed an intraocular drug delivery systems based on biodegradable polymer, PPF, which could be effectively utilized for the treatment of chronic diseases of the posterior segment of the eye. Based on the hypothesis that crosslinked PPF matrices are suitable long-term delivery devices for the sustained release of the anti-inflammatory drug fluocinolone acetonide (FA), they fabricated FA-loaded rods of 10 mm length and 0.6 mm diameter by photocrosslinking PPF with N-vinyl pyrrolidone (NVP), and studied the release behavior of FA over a period of almost 400 days.[152] Hacker et al., also designed a preliminary rabbit implantation study to investigate the function of a photocrosslinked PPF/poly(N-vinyl pyrrolidone) (PVP) matrix for the sustained release of three ophthalmic model drugs, acetazolamide (AZ), dichlorphenamide [7], and timolol maleate (TM). They suggested that monolithic implants (i.e. discs, rods, plugs, pellets or sheets) are relatively easy to fabricate, sterilize, and provide very good control of drug release rate indicating the potential of photocrosslinked PPF-based matrices as polymeric carriers for long-term ophthalmic drug delivery.[153] In another attempt, Ueda et al. developed an injectable formulation for long-term ocular delivery of the FA by dissolving the API and PPF in the biocompatible, water-miscible organic solvent, N-methyl-2-pyrrolidone (NMP).[154] Their strategy aimed at combining the advantages of a monolithic polymeric implant with the benefits of injectable drug delivery systems involving the formulation of injectable *in situ* forming implants.[154] In another study, Kempen et al. investigated the effect of the incorporation of PLGA microspheres encapsulating growth factor, BMP-2, in PPF scaffolds in a goat ectopic implantation model. Some of the scaffolds were combined with autologous BMSCs before implantation to test the influence of progenitor cells on the bone regeneration capacity of the composite.[155] Kempen et al., also tried to examine the release kinetics of TRD from PPF/PLGA blend microspheres as well as the degradation of these microspheres.[150] In another attempt, the same group developed

www.manaraa.com

PPF microspheres to enhance the bonding between the particulate and the continuous phases of the composite scaffold. The resulting PPF microspheres were expected to covalently bind to the PPF matrix through the carbon-carbon double bonds along the polymer backbone on the microsphere surface resulting in increased mechanical properties.[156] This suggests that the pro-angiogenic mediator, ginsenoside Rg_1, can potentially be incorporated into the cement formulation or designed scaffolds after encapsulation in biodegradable PPF microspheres.

1.5.1 Techniques for bioactive molecules-loaded microspheres preparation

Microstructured systems encapsulating therapeutic agents can be prepared using several techniques, including emulsion-solvent evaporation/extraction methods, polymer solution separation method, spray drying, microfluidics, with each method has its own pros and cons. The choice of a particular method depends on drug and polymer features, site of action, and therapy regimes.[157] In an optimized preparation process, the chemical stability and biological activity of the incorporated drug should be guaranteed.[149] An ideal microparticle preparation process should have reasonably high encapsulation efficiency, loading capacity, and sustained release of the loaded drug with retained bioactivity.[158] In addition, the prepared microspheres should display a homogeneous size distribution. Besides, preparation and purification processes must result in reproducible products, and the release-profile of the drug should meet the specific final application requirements.[149] High drug loading and encapsulation efficiencies are critical factors due to the extremely high price of API's such as Rg_1, which is of interest for this thesis.[158]

1.6 Scope of the research

The main objective of this project was to investigate our hypothesis that biocompatible TiO_2 and Sr-doped TiO_2 nanoparticles could be used as a reinforcement and radiopacifying agent to significantly enhance the mechanical properties and radiopacity of PPF bone cement matrix. These novel PPF-TiO_2 bone cement nanocomposites are proposed for treatment of stage III osteonecrosis. Towards this goal, the use of

www.manaraa.com

supercritical carbon dioxide ($scCO_2$) for the synthesis of TiO_2 and Sr-doped nantubes/fibers was investigated. In order to enhance the reinforcing effect of TiO_2, PPF was functionalized with maleic anhydride (MA) using a ring opening reaction producing carboxyl groups at each end point of the polymer for coordination to the n-TiO_2. Moreover, a PPF-based bone cement capable of delivering an angiogenic agent, ginsenoside Rg_1, in a localized and sustained manner would direct regeneration of bone and vascular tissue. In addition, inorganic fillers including hydroxyapatite and hydroxyapatite/titania nanocomposites were synthesized in $scCO_2$ and also using a hydrothermal technique to strengthen the mechanical and physical properties of poly(ε-caprolactone) (PCL) for tissue engineering applications.

The following were identified as specific objectives of this project:

I. Functionalization of PPF with maleic anhydride (MA) and preparation of TiO_2-PPF nanocomposites followed by mechanical properties analysis of the crosslinked bone cement nanocomposites.

II. Synthesis of Sr-dopped TiO_2, preparation of Sr-dopped TiO_2-PPF nanocomposites, and radiopacity measurement of the cross-linked bone cement nanocomposites.

III. Synthesis of hydroxyapatite and hydroxyapatite-TiO_2 in supercritical CO_2 and hydrothermal method to prepare polymer nanocomposites.

IV. Encapsulation of ginsenoside Rg_1 within PPF microspheres prepared using double emulsion and microfluidic technique, examining the release kinetics of Rg_1 from these microspheres.

V. Incorporation of ginsenoside Rg_1 within Sr-dopped TiO_2-PPF based bone cement nanocomposites and release kinetic study of the ginsenoside Rg_1 from these bone cement formulation.

VI. Tube formation (angiogenesis behavior) analysis of ginsenoside Rg_1 *in vitro* before encapsulation and after release from the PPF microspheres and PPF-based bone cement nanocomposites.

www.manaraa.com

1.7 References

1 Chang C-H, Liao T-C, Hsu Y-M, Fang H-W, Chen C-C, Lin F-H. A poly (propylene fumarate)–Calcium phosphate based angiogenic injectable bone cement for femoral head osteonecrosis. Biomaterials. 2010;31:4048-4055.

2 Mont MA, Hungerford DS. Non-traumatic avascular necrosis of the femoral head. The Journal of Bone & Joint Surgery. 1995;77:459-474.

3 Mont MA, Ragland PS, Etienne G. Core decompression of the femoral head for osteonecrosis using percutaneous multiple small-diameter drilling. Clinical orthopaedics and related research. 2004;429:131-138.

4 Wood ML, McDowell CM, Kerstetter TL, Kelley SS. Open reduction and cementation for femoral head fracture secondary to avascular necrosis: preliminary report. The Iowa orthopaedic journal. 2000;20:17.

5 Kenzora J, Steele R, Yosipovitch Z, Glimcher M. Experimental osteonecrosis of the femoral head in adult rabbits. Clinical orthopaedics and related research. 1978;130:8-46.

6 Bachiller FG-C, Caballer AP, Portal LF. Avascular necrosis of the femoral head after femoral neck fracture. Clinical orthopaedics and related research. 2002;399:87-109.

7 Baksi D. Treatment of post-traumatic avascular necrosis of the femoral head by multiple drilling and muscle-pedicle bone grafting. Preliminary report. Journal of Bone & Joint Surgery, British Volume. 1983;65:268-273.

8 d'Aubigné RM. Idiopathic Necrosis of the Femoral Head in Adults: Watson-Jones Lecture delivered at the Royal College of Surgeons of England on 26th September 1963. Annals of the Royal College of Surgeons of England. 1964;34:143.

9 Ono K, Sugioka Y. Epidemiology and risk factors in avascular osteonecrosis of the femoral head. Bone Circulation and Vascularization in Normal and Pathological Conditions: Springer; 1993. p. 243-248.

10 Wang G-J, Sweet D, Reger SI, Thompson R. Fat-cell changes as a mechanism of avascular necrosis of the femoral head in cortisone-treated rabbits. J Bone Joint Surg Am. 1977;59:729-735.

11 Agarwala S, Jain D, Joshi V, Sule A. Efficacy of alendronate, a bisphosphonate, in the treatment of AVN of the hip. A prospective open-label study. Rheumatology. 2005;44:352-359.

12 Min B-W, Kim S-J. Avascular necrosis of the femoral head after osteosynthesis of femoral neck fracture. Orthopedics. 2011;34:349.

13 Brown J. A Review of 195 Patients Treated by Sliding Nail-plate Fixation. 1964.

www.manaraa.com

14 Barnes R, Brown J, Garden R, Nicoll E. Subcapital fractures of the femur. A prospective review. Journal of Bone & Joint Surgery, British Volume. 1976;58:2-24.

15 Chryssanthou CP. Dysbaric osteonecrosis: Etiological and pathogenetic concepts. Clinical orthopaedics and related research. 1978;130:94-106.

16 Akinyoola A, Adediran I, Asaleye C, Bolarinwa A. Risk factors for osteonecrosis of the femoral head in patients with sickle cell disease. International orthopaedics. 2009;33:923-926.

17 Huijbregts PA. Osteonecrosis of the humeral head: a literature review and two case studies. Journal of Manual & Manipulative Therapy. 2000;8:175-182.

18 Assouline-Dayan Y, Chang C, Greenspan A, Shoenfeld Y, Gershwin ME, editors. Pathogenesis and natural history of osteonecrosis. Seminars in arthritis and rheumatism; 2002: Elsevier.

19 Lai K-A, Shen W-J, Yang C-Y, Shao C-J, Hsu J-T, Lin R-M. The Use of Alendronate to Prevent Early Collapse of the Femoral Head in Patients with Nontraumatic OsteonecrosisA Randomized Clinical Study. The Journal of Bone & Joint Surgery. 2005;87:2155-2159.

20 Wood ML, McDowell CM, Kelley SS. Cementation for femoral head osteonecrosis: a preliminary clinic study. Clinical orthopaedics and related research. 2003;412:94-102.

21 Hernigou P, Bachir D, Galacteros F. Avascular necrosis of the femoral head in sickle-cell disease. Treatment of collapse by the injection of acrylic cement. Journal of Bone & Joint Surgery, British Volume. 1993;75:875-880.

22 Kantor SG, Huo MH, Huk OL, Salvati EA. Cemented total hip arthroplasty in patients with osteonecrosis: a 6-year minimum follow-up study of second-generation cement techniques. The Journal of arthroplasty. 1996;11:267-271.

23 Gangji V, Rooze M, De Maertelaer V, Hauzeur J-P. Inefficacy of the cementation of femoral head collapse in glucocorticoid-induced osteonecrosis. International orthopaedics. 2009;33:639-642.

24 Koopman WJ, Boulware DW, Heudebert GR. Clinical primer of rheumatology: Lippincott Williams & Wilkins; 2003.

25 Wood ML, Kelley SS. Cement supplementation as a treatment for osteonecrosis. Current Opinion in Orthopaedics. 2003;14:23-29.

26 Poitout DG. Biomechanics and biomaterials in orthopedics: Springer; 2004.

27 Gomez PF, Morcuende JA. Early attempts at hip arthroplasty: 1700s to 1950s. The Iowa orthopaedic journal. 2005;25:25.

www.manaraa.com

28 Lai P, Chen L, Chen W, Chu I. Chemical and physical properties of bone cement for vertebroplasty. Biomedical journal. 2013;36:162.

29 Haboush E. A new operation for arthroplasty of the hip based on biomechanics, photoelasticity, fast-setting dental acrylic, and other considerations. Bulletin of the Hospital for Joint Diseases. 1953;14:242-277.

30 Charnley J. The bonding of prostheses to bone by cement. J Bone Joint Surg Br. 1964;46:518-529.

31 Webb J, Spencer R. The role of polymethylmethacrylate bone cement in modern orthopaedic surgery. Journal of Bone & Joint Surgery, British Volume. 2007;89:851-857.

32 Kowalski R, Schmaehling R. Commercial aspects and delivery systems of bone cements. Orthopaedic Bone Cements. 2008:113.

33 Ewald FC, Poss R, Pugh J, Schiller AL, Sledge CB. Hip cartilage supported by methacrylate in canine arthroplasty. Clinical orthopaedics and related research. 1982;171:273-279.

34 Lieberman IH, Togawa D, Kayanja MM. Vertebroplasty and kyphoplasty: filler materials. The Spine Journal. 2005;5:S305-S316.

35 Hu Z, Zhao G, Wang L, Pu B, Hao J, Lao H, Zhang X, Gan Q, Jiang W. Related Biological Research in the Interface between Bone Cement and Bone after Percutaneous Vertebroplasty. International journal of endocrinology. 2013;2013.

36 Huang K-Y, Yan J-J, Lin R-M. Histopathologic findings of retrieved specimens of vertebroplasty with polymethylmethacrylate cement: case control study. Spine. 2005;30:E585-E588.

37 Lu J, Huang Z, Tropiano P, d'Orval BC, Remusat M, Dejou J, Proust J-P, Poitout D. Human biological reactions at the interface between bone tissue and polymethylmethacrylate cement. Journal of Materials Science: Materials in Medicine. 2002;13:803-809.

38 Lewis G. Properties of acrylic bone cement: state of the art review. Journal of biomedical materials research. 1997;38:155-182.

39 Herman JH, Sowder W, Anderson D, Appel A, Hopson C. Polymethylmethacrylate-induced release of bone-resorbing factors. The Journal of Bone & Joint Surgery. 1989;71:1530-1541.

40 Fisher JP, Vehof JW, Dean D, van der Waerden JP, Holland TA, Mikos AG, Jansen JA. Soft and hard tissue response to photocrosslinked poly (propylene fumarate) scaffolds in a rabbit model. Journal of biomedical materials research. 2002;59:547-556.

www.manaraa.com

41 Shung AK, Timmer MD, Jo S, Engel PS, Mikos AG. Kinetics of poly (propylene fumarate) synthesis by step polymerization of diethyl fumarate and propylene glycol using zinc chloride as a catalyst. Journal of Biomaterials Science, Polymer Edition. 2002;13:95-108.

42 Lee K-W, Wang S, Yaszemski MJ, Lu L. Physical properties and cellular responses to crosslinkable poly (propylene fumarate)/hydroxyapatite nanocomposites. Biomaterials. 2008;29:2839-2848.

43 Peter SJ, Lu L, Kim DJ, Mikos AG. Marrow stromal osteoblast function on a poly (propylene fumarate)/β-tricalcium phosphate biodegradable orthopaedic composite. Biomaterials. 2000;21:1207-1213.

44 Timmer MD, Carter C, Ambrose CG, Mikos AG. Fabrication of poly(propylene fumarate)-based orthopaedic implants by photo-crosslinking through transparent silicone molds. Biomaterials. 2003;24:4707-4714.

45 Timmer MD, Shin H, Horch RA, Ambrose CG, Mikos AG. *In vitro* cytotoxicity of injectable and biodegradable poly (propylene fumarate)-based networks: unreacted macromers, cross-linked networks, and degradation products. Biomacromolecules. 2003;4:1026-1033.

46 Kasper FK, Tanahashi K, Fisher JP, Mikos AG. Synthesis of poly (propylene fumarate). Nature protocols. 2009;4:518-525.

47 Gomes ME, Reis R. Biodegradable polymers and composites in biomedical applications: from catgut to tissue engineering. Part 1 Available systems and their properties. International materials reviews. 2004;49:261-273.

48 Mikos AG, Peter SJ, Yaszemski MJ. Bone replacement compound comprising poly (polypropylene fumarate). Google Patents; 2000.

49 Peter S, Kim P, Yasko A, Yaszemski M, Mikos A. Cross-Linking Characteristics of an Injectable Poly (propylene fumarate)/β-Tricalcium Phosphate Paste and Mechanical Properties of the Cross-Linked Composite for Use as a Biodegradable Bone Cement. Journal of biomedical materials research. 1999;44:314-321.

50 Fisher JP, Dean D, Mikos AG. Photocrosslinking characteristics and mechanical properties of diethyl fumarate/poly (propylene fumarate) biomaterials. Biomaterials. 2002;23:4333-4343.

51 Peter SJ, Kim P, Yasko AW, Yaszemski MJ, Mikos AG, editors. Crosslinking characteristics of an injectable poly (propylene fumarate)/β-tricalcium phosphate paste and mechanical properties of the crosslinked composite for use as a biodegradable bone cement. MRS Proceedings; 1998: Cambridge Univ Press.

www.manaraa.com

52 Fong EL, Watson BM, Kasper FK, Mikos AG. Building bridges: leveraging interdisciplinary collaborations in the development of biomaterials to meet clinical needs. Advanced Materials. 2012;24:4995-5013.

53 Vasile C, Zaikov GE. Environmentally Degradable Materials Based on Multicomponent Polymeric Systems: Brill; 2009.

54 Gunatillake PA, Adhikari R. Biodegradable synthetic polymers for tissue engineering. Eur Cell Mater. 2003;5:1-16.

55 Sabir MI, Xu X, Li L. A review on biodegradable polymeric materials for bone tissue engineering applications. Journal of Materials Science. 2009;44:5713-5724.

56 Timmer MD, Ambrose CG, Mikos AG. *In vitro* degradation of polymeric networks of poly (propylene fumarate) and the crosslinking macromer poly (propylene fumarate)-diacrylate. Biomaterials. 2003;24:571-577.

57 Timmer MD, Jo S, Wang C, Ambrose CG, Mikos AG. Characterization of the cross-linked structure of fumarate-based degradable polymer networks. Macromolecules. 2002;35:4373-4379.

58 Peter SJ, Nolley JA, Widmer MS, Merwin JE, Yaszemski MJ, Yasko AW, Engel PS, Mikos AG. *In vitro* degradation of a poly (propylene fumarate)/β-tricalcium phosphate composite orthopaedic scaffold. Tissue Engineering. 1997;3:207-215.

59 Yaszemski MJ, Payne RG, Hayes WC, Langer RS, Aufdemorte TB, Mikos AG. The ingrowth of new bone tissue and initial mechanical properties of a degrading polymeric composite scaffold. Tissue engineering. 1995;1:41-52.

60 He S, Timmer M, Yaszemski M, Yasko A, Engel P, Mikos A. Synthesis of biodegradable poly (propylene fumarate) networks with poly (propylene fumarate)–diacrylate macromers as crosslinking agents and characterization of their degradation products. Polymer. 2001;42:1251-1260.

61 Alge DL, Bennett J, Treasure T, Voytik-Harbin S, Goebel WS, Chu TMG. Poly (propylene fumarate) reinforced dicalcium phosphate dihydrate cement composites for bone tissue engineering. Journal of Biomedical Materials Research Part A. 2012;100:1792-1802.

62 Domb AJ, Manor N, Elmalak O. Biodegradable bone cement compositions based on acrylate and epoxide terminated poly (propylene fumarate) oligomers and calcium salt compositions. Biomaterials. 1996;17:411-417.

63 Chen Q, Zhu C, Thouas GA, Kengne-Momo R, Lagarde F, Daniel P, Pilard J, Durand M. Progress and challenges in biomaterials used for bone tissue engineering: bioactive glasses and elastomeric composites. Progress in Biomaterials. 2012;1:2.

www.manaraa.com

64 Temenoff JS, Mikos AG. Injectable biodegradable materials for orthopedic tissue engineering. Biomaterials. 2000;21:2405-2412.

65 Shi X, Hudson JL, Spicer PP, Tour JM, Krishnamoorti R, Mikos AG. Rheological behaviour and mechanical characterization of injectable poly (propylene fumarate)/single-walled carbon nanotube composites for bone tissue engineering. Nanotechnology. 2005;16:S531.

66 Shi X, Hudson JL, Spicer PP, Tour JM, Krishnamoorti R, Mikos AG. Injectable nanocomposites of single-walled carbon nanotubes and biodegradable polymers for bone tissue engineering. Biomacromolecules. 2006;7:2237-2242.

67 Sitharaman B, Shi X, Tran LA, Spicer PP, Rusakova I, Wilson LJ, Mikos AG. Injectable *in situ* cross-linkable nanocomposites of biodegradable polymers and carbon nanostructures for bone tissue engineering. Journal of Biomaterials Science, Polymer Edition. 2007;18:655-671.

68 Khaled S, Miron RJ, Hamilton DW, Charpentier PA, Rizkalla AS. Reinforcement of resin based cement with titania nanotubes. dental materials. 2010;26:169-178.

69 Horch RA, Shahid N, Mistry AS, Timmer MD, Mikos AG, Barron AR. Nanoreinforcement of poly (propylene fumarate)-based networks with surface modified alumoxane nanoparticles for bone tissue engineering. Biomacromolecules. 2004;5:1990-1998.

70 Deb S, Abdulghani S, Behiri J. Radiopacity in bone cements using an organo-bismuth compound. Biomaterials. 2002;23:3387-3393.

71 Amirouche A, Mouzali M, Watts D. Radiopacity evaluation of Bis-GMA/TEGDMA/opaque mineral filler dental composites. Journal of applied polymer science. 2007;104:1632-1639.

72 Khaled S, Charpentier PA, Rizkalla AS. Synthesis and characterization of poly (methyl methacrylate)-based experimental bone cements reinforced with TiO_2–SrO nanotubes. Acta Biomaterialia. 2010;6:3178-3186.

73 Dunne N. Mechanical properties of bone cements. Orthopaedic bone cements. 2008:240-255.

74 Khaled S, Rizkalla AS, Charpentier PA. Development of a new generation of bone cements using nanotechnology. 2010, PhD thesis.

75 Lewis G, Xu J, Madigan S, Towler MR. Influence of strontia on various properties of Surgical Simplex® P acrylic bone cement and experimental variants. Acta Biomaterialia. 2007;3:970-979.

www.manaraa.com

76 Hernández L, Gurruchaga M, Goñi I. Injectable acrylic bone cements for vertebroplasty based on a radiopaque hydroxyapatite. Formulation and rheological behaviour. Journal of Materials Science: Materials in Medicine. 2009;20:89-97.

77 Abboud M, Casaubieilh L, Morvan F, Fontanille M, Duguet E. PMMA-based composite materials with reactive ceramic fillers: IV. Radiopacifying particles embedded in PMMA beads for acrylic bone cements. Journal of biomedical materials research. 2000;53:728-736.

78 Gomoll AH, Fitz W, Scott RD, Thornhill TS, Bellare A. Nanoparticulate fillers improve the mechanical strength of bone cement. Acta orthopaedica. 2008;79:421-427.

79 Ricker A. The influence of nano MgO and BaSO. International journal of nanomedicine. 2008;3:125-132.

80 Goto K, Tamura J, Shinzato S, Fujibayashi S, Hashimoto M, Kawashita M, Kokubo T, Nakamura T. Bioactive bone cements containing nano-sized titania particles for use as bone substitutes. Biomaterials. 2005;26:6496-6505.

81 Kim C, Mahar A, Perry A, Massie J, Lu L, Currier B, Yaszemski MJ. Biomechanical evaluation of an injectable radiopaque polypropylene fumarate cement for kyphoplasty in a cadaveric osteoporotic vertebral compression fracture model. Journal of spinal disorders & techniques. 2007;20:604-609.

82 Khaled S, Charpentier PA, Rizkalla AS. Physical and mechanical properties of PMMA bone cement reinforced with nano-sized titania fibers. Journal of Biomaterials Applications. 2011;25:515-537.

83 Wu C-C, Yang K-C, Yang S-H, Lin M-H, Kuo T-F, Lin F-H. *In Vitro* Studies of Composite Bone Filler Based on Poly(Propylene Fumarate) and Biphasic α-Tricalcium Phosphate/Hydroxyapatite Ceramic Powder. Artificial Organs. 2012;36:418-428.

84 Yaszemski MJ. The design, synthesis, characteriation, and mechanical testing of a novel biodegradable polymeric biomaterial for use as a bone substitute: massachusetts institute of technology. 1995, PhD thesis.

85 Tanaka S, Matsuzaka K, Sato D, Inoue T. Characteristics of newly formed bone during guided bone regeneration: analysis of cbfa-1, osteocalcin, and VEGF expression. Journal of Oral Implantology. 2007;33:321-326.

86 Kleinheinz J, Stratmann U, Joos U, Wiesmann H-P. VEGF-activated angiogenesis during bone regeneration. Journal of oral and maxillofacial surgery. 2005;63:1310-1316.

87 Yue PY, Mak NK, Cheng YK, Leung KW, Ng TB, Fan DT, Yeung HW, Wong RN. Pharmacogenomics and the Yin/Yang actions of ginseng: anti-tumor, angiomodulating and steroid-like activities of ginsenosides. Chinese medicine. 2007;2:1-21.

www.manaraa.com

88 Shi A-w, Wang X-b, Lu F-x, Zhu M-m, Kong X-q, Cao K-j. Ginsenoside Rg_1 promotes endothelial progenitor cell migration and proliferation. Acta Pharmacologica Sinica. 2009;30:299-306.

89 Kaigler D, Wang Z, Horger K, Mooney DJ, Krebsbach PH. VEGF scaffolds enhance angiogenesis and bone regeneration in irradiated osseous defects. Journal of Bone and Mineral Research. 2006;21:735-744.

90 Kent Leach J, Kaigler D, Wang Z, Krebsbach PH, Mooney DJ. Coating of VEGF-releasing scaffolds with bioactive glass for angiogenesis and bone regeneration. Biomaterials. 2006;27:3249-3255.

91 Murphy W, Simmons C, Kaigler D, Mooney D. Bone regeneration via a mineral substrate and induced angiogenesis. Journal of dental research. 2004;83:204-210.

92 Leung KW, Cheng Y-K, Mak NK, Chan KK, David Fan T, Wong RN. Signaling pathway of ginsenoside-Rg_1 leading to nitric oxide production in endothelial cells. FEBS letters. 2006;580:3211-3216.

93 Cheung LW, Leung KW, Wong CK, Wong RN, Wong AS. Ginsenoside-Rg_1 induces angiogenesis via non-genomic crosstalk of glucocorticoid receptor and fibroblast growth factor receptor-1. Cardiovascular research. 2011;89:419-425.

94 Leung KW, Pon YL, Wong RN, Wong AS. Ginsenoside-Rg_1 induces vascular endothelial growth factor expression through the glucocorticoid receptor-related phosphatidylinositol 3-kinase/Akt and β-catenin/T-cell factor-dependent pathway in human endothelial cells. Journal of Biological Chemistry. 2006;281:36280-36288.

95 Reverchon E, Caputo G, Correra S, Cesti P. Synthesis of titanium hydroxide nanoparticles in supercritical carbon dioxide on the pilot scale. The Journal of supercritical fluids. 2003;26:253-261.

96 LeGeros RZ. Properties of osteoconductive biomaterials: calcium phosphates. Clinical orthopaedics and related research. 2002;395:81-98.

97 Sun Y, Guo G, Tao D, Wang Z. Reverse microemulsion-directed synthesis of hydroxyapatite nanoparticles under hydrothermal conditions. Journal of Physics and Chemistry of Solids. 2007;68:373-377.

98 Murugan R, Ramakrishna S. Crystallographic study of hydroxyapatite bioceramics derived from various sources. Crystal growth & design. 2005;5:111-112.

99 Nakano T, Kaibara K, Tabata Y, Nagata N, Enomoto S, Marukawa E, Umakoshi Y. Unique alignment and texture of biological apatite crystallites in typical calcified tissues analyzed by microbeam X-ray diffractometer system. Bone. 2002;31:479-487.

www.manaraa.com

100 Ivanova T, Frank-Kamenetskaya O, Kol'tsov A, Ugolkov V. Crystal structure of calcium-deficient carbonated hydroxyapatite. Thermal decomposition. Journal of Solid State Chemistry. 2001;160:340-349.

101 Ota Y, Iwashita T, Kasuga T, Abe Y. Novel preparation method of hydroxyapatite fibers. Journal of the American Ceramic Society. 1998;81:1665-1668.

102 Pang Y, Bao X. Influence of temperature, ripening time and calcination on the morphology and crystallinity of hydroxyapatite nanoparticles. Journal of the European Ceramic Society. 2003;23:1697-1704.

103 Tanahashi M, Kamiya K, Suzuki T, Nasu H. Fibrous hydroxyapatite grown in the gel system: effects of pH of the solution on the growth rate and morphology. Journal of Materials Science: Materials in Medicine. 1992;3:48-53.

104 Vallet-Regı M, Gutiérrez-Ríos M, Alonso M, De Frutos M, Nicolopoulos S. Hydroxyapatite particles synthesized by pyrolysis of an aerosol. Journal of Solid State Chemistry. 1994;112:58-64.

105 Lim G, Wang J, Ng S, Chew C, Gan L. Processing of hydroxyapatite via microemulsion and emulsion routes. Biomaterials. 1997;18:1433-1439.

106 Costa DO, Dixon SJ, Rizkalla AS. One-and Three-Dimensional Growth of Hydroxyapatite Nanowires during Sol–Gel–Hydrothermal Synthesis. ACS applied materials & interfaces. 2012;4:1490-1499.

107 Salarian M, Solati-Hashjin M, Shafiei SS, Goudarzi A, Salarian R, Nemati A. Surfactant-assisted synthesis and characterization of hydroxyapatite nanorods under hydrothermal conditions. Materials Science-Poland. 2009;27:961-971.

108 Wang Y, Zhang S, Wei K, Zhao N, Chen J, Wang X. Hydrothermal synthesis of hydroxyapatite nanopowders using cationic surfactant as a template. Materials Letters. 2006;60:1484-1487.

109 Liu D-M, Troczynski T, Tseng WJ. Water-based sol–gel synthesis of hydroxyapatite: process development. Biomaterials. 2001;22:1721-1730.

110 Costa DO. Calcium Phosphate-Based Resorbable Biomaterials for Bone Regeneration. 2012, PhD thesis.

111 Salarian M, Solati-Hashjin M, Shafiei SS, Salarian R, Nemati ZA. Template-directed hydrothermal synthesis of dandelion-like hydroxyapatite in the presence of cetyltrimethylammonium bromide and polyethylene glycol. Ceramics International. 2009;35:2563-2569.

112 Yan L, Li Y, Deng Z-X, Zhuang J, Sun X. Surfactant-assisted hydrothermal synthesis of hydroxyapatite nanorods. International Journal of Inorganic Materials. 2001;3:633-637.

www.manaraa.com

113 Lin K, Chang J, Cheng R, Ruan M. Hydrothermal microemulsion synthesis of stoichiometric single crystal hydroxyapatite nanorods with mono-dispersion and narrow-size distribution. Materials Letters. 2007;61:1683-1687.

114 Xiao X, Liu R, Zheng Y. Characterization of hydroxyapatite/titania composite coatings codeposited by a hydrothermal–electrochemical method on titanium. Surface and Coatings Technology. 2006;200:4406-4413.

115 Joseph Nathanael A, Mangalaraj D, Chen PC, Ponpandian N. Mechanical and photocatalytic properties of hydroxyapatite/titania nanocomposites prepared by combined high gravity and hydrothermal process. Composites Science and Technology. 2010;70:419-426.

116 Liu Y, Hou D, Wang G. A simple wet chemical synthesis and characterization of hydroxyapatite nanorods. Materials chemistry and physics. 2004;86:69-73.

117 Zhou H, Lee J. Nanoscale hydroxyapatite particles for bone tissue engineering. Acta biomaterialia. 2011;7:2769-2781.

118 Allo BA, Costa DO, Dixon SJ, Mequanint K, Rizkalla AS. Bioactive and biodegradable nanocomposites and hybrid biomaterials for bone regeneration. Journal of Functional Biomaterials. 2012;3:432-463.

119 Chung EJ, Qiu H, Kodali P, Yang S, Sprague SM, Hwong J, Koh J, Ameer GA. Early tissue response to citric acid–based micro-and nanocomposites. Journal of Biomedical Materials Research Part A. 2011;96:29-37.

120 Pushpakanth S, Srinivasan B, Sreedhar B, Sastry T. An *in situ* approach to prepare nanorods of titania–hydroxyapatite (TiO_2–HAp) nanocomposite by microwave hydrothermal technique. Materials chemistry and physics. 2008;107:492-498.

121 Li J, Fartash B, Hermansson L. Hydroxyapatite-alumina composites and bone-bonding. Biomaterials. 1995;16:417-422.

122 Sung Y-M, Shin Y-K, Ryu J-J. Preparation of hydroxyapatite/zirconia bioceramic nanocomposites for orthopaedic and dental prosthesis applications. Nanotechnology. 2007;18:065602.

123 Santos J, Jha L, Monteiro F. *In vitro* calcium phosphate formation on SiO_2-Na_2O-CaO-P_2O_5 glass reinforced hydroxyapatite composite: a study by XPS analysis. Journal of Materials Science: Materials in Medicine. 1996;7:181-185.

124 Nathanael AJ, Mangalaraj D, Ponpandian N. Controlled growth and investigations on the morphology and mechanical properties of hydroxyapatite/titania nanocomposite thin films. Composites Science and Technology. 2010;70:1645-1651.

www.manaraa.com

125 Salarian M, Xu WZ, Wang Z, Sham T-K, Charpentier PA. Hydroxapatite-TiO_2-based Nanocomposites Synthesized in Supercritical CO_2 for Bone Tissue Engineering: Physical and Mechanical Properties. ACS Applied Materials & Interfaces. 2014.

126 Kim HM, Chae WP, Chang KW, Chun S, Kim S, Jeong Y, Kang IK. Composite nanofiber mats consisting of hydroxyapatite and titania for biomedical applications. Journal of Biomedical Materials Research Part B: Applied Biomaterials. 2010;94:380-387.

127 Wakamura M. Photocatalysis by calcium hydroxyapatite modified with Ti (IV). Fujitsu Sci Tech J. 2005;41:181-190.

128 Im K-H, Lee S-B, Kim K-M, Lee Y-K. Improvement of bonding strength to titanium surface by sol–gel derived hybrid coating of hydroxyapatite and titania by sol–gel process. Surface and Coatings Technology. 2007;202:1135-1138.

129 Teraoka K, Nonami T, Yokogawa Y, Taoda H, Kameyama T. Preparation of TiO_2-coated hydroxyapatite single crystals. Journal of Materials Research. 2000;15:1243-1244.

130 Anmin H, Tong L, Ming L, Chengkang C, Huiqin L, Dali M. Preparation of nanocrystals hydroxyapatite/TiO_2 compound by hydrothermal treatment. Applied Catalysis B: Environmental. 2006;63:41-44.

131 Siddharthan A, Kumar T, Seshadri S. *In situ* composite coating of titania–hydroxyapatite on commercially pure titanium by microwave processing. Surface and Coatings Technology. 2010;204:1755-1763.

132 Williams DF. Titanium for medical applications. Titanium in medicine: Springer; 2001. 13-24.

133 Toth C, Szabó G, Kovács L, Vargha K, Barabás J, Németh Z. Titanium implants with oxidized surfaces: the background and long-term results. Smart materials and structures. 2002;11:813.

134 Wintermantel E, Eckert K-L, Huang N-P, Textor M, Brunette DM. Titanium ceramics for cell-carriers and for medical applications. Titanium in Medicine: Springer; 2001. p. 649-671.

135 Bernard BK, Osheroff MR, Hofman A, Mennear JH. Toxicology and carcinogenesis studies of dietary titanium dioxide-coated mica in male and female Fischer 344 rats. Journal of Toxicology and Environmental Health, Part A Current Issues. 1989;28:415-426.

136 Lam C-W, James JT, McCluskey R, Hunter RL. Pulmonary toxicity of single-wall carbon nanotubes in mice 7 and 90 days after intratracheal instillation. Toxicological Sciences. 2004;77:126-134.

www.manaraa.com

137 Rayner CM. The potential of carbon dioxide in synthetic organic chemistry. Organic process research & development. 2007;11:121-132.

138 Clark JH, Tavener SJ. Alternative solvents: shades of green. Organic process research & development. 2007;11:149-155.

139 Tadros ME, Adkins CL, Russick EM, Youngman MP. Synthesis of titanium dioxide particles in supercritical CO_2. The Journal of supercritical fluids. 1996;9:172-176.

140 Tatsuda N, Itahara H, Setoyama N, Fukushima Y. Preparation of titanium dioxide/activated carbon composites using supercritical carbon dioxide. Carbon. 2005;43:2358-2365.

141 Sun D, Huang Y, Han B, Yang G. Ti-Si mixed oxides prepared by polymer *in situ* sol-gel chemistry with the aid of CO_2. Langmuir. 2006;22:4793-4798.

142 Sui R, Rizkalla AS, Charpentier PA. Formation of titania nanofibers: A direct sol-gel route in supercritical CO_2. Langmuir. 2005;21:6150-6153.

143 Sui R, Rizkalla AS, Charpentier PA. Direct synthesis of zirconia aerogel nanoarchitecture in supercritical CO_2. Langmuir. 2006;22:4390-4396.

144 Lucky R, Charpentier P. A thermal study on the structural changes of bimetallic ZrO_2-modified TiO_2 nanotubes synthesized using supercritical CO_2. Nanotechnology. 2009;20:195601.

145 Lucky RA, Charpentier PA. N-doped ZrO_2/TiO_2 bimetallic materials synthesized in supercritical CO_2: Morphology and photocatalytic activity. Applied catalysis B, Environmental. 2010;96:516-523.

146 Farhangi N, Medina-Gonzalez Y, Chowdhury RR, Charpentier PA. Growing TiO_2 nanowires on the surface of graphene sheets in supercritical CO_2: characterization and photoefficiency. Nanotechnology. 2012;23:294005.

147 Farhangi N, Medina-Gonzalez Y, Charpentier PA, editors. Fe doped TiO_2 Nanofibers on the surface of Graphene sheets for Photovoltaics applications. Photonics North 2011; 2011: International Society for Optics and Photonics.

148 Barbucci R. Integrated biomaterials science: Springer; 2002.

149 Chiellini F, Piras AM, Errico C, Chiellini E. Micro/nanostructured polymeric systems for biomedical and pharmaceutical applications. 2008;3:367-93.

150 Kempen DH, Lu L, Zhu X, Kim C, Jabbari E, Dhert WJ, Currier BL, Yaszemski MJ. Development of biodegradable poly (propylene fumarate)/poly (lactic-co-glycolic acid) blend microspheres. II. Controlled drug release and microsphere degradation. Journal of Biomedical Materials Research Part A. 2004;70:293-302.

www.manaraa.com

151 Saraf S. Applications of novel drug delivery system for herbal formulations. Fitoterapia. 2010;81:680-689.

152 Haesslein A, Ueda H, Hacker M, Jo S, Ammon D, Borazjani R, Kunzler J, Salamone J, Mikos A. Long-term release of fluocinolone acetonide using biodegradable fumarate-based polymers. Journal of controlled release. 2006;114:251-260.

153 Hacker M, Haesslein A, Ueda H, Foster W, Garcia C, Ammon D, Borazjani R, Kunzler J, Salamone J, Mikos A. Biodegradable fumarate-based drug-delivery systems for ophthalmic applications. Journal of Biomedical Materials Research Part A. 2009;88:976-989.

154 Ueda H, Hacker M, Haesslein A, Jo S, Ammon D, Borazjani R, Kunzler J, Salamone J, Mikos A. Injectable, *in situ* forming poly (propylene fumarate)-based ocular drug delivery systems. Journal of Biomedical Materials Research Part A. 2007;83:656-666.

155 Kempen DH, Kruyt MC, Lu L, Wilson CE, Florschutz AV, Creemers LB, Yaszemski MJ, Dhert WJ. Effect of autologous bone marrow stromal cell seeding and bone morphogenetic protein-2 delivery on ectopic bone formation in a microsphere/poly (propylene fumarate) composite. Tissue Engineering Part A. 2008;15:587-594.

156 Kempen DH, Lu L, Kim C, Zhu X, Dhert WJ, Currier BL, Yaszemski MJ. Controlled drug release from a novel injectable biodegradable microsphere/scaffold composite based on poly (propylene fumarate). Journal of Biomedical Materials Research Part A. 2006;77:103-111.

157 Errico C, Gazzarri M, Chiellini F. A novel method for the preparation of retinoic acid-loaded nanoparticles. International journal of molecular sciences. 2009;10:2336-2347.

158 Ye M, Kim S, Park K. Issues in long-term protein delivery using biodegradable microparticles. Journal of controlled release. 2010;146:241-260.

www.manaraa.com

Chapter 2

2 Synthesis and Characterization of Novel TiO_2-Poly(propylene fumarate) Nanocomposites for Bone Cementation

Abstract

This work reports on a new methodology for synthesizing poly(propylene fumarate) (PPF)/titania nanowire composites which would be beneficial in tissue engineering for orthopaedic bone cements. The synthetic procedure reacted PPF with maleic anhydride to create HOOC-PPF-COOH species in a ring-opening reaction at room temperature. These species were then coordinated to titania nanowires by metal carboxylate bonding through the end -COOH groups. These PPF-grafted nano-TiO_2 assemblies were then further polymerized and crosslinked in the presence of N-vinylpyrrolidone to produce the bone cements. The synthesis and modification of PPF was confirmed by NMR (^1H and ^{13}C) and XPS, while the reaction chemistry of the functionalized PPF and nano-TiO_2 was also investigated by XPS and FTIR. Mechanical testing of the resulting composites demonstrated a significant reinforcement of the tensile and flexural properties, showing the utility of this synthetic approach for bone tissue engineering.

www.manaraa.com

2.1 Introduction

Developing new materials for bone cementation and bone tissue engineering is of emerging scientific interest,[1] requiring new synthetic approaches that provide both mechanical strength and biocompatibility.[2] Driving forces include our longer life spans and the potential to treat skeletal bone defects and diseases such as osteonecrosis, which is caused by the temporary or permanent loss of blood supply to bone.[3] Cementation involves the injection of a liquid polymeric material, which hardens in the defect, providing mechanical support to the bone.[4] The most universally used injectable bone cement is made of poly(methyl methacrylate) (PMMA).[5-7] However, there are several drawbacks associated with PMMA bone cements including: (1) exothermic polymerization that can lead to impaired local blood circulation and thermal necrosis of the surrounding bone, (2) release of unreacted MMA monomer leading to chemical necrosis of the bone, (3) non-biodegradability, so PMMA cannot be replaced with new bone formation, and (4) non-bioinertness.[8] Recently, poly(propylene fumarate) (PPF) has attracted considerable interest as a promising biodegradable material for treating skeletal defects.[9-11] PPF is a linear and unsaturated polyester containing one unsaturated C=C double bond per repeating unit. The double bonds of PPF can crosslink with itself or a variety of crosslinking agents such as 1-vinyl-2-pyrrolidinone (N-VP) to form crosslinked polymer networks.[12, 13] In addition, the ester linkage allows for hydrolysis of the polymer into biocompatible and excretable degradation products of fumaric acid and propylene glycol, shown in Figure 2.1.[14, 15]

www.manaraa.com

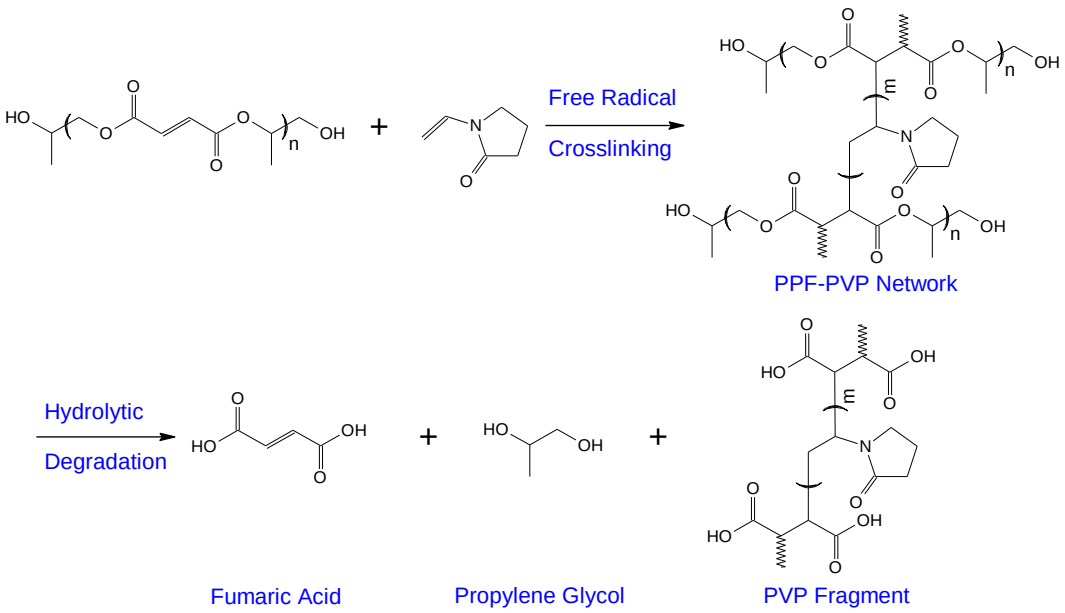

Figure 2.1. Crosslinking and degradation scheme of PPF-PPF-PVP networks.

Even though crosslinked PPF can be considered as a material for trabecular bone tissue regeneration, significant mechanical reinforcement is needed for the use of this material under load bearing conditions.[16, 17] Nanoparticles such as calcium phosphates including tetracalcium phosphate (TTCP), dicalcium phosphate (DCPA), and hydroxyapatite (HAp) have been investigated for PPF-based cements, enhancing the mechanical strength of the composite and osteoconductivity.[18-20] Shi et al. and Sitharaman et al. used single-walled carbon nanotubes (SWNTs) as reinforcing fillers in PPF because of their excellent mechanical properties and high aspect ratios; however, the addition of carbon nanotubes may impose negative effects on the aesthetic requirements and biocompatibility of the bone cement.[16, 21] It is believed that one-dimensional oxides, such as nanowires or nanotubes of SiO_2, ZrO_2, Al_2O_3, and TiO_2 would be promising for the reinforcement of bone cement compositions due to their unique properties and low cost compared to carbon nanotubes.[22, 23] Horch et al. and Mistry et al. designed a composite material utilizing surface-modified carboxylate alumoxane nanoparticles and PPF network, which showed a significant improvement in flexural properties.[17, 24] However, alumina-based implants have rarely shown to initiate apatite formation and cannot directly attach to bone.[25, 26] Essentially no studies have examined the incorporation of 1D nano-structured oxides into PPF bone cement matrix to

www.manaraa.com

enhance its mechanical properties. To the best of our knowledge, this is the first study to incorporate 1D nano-structured titania into a PPF matrix, which requires a new synthetic methodology. TiO_2 nanofibers or wires are expected to be superior to alumina nanoparticles owing to their excellent biocompatibility and unique oseointegration. Titania nanofibers or wires can directly bond to bone through the formation of a biologically active bone-like apatite layer on the surfaces of implants within the body (oseointegration).[26, 27] In addition, titania nanofibers or wires have high aspect ratios which enhances their interfacial interaction with the resin matrix leading to dramatically enhanced mechanical properties.[23, 28]

In this work we present a new method for the synthesis of functionalized PPF containing a carboxyl group at each end of the PPF chains using a ring opening reaction at room temperature in the presence of a highly nucleophilic tertiary amine catalyst, 4-dimethylaminopyridine.[29, 30] The carboxyl group allowed for coordination of PPF to nano-TiO_2, and the subsequent crosslinking reaction with 1-vinyl-2-pyrrolidinone to form crosslinked TiO_2-PPF nanocomposites. The mechanical properties of the synthesized crosslinked TiO_2-PPF nanocomposites were measured, showing potential applications in bone cementation.

2.2 Experimental details

2.2.1 Materials

Titanium isopropoxide (99.999%), glacial acetic acid (>99.7%), diethyl fumarate (98%), propylene glycol (1,2-propanediol) (≥99.5%), anhydrous zinc chloride ($ZnCl_2$, ≥99.995%), hydroquinone (99%), maleic anhydride (95%), 4-dimethylaminopyridine (DMAP), hydrochloric acid (37%), anhydrous magnesium sulfate (99.0%), anhydrous diethyl ether (≥99.0%), anhydrous dichloromethane (DCM, ≥99.8%), anhydrous tetrahydrofuran (THF, ≥99.9%), 1-vinyl-2-pyrrolidinone (N-VP), benzoyl peroxide (BPO), and N-dimethyl-p-toluidine (DMT) were purchased from Sigma-Aldrich Canada and used as received. Instrument grade carbon dioxide (99.99%) was purchased from BOC Canada.

www.manaraa.com

2.2.2 Characterization

Scanning electron microscopy images were collected using a Leo(Zeiss) 1540XB SEM. Imaging was performed at either low voltage (1 kV) for morphology or at 10 kV for backscatter imaging. Samples were coated with 5nm of osmium metal in a Filgen OPC80T. For studying the fracture surface, samples were broken by submersing in liquid nitrogen in a stainless steel mortar and broken with a stainless steel pestle. The particle diameter and aspect ratio frequency distribution of TiO_2 nanoparticles were obtained by measuring over 100 TiO_2 nanoparticles using Image J software (NIH, version 1.37). Transmission electron microscopy images were recorded using a Philips CM10 transmission electron microscope with an AMT digital camera (Eindhoven, Netherlands) operated at 100 kV.

Attenuated total reflection-Fourier transform infrared (ATR-FTIR) spectra were measured using a Nicolet 6700 FTIR spectrometer (Thermo Scientific) equipped with a smart iTR (diamond ATR). The spectra were recorded in the range of 600-4000 cm^{-1} with a resolution of 4 cm^{-1} over 32 scans. X-ray photoelectron spectroscopy (XPS) analyses were carried out with a Kratos AXIS Ultra spectrometer using a monochromatic Al K(α) source (15mA, 14kV). Samples were placed on a carbon-based double-sided adhesive tape for analysis. The Kratos charge neutralizer system was used on all specimens. Survey scan analyses were carried out with an analysis area of 300 µm × 700 µm and a pass energy of 160 eV. High resolution analyses were carried out with an analysis area of 300 µm × 700 µm and a pass energy of 20 eV. Spectra were charge corrected to the main line of the carbon 1s spectrum set to 284.8 eV. Spectra were analyzed using CasaXPS software (version 2.3.14). ^{1}H and ^{13}C NMR spectra were measured using either a Varian INOVA 600 or a Varian INOVA 400 spectrometer at 25 ^{o}C. $CDCl_3$ was used as the solvent and chemical shifts were referenced to tetramethylsilane (TMS; 0.0 ppm). Thermogravimetric analysis (TGA) was performed using a TA Q500 TGA at a heating rate of 10 ^{o}C/min under an inert (nitrogen) atmosphere.

Mechanical tensile properties were measured using an Instron 5943 universal testing machine (Instron, Canton, MA) equipped with a 500 N (tension) load cell. Tensile testing

www.manaraa.com

was conducted in accordance with ASTM D638-91a. Dogbone specimens with overall length of 60 mm and width of grip section of 10 mm were used for tensile testing. Stress-strain relationship was obtained from the load and displacement data. Young's modulus was determined by calculating the slope of the linear portion of the stress-strain curve, and tensile strength was defined as the maximum applied stress prior to failure. For each group, 5 independent specimens (n=5) were tested in tension at a crosshead speed of 10 mm/min. Flexural strength and flexural modulus of the nanocomposites were determined in accordance with ASTM D790M-92 using a dynamic mechanical analyzer, DMA Q800 (TA instruments). Flexural testing samples, rectangular bar specimens (n=5) (50 mm × 25 mm × 2 mm), were placed on a three-point bending apparatus with two supports spanning 40 mm from each other and loaded at the cross-head speed of 10 mm/min to the center of each specimen until failure. In an approach similar to that of tensile testing, flexural modulus was calculated as the slope of the initial linear region of the stress-strain curve, while flexural fracture strength was determined as the maximum applied stress prior to failure.

2.2.3 Preparation of materials

2.2.3.1 *Synthesis of poly(propylene fumarate) (PPF)*

PPF was synthesized using a two-step transesterification method described in the literature.[31] In a typical experiment, diethyl fumarate (31.56 g, 183 mmol) and propylene glycol (41.38 g, 549 mmol) were reacted in an inert atmosphere under stirring, with $ZnCl_2$ (0.250 g, 1.83 mmol) and hydroquinone (0.0403 g, 0.366 mmol) being added as a catalyst and a crosslinking inhibitor, respectively. After the reaction temperature had been increased to 110 ºC, the temperature was further increased from 110 ºC to 150 ºC in an increment of 10 ºC every 15 min. Bis(hydroxypropyl) fumarate (**1**) was formed with the continuous removal of the byproduct ethanol, as a distillate. This step was terminated by cooling down to 100 ^{o}C when ~ 90% of the theoretical yield of ethanol was collected.

The second step of the reaction, transesterification of the intermediate bis(hydroxypropyl) fumarate to form PPF (**2**), was conducted under reduced pressure (<1 mm Hg), producing propylene glycol as a byproduct. The temperature was raised gradually from 100 ºC to

www.manaraa.com

150 ºC in an increment of 10 ºC every 30 min, and the reaction proceeded until the desired molecular weight of PPF was obtained. The polymer product was then dissolved in dichloromethane followed by several acid washes with a 5% v/v solution of 1 N HCl, two washes with distilled water, and two washes with brine. After drying with magnesium sulfate, the organic phase was concentrated by rotary evaporation and then precipitated in diethyl ether to remove the hydroquinone inhibitor. The precipitated polymer was washed with diethyl ether and dried under vacuum. Yield: 73% (21 g). FTIR (cm^{-1}): 1713 ($\nu_{C=O}$), 1645 ($\nu_{C=C}$), 1251 ($\nu_{C-O-C(as)}$), 1148 ($\nu_{C-O-C(s)}$). ^{1}H NMR ($CDCl_3$, 600 MHz) δ (ppm): 6.85 (O=C-C<u>H</u>=C<u>H</u>-C=O), 5.29 (O-C<u>H</u>(CH_3)-CH_2), 4.33 & 4.25 (O-CH(CH_3)-C<u>H</u>$_2$), 1.34 (O-CH(C<u>H</u>$_3$)-CH_2), 5.10, 4.22, 4.09, 3.70, 1.29, and 1.23 (end groups of the PPF polymer chain). ^{13}C NMR ($CDCl_3$, 100 MHz) δ (ppm): 164.0-164.3(O=<u>C</u>-CH=CH-<u>C</u>=O), 133.3-134.0 (O=C-<u>C</u>H=<u>C</u>H-C=O), 69.2 (O-<u>C</u>H(CH_3)-CH_2), 66.6 (O-CH(CH_3)-<u>C</u>H$_2$), 16.3 (O-CH(<u>C</u>H$_3$)-CH_2), 73.1, 70.3, 65.8, 65.5, 19.2, and 16.0 (end groups of the PPF polymer chain).

2.2.3.2 *Functionalization of PPF*

In order to functionalize the PPF chain with maleic anhydride, to a solution of PPF (1g, 0.91 mmol of -OH group) in 10 mL of anhydrous dichloromethane were added DMAP (0.11 g, 0.91 mmol) and maleic anhydride (0.36 g, 3.64 mmol). The reaction mixture was stirred under argon at room temperature for 24 h. After completion of the reaction, 5 mL of dichloromethane was added to the flask followed by washing with 10 mL of 1 N HCl solution and distilled water. The organic phase was subsequently dried over anhydrous magnesium sulfate. After that, the organic phase was filtered and the solvent was removed by rotary evaporation to afford maleic anhydride-functionalized PPF (MA-PPF) (**3**). Yield: 59% (0.64g). ^{1}H NMR ($CDCl_3$, 600 MHz) δ (ppm): 8.19 (-COO<u>H</u>). 6.85 (O=C-C<u>H</u>=C<u>H</u>-C=O), 5.29 (O-C<u>H</u>(CH_3)-CH_2), 4.33 & 4.25 (O-CH(CH_3)-C<u>H</u>$_2$), 1.34 (O-CH(C<u>H</u>$_3$)-CH_2). ^{13}C NMR ($CDCl_3$, 100 MHz) δ (ppm): 164.0-164.3(O=<u>C</u>-CH=CH-<u>C</u>=O), 133.3-134.0 (O=C-<u>C</u>H=<u>C</u>H-C=O), 69.2 (O-<u>C</u>H(CH_3)-CH_2), 66.6 (O-CH(CH_3)-<u>C</u>H$_2$), 16.3 (O-CH(<u>C</u>H$_3$)-CH_2).

www.manaraa.com

2.2.3.3 *Synthesis of TiO_2 nanofibers via sol-gel reaction in supercritical CO_2*

High surface area TiO_2 nanofibers were synthesized using supercritical CO_2 ($scCO_2$) as reported by Sui et al.[32] Briefly, in a typical experiment, titanium isopropoxide (1 g) was quickly placed in a 10-mL stainless steel view cell, followed by addition of acetic acid (4 g). CO_2 was then added to the view cell using a syringe pump (Isco 260D) to the desired pressure (6000 psig) while increasing the temperature to 60 °C. A magnetic stirrer was used for mixing the reaction mixture. Stirring was stopped after 24 h, and normally several days of aging were required for a complete reaction. After aging, the formed gel was washed continuously using 80 mL of CO_2 at a rate of approximately 0.5 mL/min, followed by controlled venting at 0.5 mL/min to prevent collapse of the solid network. The as-prepared powder was calcined at 450 °C in air for 2 h with a heating rate of 10 °C/min and a cooling rate of 0.5 °C/min to room temperature. The calcined powder was kept in a vacuum oven at 80 °C.

2.2.3.4 *Synthesis of TiO_2-PPF nanocomposites*

To prepare TiO_2-PPF nanocomposites (**4**), 0.5, 1.25, or 2.5 wt% of the synthesized TiO_2 nanofibers (0.005, 0.0125, or 0.0250 g) was dispersed in 20 mL of THF with the aid of ultrasonic agitation for 1 h, followed by reacting with the above synthesized MA-PPF (1 g) at 70 °C under argon with constant stirring for 24 h. After filtering off the solvent and the unreacted MA-PPF, the product was further purified by dispersion in THF, centrifugation, and removal of the supernatant. This purification process was repeated several times until the supernatant became clear. Finally, the resulting solid product was dried at 55 ºC under vacuum overnight. The composition of the synthesized nanocomposites and the nano-TiO_2 concentration in each nanocomposite formulation reviewed by TGA analysis are presented which are listed in Table 2.1.

FTIR (cm^{-1}): 1713 ($\nu_{C=O}$), 1645 ($\nu_{C=C}$), 1570 & 1377 ($\nu CO_2^-{}_{(as)}$), 1251 ($\nu_{C-O-C(as)}$), 1165 ($\nu CO_2^-{}_{(s)}$), 1148 ($\nu_{C-O-C(s)}$).

www.manaraa.com

Table 2.1. Formulation of the TiO_2-PPF nanocomposites.

MA-PPF (g)	nano-TiO_2 (g)	*nano-TiO_2 wt% in the synthesized nanocomposite	Sample Name
1 g	0.005 g	5 wt%	TiO_2-PPF nanocomposite-1
1 g	0.0125 g	10 wt%	TiO_2-PPF nanocomposite-2
1 g	0.0250 g	22 wt%	TiO_2-PPF nanocomposite-3

Note: ***** the weight percentage of nano-TiO_2 in each TiO_2-PPF nanocomposite formulation is obtained from the TGA analysis.For comparison of XPS study, a mechanically mixed PPF-TiO_2 nanocomposite was fabricated by mechanical mixing of the PPF (1 g) and TiO_2 nanoparticles (0.10 g).

2.2.3.5 *Synthesis of bone cement composites*

The bone cement composites (**5**) were prepared by crosslinking the synthesized TiO_2-PPF nanocomposites (details are provided in Table 2.1) using N-VP. In a typical experiment, the above synthesized TiO_2-PPF nanocomposite (1 g) was mixed with N-VP (0.4 g) for 2 h. Initiator, BPO (0.05 g), was dissolved in 250 µL of N-VP. The 50 µL of BPO solution was then combined and mixed with the TiO_2-PPF nanocomposite solution. Subsequently, 40 µL of accelerator solution (20 µL of DMT in 980 µL of dichloromethane) was added with rapid mixing to accelerate the crosslinking reaction.[4, 19] The resulting paste was placed in a Teflon mold, then loaded in an oven at 60 °C for 1 h to facilitate crosslinking. After that, the mold was cooled down to room temperature, and the formed bone cement composite was removed before being subject to mechanical testing. Three different bone cement composites were prepared using the TiO_2-PPF nanocomposites synthesized with different amounts of TiO_2, which are listed in Table 2.2.

For comparison of mechanical testing, bone cement composites were prepared by

www.manaraa.com

crosslinking the mechanically mixed 1 g of PPF and 0.05 g of nano-TiO_2 (corresponding to the actual TiO_2 concentration in the TiO_2-PPF nanocomposite-1 reviewed by TGA analysis represented in Table 2.1) following the above procedure. The composition of the prepared mechanically mixed bone cement composite is also listed in Table 2.2.

Table 2.2. Formulation of the bone cement composites.

Entry No.	**TiO_2-PPF**	**nano-TiO_2**	**PPF**	**Formed Product**
1			1 g	Crosslinked PPF
2	1 g of TiO_2-PPF synthesized using 0.005 g of TiO_2			Bone cement composite-1
3	1 g of TiO_2-PPF synthesized using 0.0125 g of TiO_2			Bone cement composite-2
4	1 g of TiO_2-PPF synthesized using 0.0250 g of TiO_2			Bone cement composite-3
5		0.05 g	1 g	Mechanically mixed bone cement

Note: Additionally, 0.4 g of N-VP, 50 μL of BPO solution, and 40 μL of DMT solution were added in the preparation of these materials.

www.manaraa.com

2.3 Results and Discussion

2.3.1 Synthesis of poly(propylene fumarate) (PPF)

The synthesis of PPF involves firstly a transesterification reaction of diethyl fumarate with propylene glycol (Step **a** in Figure 2.2) to produce bis(hydroxypropyl) fumarate (**1**). In step **b**, poly(propylene fumarate) (PPF) (**2**) is produced by the transesterification/polymerization of **1** with $ZnCl_2$/hydroquinone. In this step, the alkoxy group of the intermediate, bis(hydroxypropyl) fumarate), is replaced with an alcohol from a second bis(hydroxypropyl) fumarate intermediate, propagating PPF polymerization and producing propylene glycol as a byproduct. The synthesized PPF was then reacted with maleic anhydride to form maleic anhydride-functionalized PPF (MA-PPF) (**3** of Figure 2.2). A small amount of $ZnCl_2$ was added in the transesterification reaction as a catalyst, while a small amount of hydroquinone was added as an inhibitor to prevent the C=C double bond from being polymerized at high temperatures up to 150 °C. Continuous removal of the byproducts ethanol in the first transesterification reaction and propylene glycol in the second transesterification reaction as the condensates is necessary to drive the step-growth condensation polymerization reactions. The esterification reaction of maleic anhydride and PPF provided PPF with a functional carboxyl group at both ends of the polymer chains **(3**), in order to provide potential coordination of the functionalized PPF to the surface of TiO_2 nanofibers.

www.manaraa.com

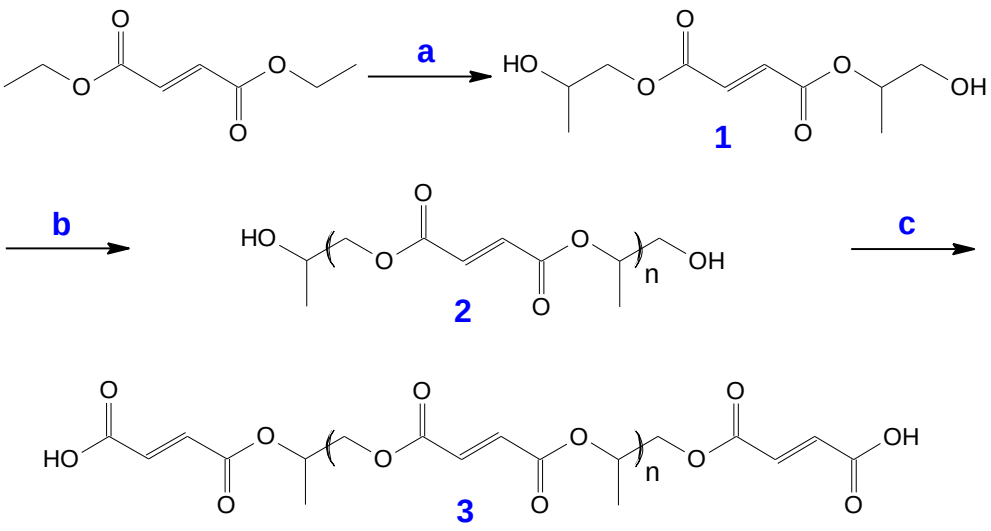

Figure 2.2. Synthetic Scheme for the Preparation and Functionalization of PPF. Reagents and conditions: (a) propylene glycol, $ZnCl_2$, hydroquinone; (b) $ZnCl_2$, hydroquinone; (c) maleic anhydride, DMAP, DCM.

The synthesis and functionalization of PPF was confirmed by NMR (^1H, ^{13}C). The ^1H NMR spectra of propylene glycol and the synthesized PPF and MA-PPF are compared in Figure 2.3. There are four distinct peaks present in the spectrum of propylene glycol (Figure 2.3a), with the peaks at 1.16, 3.39 & 3.62, and 3.90 ppm attributed to the methyl (CH_3), methylene (CH_2), and methine (CH) protons, respectively. In the spectrum of PPF (Figure 2.3b), major peaks appeared at 6.85, 5.29, 4.33 & 4.25, and 1.34 ppm, attributable to the olefinic (O=C-C<u>H</u>=C<u>H</u>-C=O), methine, methylene, and methyl protons in the repeating unit, respectively. Some minor peaks are also present in the spectrum at 5.10, 4.22, 4.09, 3.70, 1.29, and 1.23 ppm, which are attributed to the end group of the PPF polymer chain (see Figure 2.3b). By integrating these major and minor peaks (Figure 2.3), the number average molecular weight ($\overline{M_n}$) of the synthesized PPF (**2**) was estimated as ~ 2200 Da, which is within the reported range between 500 and 4,000 Da.[31] When PPF was converted to MA-PPF (**3**), these major peaks were still present in the spectrum, but the minor peaks disappeared (Figure 2.3c). In addition, a minor broad peak appeared at 8.19 ppm in the ^1H NMR spectrum of MA-PPF, attributable to the carboxyl proton (-COO<u>H</u>) located at both ends of the polymer chains. Together with the disappearance of the minor peaks present in the spectrum of PPF, this minor carboxyl

www.manaraa.com

peak in the ^{1}H NMR spectrum of MA-PPF suggested successful conversion of PPF to MA-PPF.

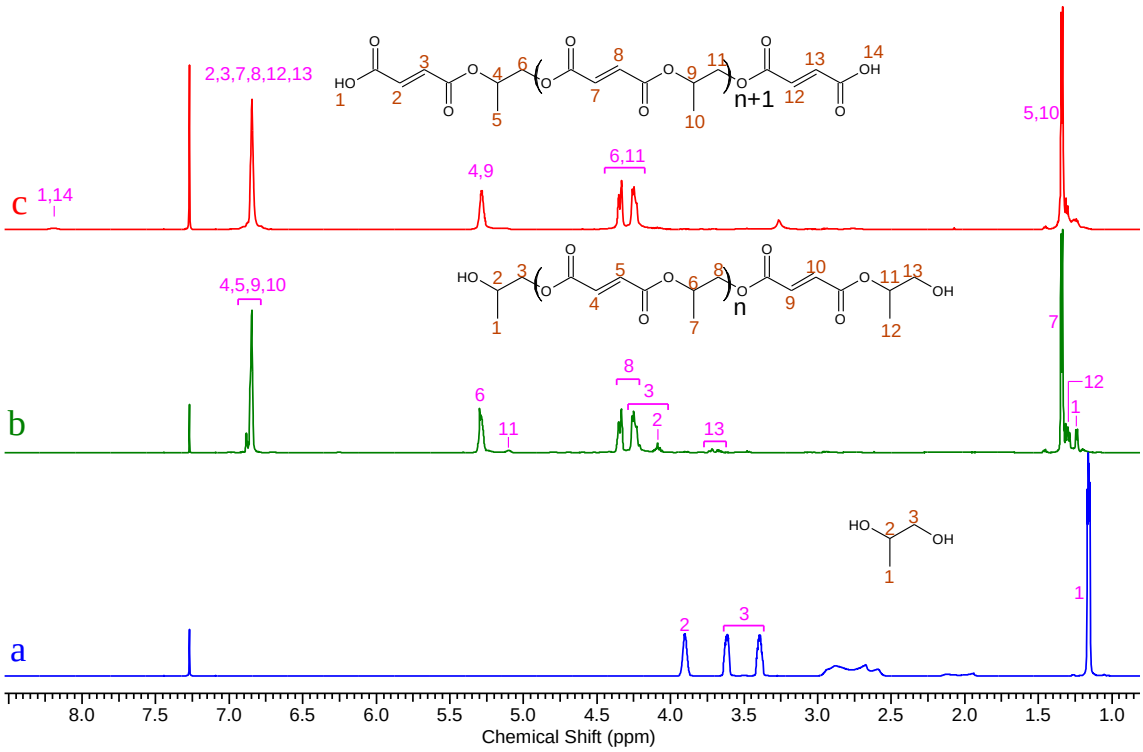

Figure 2.3. A comparison of ^{1}H NMR spectra of (a) propylene glycol, (b) the synthesized PPF, and (c) MA-PPF in $CDCl_3$.

www.manaraa.com

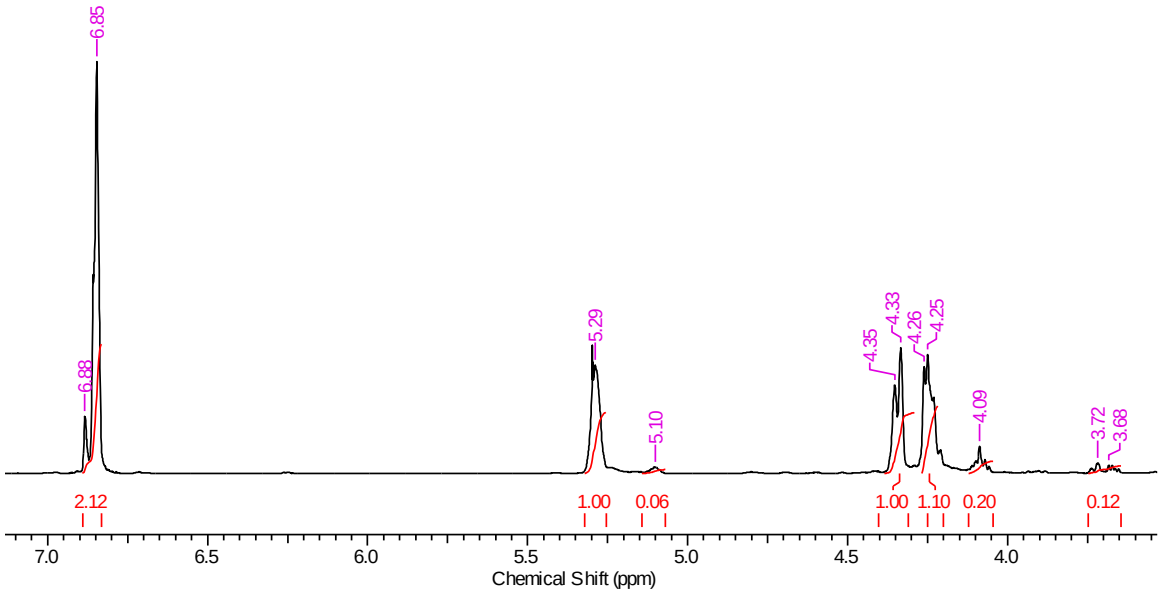

Figure 2.4. ^{1}H NMR spectrum of the synthesized PPF in $CDCl_3$ showing integrals of the peaks.

The successful conversion of PPF to MA-PPF was also evidenced by ^{13}C NMR results. A comparison of the ^{13}C spectra of propylene glycol, PPF, and MA-PPF is shown in Figure 2.5. In the spectrum of propylene glycol (Figure 2.5a), three carbon peaks appear at 68.2, 67.8, and 18.6 ppm, which are attributed to the methyl (CH_3), methylene (CH_2), and methine (CH) carbons, respectively. In the spectrum of PPF (Figure 2.5b), there are five major peaks appearing at 164.0-164.3, 133.3-134.0, 69.2, 66.6, and 16.3 ppm, attributable to the carbonyl (O=C-CH=CH-C=O), olefinic (O=C-CH=CH-C=O), methine, methylene, and methyl carbons in the repeating unit, respectively. Some minor peaks are also present in the spectrum at 73.1, 70.3, 65.8, 65.5, 19.2, and 16.0 ppm, which are attributed to the end group of the PPF polymer chains (Figure 2.5b). When PPF was converted to MA-PPF, these major peaks were still present but the minor peaks disappeared (Figure 2.5c). Although the peak of the carboxyl carbon at the end of the PPF-g-MA polymer chains was not observed due to its low concentration, the absence of the minor peaks in the spectrum of MA-PPF confirmed successful conversion of PPF to MA-PPF.

www.manaraa.com

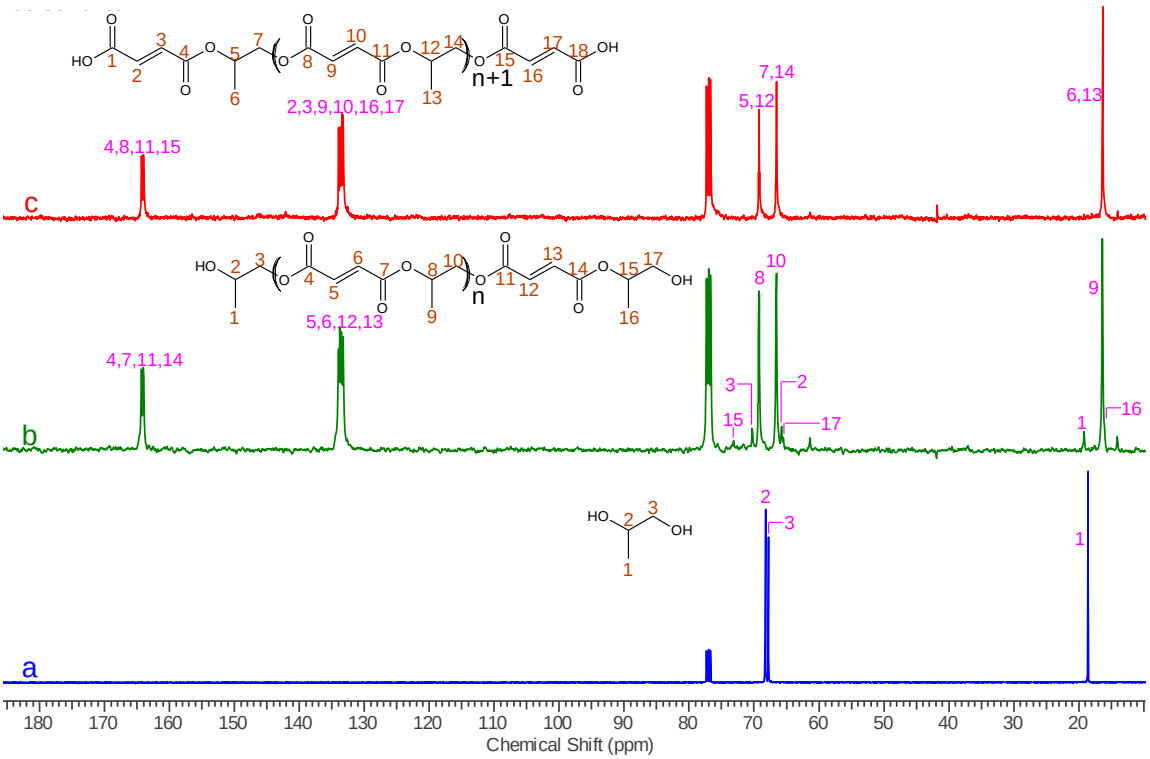

Figure 2.5. A comparison of ^{13}C NMR spectra of (a) propylene glycol, (b) the synthesized PPF, and (c) MA-PPF in $CDCl_3$

2.3.2 Preparation of TiO_2-PPF nanocomposites and bone cement composites

To prepare TiO_2-PPF nanocomposites, TiO_2 nanowires/fibers were synthesized prior to reaction with **3**. The morphology and size of the nano-TiO_2 synthesized in $scCO_2$ and calcined at 450 °C were characterized by SEM and TEM, as shown in Figure 2.6a-b and Figure 2.6c-d, respectively. The mean diameter and aspect ratio of the synthesized fiber-like nanostructures of TiO_2 were determined to be 50±10 nm and 30±5, respectively (Figure 2.6c-d). These results are in good agreement with those reported in the literature.[32, 33] The advantage of this synthetic approach in $scCO_2$ is that high aspect ratio nanowires with high porosity and high surface area are produced.

www.manaraa.com

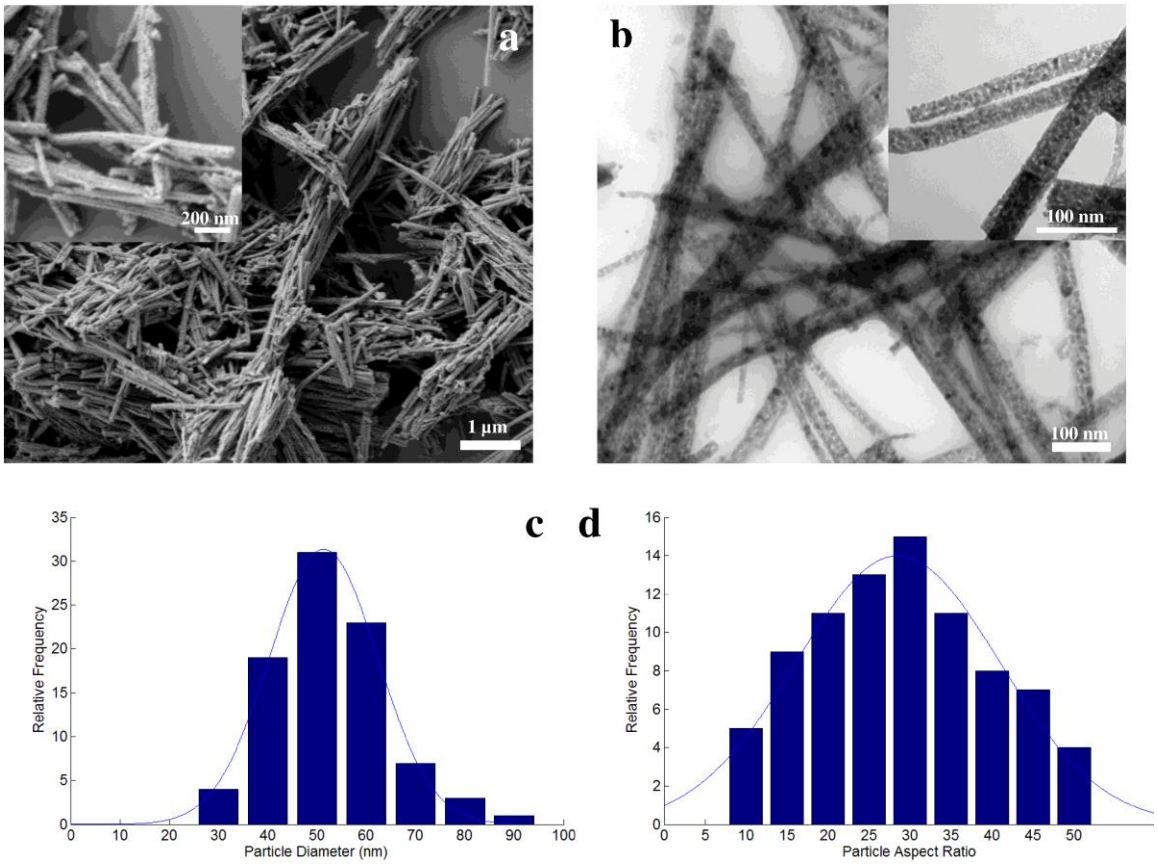

Figure 2.6. (a) SEM and (b) TEM images and the distribution of (c) diameter and (d) aspect ratio of the synthesized TiO_2 nanofibers.

With TiO_2 nanofibers being synthesized, TiO_2-PPF nanocomposites were prepared by coordination reaction of MA-PPF (**3**) to the surface of TiO_2 nanofibers, as shown in Figure 2.7. The synthesized TiO_2-PPF nanocomposites (**4**) were further crosslinked to form the desired bone cement composites (**5**).

www.manaraa.com

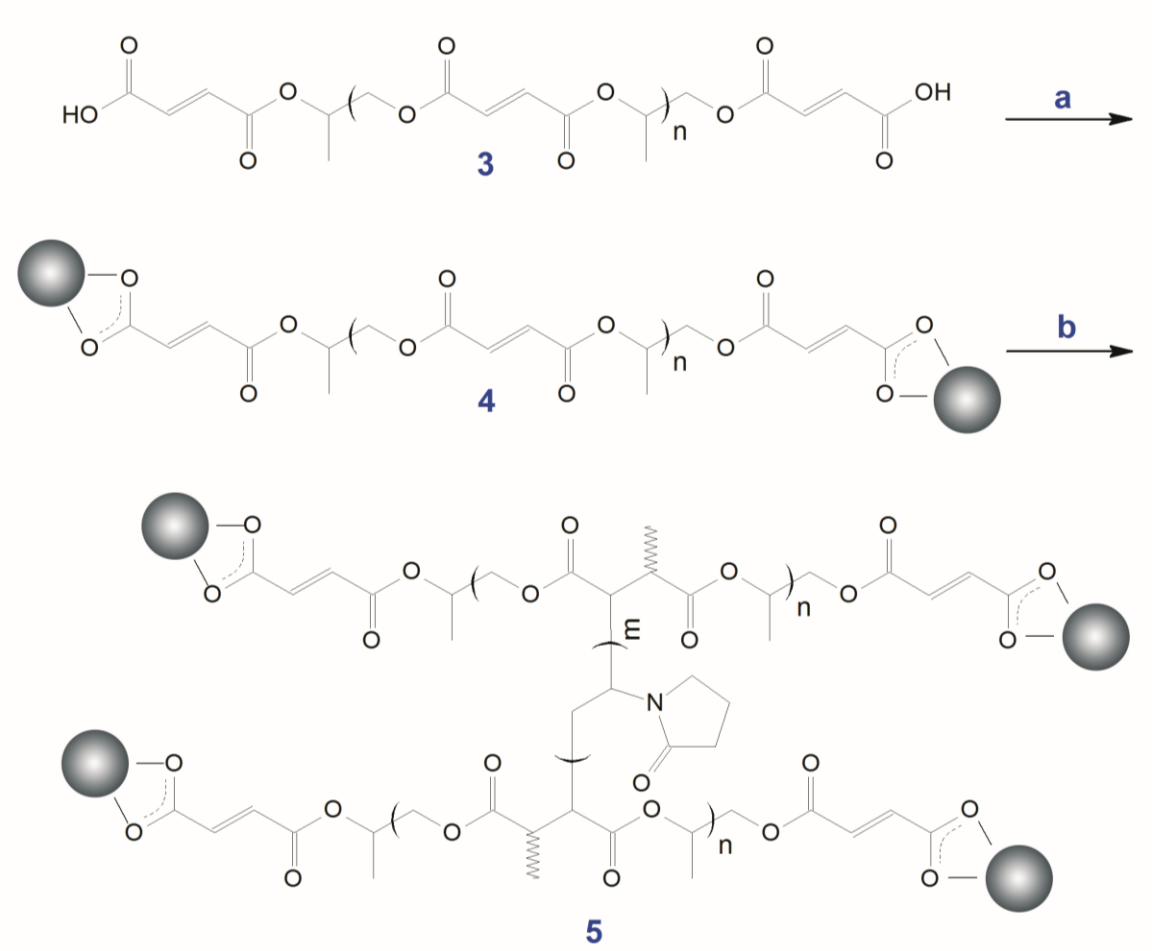

Figure 2.7. Synthetic Scheme for the preparation of (4) TiO_2-PPF nanocomposites and (5) bone cement composites.

Reagents and conditions: (a) TiO_2 nanofibers, THF; (b) N-VP, BPO, DMT.

The synthesized TiO_2-PPF nanocomposites (**4**) and cross-linked bone cement composites (**5**) were characterized with FTIR, XPS, and TGA to examine the reaction chemistry. The FTIR spectra of TiO_2, PPF, TiO_2-PPF nanocomposite (**4**), and bone cement composite (**5**) are compared in Figure 2.8. Several major characteristic peaks appeared at 1713, 1645, 1251, and 1148 cm^{-1} in the spectrum of PPF (Figure 2.8b), attributed to the C=O stretching, C=C stretching, asymmetric C-O-C stretching, and symmetric C-O-C stretching bands, respectively.[4, 34] The peak at 1645 cm^{-1} in the FTIR spectrum of both PPF and TiO_2-PPF nanocomposite shows the C=C double bond was unaffected in the polymer chains after the reaction of MA-PPF and nano-TiO_2. Additional peaks appearing at 1570, 1377 and 1165 cm^{-1} in the FTIR spectrum of the TiO_2-PPF nanocomposite

www.manaraa.com

(Figure 2.8c) are attributed to the asymmetric and symmetric CO_2^- stretching bands, respectively, indicating successful coordination of PPF to the TiO_2 nanofibers. Rotzinger et al. described three possible coordination structures of carboxylate to the surface of TiO_2, i.e., chelating bidentate, monodentate, and bridging bidentate (Figure 2.9).[34] These structures can be distinguished in infrared spectra by the separations between the carboxylate stretching bands ($\Delta\upsilon$). The band separation ($\Delta\upsilon$=405 cm^{-1}) between 1570 and 1165 cm^{-1} falls into the monodentate range (350-500 cm^{-1}) while another band separation ($\Delta\upsilon$=193 cm^{-1}) between 1570 and 1377 cm^{-1} might be indicative of a structure of bridging bidentate (150-180 cm^{-1}).[35] These coordination peaks remained evident in the spectrum of the crosslinked bone cement composite, although the peak at 1645 cm^{-1} (C=C stretching band) disappeared (Figure 5d). The disappearance of the C=C stretching band confirmed the crosslink reaction which consumed the C=C double bond (Figure 2.7).[36]

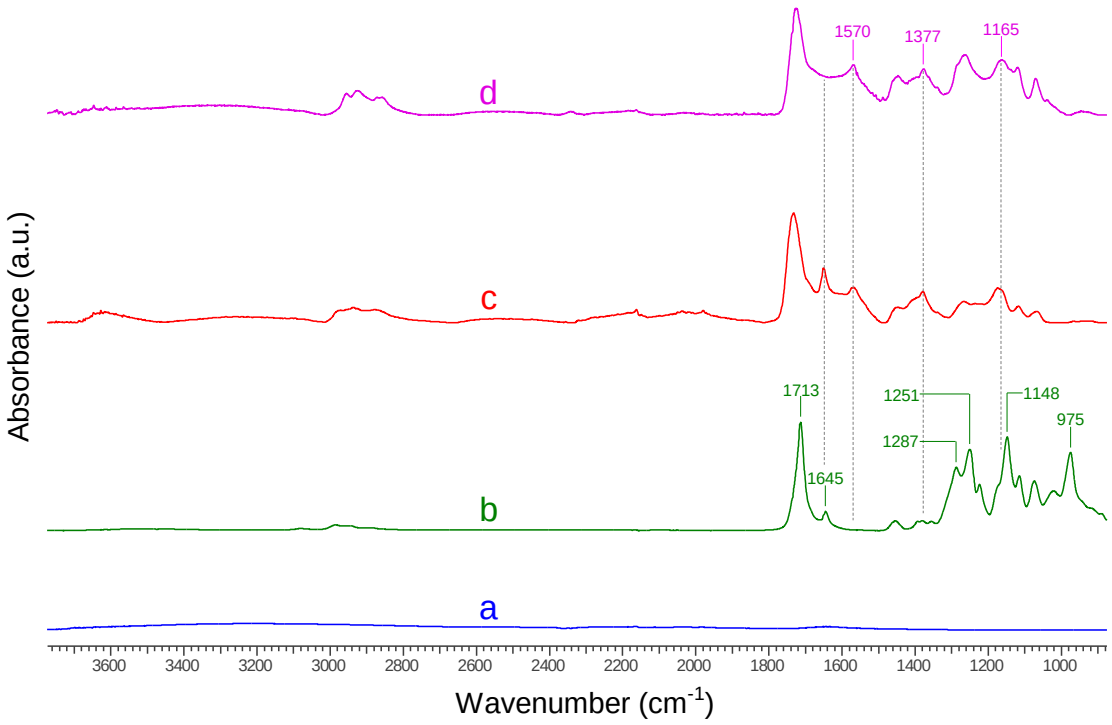

Figure 2.8. ATR-FTIR spectra of (a) TiO_2, (b) PPF, (c) TiO_2-PPF nanocomposite, and (d) crosslinked bone cement composite.

www.manaraa.com

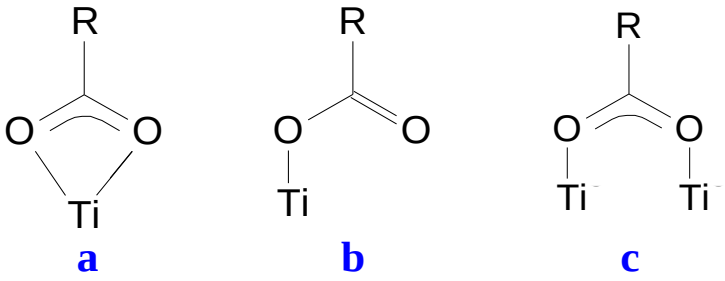

Figure 2.9. Binding modes of RCOO- with TiO_2 surface (R= H or CH_3).
(a) chelating bidentate (b) monodentate, and (c) bridging bidentate.[34]

X-ray photoelectron spectroscopy (XPS) was further employed for characterization of the synthesized PPF (**2**), MA-PPF (**3**), and non-crosslinked TiO_2-PPF (**4**) nanocomposites. The high resolution XPS scan of C 1s region for both PPF and MA-PPF (Figure 2.10a-b) represent similar patterns as expected for the chemistries involved. In both spectra, three major carbon peaks are observed with binding energies of 285 eV, 286.5, and 289.0 eV, which correspond to aliphatic carbon (C–C, C-H), alcohol and ether functionality (C–OH, C–O–C), and ester and carboxylic acid type functionality (O–C=O), respectively [6] with relatively equal peak intensities for the peaks at 286.5 eV and 289.0 eV. Some of the intensity associated with the aliphatic carbon are attributed to adventitious carbon on the surface of the samples. In addition, the core level spectrum of O 1s for both PPF and MA-PPF, shown in Figure 2.10c-d, are resolved into two peaks at binding energies of 532 eV and 533.5 eV, which are attributed to O-C=O* and O*-C=O, respectively (* denotes the O of interest).[6]

In the recorded survey spectrum for the non-crosslinked TiO_2-PPF nanocomposite, the expected peaks for O, C, and Ti were detected (Figure 2.10e). In the high resolution XPS scan of the C 1s region (Figure 2.10f), the three major peaks observed for PPF and MA-PPF are still evident. In addition, a new peak appeared at 288.2 eV, which is assigned to the C atom of the carbonyl group from the successful covalent interaction of carboxylate to TiO_2.[37, 38] In order to verify the coordination of MA-PPF to the surface of TiO_2 nanofibers, a C 1s spectrum of the mechanically mixed TiO_2-PPF nanocomposite sample prepared by mechanical mixing of PPF (1g) with nano-TiO_2 (0.10 g) was measured (Figure 2.10g). As expected, no peak shifting or extra peaks were seen in the C 1s

www.manaraa.com

spectrum, indicating no chemisorption of PPF to the surface of nano-TiO_2. In the high resolution O 1s spectrum of non-crosslinked TiO_2-PPF-nanocomposite (Figure 2.10h), a new peak appeared at 529.3 eV, which is related to the lattice oxygen atoms in TiO_2 (Ti-O bonds).[39] Furthermore, the core level spectrum of Ti 2p for the non-crosslinked TiO_2-PPF-nanocomposite (Figure 2.10i) could be resolved into two spin-orbit pairs of 2p3/2 and 2p1/2 with binding energies of 458.3 eV and 464 eV, respectively, attributable to Ti^{4+} implying that the chemical state of titanium remains as Ti^{4+}.[39, 40] Therefore, this XPS data confirms the successful coordination of MA-PPF to the surface of TiO_2 nanofibers without changing the state of nano-TiO_2.

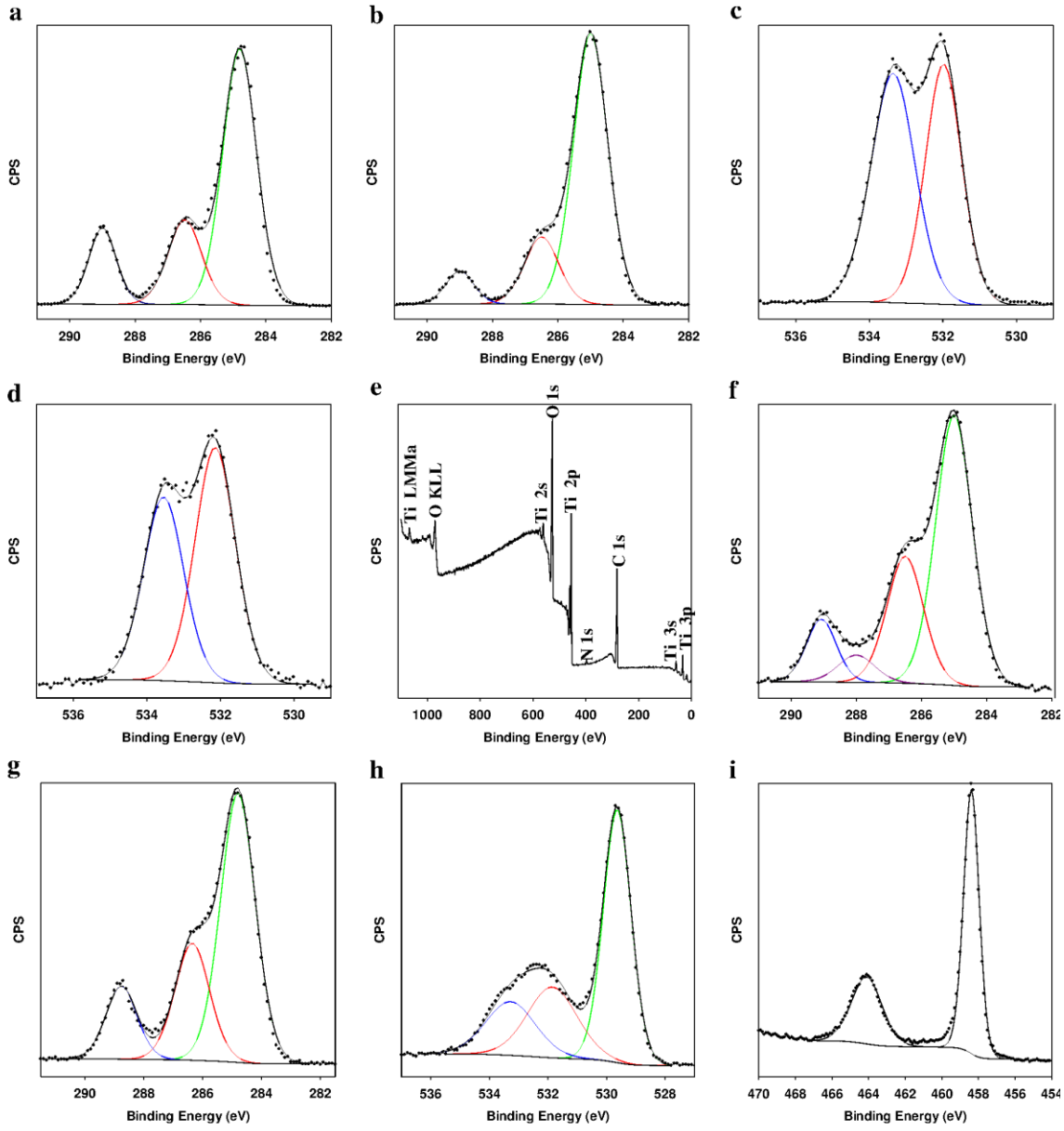

www.manaraa.com

Figure 2.10. High resolution XPS record of C 1s region of (a) PPF and (b) MA-PPF, high resolution XPS record of O 1s region of (c) PPF and (d) MA-PPF, (e) XPS full-scan spectrum of the TiO_2-PPF nanocomposite, high resolution XPS scan of the C 1s region of (f) the TiO_2-PPF nanocomposite and (g) the mechanically mixed TiO_2-PPF nanocomposite, high resolution XPS scan of the O 1s region of (h) the TiO_2-PPF nanocomposite, and high resolution XPS scan of the Ti 2p region of (i) the TiO_2-PPF nanocomposite.

Thermogravimetric analysis (TGA) was also employed in the measurement of PPF attached to the surface of nano-TiO_2 in the synthesized TiO_2-PPF nanocomposites. The TGA characteristics of the nanocomposites are shown by the thermal weight loss and derivative of weight loss (DTG) of the composites with temperature. Figure 2.11 compares the calcined TiO_2, non-crosslinked PPF (**2**) and crosslinked PPF, non-crosslinked TiO_2-PPF (**4**) nanocomposites, and crosslinked TiO_2-PPF (**5**) bone cement composites. A typical TGA result of TiO_2-PPF nanocomposite shows two obvious regions when the temperature increased: the first region started from 30 °C and ended at 200 °C with a relatively small slope (due to evaporation of the entrapped water, solvent, or free carboxyl groups); while the second region started at 200 °C and ended at 400 °C with a large slope indicating more weight loss, which is attributed to the random internal scission of the PPF chains chemically attached to the TiO_2 nanoparticles. The sample of TiO_2-PPF nanocomposite displayed a weight loss of 74% compared to the calcined TiO_2 with the weight loss of 3%. PPF functionalization allowed a relatively high number of polymer chains to be attached on the surface of TiO_2 nanofibers, resulting in an increased weight loss for the TiO_2-PPF nanocomposites.

In addition, the effect of functionalization of the PPF on the nanocomposites can be observed by an enhanced thermal stability of the synthesized bone cement composite compared to the unmodified PPF. As shown in Figure 2.12, the onset degradation temperature T_d for non-crosslinked PPF, crosslinked PPF, TiO_2-PPF nanocomposites, and bone cement composite is 332 ºC, 345 ºC, 336 ºC, and 355 ºC, respectively, with bone cement composite representing the highest thermal dissociation temperature. This thermal stability enhancement is attributed to the strong interfacial adhesion between the nano-

www.manaraa.com

TiO_2 and PPF matrix, which results from the excellent chemical interaction of nano-TiO_2 and functionalized polymer chains, with this strong adhesion providing a barrier effect to the polymer molecules evaporated during the thermal degradation of the nanocomposites.

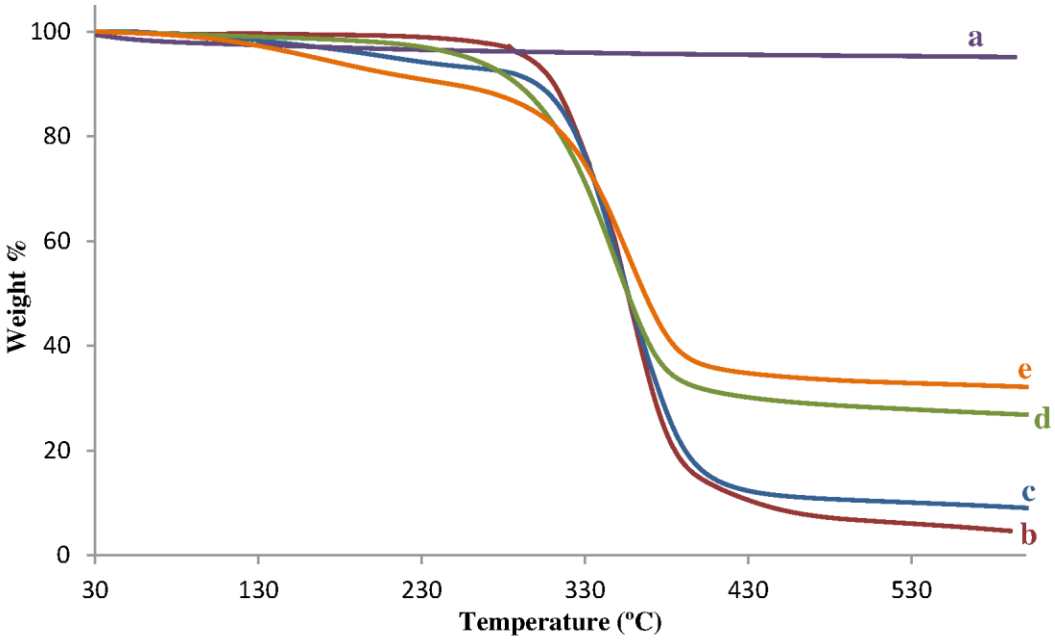

Figure 2.11. TGA curves of: (a) TiO_2, (b) PPF, (c) crosslinked PPF, (d) TiO_2-PPF nanocomposite (synthesized using 1 g of MA-PPF and 0.0250 g of TiO_2) and (e) crosslinked bone cement composite (made of 1 g of TiO_2-PPF synthesized using 0.0250 g of TiO_2).

www.manaraa.com

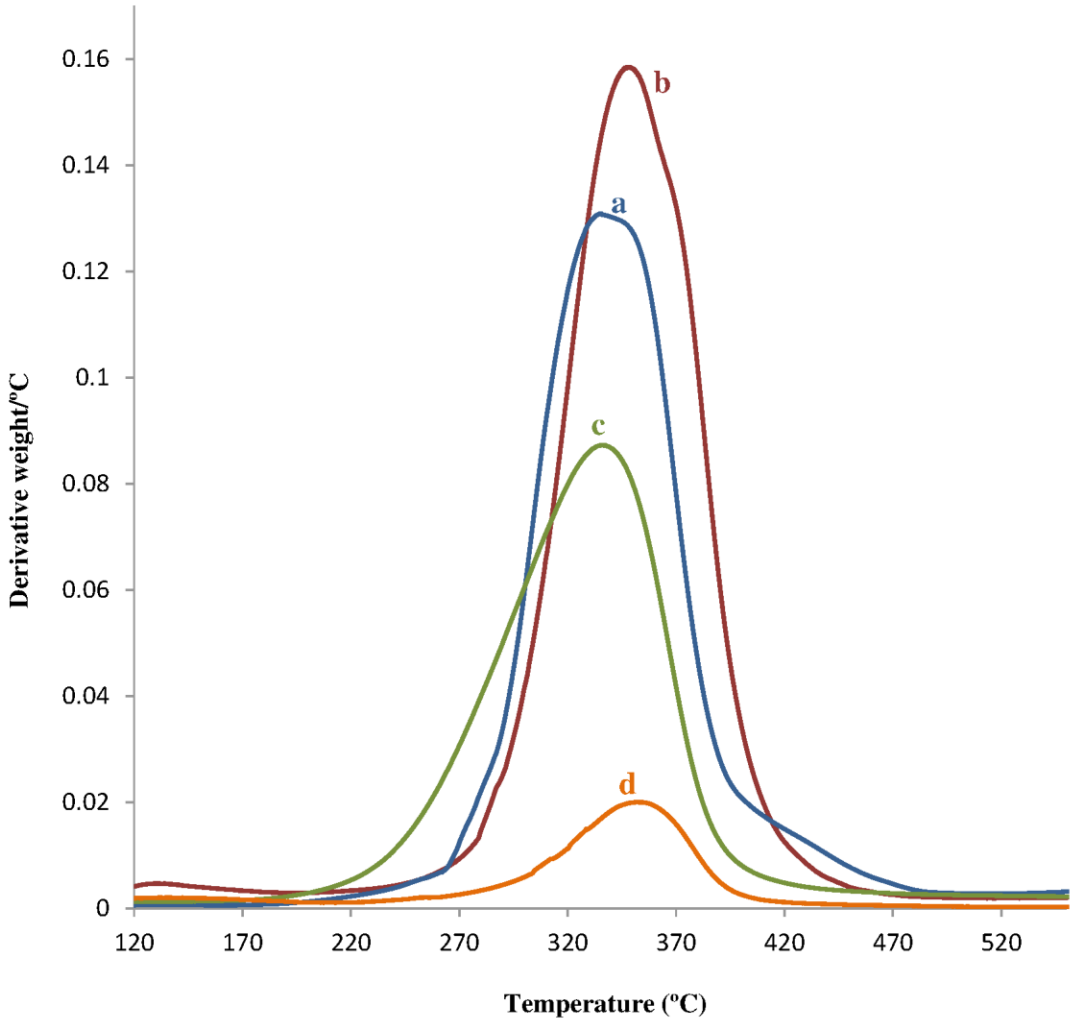

Figure 2.12. Derivative thermogravimetric (DTG) curves of: (a) PPF, (b) crosslinked PPF, (c) (d) TiO_2-PPF nanocomposite (synthesized using 1 g of MA-PPF and 0.0250 g of TiO_2) and (e) crosslinked bone cement composite (made of 1 g of TiO_2-PPF synthesized using 0.0250 g of TiO_2).

2.3.3 Mechanical properties of crosslinked PPF and bone cement composites

The Young's modulus and tensile strength were measured for the crosslinked PPF and bone cement composites with varying nanowire-TiO_2 concentrations, and mechanically mixed bone cement composites. The incorporation of nano-TiO_2 reinforced the mechanical properties of the PPF, as shown in Table 2.3. The Young's modulus and ultimate tensile strength of crosslinked composites increased with the initial relatively

www.manaraa.com

low concentrations of TiO_2, peaked for bone cement composite-1 and bone cement composite-2, and then plateaued or decreased at higher loading concentrations. There was a 2.5-fold increase in the Young's modulus for the bone cement composite-1 compared to the pure polymer. Moreover, the tensile strength, similar to the Young's modulus, decreased with loading of nano-TiO_2 over 0.5-1% in the starting composition. It is clear from Table 2.3 that bone cement composite-1 (Sample 2) possesses the highest value of Young's modulus and ultimate tensile strength amongst the different composites tested. This high value of Young's modulus and tensile strength is attributed to the strong interfacial bonding of the functionalized PPF with nano-TiO_2 fibers as shown by Figure 2.13, which facilitates the transfer of interfacial stress from the filler to the matrix. It can be seen that the unfilled polymer exhibited a smooth plain surface (Figure 2.13a), while the bone cement composite-1 showed a rough surface with the nano-TiO_2 fibers delaminated from the PPF matrix (Figure 2.13b). Figure 2.13b also reveals that the individual nano-TiO_2 fibers were dispersed homogeneously throughout the bone cement composite-1, with strong adhesion to the matrix when reacted to the PPF after being functionalized. The dispersion of individual nanofibers in a polymer matrix may prevent slippage between TiO_2 nanowires while enhancing the transfer of applied load to the nano-TiO_2, which further enhances the mechanical reinforcement. This synthesis methodology provided better compatibility with nano-TiO_2 while establishing chemical bonding through the carboxylic group, resulting in strong interfacial adhesion between the fibers and the matrix as the partially broken or pulled out fibers on their surface is shown by the arrows in Figure 2.13b. In addition to the strong adhesion with the matrix, these partially pulled out fibers are also shown to bridge the cracks in the matrix (Figure 2.13c). However, at higher loading concentration (bone cement composite-2), the measured mechanical properties of these nanocomposites began to decline. This is attributed to the nano-TiO_2 fibers agglomerating at higher concentrations within the polymer matrix, i.e., 10 wt% (Figure 2.13d). The formed agglomerates are considered to be responsible for accelerating crack propagation through local stress concentrators (voids).

www.manaraa.com

Table 2.3. Mechanical Properties of the crosslinked PPF and the synthesized bone cement composites.

*Sample	**TiO_2 (g) for 1 g of MA-PPF	***TiO_2 (g) for 1 g of PPF	Young's modulus (MPa)	Tensile strength (MPa)	Flexural modulus (MPa)	Flexural strength (MPa)
1	0	-	228 ± 42	10.6 ± 2.1	365 ± 66	18.8 ± 2.6
2	0.005	-	578 ± 37	22.6 ± 2.9	1084 ± 115	42.5 ± 6.1
3	0.0125	-	512 ± 26	22.3 ± 3.3	815 ± 83	35.9 ± 0.5
4	0.0250	-	378 ± 65	15.8 ± 0.9	983 ± 34	28.2 ± 6.8
5	-	0.05	318 ± 40	14.7 ± 1.4	583 ± 58	20.6 ± 8.7

Note: the average values and deviations were calculated from 5 sets of repeating experiments.***** The sample number corresponds to the entry number in Table 2.2. ****** The TiO_2 concentration corresponds to the amount of nanowires/fibers used for the formation of TiO_2-PPF nanocomposites, presented in detail in Table 2.1. *** The TiO_2 concentration corresponds to the actual TiO_2 concentration in the TiO_2-PPF nanocomposite-1 obtained by TGA analysis represented in Table 2.1.

In addition, flexural modulus and flexural strength values of the bone cement composite reflect its resistance to flexural loading which is a combination of tension and compression forces. Similarly, dramatic reinforcements in the flexural properties (FS and FM) were achieved with bone cement composites, as evident in Table 2.3. This extraordinary mechanical reinforcement provided by bone cement composites exceeded the enhancements observed with the mechanically mixed bone cement composite (Sample 5), indicating the importance of mechanical coupling between the nanowire and the functionalized PPF matrix. Bone cement composite-1 formulation exhibited a roughly 3-fold increase in flexural modulus and a greater than 2-fold increase in flexural strength compared to blank polymer. Loadings beyond 0.5 wt% nano-TiO_2 in the starting material led to a decrease in the flexural properties of these bone cement composites, due in part

www.manaraa.com

to aggregation of nanowires (Figure 2.13d).

Due to the complexity of bone cement preparation chemistry including the type of polymers, nanofillers, and crosslinking agents, as well as the loading concentration, it is difficult to compare their mechanical properties. Previously Khaled et al. prepared bone cement materials by incorporating TiO_2-SrO nanotubes into PMMA, achieving a flexural modulus of 2220 ± 100 MPa and a flexural strength 69.98 ± 1.40 MPa.[41] The highest flexural modulus and flexural strength measured in the present study are 1084 ± 115 MPa and 42.5 ± 6.1 MPa, respectively. These values are comparable with those obtained by utilizing high molecular weight PMMA (207 kDa),[41] although much lower molecular weight of PPF (2.2 kDa) was employed in this study. Studies employing functionalized single-walled carbon nanotubes in PPF showed flexural modulus of 769 ± 114 MPa and a flexural strength of 42.8 ± 3.7 MPa,[16] although the crosslinker, poly(propylene fumarate)-diacrylate (PPF-DA), used in their work may also be contributing to the reported improved mechanical properties. Considering previously reported flexural modulus of human trabecular bone, our results show that TiO_2-PPF nanocomposites have sufficient mechanical strength for bone tissue engineering applications.[17]

It should be noted that nano-titania is an established biocompatible material.[28, 41] The maleic anhydride-functionalized PPF having two small functional groups at each end of a biocompatible polymer (PPF) chain should also be biocompatible. Hence, the prepared TiO_2-PPF bone cement materials are expected to be biocompatible; however, a future study will be needed to further explore the biocompatibility of functionalized-PPF and TiO_2-PPF bone cement composites. From the above discussion it can be deduced that TiO_2 nanofibers can act as an excellent reinforcing agent for an experimental functionalized PPF matrix in order to produce a new generation of bone cements. Chemical bonding between the filler and the polymer helps the resulting bone cement composites exhibit significantly enhanced mechanical properties. In addition, a study of degradation behavior of the prepared bone cement composites is planned as the next stage for this work.

www.manaraa.com

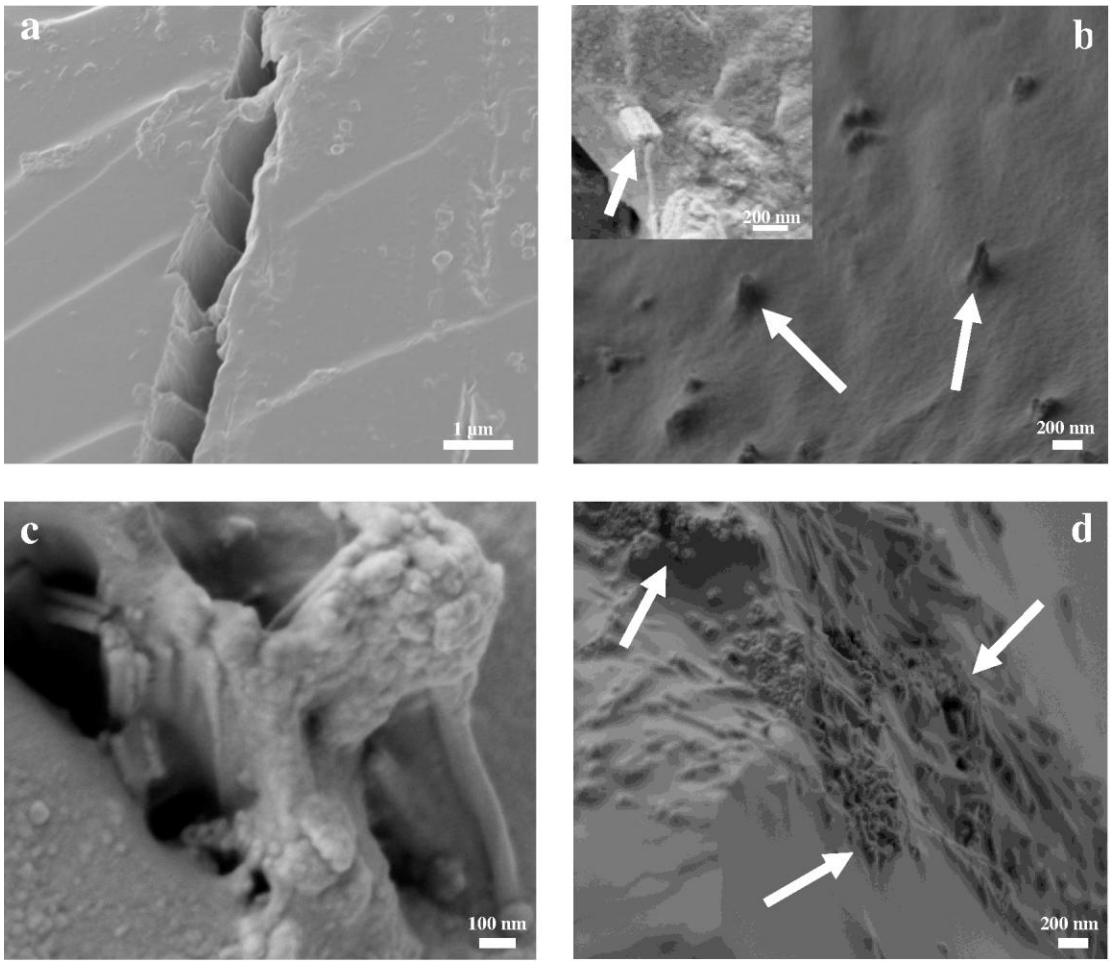

Figure 2.13. SEM images of the fracture planes of (a) crosslinked unmodified PPF, (b) bone cement composite-1, (c) crack bridging within the bone cement composite-1, and (d) bone cement composite-2.
(the arrows show TiO_2 nanofibers are covered by polymer and aligned perpendicularly to the fracture surface).

2.4 Conclusions

Poly(propylene fumarate) (PPF) was synthesized and then functionalized with maleic anhydride. Successful synthesis and functionalization of PPF was confirmed by ^{1}H and ^{13}C NMR and XPS. The functionalized PPF was grafted to the surface of TiO_2 nano-fibers synthesized using a sol-gel reaction in supercritical CO_2. Bone cement composites were obtained by polymerization of the PPF-grafted nano-TiO_2 and a crosslinker N-vinylpyrrolidone. The polymerization was confirmed by FTIR while TGA results

www.manaraa.com

revealed improved thermal stability of the crosslinked bone cement composites. Mechanical testing demonstrated much enhanced tensile and flexural properties of the bone cement composites after the incorporation of TiO_2 nano-fiber into the polymer matrix, suggesting potential application in bone cementation.

www.manaraa.com

2.5 References

1 Shah NJ, Hyder, M.N., Moskowitz, J.S., Quadir,M.A., Morton, S.W., Seeherman,H. J., Padera,R. F., Spector,M., Hammond, P.T. Surface-Mediated Bone Tissue Morphogenesis from Tunable Nanolayered Implant Coatings. Sci Transl Med. 2013;5:1-10.

2 Kaur G, Pandey OP, Singh K, Homa D, Scott B, Pickrell G. A review of bioactive glasses: Their structure, properties, fabrication, and apatite formation. Journal of Biomedical Materials Research Part A. 2014;102:254-274.

3 Wood ML, McDowell CM, Kelley SS. Cementation for femoral head osteonecrosis: a preliminary clinic study. Clinical orthopaedics and related research. 2003;412:94-102.

4 Chang C-H, Liao T-C, Hsu Y-M, Fang H-W, Chen C-C, Lin F-H. A poly (propylene fumarate)–Calcium phosphate based angiogenic injectable bone cement for femoral head osteonecrosis. Biomaterials. 2010;31:4048-4055.

5 Goto K, Tamura J, Shinzato S, Fujibayashi S, Hashimoto M, Kawashita M, Kokubo T, Nakamura T. Bioactive bone cements containing nano-sized titania particles for use as bone substitutes. Biomaterials. 2005;26:6496-6505.

6 Maiti P, Kapusetti G, Misra N, Singh V, Srivastava S, Roy P, Dana K. Bone cement based nanohybrid as super biomaterial for bone healing. Journal of Materials Chemistry B. 2014.

7 Fang C, Hou R, Zhou K, Hua F, Cong Y, Zhang J, Fu J, Cheng Y-J. Surface functionalized barium sulfate nanoparticles: controlled *in situ* synthesis and application in bone cement. Journal of Materials Chemistry B. 2014.

8 Lewis G. Alternative acrylic bone cement formulations for cemented arthroplasties: Present status, key issues, and future prospects. . J Biomed Mater Res B Appl Biomater 2007;84:301–319.

9 Anitha N, Thomas V, Jayabalan M. Poly (propylene fumarate)/n-vinyl pyrrolidone copolymerbased bone cement: Setting and in-vitro biodegradation. Journal of the Indian Institute of Science. 2013;79:431.

10 Henslee AM, Gwak DH, Mikos AG, Kasper FK. Development of a biodegradable bone cement for craniofacial applications. Journal of Biomedical Materials Research Part A. 2012;100:2252-2259.

11 Alge DL, Bennett J, Treasure T, Voytik-Harbin S, Goebel WS, Chu TMG. Poly (propylene fumarate) reinforced dicalcium phosphate dihydrate cement composites for bone tissue engineering. Journal of Biomedical Materials Research Part A. 2012;100:1792-1802.

www.manaraa.com

12 He S, Timmer M, Yaszemski M, Yasko A, Engel P, Mikos A. Synthesis of biodegradable poly (propylene fumarate) networks with poly (propylene fumarate)–diacrylate macromers as crosslinking agents and characterization of their degradation products. Polymer. 2001;42:1251-1260.

13 Zhao W, Yang D, Li Z, Xu T. Progress in researches on the synthesis of poly (propylene fumarate) and its crosslinking characteristics]. Sheng wu yi xue gong cheng xue za zhi= Journal of biomedical engineering= Shengwu yixue gongchengxue zazhi. 2005;22:381.

14 Shung AK, Timmer MD, Jo S, Engel PS, Mikos AG. Kinetics of poly (propylene fumarate) synthesis by step polymerization of diethyl fumarate and propylene glycol using zinc chloride as a catalyst. Journal of Biomaterials Science, Polymer Edition. 2002;13:95-108.

15 Fisher JP, Holland TA, Dean D, Mikos AG. Photoinitiated cross-linking of the biodegradable polyester poly (propylene fumarate). Part II. *In vitro* degradation. Biomacromolecules. 2003;4:1335-1342.

16 Shi X, Hudson JL, Spicer PP, Tour JM, Krishnamoorti R, Mikos AG. Rheological behaviour and mechanical characterization of injectable poly (propylene fumarate)/single-walled carbon nanotube composites for bone tissue engineering. Nanotechnology. 2005;16:S531.

17 Horch RA, Shahid N, Mistry AS, Timmer MD, Mikos AG, Barron AR. Nanoreinforcement of poly (propylene fumarate)-based networks with surface modified alumoxane nanoparticles for bone tissue engineering. Biomacromolecules. 2004;5:1990-1998.

18 Hakimimehr D, Liu D-M, Troczynski T. *In-situ* preparation of poly (propylene fumarate)—hydroxyapatite composite. Biomaterials. 2005;26:7297-7303.

19 Lee K-W, Wang S, Yaszemski MJ, Lu L. Physical properties and cellular responses to crosslinkable poly (propylene fumarate)/hydroxyapatite nanocomposites. Biomaterials. 2008;29:2839-2848.

20 Wu CC, Yang KC, Yang SH, Lin MH, Kuo TF, Lin FH. *In Vitro* Studies of Composite Bone Filler Based on Poly (Propylene Fumarate) and Biphasic α-Tricalcium Phosphate/Hydroxyapatite Ceramic Powder. Artificial organs. 2012;36:418-428.

21 Sitharaman B, Shi X, Walboomers XF, Liao H, Cuijpers V, Wilson LJ, Mikos AG, Jansen JA. *In vivo* biocompatibility of ultra-short single-walled carbon nanotube/biodegradable polymer nanocomposites for bone tissue engineering. Bone. 2008;43:362-370.

22 Khaled S, Sui R, Charpentier PA, Rizkalla AS. Synthesis of TiO_2-PMMA nanocomposite: using methacrylic acid as a coupling agent. Langmuir. 2007;23:3988-3995.

www.manaraa.com

23 Khaled S, Charpentier PA, Rizkalla AS. Physical and mechanical properties of PMMA bone cement reinforced with nano-sized titania fibers. Journal of Biomaterials Applications. 2011;25:515-537.

24 Mistry A, Mikos A, Jansen J. Degradation and biocompatibility of a poly (propylene fumarate)-based/alumoxane nanocomposite for bone tissue engineering. Journal of Biomedical Materials Research Part A. 2007;83:940-953.

25 Li P, Ohtsuki C, Kokubo T, Nakanishi K, Soga N, de Groot K. The role of hydrated silica, titania, and alumina in inducing apatite on implants. Journal of biomedical materials research. 1994;28:7-15.

26 Trabandt N, Brandes G, Wintermantel E, Lenarz T, Stieve M. Limitations of titanium dioxide and aluminum oxide as ossicular replacement materials: an evaluation of the effects of porosity on ceramic prostheses. Otology & Neurotology. 2004;25:682-693.

27 Uchida M, Kim HM, Kokubo T, Fujibayashi S, Nakamura T. Structural dependence of apatite formation on titania gels in a simulated body fluid. Journal of Biomedical Materials Research Part A. 2003;64:164-170.

28 Khaled S, Miron RJ, Hamilton DW, Charpentier PA, Rizkalla AS. Reinforcement of resin based cement with titania nanotubes. dental materials. 2010;26:169-178.

29 West J, Brennan A, Clark A, Zamora M, Hench L. Cyclic anhydride ring opening reactions: Theory and application. Journal of biomedical materials research. 1998;41:8-17.

30 Spivey AC, Andrews BI. Catalysis of the Asymmetric Desymmetrization of Cyclic Anhydrides by Nucleophilic Ring-Opening with Alcohols. Angewandte Chemie International Edition. 2001;40:3131-3134.

31 Kasper FK, Tanahashi K, Fisher JP, Mikos AG. Synthesis of poly (propylene fumarate). Nature protocols. 2009;4:518-525.

32 Sui R, Rizkalla AS, Charpentier PA. Formation of titania nanofibers: A direct sol-gel route in supercritical CO_2. Langmuir. 2005;21:6150-6153.

33 Sui R, Rizkalla AS, Charpentier PA. FTIR study on the formation of TiO_2 nanostructures in supercritical CO_2. The Journal of Physical Chemistry B. 2006;110:16212-16218.

34 Rotzinger FP, Kesselman-Truttmann JM, Hug SJ, Shklover V, Grätzel M. Structure and vibrational spectrum of formate and acetate adsorbed from aqueous solution onto the TiO_2 rutile (110) surface. The Journal of Physical Chemistry B. 2004;108:5004-5017.

35 Dobson KD, McQuillan AJ. *In situ* infrared spectroscopic analysis of the adsorption of aliphatic carboxylic acids to TiO_2, ZrO_2, Al_2O_3, and Ta_2O_5 from aqueous

www.manaraa.com

solutions. Spectrochimica Acta Part A: Molecular and Biomolecular Spectroscopy. 1999;55:1395-1405.

36 Jayabalan M. Studies on Poly (propylene fumarate-co-caprolactone diol) Thermoset Composites towards the Development of Biodegradable Bone Fixation Devices. International journal of biomaterials. 2009;2009.

37 Wu X, Wang D, Yang S. Preparation and characterization of stearate-capped titanium dioxide nanoparticles. Journal of colloid and interface science. 2000;222:37-40.

38 Hojjati B, Charpentier PA. Synthesis and kinetics of graft polymerization of methyl methacrylate from the RAFT coordinated surface of nano-TiO_2. Journal of Polymer Science Part A: Polymer Chemistry. 2008;46:3926-3937.

39 Biesinger MC, Lau LW, Gerson AR, Smart RSC. Resolving surface chemical states in XPS analysis of first row transition metals, oxides and hydroxides: Sc, Ti, V, Cu and Zn. Applied Surface Science. 2010;257:887-898.

40 Farhangi N, Chowdhury RR, Medina-Gonzalez Y, Ray MB, Charpentier PA. Visible light active Fe doped TiO_2 nanowires grown on graphene using supercritical CO_2. Applied Catalysis B: Environmental. 2011;110:25-32.

41 Khaled S, Charpentier PA, Rizkalla AS. Synthesis and characterization of poly (methyl methacrylate)-based experimental bone cements reinforced with TiO_2–SrO nanotubes. Acta Biomaterialia. 2010;6:3178-3186.

www.manaraa.com

Chapter 3

3 Delivery of an angiogenic mediator for bone regeneration in a radiopaque Sr-doped TiO_2/poly(propylene fumarate) based bone cement

Abstract

Recently developed TiO_2-poly(propylene fumarate) nanocomposites for bone cementation showed significantly enhanced mechanical properties. However, bone formation is an angiogenesis-dependent process, and the need for enhanced neovascularization in necrotic bone is especially important for bone regeneration. Moreover, it is very important to monitor healing and loosening processes to differentiate between bone, bone cement, and osteolysis after surgery. In the present study, a novel bone cement composite was developed by incorporation of an agniogenic modulator, ginsenoside Rg_1, and a radiopaque component, Sr-doped TiO_2 nanofiber, into poly(propylene fumarate) (PPF), a biodegradable polymer. Sr-doped TiO_2 nanofibers were synthesized using the green solvent, supercritical carbon dioxide and characterized by SEM, EDX, and XPS, showing a new phase, $SrTiO_3$, in the crystalline matrix of anatase. The strong interfacial adhesion between PPF and nanofibers was examined by SEM, FTIR, XPS, thermal analyses, and mechanical testing. The radiopacity, drug release, and angiogenesis behavior of the formed bone cement composites were tested and compared with control samples, demonstrating superior radiopacity and excellent release of ginsenoside Rg_1 *in vitro*, as well as a dose-dependent increase in the branching point numbers, suitable for the development of next generation bone cement materials.

www.manaraa.com

3.1 Introduction

Osteonecrosis is a disease with a wide ranging etiology and poorly understood pathogenesis, most common in grownups between the ages of 20 and 50 years.[1] There are many risk factors, including trauma,[2] obesity,[3] gout,[2] alcoholism,[4] exposure to corticosteroids,[5] and radiation damage[6] which can cause the temporary or permanent loss of blood supply to bone.[7] Certain diseases such as sickle-cell anaemia,[8] Gaucher disease,[9] and altered lipid metabolism[10] are also associated with the development of this condition. Reduced blood flow to bone causes bone cell death, termed osteonecrosis, which mainly occurs in the weight-bearing parts of the body, and therefore with the stress of weight-bearing the necrotic segment of bone is likely to collapse leading to painful degenerative arthritis.[7, 11]

Cement fixation is a recently introduced method in treating osteonecrosis of the femoral head.[7, 12] Bone cementation involves the injection of fluid material, which instantly hardens in the defect, and provides mechanical support to prevent collapse. Bone cements make the treatment of irregular defects easier. They are also easy to use for clinical practice, providing immediate symptomatic relief and faster recovery for the patient, while allowing improvement in mobility.[13]

Bioactive bone cements possessing easy injectability, good biocompatibility, high radiopacity, and mechanical efficiency are required for cement fixation.[14, 15] Only a few bone cement formulations, acrylic cements based on polymethylmethacrylate (PMMA) and calcium phosphate cements, are specifically designed for use in these procedures, and even these formulations are not considered as ideal injectable bone cements. There are several disadvantages associated with commercial formulations of both bone cements families including an exothermic reaction during the curing process, release of cytotoxic methylmethacrylate monomer, high rigidity, nonbiodegradability, nonbioactivity, and poor adhesion to bone surfaces for acrylic cements based on PMMA[16, 17] and early resorption, poor mechanical properties, and poor handling for calcium phosphate cements.[18]

Recently, poly(propylene fumarate) (PPF) has attracted considerable interest as a

www.manaraa.com

promising degradable, injectable, and non-toxic material for cement augmentation of necrotic bone.[19] However, PPF does not provide for bone growth,[20, 21] and development of endothelial cell-based microvascularization and microcirculation is undoubtedly critical for the structure preservation and bone regeneration, because bone formation is an angiogenesis-dependent process.[22, 23] Angiogenesis is defined as the process of new blood vessel formation from pre-existing vessels from the surrounding tissues.[24] The vasculature provides enhanced mass transport requirements for the tissue, and delivers circulating stem cells participating in bone formation. It also facilitates cross-talk between endothelial cells and pre-osteoblasts to direct their differentiation. [25, 26]

A variety of growth factors that direct angiogenesis including vascular endothelial growth factor (VEGF) have been identified.[26, 27] Also, among numerous pro-angiogenic mediators, ginsenoside Rg_1 has been shown to be a highly stable pro-angiogenic compound by upregulating *in vitro* proliferation, migration, chemo-invasion, and tube formation in human umbilical vein endothelial cells (HUVECs).[28] Rg_1 stimulates angiogenesis through enhancing the production of nitric oxide (NO) and vascular endothelial growth factor (VEGF).[29, 30] So, we hypothesized that a synthetic system based on PPF capable of delivering an angiogenic agent in a localized and sustained manner would direct simultaneous regeneration of bone and vascular tissue. Chang et al. reported the formation of ginsenoside-Rg_1 incorporated PPF-tetracalcium phosphate (TTCP)/dicalcium phosphate (DCPA) orthopedic composite formulation.[12] However, the limition of Chang's study is that the proposed bone cements did not possess high X-ray contrast along with extremely low Young's modulus. Alike to conventional polymers, radiopacity of PPF is expected to be similar to soft tissue, since both are primarily composed of hydrogen, oxygen, nitrogen, and carbon yielding poorly resolved images.[31] Therefore, it is impossible to directly monitor new bone formation and determine the boundaries of bone cement having a pure PPF matrix during the surgery by ordinary X-ray imaging techniques, since the image resolution is limited. [32]

Radiopacity is a desirable property in bone cements allowing post-operative assessment using X-radiography.[33] It is important that the orthopaedic surgeon can easily monitor

www.manaraa.com

healing and loosening processes to differentiate between bone, bone cement, and osteolysis after surgery.[32] Therefore, to use PPF bone cement as a bone substitute, it is necessary to add X-ray contrast agents, such as zirconium dioxide or barium sulphate, to improve radiopacity and visual control.[34] Only once did Kim et al. introduce PPF biopolymer containing 30 Wt% barium sulfate as a radiopaque PPF cement suitable for kyphoplasty.[16] However, a major drawback associated with the presence of barium sulphate or zirconium dioxide is poor dispersion of these radiopacifiers into the polymer resin, which can affect both crack initiation and crack propagation in the hardened cement, as the radiopacifier agglomerates act as sites of high stress concentration leading to degradation of physical and mechanical properties.[14, 35] Later Wu et al. examined a newly developed bone filler, a-TCP/HAp, with PPF, and sought to quantify the radiopacity by CT scanning.[18] However, CT scanning costs more and takes more time than a regular X-ray. In addition, patients are exposed to higher doses of radiation compared to X-ray since a CT scan takes a much greater number of X-ray images.[36] In this work, biocompatible and radiopaque Sr^{2+} component ($SrTiO_3$) is incorporated into the titania nanorods/fibers using a sol-gel reaction in supercritical CO_2 as a green solvent. Then, a bioactive bone cement is prepared by incorporating Sr-doped titania nanorods/fibers into a cement formulation based on PPF. There are very few studies regarding the Sr^{2+}-modification of TiO_2 nanostructures. Bhattacharyya et al. immobilized strontium in the crystalline matrix of rutile titania using a co-precipitation method presenting some structural changes with the formation of new phases, $SrTiO_3$+Sr_2TiO_4 and $SrTiO_3$.[37] Khaled et al. incorporated strontium oxide (SrO), into the n-TiO_2 tube *in-situ* during the synthesis of the tubes through the alkaline hydrothermal technique.[33] Also, Kumaresan et al. synthesized Sr^{2+}-doped TiO_2 nanoplates by sol-gel method.[38] However, this is the first study, to our knowledge, to synthesize Sr-doped TiO_2 nanorods/fibers in $scCO_2$. There are several favorable characteristics that make CO_2 an attractive solvent for the synthesis and processing of high-quality materials, as previously described.[39, 40]

TiO_2 itself is an oxidized metal and a highly radiopaque material.[41] Moreover, TiO_2 nanorods/fibers have a high aspect ratio and high surface area to volume ratio, and their incorporation into cement formulation may lead to significantly enhanced mechanical

www.manaraa.com

properties.[42, 43] Besides, TiO_2 has shown excellent *in vitro* apatite-forming ability and *in vivo* osteoconductivity.[41, 44] On the other hand, strontium is currently included as a radiopacifier in some commercially available dental cement brands improving their anti-bacterial effectiveness.[35] Therefore, the Sr-doped TiO_2 nanoparticles synthesized in this study are expected to provide reasonably higher radiopacity and also mechanical characteristics to the PPF matrix. In addition, to avoid the problem of phase separation and agglomeration of nanofillers in the polymer matrix and improve the compatibility between PPF and nanofillers, the polyester matrix was functionalized using maleic anhydride through the alcoholytic ring opening reaction, which produces carboxyl groups at each end point of the polymer for coordination onto the Sr^{2+}-doped n-TiO_2.[42] The hypothesis of this study is that Sr^{2+}-doped TiO_2 rods/fibers added to the functionalized PPF matrix will significantly enhance its mechanical properties and radiopacity as well as the angiogenesis characteristics provided by ginsenoside Rg_1.

3.2 Experimental details

3.2.1 Materials

Titanium isopropoxide (TIP, 99.999%), glacial acetic acid (>99.7%), zirconium (IV) propoxide solution 70 wt. % in 1-propanol (ZPO), barium sulfate ($BaSO_4$, 99%), strontium nitrate ($Sr(NO_3)_2$, ≥99.0%) were received from Sigma-Aldrich Canada. A stock solution of $Sr(NO_3)_2$ in water was prepared by dissolving strontium nitrate (6.6 g) in 10 mL of double distilled water, which was generated from Milli-Q water purification system (18.2 MΩ·cm resistivity, Barnstead EasyPureII, Thermo Scientific, USA). Diethyl fumarate (98%), propylene glycol (1,2-Propanediol) (≥99.5%), zinc chloride anhydrous ($ZnCl_2$, ≥99.995%), hydroquinone (99%), maleic anhydride (95%), 4-dimethylaminopyridine (DMAP), hydrochloric acid (37%), anhydrous magnesium sulfate (≥99.0%), diethyl ether anhydrous (≥99.0%), anhydrous methylene chloride (DCM, ≥99.8%), anhydrous tetrahydrofuran (THF, ≥99.9%), benzoyl peroxide (BPO), N-dimethyl-p-toluidine (DMT), and 0.1 mol/L phosphate-buffered saline solution (PBS, pH 7.4) were purchased from Sigma-Aldrich Canada and used as received. Calcium nitrate

www.manaraa.com

tetrahydrate ($Ca(NO_3)_2.4H_2O$), diammonium hydrogen phosphate ($(NH_4)_2HPO_4$), cetyltrimethylammonium bromide (CTAB), polyethylene glycol (PEG 600), ammonium hydroxide (NH_4OH, 30%), and anhydrous ethanol (EtOH) were also obtained from Sigma-Aldrich, Canada and used with no further purification. Instrument grade carbon dioxide (99.99%) was obtained from BOC Canada. Ginsenoside Rg_1 was donated by Dr. Edmund Lui, Department of Physiology and Pharmacology, the University of Western Ontario, London, Canada. Human umbilical vein cell lines (EA.hy926) were provided by Dr. Jeff Dixon, Department of Physiology and Pharmacology, the University of Western Ontario, London, Canada. Growth factor-reduced Matrigel was purchased from VWR. Cell culture medium and reagents were purchased from Gibco laboratories (USA).

3.2.2 Characterization

Scanning electron microscopy (SEM) images were collected using a Leo(Zeiss) 1540XB SEM. Imaging was performed at either low voltage (1 kV) for morphology or at 10 kV for backscatter imaging. Samples were prepared by applying the powder directly to a carbon adhesive tape, and coated with 5 nm of osmium metal in a Filgen OPC80T. The bulk composition was analyzed using energy-dispersive Quartz XOne x-ray spectroscopy (EDX) attached to a Hitachi S-4500 field emission scanning electron microscopy to investigate the dispersion of Sr^{2+} in the n-TiO_2. EDX analysis was performed by taking spectra at three different sites in the sample. For studying the fracture surface, samples were broken by submersing in liquid nitrogen in a stainless steel mortar and broken with a stainless steel pestle.

To identify the functional chemical groups in the synthesized polymer and coordination of carboxylate groups to Sr-doped n-TiO_2 in the Sr^{2+}-TiO_2/PPF nanocomposites, attenuated total reflection-Fourier transform infrared (ATR-FTIR) spectra were measured using a Nicolet 6700 FTIR spectrometer (Thermo Scientific) equipped with a smart iTR (diamond ATR). The spectra were recorded in the range of 600-4000 cm^{-1} with a resolution of 4 cm^{-1} over 32 scans. Structural analysis of the Sr-doped TiO_2 particles was performed using an x-ray powder diffractometer (Rigaku Miniflex XRD, TX, USA), fitted with a rotating sample holder, a scintillation counter detector and a divergent beam utilizing a CuKα source of x-rays (λ=1.5418A°). X-ray photoelectron spectroscopy

www.manaraa.com

(XPS) analyses were carried out with a Kratos AXIS Ultra spectrometer using a monochromatic Al K(α) source (15mA, 14kV). Samples were placed on a carbon-based double-sided adhesive tape for analysis. The Kratos charge neutralizer system was used on all specimens. Survey scan analyses were carried out with an analysis area of 300 μm × 700 μm and a pass energy of 160 eV. High resolution analyses were carried out with an analysis area of 300 μm × 700 μm and a pass energy of 20 eV. Spectra were charge corrected to the main line of the carbon 1s spectrum set to 284.8 eV. Spectra were analyzed using CasaXPS software (version 2.3.14).

Thermogravimetric analysis (TGA) was performed using a TA Q500 TGA at a heating rate of 10 ºC/min under an inert (nitrogen) atmosphere.

Mechanical tensile properties were measured using an Instron 5943 universal testing machine (Instron, Canton, MA) equipped with a 500 N (tension) load cell. Tensile testing was conducted in accordance with ASTM D638-91a. Dogbone specimens with overall length of 60 mm and width of grip section of 10 mm were used for tensile testing. Stress-strain relationship was obtained from the load and displacement data. Young's modulus was determined by calculating the slope of the linear portion of the stress-strain curve, and tensile strength was defined as the maximum applied stress prior to failure. For each group, 5 independent specimens (n=5) were tested in tension at a cross-head speed of 10 mm/min. Flexural strength and flexural modulus of the nanocomposites were determined in accordance with ASTM D790M-92 using a dynamic mechanical analyzer, DMA Q800 (TA instruments). Flexural testing samples, rectangular bar specimens (n=5) (50 mm × 25 mm × 2 mm), were placed on a three-point bending apparatus with two supports spanning 40 mm from each other and loaded at the cross-head speed of 10 mm/min to the center of each specimen until failure. In an approach similar to that of tensile testing, flexural modulus was calculated as the slope of the initial linear region of the stress-strain curve, while flexural fracture strength was determined as the maximum applied stress prior to failure.

The radiopacity of the bone cement composites reinforced n-TiO_2 nanotubes/nanofibers, ZrO_2-modified TiO_2 nanofibers, Sr-doped TiO_2 nanofibers, and hydroxyapatite nanorods,

www.manaraa.com

as well as the control (crosslinked unfilled PPF and specimen containing $BaSO_4$ as radiopacifier) was determined in terms of equivalent aluminum thickness according to a technique introduced by Amirouche et al.[45] using rectangular specimens (n = 5) (30 mm × 3 mm × 2 mm) with a dental X-ray source (accelerating voltage: 40 kVp, intensity: 0.1 mAs, source-to-film distance: 80 cm, and exposure time: 1 ms). To measure radiopacity, specimens were placed on a medical X-ray film along with a high-purity aluminum (Al) step-wedge of varying thickness from 0.5 to 5.0 mm with increments of 0.5 mm. To minimize back-scatter, the X-ray film was positioned on a sheet of lead, and a standard dental X-ray source was positioned perpendicularly to the radiographic film. Following standard techniques, the films were developed in an automatic X-ray processor. Then, a transmission densitometer was employed to measure the optical density of each material image on the film. Five readings were taken for each image of each material as well as for each step of the Al step-wedge, and the average of these five readings was calculated. The optical density data obtained from the Al step-wedge images were used to construct a calibration curve of optical density of aluminum as function of its thickness. Finally, the radiopacity of bone cement specimens was expressed in terms of the equivalent thickness of aluminum (mm Al) per unit thickness of material, deducted in reference to the calibration curve of the radiographic optical density of the Al step-wedge.

For the drug release assay, bone cement composite samples (30 mm × 3 mm × 2 mm) of optimal formulation were loaded with the angiogenic agent, ginsenoside Rg_1, and immersed in 10 mL of pH 7.4 phosphate-buffered saline (PBS) in a small vial and incubated at 37 °C. At specific time points, 2 ml of the extract was collected and replaced with 2 ml fresh PBS. The collected supernatant was stored at -20 °C. After all the samples were collected, the absorption at 189 nm wavelength was measured using a UV-Vis spectrophotometer (Shimadzu UV-Vis 3600) to determine the amount of ginsenoside Rg_1 within the bone cement composites. Cumulative release of ginsenoside Rg_1 profiles were acquired with the volume loss correction and plotted against time. All the experiments were repeated in triplicate for each time interval. Collected extracts were also used for following bioassay studies.

www.manaraa.com

In order to measure angiogenic activity of ginsenoside Rg_1 before incorporation into and after release from the bone cement composites, tube formation bioassays were performed using the EA.hy926 cell line derived from the fusion of human umbilical vein endothelial cells (HUVEC) with the A549 human pulmonary adenocarcinoma cell line. EA.hy926 cell line was used to show the ability to attach, migrate, and form tubular structures after seeding on a Matrigel substrate. EA.hy926 cell lines were cultured in Dulbecco's modified Eagle medium (DMEM) supplemented with ECGS (20 mg/ml), 10% fetal buvine serum (FBS), 1% antibiotic, and 1 ml (5X) per 50 ml of medium Hat media supplement. The cells were grown at 37 °C in humidified air with 5% CO_2 incubator. When the cell cultures were 80-90% confluent, cells were harvested following trypsin treatment and released cells were resuspended to the cell density required for tube formation assay. To examine the angiogenic activity of ginsenoside Rg_1 *in vitro*, tube formation bioassay was performed on 96-well tissue culture plates coated with 10 mL of growth factor-reduced Matrigel per well. An amount of 4.5×10^4 cells/well of EA.hy926 cell line was seeded on the Matrigel-coated plate loaded with medium and various concentrations of ginsenoside Rg_1 before incorporation into the bone cement composites and after release from the bone cement formulations. After incubation for eighteen hours, images from a total of five microscopic fields per well were captured by an inverted microscope (Nikon TMS, Japan) using a 40x objective. The angiogenic effect was estimated by counting the branch points of the formed tubes, and the average numbers of branch points were calculated. Each experiment is repeated at least three times, with each experiment yielding essentially identical results. Data were expressed as mean ± standard deviation (SD).

All the mechanical property measurements and bioassay experiments were conducted in quintuplicate and triplicate, respectively, and were measured with statistical analyses accomplished using GraphPad prism 4.0a Software (GraphPad Software Inc., USA). The data were expressed as mean ± SD.

www.manaraa.com

3.2.3 Preparation of materials

3.2.3.1 *Synthesis of Sr-doped TiO_2 nanotubes/fibers via sol-gel reaction in $scCO_2$*

The schematic diagram of the experimental setup and details of the synthesis procedure can be found in Sui's work.[46] To synthesize the Sr-doped TiO_2 in $scCO_2$, a 10 mL stainless steel view cell was connected to a syringe pump for pumping CO_2. In a typical experiment, titanium isopropoxide (1 g) was quickly placed in the view cell, followed by addition of an aqueous $Sr(NO_3)_2$ (5 wt% of the TIP concentration, 0.05 g or 20 wt% of the TIP concentration, 0.2 g), acetic acid (6 g), and CO_2 to the desired pressure and temperature. A magnetic stirrer was used for mixing the reaction mixture. It was found that the mixture of strontium nitrate/water, titanium isopropoxide, and acetic acid was miscible with CO_2 at 60 °C and 6000 psig pressure. Stirring was stopped after 24 h, and 6-7 days of aging were required for complete reaction. After aging, the formed gel was washed continuously using 80 ml of CO_2 at a rate of approximately 0.5 mL/min, followed by controlled venting at 0.5 mL/min to prevent collapse of the solid network. The as-prepared powder was calcined at 450 °C in air for 2 h using a heating rate of 10 °C/min, and the cooling rate to room temperature was 0.5 °C/min. The calcined powder was kept in a vacuum oven at 80 °C to remove moisture.

3.2.3.2 *Synthesis of other radiopacifiers: TiO_2 nanotubes/nanofibers, ZrO_2-modified TiO_2 nanofibers, and hydroxyapatite nanorods*

For comparative radiopacity measurements, nano-structured TiO_2, ZrO_2-modified TiO_2, and hydroxyapatite were also synthesized. TiO_2 nanoparticles were prepared using the method described in Salarian et al.[42] Briefly, titanium isopropoxide (1 g) was quickly placed in a 10-mL view cell, followed by adding acetic acid (4 g). CO_2 was then added to the view cell up to 6000 psig pressure while increasing the temperature to 60 °C. After stirring for 24 h and four days of aging, the formed gel was washed continuously using 80 mL of CO_2, followed by controlled venting. The as-prepared powder was calcined at 450 °C in air for 2 h and kept in a vacuum oven at 80 °C.

ZrO_2-modified TiO_2 nanoparticles were synthesized and loaded within the bone cement

www.manaraa.com

composite. To synthesize ZrO_2-modified TiO_2, in a typical experiment, TIP (1 g) was quickly placed in the view cell, followed by addition of acetic acid (6 g), ZPO (0.5 g) and CO_2 up to the desired temperature (60 °C) and pressure (6000 psi), and a magnetic stirrer system was used for mixing the reaction mixture. The aging, washing, and calcination were conducted following the reported procedure for the synthesis of Sr-doped TiO_2 nanoparticels.

In addition, nanorods of hydroxyapatite were prepared following the experimental procedure introduced in Salarian et al.[47] Briefly, 0.03 mole of $(NH_4)_2HPO_4$ and 0.021 mole of CTAB were dissolved completely in 125 ml of deionized water, and stirred with a magnetic stirrer for 30 min. Then, the pH value was adjusted to 4.5 by adding pure acetic acid. Next, 0.05 mole of $Ca(NO_3)_2.4H_2O$ was dissolved in 175 ml of deionized water, and PEG 600 (20 wt%) was added to the solution under constant stirring for 30 min. After that, the mixed solution of $Ca(NO_3)_2.4H_2O$ and PEG 600 was added to the latter dropwise under continuous magnetic stirring in air, and the pH value of reaction solution was adjusted to 11 using ammonia. The final milky suspension was transferred to a stainless steel autoclave; sealed tightly, and hydrothermally treated in an oven at 120 °C for 22 h. The precipitates were separated from the suspension by centrifuging, washed three times with ethanol and three times with deionized water, and freeze-dried to yield white powder.

3.2.3.3 *Synthesis and functionalization of PPF*

PPF was synthesized using a two-step transesterification method[48] and functionalized using a recently introduced method by Salarian et al.[42] Figure 3.1 displays the synthetic scheme for the preparation and funtionalization of PPF and the synthesis of Sr^{2+}-TiO_2/PPF nanocomposite and bone cement composite. In a typical experiment, diethyl fumarate and propylene glycol were reacted in an inert atmosphere. Additionally, $ZnCl_2$ and hydroquinone were added as a catalyst and a crosslinking inhibitor, respectively. The first step of the reaction occurred with a gradual increase in temperature from 110 to 150 ºC resulting in the production of bis(hydroxypropyl) fumarate intermediate and ethanol, which was collected as a distillate. This step was terminated when ~ 90% of the theoretical yield of ethanol was collected. The second step of the reaction,

www.manaraa.com

transesterification of the bis(hydroxypropyl) fumarate intermediate, was conducted under reduced pressure (<1 mm Hg) with a gradual increase in temperature from 100 to 150 ºC producing propylene glycol as a byproduct. The reaction proceeded until the desired molecular weight of PPF was obtained. The polymer product was then purified by several acid washes with 1 N HCl, two washes with distilled water, and two washes with brine. After drying with magnesium sulfate, the polymer was concentrated by rotoevaporation and then precipitated in ethyl ether. The ethyl ether was decanted and the purified polymer was vacuum dried to remove any residual solvent.

In order to functionalize PPF chain with maleic anhydride, PPF was dissolved in anhydrous dichloromethane, and DMAP was added to the solution under argon, followed by reacting with maleic anhydride with constant stirring for 24 h at room temperature. The product was then washed with 1 N HCl solution and distilled water. Magnesium sulfate was used to absorbed water. Finally, the solvents were removed from the product by rotary evaporation and reduced pressure to afford maleic anhydride-functionalized PPF. The obtained MA-PPF was well characterized in Salarian et al.[42]

www.manaraa.com

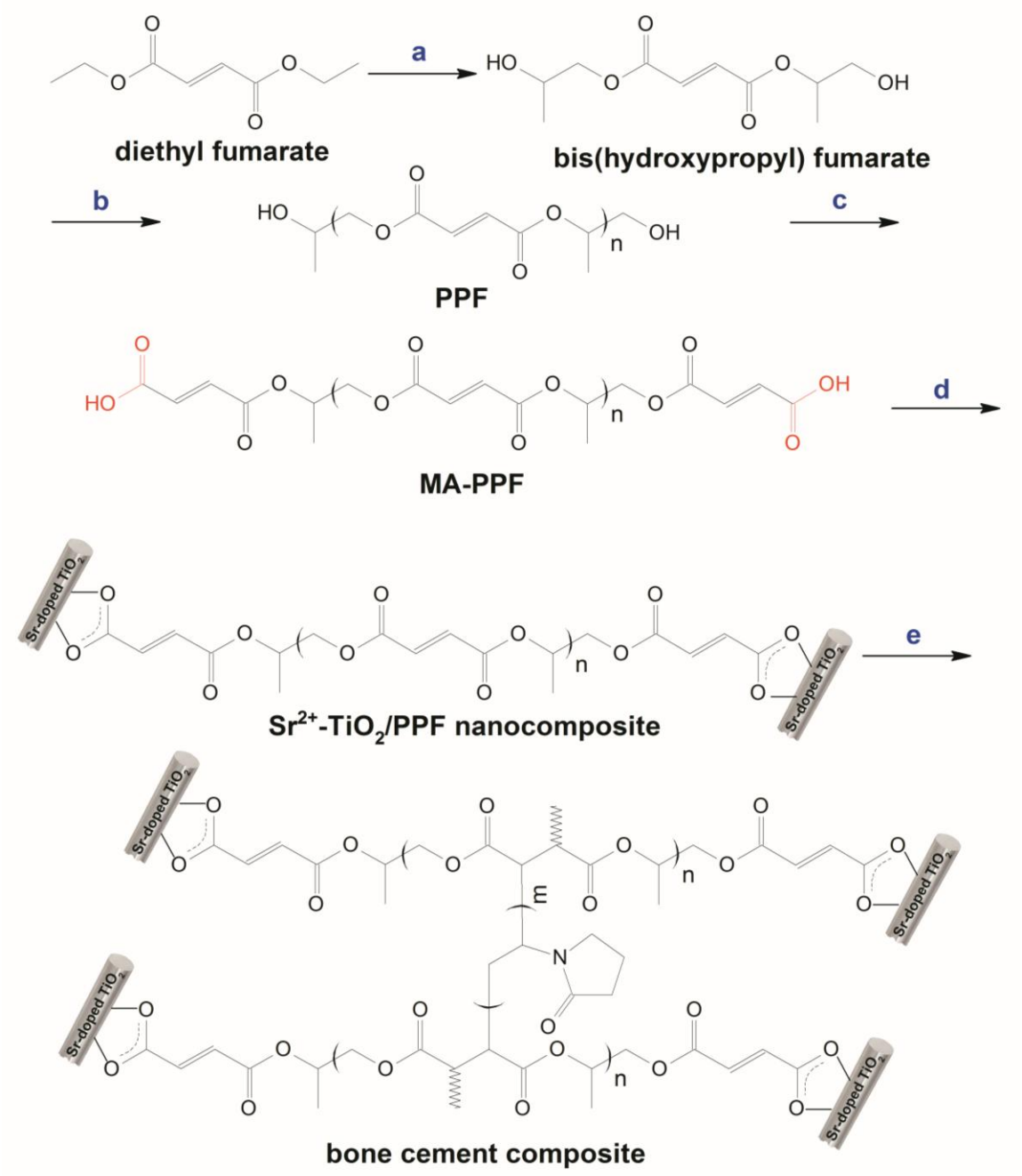

Figure 3.1. Synthetic scheme for the preparation and functionalization of PPF and the synthesis of Sr^{2+}-TiO_2/PPF nanocomposite and bone cement composite.

Reagents and conditions: (a) propylene glycol, $ZnCl_2$, hydroquinone; (b) $ZnCl_2$, hydroquinone; (c) maleic anhydride, DMAP, DCM; (d) Sr-doped TiO_2, THF; (e) N-VP, BPO, DMT, w/wo ginsenoside Rg_1.

www.manaraa.com

3.2.3.4 *Synthesis of Sr^{2+}-TiO_2/PPF nanocomposites*

To prepare Sr^{2+}-TiO_2/PPF nanocomposites, 0.5, 1, 1.5, or 2 wt% of the synthesized Sr-doped TiO_2 nanofibers (0.005, 0.01, 0.015, or 0.02 g) were dispersed in 20 mL of THF with the aid of ultrasonic agitation for 1 h, followed by reacting with the above synthesized MA-PPF (1 g) at 70 °C under argon with constant stirring for 24 h. After filtering off the solvent and the unreacted MA-PPF, the product was further purified by dispersion in THF, centrifugation, and removal of the supernatant. This purification process was repeated several times until the supernatant became clear. Finally, the resulting solid product was dried at 55 ºC under vacuum overnight. The composition of the synthesized nanocomposites and the Sr-doped TiO_2 concentration in each nanocomposite formulation reviewed by TGA analysis are presented in Table 3.1.

Table 3.1. Formulation of the Sr^{2+}-TiO_2/PPF nanocomposites.

MA-PPF (g)	Sr-doped TiO_2 (g)	*Content of Sr-doped TiO_2 in the synthesized nanocomposite	Sample Name
1 g	0.005 g (synthesized from 20 wt% $Sr(NO_3)_2$)	5 wt%	Sr^{2+}-TiO_2/PPF nanocomposite-1
1 g	0.01 g (synthesized from 20 wt% $Sr(NO_3)_2$)	9 wt%	Sr^{2+}-TiO_2/PPF nanocomposite-2
1 g	0.015 g (synthesized from 20 wt% $Sr(NO_3)_2$)	14 wt%	Sr^{2+}-TiO_2/PPF nanocomposite-3
1 g	0.02 g (synthesized from 20 wt% $Sr(NO_3)_2$)	18 wt%	Sr^{2+}-TiO_2/PPF nanocomposite-4
1 g	0.01 g (synthesized from 5 wt% $Sr(NO_3)_2$)	9 wt%	Sr^{2+}-TiO_2/PPF nanocomposite-5

Note: *the weight percentage of nano-Sr-doped TiO_2 in each Sr^{2+}-TiO_2/PPF nanocomposite is obtained from the TGA analysis.

3.2.3.5 *Synthesis of bone cement composites*

For preparation of bone cement composites, Sr^{2+}-TiO_2/PPF nanocomposite (1 g) was

www.manaraa.com

mixed with N-VP (0.4 g) for 2 h. The initiator, BPO, was dissolved in 250 μL of N-VP. Then, 50 μL of BPO solution was added into Sr^{2+}-TiO_2/PPF nanocomposite solution and mixed thoroughly into a paste formation. Afterwards, 40 μL of accelerator solution (20 μL of DMT in 980 μL of dichloromethane) was added with rapid mixing to accelerate the cross-linking reaction. The resulting paste was placed in a Teflon mold, then loaded in an oven at 60 °C for 1 h to facilitate crosslinking. After that, the mold was cooled down to room temperature, and the cross-linked samples were removed from the molds, and used for mechanical testing and radiopacity measurement analyses.

For comparative mechanical testing, mechanically mixed bone cement composites were prepared by mechanical mixing of the PPF and Sr-doped TiO_2 nanoparticles. Briefly, 1 g of PPF was mixed with 0.4 g of N-VP followed by adding 0.05 g and 0.09 g of Sr-doped TiO_2 nanoparticles (corresponding to the Sr-doped TiO_2 concentration in the Sr^{2+}-TiO_2/PPF nanocomposite-1 and Sr^{2+}-TiO_2/PPF nanocomposite-2, respectively, reviewed by TGA analysis represented in Table 3.1). Then, BPO and DMT were added and mixed thoroughly following the explained procedure for the preparation of bone cement composites. The obtained pastes were molded and samples were used for mechanical tensile and flexural testing and radiopacity measurements. The compositions of the prepared mechanically mixed bone cement composites are also listed in Table 3.2.

For comparative radiopacity measurement studies, several PPF bone cement systems containing different radiopaciers/ additives including TiO_2 nanotubes/nanofibers, ZrO_2-modified TiO_2 nanofibers, hydroxyapatite nanorods, and $BaSO_4$ particles were prepared. Specimens of the bone cement were prepared by mixing of the PPF solution in N-VP (1 g of PPF dissolved in 0.4 g of N-VP) and TiO_2 nanoparticles (0.09 g), ZrO_2-modified TiO_2 nanofibers (0.09 g), hydroxyapatite nanoparticles (0.09 g), or $BaSO_4$ particles (0.09 g) (corresponding to the Sr-doped TiO_2 concentration in the Sr^{2+}-TiO_2/PPF nanocomposite-2, reviewed by TGA analysis represented in Table 3.1), respectively. Then, the BPO solution and DMT were added and mixed thoroughly to prepare bone cement composites.

In addition, for the drug release and tube formation assays, bone cement composites of optimal formulations were loaded with the angiogenic agent, ginsenoside Rg_1. In a

www.manaraa.com

typical procedure, Sr^{2+}-TiO_2/PPF nanocomposite-2 (1 g) was mixed with N-VP (0.4 g). Next, the ginsenoside Rg_1 (0.01, 0.05, and 0.1 g) was added to give a final concentration of 1, 5, and 10 wt% of the PPF, followed by the addition of BPO (50 μL of BPO solution). After that, 40 μL of DMT solution was used to initiate the crosslinking reaction. Three different angiogenic bone cement combinations were prepared using the following ratios: 0.01 g of ginsenoside Rg_1 to 1 g of Sr^{2+}-TiO_2/PPF nanocomposite, 0.05 g of ginsenoside Rg_1 to 1 g of Sr^{2+}-TiO_2/PPF nanocomposite, and 0.1 g of ginsenoside Rg_1 to 1 g of Sr^{2+}-TiO_2/PPF nanocomposite. The composition of the prepared bone cement composites are listed in Table 3.2.

Table 3.2. The different compositions for the bone cement composites in each system.

Entry No.	**Sr^{2+}-TiO_2/PPF**	**PPF**	**Additive**	**Ginsenoside Rg_1**	**Formed Product**
1		1g			Crosslinked PPF
2		1 g	Sr-doped TiO_2 (0.05 g)		Mechanically mixed bone cement-1
3		1 g	Sr-doped TiO_2 (0.09 g)		Mechanically mixed bone cement-2
4	1 g of Sr^{2+}-TiO_2/PPF nanocomposite-1				Bone cement composite-1
5	1 g of Sr^{2+}-TiO_2/PPF nanocomposite-2				Bone cement composite-2
6	1 g of Sr^{2+}-TiO_2/PPF nanocomposite-3				Bone cement composite-3
7	1 g of Sr^{2+}-TiO_2/PPF nanocomposite-4				Bone cement composite-4
8	1 g of Sr^{2+}-TiO_2/PPF nanocomposite-5				Bone cement composite-5

www.manaraa.com

9		1 g	TiO_2 (0.09 g)		TiO_2-loaded bone cement
10		1 g	ZrO_2-modified TiO_2 (0.09 g)		ZrO_2-TiO_2-loaded bone cement
11		1 g	hydroxyapatite (0.09 g)		HAp-loaded bone cement
12		1g	$BaSO_4$ (0.09 g)		$BaSO_4$-loaded bone cement
13	1 g of Sr^{2+}-TiO_2/PPF nanocomposite-2			0.01 g	Rg_1-loaded bone cement composite-1
14	1 g of Sr^{2+}-TiO_2/PPF nanocomposite-2			0.05 g	Rg_1-loaded bone cement composite-2
15	1 g of Sr^{2+}-TiO_2/PPF nanocomposite-2			0.1 g	Rg_1-loaded bone cement composite-3

Note: Additionally, 0.4 g of N-VP, 50 μL of BPO solution, and 40 μL of DMT solution were added in the preparation of these materials.

3.3 Results and Discussion

3.3.1 X-ray diffraction analysis of Sr-doped TiO_2 nanoparticles synthesized in supercritical CO_2

XRD analysis was used to investigate the effect of the dopant composition on the phase structure. Typical XRD patterns of the TiO_2, ZrO_2-modified TiO_2, and Sr-doped TiO_2 particles synthesized in $scCO_2$ are illustrated in Figure 3.2. In the XRD pattern of the TiO_2 particles (Figure 3.2a) all diffraction peaks in the range of $20^o < 2\theta < 80^o$ correspond to the 101, 004, 100, 200, 105, 211, 204, 116, 220, and 215 reflections of

www.manaraa.com

anatase crystal structure of TiO_2.[49] The as-prepared materials were amorphous, while after calcination at 450 °C the material reorganized itself, and the anatase particles began to grow, resulting in the crystalline material. The XRD pattern of ZrO_2-modified TiO_2 powder (Figure 3.2c) indicates that the ZrO_2-TiO_2 nanofibers consist of anatase crystals, with no rutile phase. A new peak appeared at $2\theta = 30.4°$, which is assigned to zirconium titanium oxide ($ZrTiO_4$).[50] In the XRD pattern of Sr-doped TiO_2 nanoparticles shown in Figure 3.2b, all peaks correspond to anatase phase, which indicates that the as-prepared materials transferred from the amorphous to anatase phase during heat treatment. In addition, there was no distinct SrO peak indicating no phase separation,[51] and that the SrO is well-integrated into the anatase crystal structure for both investigated compositions. It is also believed that it is difficult for the Sr^{2+} ion to enter the TiO_2 lattice, as its ionic radius is too high (1.12 Å) compared to Ti^{4+} (0.605 Å).[38] Therefore, it is very difficult to predict whether Sr^{2+} exists as Sr-O on the surface of TiO_2 or as $SrTiO_3$ from the XRD pattern owing to the low dopant concentration.

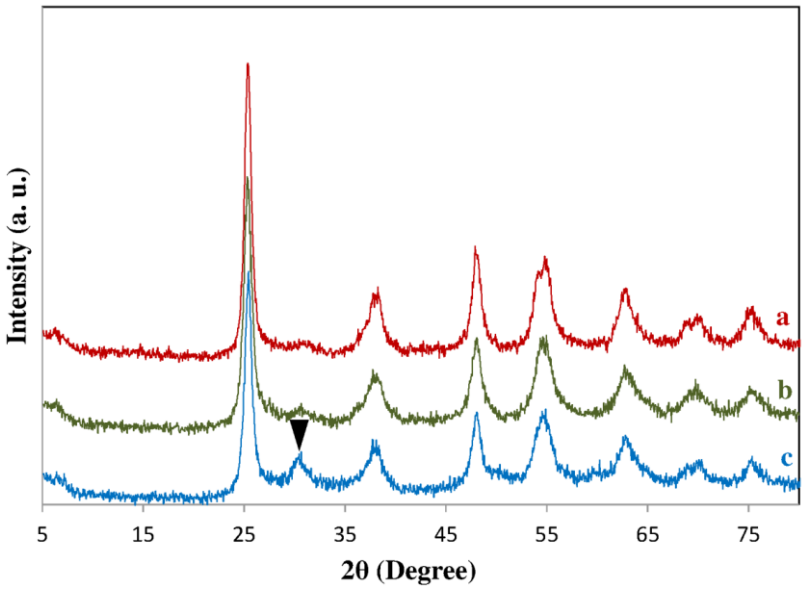

Figure 3.2. Powder XRD spectra of (a) TiO_2, (b) Sr-doped TiO_2 synthesized using 20 wt% of $Sr(NO_3)_2$, and (c) ZrO_2-modified TiO_2 nanofibers.

www.manaraa.com

3.3.2 Scanning electron microscopy (SEM) and energy-dispersive X-ray spectroscopy (EDX) analyses of Sr-doped TiO_2 nanoparticles synthesized in supercritical CO_2

The morphology and size of the calcined Sr-doped TiO_2 synthesized in $scCO_2$ with two different dopant concentrations were characterized by SEM analysis. The presence of Sr^{2+} in the TiO_2 matrix results in the formation of rod-like and fiber-like structures regardless of the dopant concentrations. However, a higher amount of Sr^{2+} precursor (20 wt% of $Sr(NO_3)_2$ solution) increased the mean particle size to 60-100 nm in diameter, as can be seen in Figure 3.3a. Using a lower concentration of the same precursor (5 wt% of $Sr(NO_3)_2$ solution), nanoparticles with typical diameters of about 30-60 nm and an increased aspect ratio of about 40-50 (Figure 3.3b) were formed. EDX elemental analysis was also performed to investigate the bulk atomic composition of the elements in the synthesized Sr-doped TiO_2 particles. EDX spectra of the two samples are presented in Figure 3.3c & d. Carbon, oxygen, strontium, and titanium are evident in both cases, with the elemental compositions of the two Sr-doped TiO_2 samples along with the standard deviation being provided in Table 3.3. It has been revealed that the amount of strontium was less when the smaller amount of dopant was used. In addition, the atomic composition of strontium is less than the atomic composition of Sr in the starting precursor mixture; for example, Sr atomic% of 3.0 ± 0.1 was observed for the 20 wt% Sr-doped TiO_2. This indicates that not all $Sr(NO_3)_2$ (Sr^{2+}) was integrated into the product, and this free Sr^{2+} not integrated into the nanofibers are believed to be washed away during the washing steps using CO_2. The carbon in these samples arose from the reaction under $scCO_2$, unreacted acetic acid, and washing with $scCO_2$.

www.manaraa.com

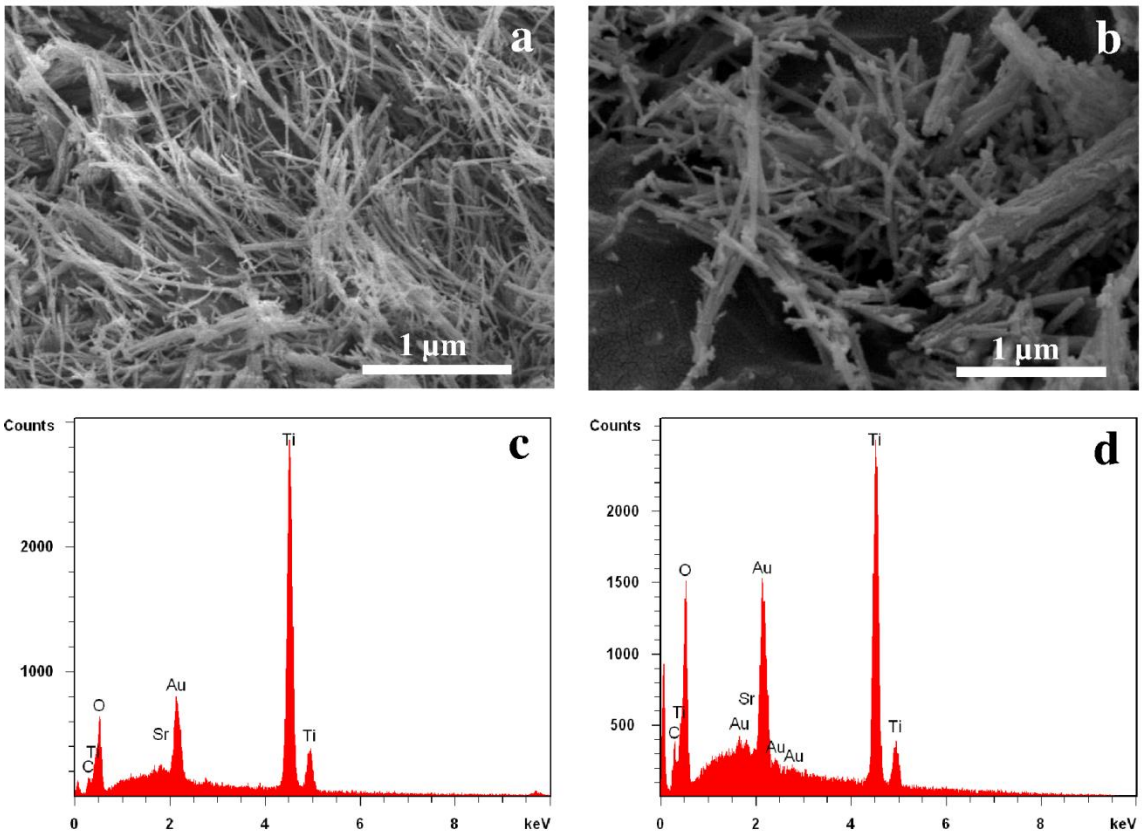

Figure 3.3. SEM images of (a) the 5 wt% Sr-doped TiO_2 and (b) the 20 wt% Sr-doped TiO_2 and EDX Spectra of (c) the 5 wt% Sr-doped TiO_2 and (d) the 20 wt% Sr-doped TiO_2.

Table 3.3. Elemental composition of Sr-doped TiO_2 nanofibers (n = 3, mean ± SD).

	Atomic %			
	Ti	O	Sr	C
5 wt% Sr-doped TiO_2	18.6 ± 1.2	57.6 ± 1.7	1.6 ± 0.1	22.2 ± 0.1
20 wt% Sr-doped TiO_2	15.2 ± 2.3	59.5 ± 1.3	3.0 ± 0.1	22.3 ± 0.1

3.3.3 X-ray photoelectron spectroscopy (XPS) measurement of Sr-doped TiO_2 and Sr^{2+}-TiO_2/PPF nanocomposites nanocomposites

X-ray photoelectron spectroscopy (XPS) was used to elucidate both the TiO_2 structure

www.manaraa.com

and the chemical state of the Sr^{2+}-doped TiO_2 particles. In the recorded survey spectrum for the Sr-doped TiO_2 (prepared from 20 wt% of $Sr(NO_3)_2$ solution), the expected peaks for O, C, Ti, and Sr were detected (Figure 3.4a). The high resolution XPS scan of the Ti 2p region of Sr-doped TiO_2 shows two peaks (Figure 3.4c), the Ti $2p_{3/2}$ peak at 458.6 and the Ti $2p_{1/2}$ peak at 464.3 eV binding energy, which are attributed to Ti in the 4+ state.[52] The O 1s XPS spectrum has two peaks (Figure 3.4b), with the first at 529.8 eV assigned to the lattice oxygen atoms TiO_2 (Ti-O bonds), and the second at 531.0 eV being due to surface hydroxyl and defective oxide sites.[52] Besides, in the core level spectrum of Sr 3d, the Sr $3d_{5/2}$ peak shows a binding energy of 133.5 eV, which can be assigned to $SrTiO_3$ (Figure 3.4d).[53]

In the high resolution XPS scan of the C 1s region of non-crosslinked Sr^{2+}-TiO_2/PPF nanocomposite (Figure 3.4e), the three major carbon peaks are observed with binding energies of 284.8, 286.3, and 288.9 eV, which correspond to aliphatic carbon (C–C, C-H), alcohol and ether functionality (C–OH, C–O–C), and ester and carboxylic acid type functionality (O–C=O), respectively.[54] In addition, a peak appearing at 287.8 eV is assigned to the C atom of the carbonyl group from the successful covalent interaction of carboxylate to Sr-doped TiO_2.[42, 55, 56] The high resolution O 1s spectrum of non-crosslinked Sr^{2+}-TiO_2/PPF nanocomposite (Figure 3.4f), shows three different peaks at binding energies of 529.4, 531.9, and 533.3 eV, attributable to the lattice oxygen atoms in TiO_2 (Ti-O bonds),[52] O–C=O*, and O*–C=O, respectively (* denotes the O of interest).[54] Furthermore, the core level spectrum of Ti 2p for the non-crosslinked Sr^{2+}-TiO_2/PPF nanocomposite (Figure 3.4g) could be resolved into two spin-orbit pairs of 2p3/2 and 2p1/2 with binding energies of 458.1 and 463.8 eV, respectively, attributable to Ti^{4+} implying that the chemical state of titanium remains as Ti^{4+} that the chemical state of titanium remains as Ti(IV)(TiO_2), and does not change to Ti(II) and Ti(III) species.[42, 57] In addition, in the high resolution XPS scan of the Sr 3d region (Figure 3.4h), the two peaks at binding energies of 133.1 and 135 eV are evident, which were observed for the Sr-doped TiO_2 nanoparticles. Therefore, the XPS results confirm the successful coordination of MA-PPF to the surface of Sr-doped TiO_2 nanofibers without changing the oxidation state of nano Sr^{2+}-doped TiO_2, which indicates that any other Ti(II) and Ti(III) oxides, TiO and Ti_2O_3, were not formed.

www.manaraa.com

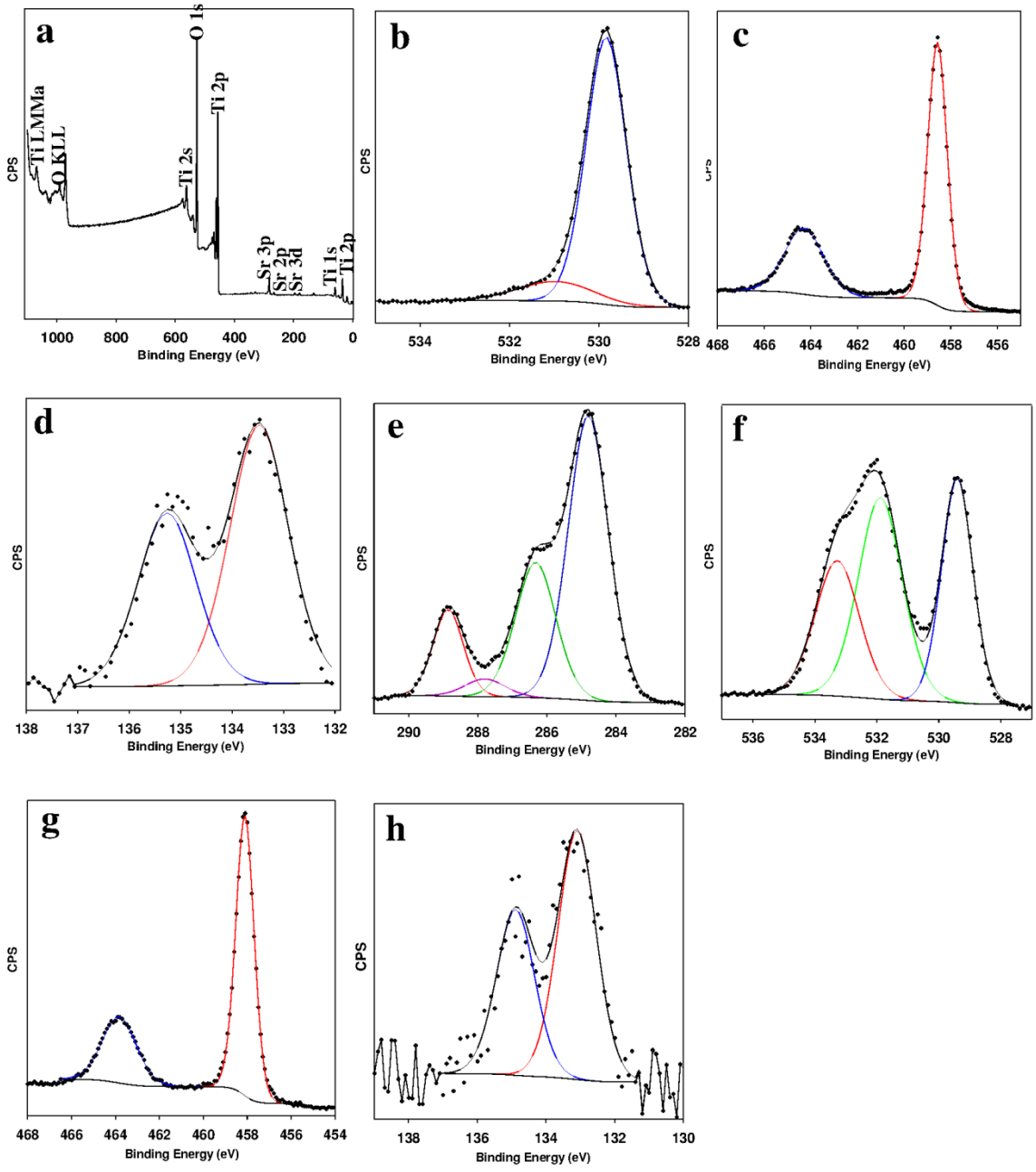

Figure 3.4. (a) XPS full-scan spectrum of the Sr-doped TiO_2 nanoparticles, high resolution XPS record of O 1s region (b), high resolution XPS scan of the Ti 2p region (c), and high resolution XPS scan of the Sr 3d region (d) of the Sr-doped TiO_2 nanoparticles and high resolution XPS record of the C 1s region (e), high resolution XPS record of the O 1s region (f), high resolution XPS scan of the Ti 2p region (g), and high

www.manaraa.com

resolution XPS scan of the Sr 3d region (h) of the Sr^{2+}-TiO_2/PPF nanocomposite-3.

3.3.4 Fourier transform infrared (FTIR) spectroscopy of Sr^{2+}-TiO_2/PPF nanocomposites

The FTIR spectra of TiO_2 nanoparticles, Sr-doped TiO_2 nanoparticles, PPF, non-crosslinked Sr^{2+}-TiO_2/PPF composite, and crosslinked bone cement composite-1 were measured and compared. There was no significant difference between the spectra of TiO_2 nanoparticles and Sr-doped TiO_2 nanoparticles in the wavenumber range of 600-4000 cm^{-1} (data not shown). This is because SrO_2 vibrations occur only below 350 cm^{-1}.[38] The FTIR spectra of PPF, non-crosslinked Sr^{2+}-TiO_2/PPF composites, and cross-linked Sr^{2+}-TiO_2/PPF bone cement composites are compared in Figure 3.5. PPF exhibits several major characteristic peaks at 1713, 1645, 1251, and 1148 cm^{-1} (Figure 3.5a), attributed to the C=O stretching, C=C stretching, asymmetric C-O-C stretching, and symmetric C-O-C stretching bands, respectively. These characteristic peaks are evident in the FTIR spectrum of non-crosslinked Sr^{2+}-TiO_2/PPF composites (Figure 3.5b), indicating the well-preserved C=C groups during the functionalization of Sr^{2+}-TiO_2 using MA-PPF. In addition, the FTIR spectrum of the non-crosslinked Sr^{2+}-TiO_2/PPF composites exhibits new peaks at 1568, 1379, and 1173 cm^{-1}. These peaks are assigned to the bridging or chelating bidentate coordination between titanium atoms and the carboxyl groups. The band separation ($\Delta\upsilon$=395 cm^{-1}) between 1568 and 1173 cm^{-1} falls into the monodentate range (350-500 cm^{-1}) while another band separation ($\Delta\upsilon$=189 cm^{-1}) between 1568 and 1379 cm^{-1} might be indicative of a structure of bridging bidentate (150-180 cm^{-1}).[58] These bands confirmed the coordination of the PPF-g-MA (functionalized PPF) with Sr-doped TiO_2. These coordination peaks appear in the FTIR spectrum of cross-linked Sr^{2+}-TiO_2/PPF bone cement composites (Figure 3.5c), suggesting the well-preseved coordination bonds during the crosslink reaction. The disappearance of the peak at 1645 cm^{-1} in Figure 3.5c confirmed the cross-link reaction where the C=C double bonds were consumed.

www.manaraa.com

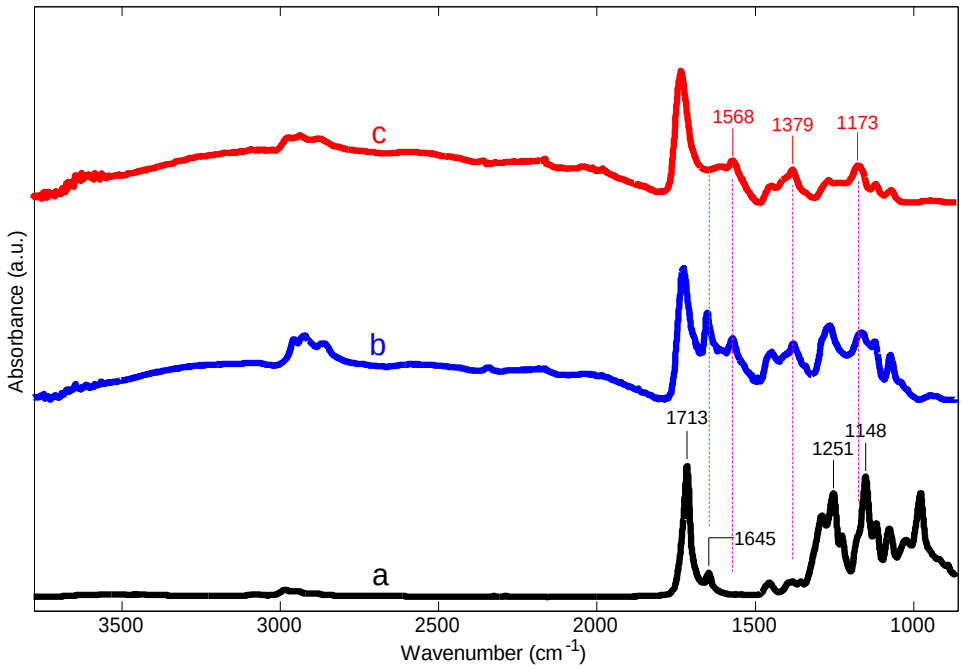

Figure 3.5. ATR-FTIR spectra of (a) PPF, (b) Sr^{2+}-TiO_2/PPF nanocomposite-3, and (c) crosslinked bone cement composite-3.

3.3.5 TGA

In order to determine PPF attachment to the surface of Sr-doped TiO_2 nanofibers and investigate the effect of PPF functionalization on the thermal stability of the proposed Sr^{2+}-TiO_2/PPF nanocomposites, thermogravimetric analysis (TGA) was performed on the non-crosslinked PPF, crosslinked PPF, non-crosslinked Sr^{2+}-TiO_2/PPF nanocomposites, and crosslinked Sr^{2+}-TiO_2/PPF bone cement composites. The sample of Sr^{2+}-TiO_2/PPF nanocomposite-3 displayed a weight loss of 80% compared to the calcined Sr-doped TiO_2 nanofibers with a weight loss of 3%. Therefore, it can be concluded that PPF functionalization allowes a relatively high number of polymer chains to be attached to the surface of Sr-doped TiO_2 nanofibers, resulting in an increased weight loss for the Sr^{2+}-TiO_2/PPF nanocomposite-3. A typical DTG curve of the unfilled PPF and Sr^{2+}-TiO_2/PPF nanocomposite appears to have two degradation steps (Figure 3.6B), amongst which the main peak (at 330-360 °C) is attributed to the scission of the polymer chains attached to the Sr-doped TiO_2 nanoparticles. For the Sr^{2+}-TiO_2/PPF nanocomposite-3, this peak is shifted to a higher temperature by 7 ºC, which is attributed to the polymer chains being

www.manaraa.com

chemically attached to the nanofibers. The higher thermal dissociation temperature revealed from the TGA results of the nanocomposites is attributed to the excellent chemical interaction of nano-Sr-doped TiO_2 and functionalized polymer chains, providing a barrier effect to the polymer molecules evaporated during the thermal degradation of the nanocomposites.

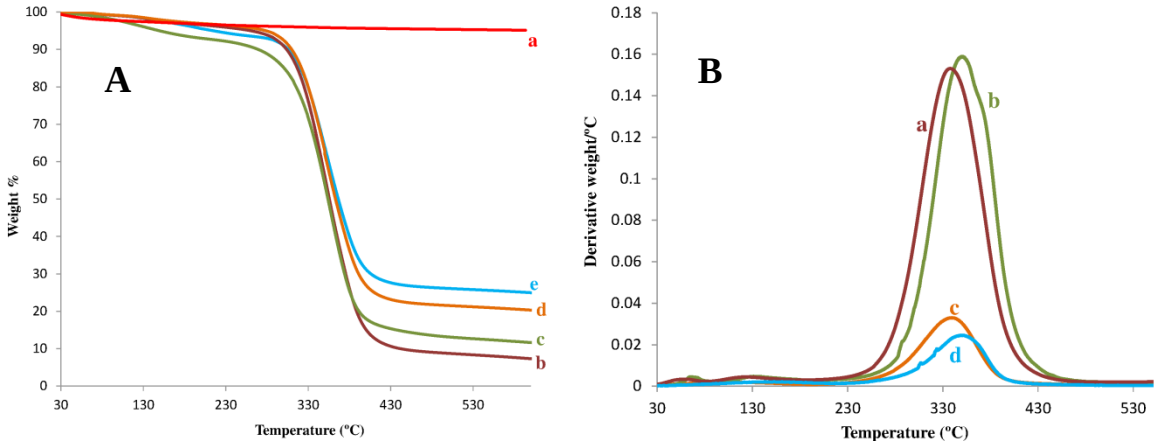

Figure 3.6. (A) TGA curves of: (a) TiO_2, (b) PPF, (c) crosslinked PPF, (d) Sr^{2+}-TiO_2/PPF nanocomposite-3 (synthesized using 1 g of MA-PPF and 0.015 g of Sr-doped TiO_2), and (e) crosslinked bone cement composite-3 (made of 1 g of Sr^{2+}-TiO_2/PPF synthesized using 0.015 g of Sr-doped TiO_2). (B) Derivative thermogravimetric (DTG) curves of: (a) PPF, (b) crosslinked PPF, (c) Sr^{2+}-TiO_2/PPF nanocomposite-3 (synthesized using 1 g of MA-PPF and 0.015 g of Sr-doped TiO_2), and (d) crosslinked bone cement composite-3 (made of 1 g of Sr^{2+}-TiO_2/PPF synthesized using 0.015 g of Sr-doped TiO_2).

3.3.6 Mechanical testing (tensile and flexural strength and modulus)

Figure 3.7 summarizes the results of the tensile and flexural moduli and strengths of the bone cement composites tested in this work. Bone cement composites prepared using Sr-doped TiO_2 nanoparticles showed no significant difference in flexural modulus and strength compared to composites prepared using TiO_2 nanofibers. The flexural modulus of crosslinked PPF alone is 365 ± 66 MPa. With a loading of 0.5 wt % in the starting

www.manaraa.com

composition, bone cement composites-1 exhibited a flexural modulus of 1062 ± 90 MPa, representing a roughly 3-fold increase compared to crosslinked PPF. The flexural modulus increased to a maximum (1176 ± 152 MPa) and then slowly decreased with increased Sr-doped TiO_2 nanoparticles loading. Flexural strength of the reinforced bone cement composites exhibits similar behavior as in the case of Flexural modulus with bone cement composite-2 exhibiting a nearly 2.5-fold increase in the flexural strength (Figure 3.7d). Similar to the flexural modulus, a significant decrease in flexural strength was also observed between the 0.5 and 2 wt % loadings. Flexural moduli and strengths of reinforced bone cement composites are mainly influenced by the transfer of applied load from matrix to filler.[33] The effectiveness of load transfer is controlled by a number of factors such as distribution and orientation of fillers within the matrix and most importantly interfacial shear strength between the fillers and matrix. In the case of one dimensional nano-fillers (Sr-doped TiO_2 nanofibers), the load is transferred from the matrix to the filler via interfacial shear stresses between the two phases.[59] Functionalization of PPF establishes an enhanced chemical bonding between the Sr-doped TiO_2 nanofibers and matrix, which ensures stronger interfacial shear strength between the fillers and matrix, allowing flexural stress to be more effectively transferred from the matrix to the filler and vice versa.[60] Therefore, bone cement composites significantly exceeded the enhancements observed for the mechanically mixed composites at the same loading concentration. In addition, bone cement composites-3 loaded with 14 wt% Sr-doped TiO_2 nanofibers, demonstrated lower flexural properties, which is partly due to the agglomeration of nanofibers as shown by arrows in Figure 8e. The Young's modulus of crosslinked PPF is 228 ± 46 MPa. The Young's modulus values of crosslinked composites increased with the initial low concentrations of Sr-doped TiO_2 nanofibers, peaked for bone cement composite-2 and bone cement composite-3, and then decreased at higher loading concentrations. Tensile strength showed little variation between different cement formulations; however, a noticeable trend was observed with respect to loading concentration (Figure 3.7b). The tensile strength starts decreasing with increased loading of Sr-doped TiO_2 nanofibers over 1 wt% in the starting composition, which is also attributed to the observed agglomeration of nanofibers in the cement matrix. The SEM micrographs of the fracture surfaces of the unfilled PPF and the bone cement

www.manaraa.com

composite-2 loaded with 9 wt% Sr-doped TiO_2 nanofibers are shown in Figure 3.8. The plain crosslinked PPF exhibits a smooth plain surface (Figure 3.8a), while the bone cement composite-2 shows a rough surface (Figure 3.8b) with a certain amount of Sr-doped TiO_2 nanofibers "pull out" occurring within the fractured plane of the composite (Figure 3.8d). These partially pulled out nanofibers can take part in bridging the crack during propagation.[61] In addition to the strong interfacial adhesion between the fibers and the matrix resulting from the chemical bonding through the carboxylic group, Sr-doped TiO_2 fibers are dispersed homogeneously throughout the bone cement composite-2 (Figure 3.8c), when reacted to the PPF after being functionalized.

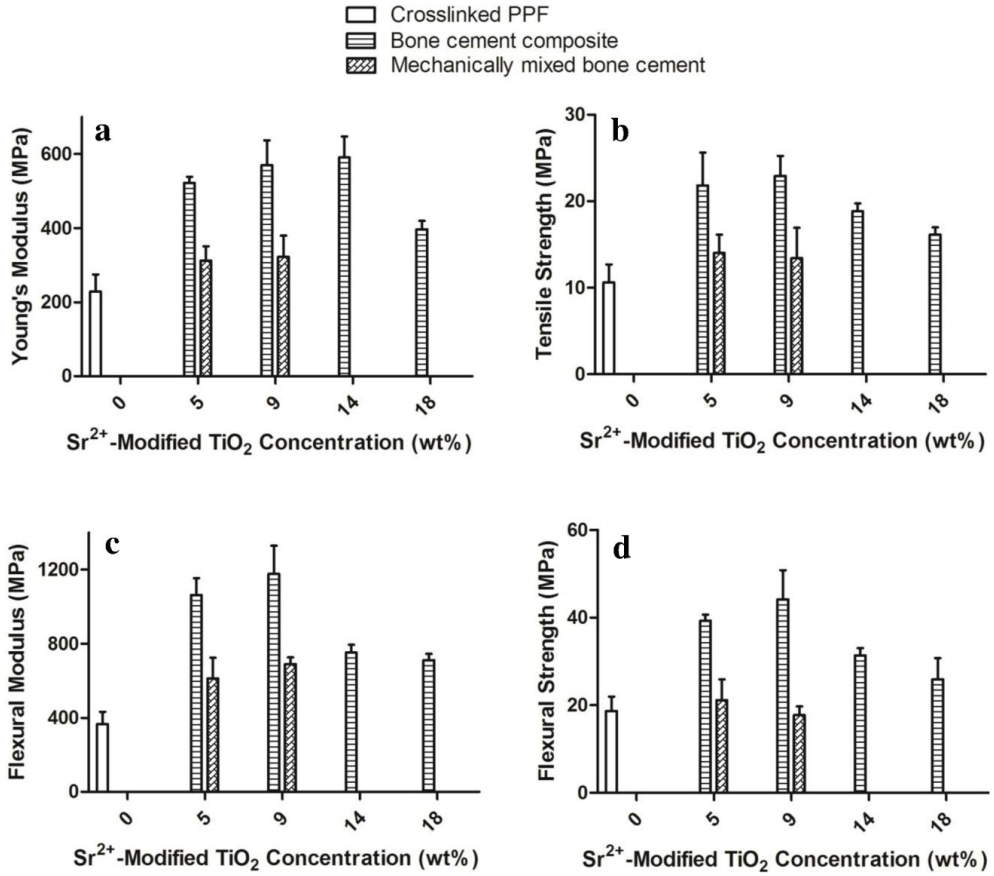

Figure 3.7. Mechanical properties of cross-linked bone cement composites as a function of the Sr-doped TiO_2 nanofibers concentration.

(a) Young's modulus, (b) tensile strength, (c) flexural modulus, and (d) flexural strength.

www.manaraa.com

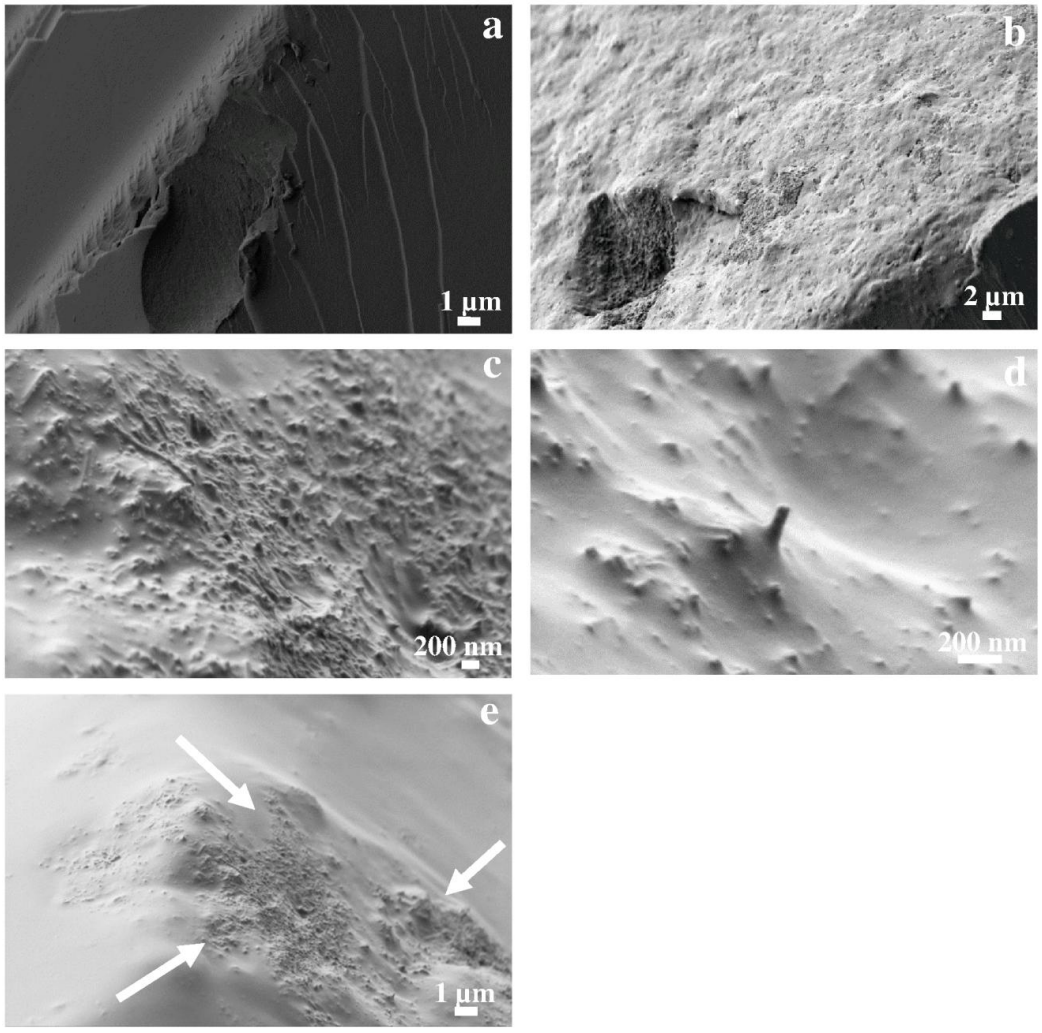

Figure 3.8. SEM images of the fracture planes of: (a) crosslinked unmodified PPF, (b-d) bone cement composite-2, and (e) bone cement composite-3 (the arrows show Sr-doped TiO_2 nanofibers are agglomerating at higher concentrations within the polymer matrix).

It has been believed that drug-loaded cement is mechanically less strong than plain cement.[62] However, our results show that plain bone cement displays a slightly better flexural and tensile strength than those of the ginsenoside Rg_1-loaded bone cement. For example, Rg_1-loaded bone cement-3 exhibited a Young's modulus and tensile strength of 545.2 ± 86 MPa and 21.3 ± 1.6 MPa and flexural modulus and strength of 1014 ± 105 MPa and 41.5 ± 5.4 MPa, respectively.

www.manaraa.com

3.3.7 Radiopacity

The radiopacity values in Al equivalent of 1mm specimen thickness for crosslinked unfilled PPF and bone cement composites loaded with 9 wt% n-TiO_2 nanofibers, ZrO_2-modified TiO_2 nanofibers, Sr-doped TiO_2 nanofibers, hydroxyapatite nanorods, as well as $BaSO_4$ particles (corresponding to the Sr-doped TiO_2 concentration in the Sr^{2+}-TiO_2/PPF nanocomposite-2 reviewed by TGA analysis represented in Table 3.1) are presented in Table 3.4. As shown in this Table, crosslinked PPF loaded with 9 wt% $BaSO_4$ exhibits a radiopacity of 0.36 mm Al, which is the highest value of radiopacity among different formulations examined in this study, while hydroxyapatite-loaded bone cement composite exhibits the lowest value of radiopacity, 0.15 mm Al. Moreover, bone cement composite containing 9 wt% n-TiO_2 fibers exhibiting a low level of radiopacity (0.20 mm Al), which is not significantly different from the unfilled PPF. The bone cement composite-2 exhibited a slightly higher level of radiopacity (0.32 mm Al) compared to the composite loaded with ZrO_2-modified nanofibers at the same amount of loading exhibiting a radiopacity of 0.29 mm Al. The bone cement composite-2 increased the radiopacity of PPF matrix to approximately 88% of the radiopacity shown by the specimen containing 9 wt% $BaSO_4$, and is deemed sufficient. Besides, it is possible to integrate more Sr^{2+} into the TiO_2 nanofibers by adjusting the synthesis conditions.

In addition, as shown in Table 3.4, the radiopacity of bone cement composite-2 formulation does not decrease significantly when loaded with 0.1 g of ginsenoside Rg_1.

Table 3.4. Radiopacity values (mm Al) of bone cement composites of equivalent Al thickness (means ± SD).

Sample	**Radiopacity (mmA1)**
Crosslinked PPF	0.18 ± 0.01
Bone cement composite-1	0.30 ± 0.02
Bone cement composite-2	0.32 ± 0.03
Bone cement composite-3	0.32 ± 0.02

www.manaraa.com

Bone cement composite-4	0.35 ± 0.04
Bone cement composite-5	0.29 ± 0.03
TiO_2-loaded bone cement	0.20 ± 0.01
ZrO_2-TiO_2-loaded bone cement	0.29 ± 0.01
HAp-loaded bone cement	0.15 ± 0.01
$BaSO_4$-loaded bone cement	0.36 ± 0.03
Rg_1-loaded bone cement composite-3	0.30 ± 0.12

3.3.8 Angiogenesis effect/tube formation of HUVEC cell line

Figure 3.9 displays the tube formation of EA.hy926 cell line seeded in a growth factor-reduced Matrigel-coated 96-well plate untreated or treated with ginsenoside Rg_1 at different concentrations before and after incorporation into the bone cement composite formulations. As shown in Figure 3.9a, after seeding for twelve to eighteen hours, the EA.hy926 cell line aligned and formed tube-like structures on Matrigel. In the presence of Rg_1, the cells formed relatively complete, condensed, and narrow tube-like structures indicating the proangiogenesis activity of ginsenoside Rg_1, as shown in Figure 3.9b-g. This stimulation occurs in a dose-dependent manner within the dose range of 1-32 µg/ml Rg_1 extract. Therefore, it is concluded that above a concentration of 1 µg/ml, Rg_1 significantly stimulated the EA.hy926 cell line to proliferate. It was also found that the tube formation was considerably augmented in the presence of 8 µg/ml Rg_1 (Figure 3.9e), as cells tend to aggregate to form a denser structure by stimulation of Rg_1 leading to higher area coverage per photographed field.

Tube formation stimulation activity of ginsenoside Rg_1 did not change significantly before and after release from the delivery carrier indicating that the prepared bone cement composites did not significantly affect the angiogenic activity of Rg_1. The extract liquid in 2 mL of medium from the second day to the third day and from the ninetieth to twentieth day of release was collected. The concentration of Rg_1 in the collected medium was measured using UV-Vis spectrophotometry. It was found that the Rg_1 released from

www.manaraa.com

composites were above the functional concentration in our selected time intervals, 1 µg/ml, for the second day to the third day and the ninetieth to twentieth day, as the release amount in PBS and lasted for twenty five days (Figure 3.9). These concentrations in collected medium were diluted to different concentrations of 1-32 µg/ml. As illustrated in Figure 3.10i-n, ginsenoside Rg_1 released from the bone cements exhibits similar potency towards the formation of networks of honeycomb-like or tube-like structures in the EA.hy926 cell line in a dose-dependent manner. These results indicate that similar to Chang's study cells treated with ginsenoside were incorporated into the developing network to a greater extent;[12] however, we were able to show the dose-dependent increase in the Rg_1-induced angiogenic tube formation of HUVESc cell line.

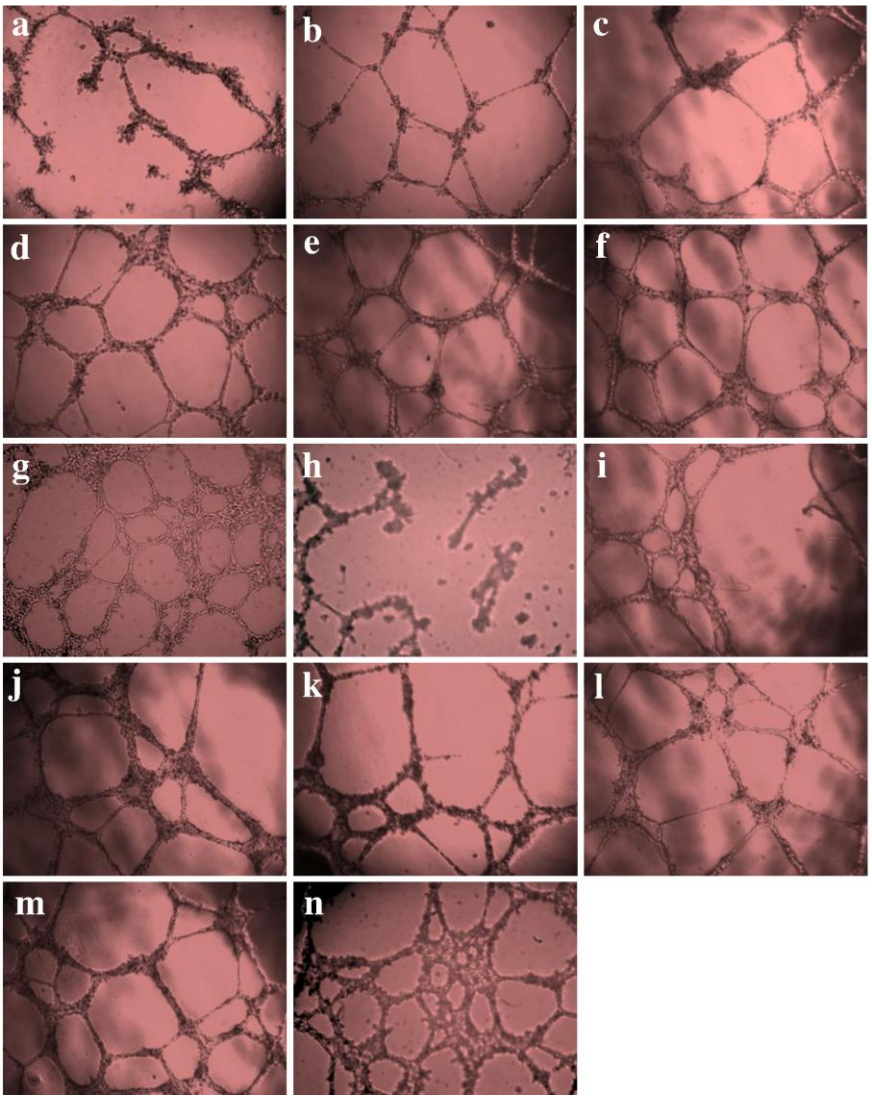

www.manaraa.com

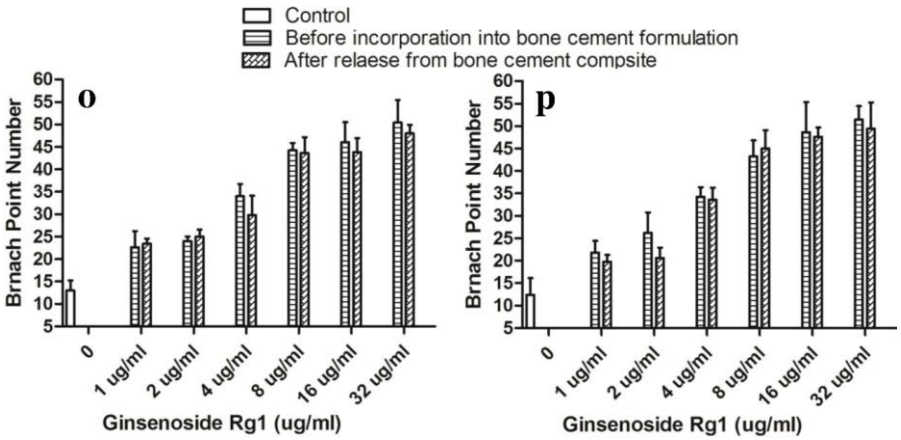

Figure 3.9. Tube formation of HUVECs cell line cultured in different extract-contained media from bone cements.

Effect of 18 h incubation with ginsenoside Rg_1 (before incorporation into bone cement) on tube formation of EA.hy926 cell line: Control (a), cells treated with 1 μg/ml (b), 2 μg/ml (c), 4 μg/ml (d), 8 μg/ml (e), 16 μg/ml (f), and 32 μg/ml ginsenoside Rg_1 (g), Rg_1-induced angiogenic tube formation of EA.hy926 cell line cultured in media contained extract released from Rg_1-loaded bone cement composite-2 for the second day to the third day of release at 1 μg/ml (i), 2 μg/ml (j), 4 μg/ml (k), 8 μg/ml (l), 16 μg/ml (m), and 32 μg/ml (n) ginsenoside Rg_1 concentration compared to blank (h), a dose-dependent increase in the branching points up to 32 μg/ml ginsenoside Rg_1 released from Rg_1-loaded bone cement composite-2 for the second day to the third day (o), and for the ninetieth to twentieth day (p) of release.

3.3.9 *In vitro* drug release behavior of Rg_1

Bone cement composites should have the ability to deliver angiogenic agents such as ginsenoside Rg_1 as examined in this work. The optimal bone cement formulation, which was found to be Sr^{2+}-modified TiO_2/PPF bone cement-2 for providing better mechanical and radiopacity properties, was examined for drug release. As shown in Figure 3.10, the three groups of drug-loaded bone cements have nearly identical release profiles; after a high initial release of ginsenoside Rg_1, a reduced yet constant, sustained release was observed. In the first 5 days, 46.5% of the Rg_1 was released promptly from Rg_1-loaded bone cement composite-3, which can be attributed to either dissolution of the adsorbed particles or diffusion of ginsenoside Rg_1 particles close to the surface of the bone

www.manaraa.com

cement.[62, 63] The burst phase, lasting approximately 5 days, ranged from 29.5% to 59.3% for Rg_1-loaded bone cement composite-1 and Rg_1-loaded bone cement composite-2, respectively. After day 5, the profiles showed a decrease in the amount of Rg_1 released over time to the day 40. Typically, the release rate is decreased with time due to a decreased driving force, as the Rg_1 is depleted from the surface matrix. During this phase, the release depends on various other chemical and physical processes, such as polymer chain cleavage, diffusion of the drug (Rg_1) and of polymer degradation products out of the bone cement, and the breakdown of the polymeric structure.[64] After 40 days, the release varied between 63% and 86.5% for Rg_1-loaded bone cement composite-1 and Rg_1-loaded bone cement composite-3, respectively. Additionally, the amount of ginsenoside Rg_1 released from Rg_1-loaded bone cement composite-3 was higher than that from the Rg_1-loaded bone cement composite-1 and Rg_1-loaded bone cement composite-2 over the 40-day period, which is in agreement with the report by chang et al. presenting a higher amount of ginsenoside Rg_1 released *in vitro* from the bone cement composite containing higher Rg_1 content.[12]

The Rg_1 release from bone cement formulations examined here is rather slow, as the PPF matrix is hydrophobic and thus impervious to Rg_1 diffusion. In addition, Sr^{2+}-TiO_2/PPF based bone cement composites are crosslinked due to the interfacial covalent bonding. Consequently, the ginsenoside Rg_1 needs to diffuse entirely through the tightly crosslinked PPF matrix, leading to a slow release.[65] The tube formation bioassays showed that the optimal concentration for ginsenoside Rg_1 to stimulate cell lines to proliferate is 8 µg/ml. In our system, the Rg_1 released from bone cement composites were above this functional concentration and last for almost twenty five days (Figure 3.10).

www.manaraa.com

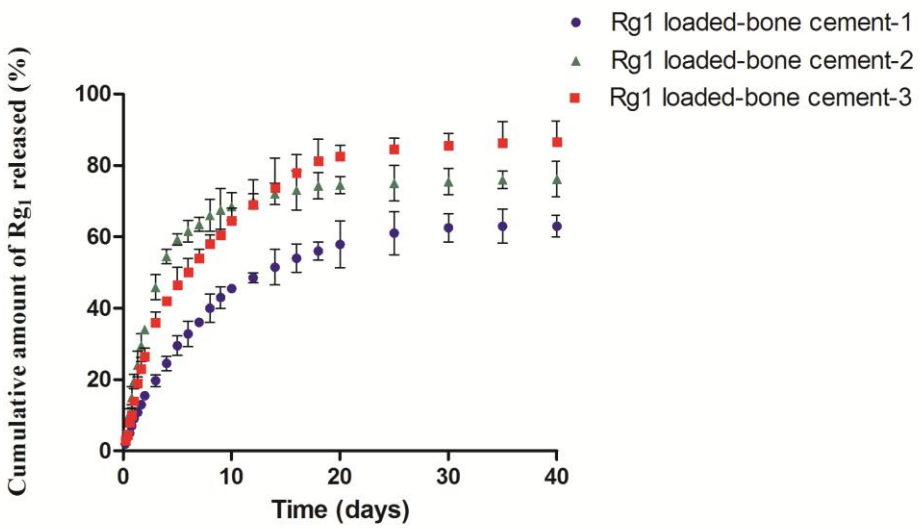

Figure 3.10. The cumulative amount of released ginsenoside Rg_1 from Rg_1-loaded bone cement composite-1, Rg_1-loaded bone cement composite-2, and Rg_1-loaded bone cement composite-3.

In addition, Sr is a natural bone-seeking trace element that accumulates in the skeleton, since strontium is chemically closely related to calcium (both Sr and Ca are in the same group in the periodic table), and it is incorporated into bone at the same rate as calcium.[66] It is believed that Sr stimulates the proliferation and growth of bone cells as a result of its chemical similarity to calcium.[33] Moreover, Sr stimulates bone formation and reduces bone resorption, leading to increased bone mass in osteopenic subjects.[66] Therefore, Sr^{2+} incorporated bone cement formulation can be potentially useful for the treatment of osteonecrosis in humans. These factors may exert an important role in biocompatibility of bone cements containing n-Sr-doped TiO_2 nanoparticles. Therefore, a study of biocompatibility behavior of these bone cement nanocomposites is recommended for future work. From the above discussion it can be deduced that TiO_2 nanofibers can act as an effective reinforcing agent for an experimental functionalized PPF matrix in order to produce a new generation of bone cements when modified with Sr^{2+}. Chemical bonding between the filler and the polymer helps the resulting nanocomposites retain the enhanced mechanical properties of the unmodified counterpart, while the incorporation of ginsenoside Rg_1 did not alter other important physical properties of the bone cement such as radiopacity and mechanical characteristics.

www.manaraa.com

3.4 Conclusions

This study shows a novel pathway to develop an alternative radiopacifier for PPF-based bone cement, which also can act as a reinforcing agent. Radiopaque Sr^{2+} component ($SrTiO_3$) was successfully incorporated into the titania nanorods/fibers using a sol-gel reaction in supercritical CO_2. In order to enhance the reinforcing effect, the polyester was functionalized with maleic anhydride (MA) using a ring opening reaction. Sr-doped TiO_2 particles showed strong chemical interaction with the functionalized polymer, as confirmed by X-ray photoelectron spectroscopy (XPS) and micrographic analyses of the nanocomposites. The prepared bone cement nanocomposites provided higher thermal stability than mechanically mixed bone cement nanocomposites, confirmed by thermogravimetric analysis (TGA) as well as higher mechanical properties. The ginsenoside Rg_1 release analysis revealed that the bone cement composites loaded with higher Rg_1 content released relatively higher Rg_1 into the surrounding environment *in vitro.* The tube formation stimulation of released Rg_1 was statistically significant as Rg_1 both before and incorporation into the cement composition. In addition. mechanical testing of Rg_1-loaded bone cement showed that the incorporation of ginsenoside Rg1 did not adversely affect the mechanical properties.

www.manaraa.com

3.5 References

1 Mont MA, Ragland PS, Etienne G. Core decompression of the femoral head for osteonecrosis using percutaneous multiple small-diameter drilling. Clinical orthopaedics and related research. 2004;429:131-138.

2 Weinstein RS, Nicholas RW, Manolagas SC. Apoptosis of Osteocytes in Glucocorticoid-Induced Osteonecrosis of the Hip 1. The Journal of Clinical Endocrinology & Metabolism. 2000;85:2907-2912.

3 Karlson EW, Mandl LA, Aweh GN, Sangha O, Liang MH, Grodstein F. Total hip replacement due to osteoarthritis: the importance of age, obesity, and other modifiable risk factors. The American journal of medicine. 2003;114:93-98.

4 Gangji V, Toungouz M, Hauzeur J-P. Stem cell therapy for osteonecrosis of the femoral head. Expert opinion on biological therapy. 2005;5:437-442.

5 Gangji V, De Maertelaer V, Hauzeur J-P. Autologous bone marrow cell implantation in the treatment of non-traumatic osteonecrosis of the femoral head: Five year follow-up of a prospective controlled study. Bone. 2011;49:1005-1009.

6 Cherian JJ, Kapadia BH, Banerjee S, Jauregui JJ, Mont MA. Corticosteroid Usage and Osteonecrosis of the Hip. Osteonecrosis: Springer; 2014. p. 91-93.

7 Wood ML, McDowell CM, Kelley SS. Cementation for femoral head osteonecrosis: a preliminary clinic study. Clinical orthopaedics and related research. 2003;412:94-102.

8 Mukisi-Mukaza M, Elbaz A, Samuel-Leborgne Y, Keclard L, Le Turdu-Chicot C, Christophe-Duchange E, Mérault G. Prevalence, clinical features, and risk factors of osteonecrosis of the femoral head among adults with sickle cell disease. Orthopedics. 2000;23:357-363.

9 Rodrigue SW, Rosenthal DI, Barton NW, Zurakowski D, Mankin HJ. Risk factors for osteonecrosis in patients with type 1 Gaucher's disease. Clinical orthopaedics and related research. 1999;362:201-207.

10 Assouline-Dayan Y, Chang C, Greenspan A, Shoenfeld Y, Gershwin ME, editors. Pathogenesis and natural history of osteonecrosis. Seminars in arthritis and rheumatism; 2002: Elsevier.

11 Lai K-A, Shen W-J, Yang C-Y, Shao C-J, Hsu J-T, Lin R-M. The Use of Alendronate to Prevent Early Collapse of the Femoral Head in Patients with Nontraumatic OsteonecrosisA Randomized Clinical Study. The Journal of Bone & Joint Surgery. 2005;87:2155-2159.

www.manaraa.com

12 Chang C-H, Liao T-C, Hsu Y-M, Fang H-W, Chen C-C, Lin F-H. A poly (propylene fumarate)–Calcium phosphate based angiogenic injectable bone cement for femoral head osteonecrosis. Biomaterials. 2010;31:4048-4055.

13 Wood ML, McDowell CM, Kerstetter TL, Kelley SS. Open reduction and cementation for femoral head fracture secondary to avascular necrosis: preliminary report. The Iowa orthopaedic journal. 2000;20:17.

14 Khaled S, Charpentier PA, Rizkalla AS. Physical and mechanical properties of PMMA bone cement reinforced with nano-sized titania fibers. Journal of Biomaterials Applications. 2011;25:515-537.

15 Khaled S, Miron RJ, Hamilton DW, Charpentier PA, Rizkalla AS. Reinforcement of resin based cement with titania nanotubes. dental materials. 2010;26:169-178.

16 Kim C, Mahar A, Perry A, Massie J, Lu L, Currier B, Yaszemski MJ. Biomechanical evaluation of an injectable radiopaque polypropylene fumarate cement for kyphoplasty in a cadaveric osteoporotic vertebral compression fracture model. Journal of spinal disorders & techniques. 2007;20:604-609.

17 Lewis G. Properties of acrylic bone cement: state of the art review. Journal of biomedical materials research. 1997;38:155-182.

18 Wu C-C, Yang K-C, Yang S-H, Lin M-H, Kuo T-F, Lin F-H. *In Vitro* Studies of Composite Bone Filler Based on Poly(Propylene Fumarate) and Biphasic α-Tricalcium Phosphate/Hydroxyapatite Ceramic Powder. Artificial Organs. 2012;36:418-428.

19 Lee K-W, Wang S, Lu L, Jabbari E, Currier BL, Yaszemski MJ. Fabrication and characterization of poly (propylene fumarate) scaffolds with controlled pore structures using 3-dimensional printing and injection molding. Tissue engineering. 2006;12:2801-2811.

20 Yaszemski MJ, Payne RG, Hayes WC, Langer RS, Aufdemorte TB, Mikos AG. The ingrowth of new bone tissue and initial mechanical properties of a degrading polymeric composite scaffold. Tissue engineering. 1995;1:41-52.

21 Hedberg EL, Shih CK, Lemoine JJ, Timmer MD, K Liebschner MA, Jansen JA, Mikos AG. *In vitro* degradation of porous poly (propylene fumarate)/poly (dl-lactic- co-glycolic acid) composite scaffolds. Biomaterials. 2005;26:3215-3225.

22 Tanaka S, Matsuzaka K, Sato D, Inoue T. Characteristics of newly formed bone during guided bone regeneration: analysis of cbfa-1, osteocalcin, and VEGF expression. Journal of Oral Implantology. 2007;33:321-326.

23 Kleinheinz J, Stratmann U, Joos U, Wiesmann H-P. VEGF-activated angiogenesis during bone regeneration. Journal of oral and maxillofacial surgery. 2005;63:1310-1316.

www.manaraa.com

24 Laschke MW, Harder Y, Amon M, Martin I, Farhadi J, Ring A, Torio-Padron N, Schramm R, Rücker M, Junker D. Angiogenesis in tissue engineering: breathing life into constructed tissue substitutes. Tissue engineering. 2006;12:2093-2104.

25 Villars F, Bordenave L, Bareille R, Amedee J. Effect of human endothelial cells on human bone marrow stromal cell phenotype: role of VEGF? Journal of cellular biochemistry. 2000;79:672-685.

26 Murphy W, Simmons C, Kaigler D, Mooney D. Bone regeneration via a mineral substrate and induced angiogenesis. Journal of dental research. 2004;83:204-210.

27 Deckers MM, van Bezooijen RL, van der Horst G, Hoogendam J, van der Bent C, Papapoulos SE, Löwik CW. Bone morphogenetic proteins stimulate angiogenesis through osteoblast-derived vascular endothelial growth factor A. Endocrinology. 2002;143:1545-1553.

28 Cheung LW, Leung KW, Wong CK, Wong RN, Wong AS. Ginsenoside-Rg_1 induces angiogenesis via non-genomic crosstalk of glucocorticoid receptor and fibroblast growth factor receptor-1. Cardiovascular research. 2011;89:419-425.

29 Leung KW, Cheng Y-K, Mak NK, Chan KK, David Fan T, Wong RN. Signaling pathway of ginsenoside-Rg_1 leading to nitric oxide production in endothelial cells. FEBS letters. 2006;580:3211-3216.

30 Leung KW, Pon YL, Wong RN, Wong AS. Ginsenoside-Rg_1 induces vascular endothelial growth factor expression through the glucocorticoid receptor-related phosphatidylinositol 3-kinase/Akt and β-catenin/T-cell factor-dependent pathway in human endothelial cells. Journal of Biological Chemistry. 2006;281:36280-36288.

31 Yang Y, Dorsey SM, Becker ML, Lin-Gibson S, Schumacher GE, Flaim GM, Kohn J, Simon Jr CG. X-ray imaging optimization of 3D tissue engineering scaffolds via combinatorial fabrication methods. Biomaterials. 2008;29:1901-1911.

32 Dunne N. Mechanical properties of bone cements. Orthopaedic bone cements. 2008:240-255.

33 Khaled S, Charpentier PA, Rizkalla AS. Synthesis and characterization of poly (methyl methacrylate)-based experimental bone cements reinforced with TiO_2–SrO nanotubes. Acta Biomaterialia. 2010;6:3178-3186.

34 Deb S, Abdulghani S, Behiri J. Radiopacity in bone cements using an organo-bismuth compound. Biomaterials. 2002;23:3387-3393.

35 Lewis G, Xu J, Madigan S, Towler MR. Influence of strontia on various properties of Surgical Simplex® P acrylic bone cement and experimental variants. Acta Biomaterialia. 2007;3:970-979.

www.manaraa.com

36 Semelka RC, Armao DM, Elias J, Huda W. Imaging strategies to reduce the risk of radiation in CT studies, including selective substitution with MRI. Journal of Magnetic Resonance Imaging. 2007;25:900-909.

37 Bhattacharyya D, Dutta N. A study of the immobilization of strontium over crystalline titania. Journal of materials science. 1995;30:2248-2250.

38 Kumaresan L, Mahalakshmi M, Palanichamy M, Murugesan V. Synthesis, characterization, and photocatalytic activity of Sr^{2+} doped TiO_2 nanoplates. Industrial & Engineering Chemistry Research. 2010;49:1480-1485.

39 Lucky RA, Charpentier PA. A One-Step Approach to the Synthesis of ZrO_2-Modified TiO_2 Nanotubes in Supercritical Carbon Dioxide. Advanced Materials. 2008;20:1755-1759.

40 Salarian M, Xu WZ, Wang Z, Sham T-K, Charpentier PA. Hydroxapatite-TiO_2-based Nanocomposites Synthesized in Supercritical CO_2 for Bone Tissue Engineering: Physical and Mechanical Properties. ACS Applied Materials & Interfaces. 2014.

41 Goto K, Tamura J, Shinzato S, Fujibayashi S, Hashimoto M, Kawashita M, Kokubo T, Nakamura T. Bioactive bone cements containing nano-sized titania particles for use as bone substitutes. Biomaterials. 2005;26:6496-6505.

42 Salarian M, Xu WZ, Biesinger MC, Charpentier PA. Synthesis and characterization of novel TiO_2-poly(propylene fumarate) nanocomposites for bone cementation. Journal of Materials Chemistry B. 2014;2:5145-5156.

43 Khaled S, Sui R, Charpentier PA, Rizkalla AS. Synthesis of TiO_2-PMMA nanocomposite: using methacrylic acid as a coupling agent. Langmuir. 2007;23:3988-3995.

44 Goto K, Hashimoto M, Fujibayashi S, Kokubo T, Nakamura T. New bioactive bone cement containing nano-sized titania particles. Key Engineering Materials. 2005;284:97-100.

45 Amirouche A, Mouzali M, Watts D. Radiopacity evaluation of Bis-GMA/TEGDMA/opaque mineral filler dental composites. Journal of applied polymer science. 2007;104:1632-1639.

46 Sui R, Rizkalla AS, Charpentier PA. Formation of titania nanofibers: A direct sol-gel route in supercritical CO_2. Langmuir. 2005;21:6150-6153.

47 Salarian M, Solati-Hashjin M, Shafiei SS, Salarian R, Nemati ZA. Template-directed hydrothermal synthesis of dandelion-like hydroxyapatite in the presence of cetyltrimethylammonium bromide and polyethylene glycol. Ceramics International. 2009;35:2563-2569.

www.manaraa.com

48 Kasper FK, Tanahashi K, Fisher JP, Mikos AG. Synthesis of poly (propylene fumarate). Nature protocols. 2009;4:518-525.

49 Farhangi N, Medina-Gonzalez Y, Chowdhury RR, Charpentier PA. Growing TiO_2 nanowires on the surface of graphene sheets in supercritical CO_2: characterization and photoefficiency. Nanotechnology. 2012;23:294005.

50 Lucky R, Charpentier P. A thermal study on the structural changes of bimetallic ZrO_2-modified TiO_2 nanotubes synthesized using supercritical CO_2. Nanotechnology. 2009;20:195601.

51 Lucky RA, Charpentier PA. N-doped ZrO_2/TiO_2 bimetallic materials synthesized in supercritical CO_2: morphology and photocatalytic activity. Applied catalysis B, Environmental. 2010;96:516-523.

52 Biesinger MC, Lau LW, Gerson AR, Smart RSC. Resolving surface chemical states in XPS analysis of first row transition metals, oxides and hydroxides: Sc, Ti, V, Cu and Zn. Applied Surface Science. 2010;257:887-898.

53 Wagner C, Naumkin A, Kraut-Vass A, Allison J, Powell C, Rumble Jr J. NIST X-ray Photoelectron Spectroscopy Database, NIST Standard Reference Database 20, Version 3.4 (Web Version). U S Department of Commerce. 2003.

54 Beamson G, Briggs D. High resolution XPS of organic polymers: the Scienta ESCA300 database: Wiley Chichester; 1992.

55 Wu X, Wang D, Yang S. Preparation and characterization of stearate-capped titanium dioxide nanoparticles. Journal of colloid and interface science. 2000;222:37-40.

56 Hojjati B, Charpentier PA. Synthesis and kinetics of graft polymerization of methyl methacrylate from the RAFT coordinated surface of nano-TiO_2. Journal of Polymer Science Part A: Polymer Chemistry. 2008;46:3926-3937.

57 Farhangi N, Chowdhury RR, Medina-Gonzalez Y, Ray MB, Charpentier PA. Visible light active Fe doped TiO_2 nanowires grown on graphene using supercritical CO_2. Applied Catalysis B: Environmental. 2011;110:25-32.

58 Dobson KD, McQuillan AJ. *In situ* infrared spectroscopic analysis of the adsorption of aliphatic carboxylic acids to TiO_2, ZrO_2, Al_2O_3, and Ta_2O_5 from aqueous solutions. Spectrochimica Acta Part A: Molecular and Biomolecular Spectroscopy. 1999;55:1395-1405.

59 Segerström S, Ruyter I. Effect of thermal cycling on flexural properties of carbon–graphite fiber-reinforced polymers. dental materials. 2009;25:845-851.

60 Vallo C, Abraham G, Cuadrado T, San Román J. Influence of cross-linked PMMA beads on the mechanical behavior of self-curing acrylic cements. Journal of Biomedical Materials Research Part B: Applied Biomaterials. 2004;70:407-416.

www.manaraa.com

61 Gojny F, Wichmann M, Köpke U, Fiedler B, Schulte K. Carbon nanotube-reinforced epoxy-composites: enhanced stiffness and fracture toughness at low nanotube content. Composites science and technology. 2004;64:2363-2371.

62 Nien Y-H, Lin S-w, Hsu Y-N. Preparation and characterization of acrylic bone cement with high drug release. Materials Science and Engineering: C. 2013;33:974-978.

63 Samimi R, Salarian M, Xu WZ, Lui EMK, Charpentier PA. Encapsulation of Acetyl Ginsenoside Rb1 within Monodisperse Poly(dl-lactide-co-glycolide) Microspheres Using a Microfluidic Device. Industrial & Engineering Chemistry Research. 2014;53:11333-11344.

64 Kempen DH, Lu L, Zhu X, Kim C, Jabbari E, Dhert WJ, Currier BL, Yaszemski MJ. Development of biodegradable poly (propylene fumarate)/poly (lactic-co-glycolic acid) blend microspheres. II. Controlled drug release and microsphere degradation. Journal of Biomedical Materials Research Part A. 2004;70:293-302.

65 Kempen DH, Lu L, Kim C, Zhu X, Dhert WJ, Currier BL, Yaszemski MJ. Controlled drug release from a novel injectable biodegradable microsphere/scaffold composite based on poly (propylene fumarate). Journal of Biomedical Materials Research Part A. 2006;77:103-111.

66 Marie P, Ammann P, Boivin G, Rey C. Mechanisms of action and therapeutic potential of strontium in bone. Calcified tissue international. 2001;69:121-129.

www.manaraa.com

Chapter 4

4 Encapsulation of ginsenoside Rg_1 within PPF Microspheres using Microfluidic Technique

Abstract

This study sought to encapsulate the pro-angiogenic mediator, ginsenoside Rg_1, into biodegradable poly(propylene fumarate) (PPF) microspheres to induce bone formation. We examine the fabrication of ginsenoside Rg_1-loaded PPF microspheres using both an emulsion method and a microfluidic device. These PPF microspheres were engineered with defined sizes, ranging from 3 μm to 52 μm and standard deviations less than 10% depending on the system flow rate. The morphology and size of the Rg_1-loaded PPF microspheres were characterized using SEM while FTIR was used to verify the formation of Rg_1-loaded PPF microspheres and the chemical stability of Rg_1 in the microspheres. X-ray diffraction (XRD) revealed that ginsenoside Rg_1 was uniformly distributed in the polymer matrix. Using synchrotron X-ray absorption spectroscopy, the interactions between the ginsenoside Rg_1 and PPF were studied on an atom-by-atom basis, showing how the ginsenoside Rg_1 could be loaded into the PPF microspheres. Release profiles were studied and quantified by UV-Vis spectrophotometry. The results showed that the microfluidic approach gave good physical properties (spherical and discrete) and high encapsulation efficiency of Rg_1-loaded PPF microspheres, 95.35 ± 0.82%. Kinetic analysis showed that the release of Rg_1 from PPF microspheres fabricated using the microfluidic method was slower than that from conventional method of the same average size giving a significantly smaller initial burst, is attributed to the uniform distribution of Rg_1 inside the particles generated using the microfluidic method. Moreover, on investigating the angiogenesis behavior of the PPF-based Rg_1 delivery systems, the released ginsenoside Rg_1 maintained its angiogenic effect *in vitro*. The obtained results suggest that the PPF microspheres developed in this study are promising to serve as

www.manaraa.com

vehicles for long-term controlled drug delivery leading to therapeutic angiogenesis in bone tissue engineering strategies.

4.1 Introduction

Biodegradable polymers are attractive as scaffold materials for bone tissue engineering applications. Polymer scaffolds must possess a number of specific properties in order to be successful, such as biocompatibility, biodegradability, highly porous and well-interconnected structure sufficient for cellular infiltration, appropriate surface chemistry, and mechanical properties similar to the surrounding host tissue.[1, 2] The scaffold must also support cellular migration and proliferation to allow for the infiltration of osteoblasts and the formation of bone.[3, 4]

One promising material for treating bone defects and non-unions caused by disease trauma, or abnormal development is poly(propylene fumarate) (PPF) (Figure 4.1). PPF is of interest as an injectable material for making preformed scaffolds for bone tissue engineering applications.[5, 6] It is an unsaturated linear polyester that can be cross-linked through its carbon-carbon double bonds and can be degraded by simple hydrolysis of the ester bonds into nontoxic products.[7, 8] An advantage of PPF over many other biodegradable synthetic polymers is that it can be utilized as an injectable system, allowing for direct application into a defect site and cross-linking *in situ*.[9, 10]

In addition, development of endothelial cell-based microvascularization and microcirculation is of critical importance for bone regeneration.[11] Angiogenesis is the formation of capillaries as outgrowths from preexisting vasculature; it is a complex multi-step process comprising activation, chemotactic invasion and migration, morphological alteration, proliferation, and capillary tube formation of endothelial cells from preexisting blood vessels. [11, 12] The influence of angiogenesis on osteogenesis has been previously shown. Particularly, the vasculature provides for mass transport requirements of the tissue, and delivers circulating stem cells participating in bone formation. It also facilitates cross-talk between endothelial cells and pre-osteoblasts to direct their differentiation.[13]

www.manaraa.com

Among the angiogenic regulators, vascular endothelial growth factor (VEGF) and nitric oxide (NO) are the critical angiogenic stimulators that work closely with one another in the modulation of angiogenesis. Also, among other angiogenic mediators and growth factors, ginsenoside Rg_1 (Figure 4.1) has been shown to be a highly stable pro-angiogenic compound which stimulates angiogenesis through enhancing the production of NO and up-regulating the VEGF expression.[14, 15] Interestingly, ginsenoside Rg_1-induced angiogenesis was found to be comparable to or even better than bFGF-induced angiogenesis *in vivo*. So, we hypothesized that a synthetic system based on PPF capable of delivering an angiogenic agent, ginsenoside Rg_1, in a localized and sustained manner would direct simultaneous regeneration of bone and vascular tissue.

To incorporate the pro-angiogenic mediator, ginsenoside Rg_1, into the scaffolds, it can be encapsulated in biodegradable microspheres.[16-18] These polymeric microspheres can be used as a local delivery vehicle capable of preserving the injectability of the PPF composite. [18] Controlled local delivery potentially optimizes local therapeutic responses, which reduces the incidents of peak-related side effects and systemic toxic effects.[19] Furthermore, these microspheres protect the pro-angiogenic mediator during the crosslinking reaction of the PPF, thereby preserving the bioactivity of the ginsenoside Rg_1. They also offer more variables for the attenuation of the release kinetics of the mediator from the scaffold adding the advantage of controlled release over a prolonged period of time; therefore, there is no requirement for multiple doses during prolonged therapy.[19] Besides, the microspheres have the potential capacity to covalently bind to the PPF scaffold through carbon-carbon double bonds along the PPF backbone, thus achieving better immobilization of the microspheres and improving the mechanical properties of the microsphere/scaffold composite.[18, 20] Kempen et al. developed PPF microspheres encapsulating the model drug Texas red dextran (TRD) and demonstrated the effects of various processing parameters on the release kinetics of the model drug from these microspheres prepared using a double emulsion-solvent extraction technique.[20] However, monodispersity of PPF microspheres and its effect on controlling the drug release kinetics, reproducibility, and bioavailability was not investigated in their study.

www.manaraa.com

Recently, the microfluidic method has attracted considerable attention owing to the flexibility to generate microdroplets with controlled morphology and size.[21, 22] Conventional techniques such as double emulsion creates microspheres with broad size distributions due to inhomogeneous forces involved, which results in an unpredictable degradation rate and kinetics of drug release, limiting their clinical application.[23] The microfluidic approach has been shown to produce microspheres with high-drug loading and encapsulation efficiency, and sustained release behavior due to outstanding monodispersity.[23, 24] To the best of our knowledge, no previous study has addressed the fabrication of PPF microspheres via the microfluidics method and fundamental differences between the drug delivery behavior of PPF microparticles produced via traditional method to generate emulsions and those prepared via microfluidics. In addition, very little is known about the interaction between the Rg_1 molecules and the PPF-based carriers. For the first time this paper reports the use of C K-edge XANES spectroscopy, which is a type on syncotron radiation, to identify how ginsenoside Rg_1 molecules interact with PPF microspheres. The success of the procedure showed a high Rg_1 carrying ability of PPF microspheres and excellent sustained release behaviors could lead to new biomedical applications. The hypothesis underlying this study is that delivery of ginsenoside Rg_1, pro-angiogenic mediator, from PPF microspheres can sufficiently enhance angiogenesis to enable bone regeneration in osseous defects. Hence, we addressed the following questions: (1) How does alteration in the PPF microparticle preparation in terms of spherical shape, narrow size distribution, and high encapsulation efficiency, influence the kinetics of drug release? (2) How is the mechanism and kinetics of ginsenoside Rg_1 released from monodisperse PPF microspheres?, and (3) How does the pro-angiogenic mediator, ginsenoside Rg_1, maintain its angiogenic effect before encapsulation into the PPF microspheres and after release from the microparticles?

www.manaraa.com

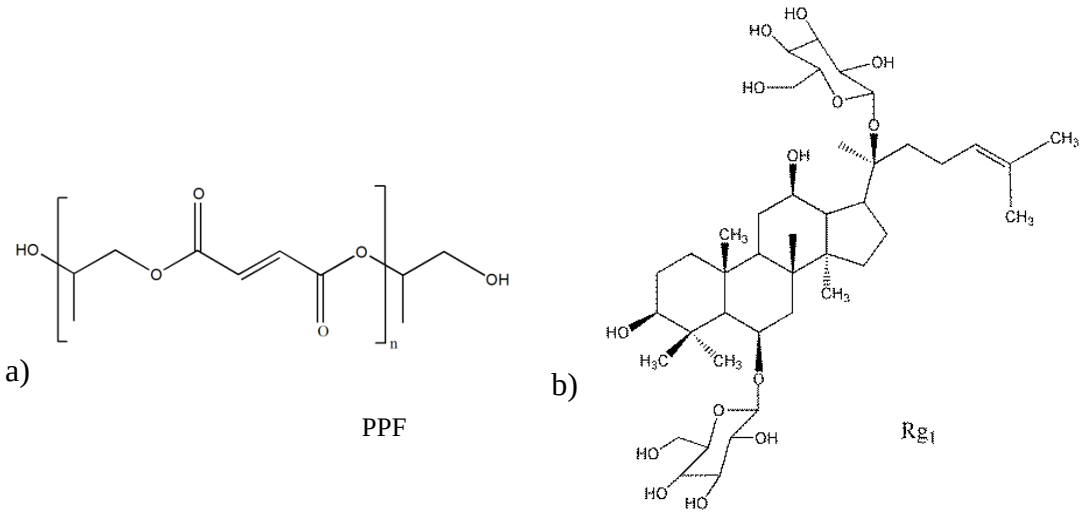

Figure 4.1. Chemical structure of (a) ginsenoside Rg_1 and (b) PPF

4.2 Experimental details

4.2.1 Materials

Polymer synthesis: Diethyl fumarate (98%), propylene glycol (1,2-Propanediol) (≥99.5%), zinc chloride anhydrous ($ZnCl_2$, ≥99.995%), hydroquinone (99%), hydrochloric acid (37%), anhydrous magnesium sulfate (99.0%), anhydrous diethyl ether (≥99.0%), diethyl ether anhydrous (≥99.0%), methylene chloride anhydrous (DCM, ≥99.8%) were purchased from Sigma-Aldrich Canada and used as received.

Microsphere preparation, microfluidic chip fabrication, *in vitro* release study, and bioassays: Ginsenoside Rg_1 was donated by Dr. Edmund Lui, Department of Physiology and Pharmacology, the University of Western Ontario, London, Canada. Poly(vinyl alcohol) (PVA) (87–89% hydrolyzed, Mw=13,000–23,000), methylene chloride anhydrous (DCM, ≥99.8%), HPLC grade methanol (≥99.9%), and 0.1 mol/L phosphate-buffered saline solution (PBS, pH 7.4) were purchased from Sigma-Aldrich, and used as received. Poly(dimethylsiloxane) (PDMS; Sylgard 184) was obtained from Dow Corning (Midland, USA). Double distilled water used throughout the experiments was generated from a Milli-Q water purification system (18.2 MΩ·cm resistivity, Barnstead EasyPureII,

www.manaraa.com

Thermo Scientific, USA). Glass syringes (1000 series, Hamilton Co., NV) and syringe pumps (KD scientific pump, Inc. Legato 2200, 1100) were used for sending liquids into microchannels. Human umbilical vein cell lines (EA.hy926) were provided by Dr. Jeff Dixon, Department of Physiology and Pharmacology, the University of Western Ontario, London, Canada. Growth factor-reduced Matrigel was purchased from VWR. Cell culture medium and reagents were purchased from Gibco laboratories [25].

4.2.2 Characterization of PPF microspheres encapsulating ginsenoside Rg_1

The surface morphology of microspheres was analyzed using scanning electron microscopy (SEM) (model: Hitachi S-4500). Samples for SEM imaging were prepared by applying the powder directly to a carbon adhesive tape. Samples were sputter-coated for 1 min with gold to reduce charging problems. The particle size distribution was characterized by measuring the particle diameter in the SEM images using version 1.37 Image J software, which is a Java based image processing program developed at the National Institute of Health for analyzing images. The Image J software calculated the mean diameters and standard deviations of the microspheres. FTIR-ATR (Nicolet 6700, Thermo Scientific) was used to investigate the chemical structure of the PPF, Rg_1, and Rg_1-loaded PPF microspheres. The spectra were recorded in the range of 500-4000 cm^{-1} with a resolution of 4 cm^{-1} over 32 scans. To evaluate the crystallinity of Rg_1 after encapsulation, XRD data for Rg_1, placebo PPF microspheres, and Rg_1-loaded PPF microspheres were obtained using an Inel CPS Powder Diffractometer. The instrument was equipped with a Cu-X-ray radiation Tube, an Inel XRG3000 generator, and an Inel CPS 120 detector. The CPS is a curved detector and performed the simultaneous collection of X-rays diffracted by the samples over 120 °2θ. Powder samples were ground to a uniform composition and placed on a flat aluminum sample holder. To investigate the interaction between the Rg_1 and PPF, C K-edge X-ray absorption near edge structures (XANES) of the Rg_1 molecules, PPF microspheres and Rg_1-loaded PPF microspheres were measured at the high-resolution spherical grating monochromator (SGM) beamline at the Canadian Light Source (CLS), the University of Saskatchewan. The samples were mounted on indium foils with an angle of 20° facing toward the photon

www.manaraa.com

beam. XANES spectra were recorded in partial fluorescence yield (PFY) that was measured by detecting the X-ray fluorescence photons emitted from the element of interest (e.g.: carbon). All XANES spectra were normalized to the incident photon flux (I_0), which was measured using a silicon wafer as the photodiode.

4.2.3 Preparation of materials

4.2.3.1 *Synthesis of poly(propylene fumarate) (PPF)*

PPF was synthesized using a two-step transesterification method explained in Salarian et al.[26] In a typical experiment, diethyl fumarate (31.56 g, 183 mmol) and propylene glycol (41.38 g, 549 mmol) were reacted in an inert atmosphere. Additionally, $ZnCl_2$ (0.250 g, 1.83 mmol) and hydroquinone (0.0403 g, 0.366 mmol) were added as a catalyst and a crosslinking inhibitor, respectively. The first step of the reaction occurred with a gradual increase in temperature from 110 to 150 ºC in an increment of 10 ºC every 15 min resulting in the production of bis(hydroxypropyl) fumarate intermediate and ethanol, which was collected as a distillate. This step was terminated when ~ 90% of the theoretical yield of ethanol was collected. The second step of the reaction, transesterification of the bis(hydroxypropyl) fumarate intermediate to produce PPF, was conducted under reduced pressure (<1 mm Hg) with a gradual increase in temperature from 100 to 150 ºC in an increment of 10 ºC every 30 min producing propylene glycol as a byproduct. The reaction proceeded until the desired molecular weight of PPF was obtained. The polymer product was then dissolved in methylene chloride followed by several acid washes with a 5% v/v solution of 1 N HCl to remove the $ZnCl_2$ catalyst, two washes with distilled water, and two washes with brine. Sodium sulfate was then used to dry the organic polymer phase. After drying with magnesium sulfate, the polymer was concentrated by rotoevaporation and then precipitated in ethyl ether to remove the hydroquinone inhibitor. The ethyl ether was decanted and the purified polymer was vacuum dried to remove any residual solvent.

4.2.3.2 *Preparation of PPF microspheres encapsulating ginsenoside Rg_1 using W/O/W double emulsion method*

A water-in-oil-in-water (W/O/W) double emulsion-solvent extraction technique, which

www.manaraa.com

includes encapsulation of water-soluble therapeutic agents for targetable drug delivery,[16] was employed to prepare PPF microspheres encapsulating ginsenoside Rg_1, as illustrated in Figure 4.2. Briefly, 100 mg of PPF was dissolved in 10 mL of dichloromethane, and 10 mg of Rg_1 was dissolved in 5 mL of solution [V(methanol):V(double distilled water) = 4:6]. The ginsenoside Rg_1 solution was added to the PPF solution to create the first emulsion W/O. After stirring for 2h using a magnetic stirring bar at 1200 rpm, the entire mixture was re-emulsified in 20 mL of an aqueous PVA solution (4% w/v) to create the W/O/W double emulsion. After stirring for 0.5h using a magnetic stirrer bar at 400 rpm, the emulsion was poured into a beaker containing 40 mL of an aqueous PVA solution (0.5% w/v) and stirred for 2h. This solution was then added to double-distilled water and stirred for another 3h, at room temperature. Finally, the emulsion was ultrasonically agitated for 10 min at 30 °C. After removing DMC by evaporation, the formed microspheres were centrifuged at 5000 rpm for 5 min, followed by washing with distilled water twice to remove PVA and freeze-drying to remove water. The Rg_1-loaded microspheres were stored at −20°C.

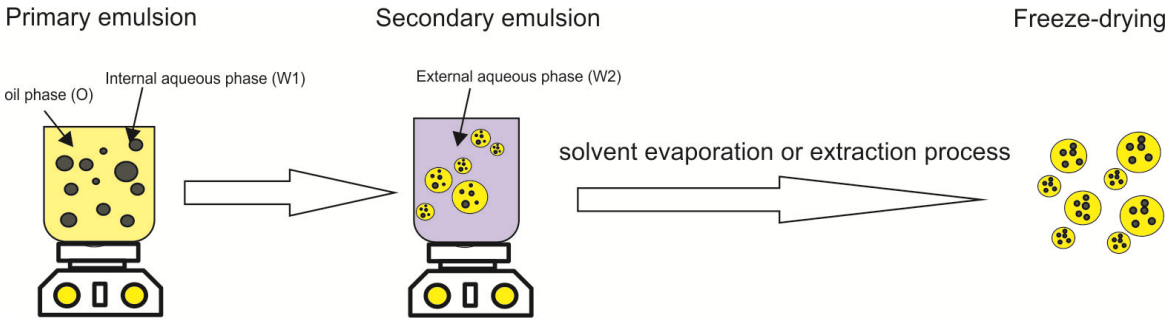

Figure 4.2. Schematic of the double emulsion method.

4.2.3.3 *Fabrication of microfluidic device*

Microfluidic chips with typical channel dimensions of 100 µm in depth and 200 µm in width were fabricated using conventional soft lithography techniques in collaboration with Dr. Jun Yang, Mechanical and Material Engineering Department, Western University, Canada.[27] The microfluidic chip was molded by a mixture of PDMS elastomer base/curing agent in 10:1 ratio from SU-8 mold, and bonded to a flat PDMS

www.manaraa.com

substrate under plasma treatment for 35 seconds in a PX-250 plasma chamber (March Instruments, Concord, MA), and then immediately placed in contact to bond the surfaces irreversibly. The devices were then bonded using a homemade UV-ozone generator. Since there is a favorable wettability between the disperse phase and the inner surface of the device, surface treatment is applied to the channels to make the PDMS surface hydrophilic.[23] The plasma-treated chip was immediately filled with a 4% PVA aqueous solution (continuous phase) and then placed at room temperature for 30 min. Then, the channels were emptied by a vacuum pump and the PDMS chip was placed in a 60 °C oven for 2h to dry and immobilize the PVA. The above procedure was repeated, resulting in a two layer coating. Finally, the coating was thermally immobilized in an oven at 100 °C for 20 min, and then the chip was allowed to cool to room temperature inside the oven.[28]

4.2.3.4 *Preparation of PPF microspheres encapsulating ginsenoside Rg_1 using droplet microfluidic method*

The schematic drawing of the microfluidic device is shown in Figure 4.3. The disperse phase was prepared by emulsifying the ginsenoside Rg_1 solution (2 mg/ml or 10 mg of Rg_1 in 5 ml of solution of methanol/double distilled water (2:3 v/v)) in PPF organic solvent solution (10 mg/ml or 100 mg of PPF in 10 ml of DCM), that flowed into inlet 1. The continuous phase, an aqueous solution of PVA (4% w/v), flowed into inlet 2. Both liquid phases were loaded into glass syringes, and digitally controlled syringe pumps delivered to the microfluidic device using Teflon tubing (1.6 mm OD, 0.6 mm ID). Following the previous studies in our group, the flow rate of the continuous phase ranged between 0.05-0.2 ml/min while the flow rate of the dispersed phase was constant and held at 0.01 ml/min.[28] The outlet of the device was a Teflon tubing submerged into a 10 ml beaker containing 0.5% PVA aqueous solution to collect the monodisperse droplets. Next, the solvent within the droplets was removed by evaporation at room temperature, and hardened microparticles were then centrifuged (5000 rpm, 5 min), washed twice with distilled water to remove excess PVA, freeze-dried, and stored at -20 ºC.

www.manaraa.com

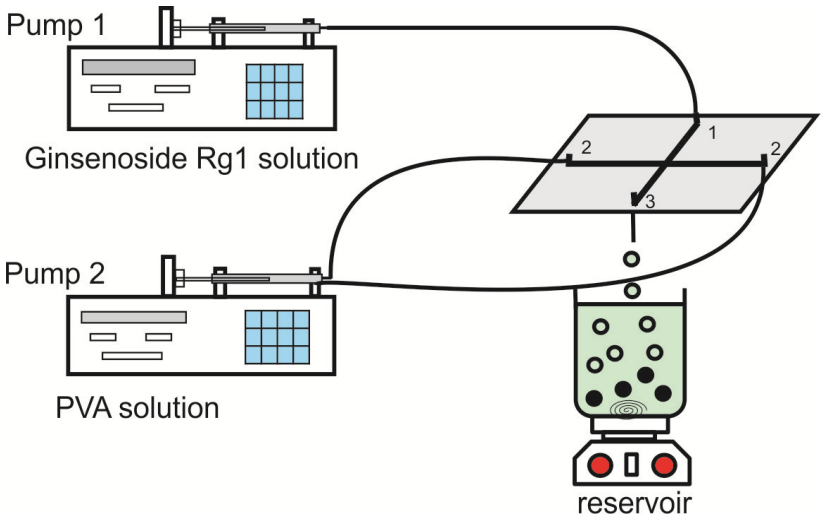

Figure 4.3. Schematic of the microfluidic system.

(1) disperse phase inlet (ginsenoside Rg_1 solution emulsified in PPF in DCM solution), (2) continuous phase inlet (4% w/v PVA aqueous solution), and (3) outlet.

4.2.4 Determination of encapsulation efficiency (EE) of Rg_1-loaded PPF microspheres

Encapsulation efficiency (EE) for Rg_1-loaded PPF microspheres prepared using the conventional double emulsion and microfluidic methods was determined by dissolving dried Rg_1-loaded microspheres in NaOH solution. Specifically, 5mg microspheres were dissolved in 1 ml of a 1N NaOH solution.[20] The Rg_1 concentration was determined by absorption at the λmax value of 189 nm in a UV-Vis spectrophotometer (Shimadzu UV-Vis 3600). A calibration curve was constructed from Rg_1 solutions with known concentrations. Encapsulation efficiency of Rg_1 in the PPF microspheres was determined by normalizing the amount of Rg_1 actually entrapped to the starting amount,[18] the ratio between the actual Rg_1 content of the microspheres and the amount initially added to them.[29] Each experiment was carried out in triplicate. The EE of drug was defined as:

$$EE\% = \frac{\text{weight of } Rg_1 \text{ recovered in PPF microspheres which is measured by UV spectrometer}}{\text{weight of } Rg_1 \text{ initially added to the microspheres}} \times 100$$

www.manaraa.com

4.2.5 *In vitro* release of ginsenoside Rg_1

For the release study, 5 mg of Rg_1-loaded PPF microspheres was dispersed into 10 mL of pH 7.4 phosphate-buffered saline (PBS) in a small centrifuge tube. The tubes were sealed and placed in a shaking water bath with a rotation rate of 100 rpm at 37 °C. At specific time intervals, the tubes were centrifuged at 2500 rpm for 5 min, and 2 ml of the supernatant was collected and replaced by fresh PBS. The supernatant was stored at -20 °C. After all the samples were collected, the absorption at 189 nm wavelength was measured using a UV-Vis spectrophotometer (Shimadzu UV-Vis 3600) to determine the amount of released Rg_1. Cumulative release of Rg_1 profiles were acquired with the volume loss correction and plotted against time. All the experiments were repeated in triplicate for each time interval. Collected extracts were also used for the following bioassay studies.

4.2.6 Angiogenic activity of ginsenoside Rg_1 before encapsulation into and after release from the PPF microspheres

Tube formation bioassays were performed using the EA.hy926 cell line derived from the fusion of human umbilical vein endothelial cells (HUVEC) with the A549 human pulmonary adenocarcinoma cell line. The HUVEC cell line has been shown to attach, migrate, and form tubular structure after seeding on a Matrigel substrate.[30, 31] Cell lines were cultured in Dulbecco's modified Eagle medium (DMEM) supplemented with ECGS (20 mg/ml), 10% fetal buvine serum (FBS), 1% antibiotic, and 1 ml (5X) per 50 ml of medium Hat media supplement. The cells were grown at 37 °C in humidified air with 5% CO_2 incubator. When the cell cultures were 80%-90% confluent, cells were harvested following trypsin treatment, and the released cells were resuspended to the cell density required for tube formation assay. To examine the angiogenic activity of ginsenoside Rg_1 *in vitro*, 4.5×10^4 cells/well of EA.hy926 cell line were seeded in a growth factor-reduced Matrigel-coated 96-well tissue culture plate loaded with medium. Various concentrations of ginsenoside Rg_1 were examined before encapsulation into the PPF microspheres and after release from the microparticles. After incubation for eighteen hours, images from a total of five microscopic fields per well were captured by an inverted microscope (Nikon TMS, Japan) using a 40x objective. Tube formations were

www.manaraa.com

analyzed by Motic Image Plus 2.0 software (Motic Instruments Inc., Richmond, Canada). The angiogenic effect was estimated by counting the branch points of the formed tubes, and then the average numbers of branch points were calculated. Each experiment was repeated at least three times, with each experiment yielding essentially identical results.

4.3 Results and Discussion

4.3.1 Surface morphology and particle size analysis of the Rg_1-loaded PPF microspheres

SEM images of the PPF microspheres encapsulating ginsenoside Rg_1 prepared using both a conventional solvent evaporation/extraction method based on the W/O/W double emulsion method and a microfluidic approach are displayed in Figure 4.4. The size distribution of the microspheres were analyzed using Image J software and are displayed in Figure 4.5. The results show that polydisperse microspheres with an average size of 13.5 μm in diameter and a standard deviation of 11.11 μm were obtained using the conventional double emulsion method. SEM and Image J size distribution images of these microspheres highlight that these particles have a broad size distribution of 2-45 μm, evident in Figure 4.4a, b. Figure 4.4c, d represent SEM images of PPF microcapsules prepared using the droplet microfluidic method when the flow rate for continuous phase and disperse phase were set at 0.1 and 0.01 ml/min, respectively. These observations demonstrate that by using the microfluidic device, spherical and discrete microspheres with an average diameter of 52 μm and a standard deviation of 7 μm are formed. In addition, the microfluidic approach gave much more uniform microspheres (50-65 μm) compared to the conventional double emulsion method. The size of these microspheres renders them suitable for mixing the prefabricated components in a syringe and fabrication of microsphere/scaffold composites, as microsphere with the diameter ranged from 1 to 110 are considered to be ideal for effortless injection of the composite through a small needle (14-gauge needle) indicating very good handling properties.[18] The size of the particles could be regulated by changing the flow rates of the two continuous and disperse phases. When the flow rates of 0.2 and 0.01 ml/min were chosen for the continuous phase and disperse phase, respectively, microparticles with an average diameters of about 3 μm and standard deviation of 1.78 μm revealing the narrower size

www.manaraa.com

distribution of 1-10 µm are fabricated using the same microfluidic device. Lowering the flow rate of the continuous phase to the 0.05 ml/min, the system could not produce any droplets and microspheres. Our experimental results illustrate that the size of the microparticles obtained using the microfluidic method are tunable by changing the flow rate; however, only a narrow experimental window enabled microsphere formation.

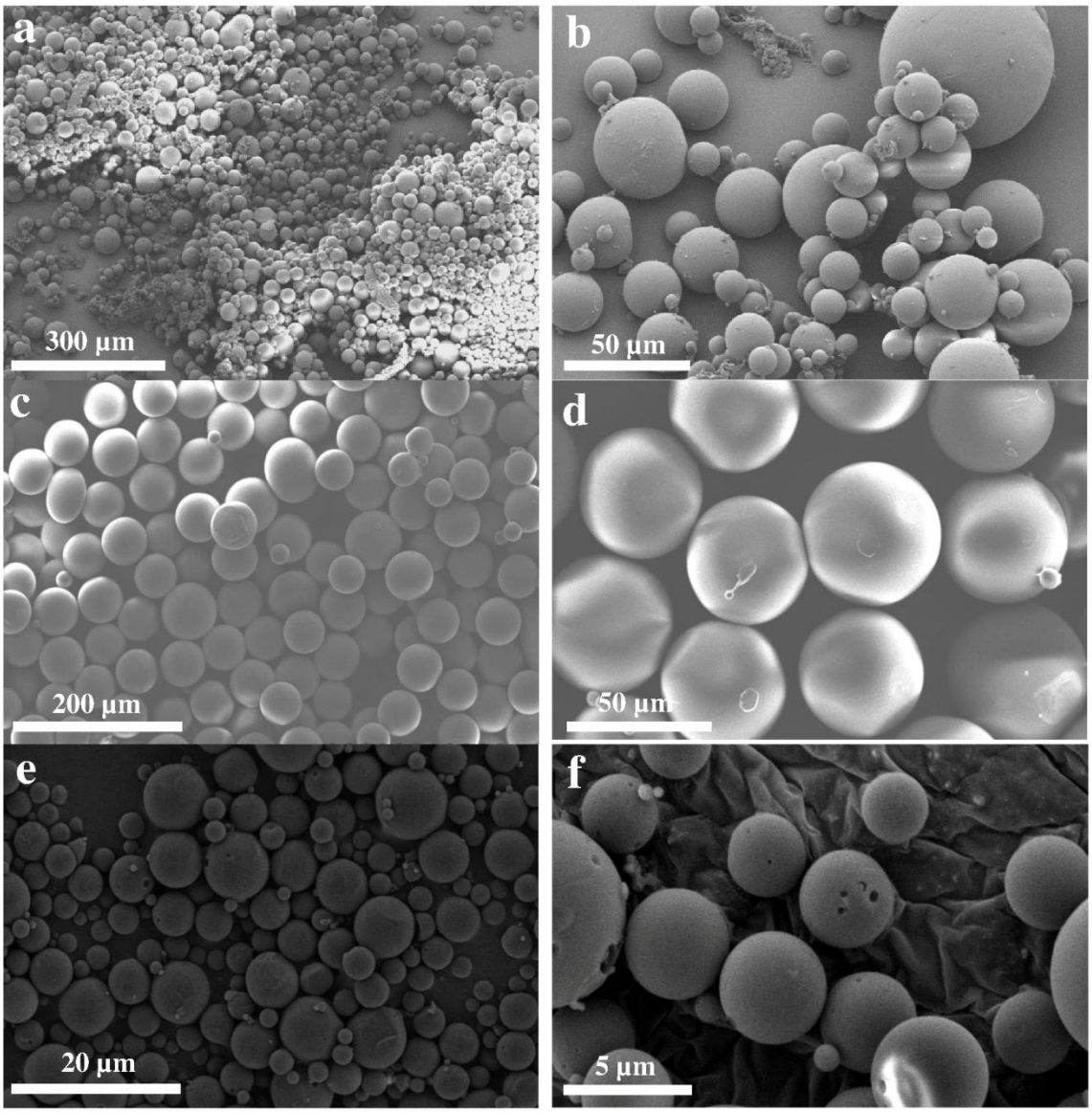

Figure 4.4. SEM images of Rg_1-loaded PPF microspheres from (a, b) double emulsion method and (c, d) microfluidic method where the continuous phase flow rate and disperse phase flow rate was 0.1 and 0.01 ml/min, respectively, and (e, f) microfluidic method

www.manaraa.com

where the continuous phase flow rate and disperse phase flow rate was 0.2 and 0.01 ml/min, respectively.

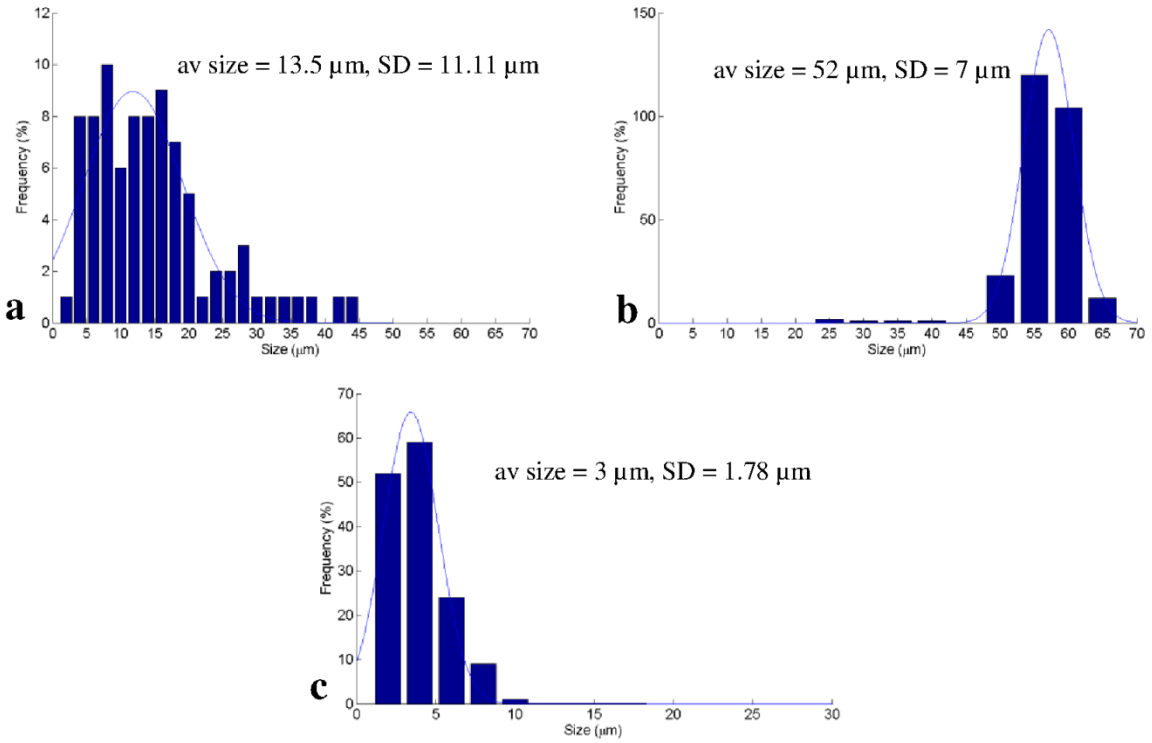

Figure 4.5. Image J number of size distributions for Rg_1-loaded PPF microspheres. prepared using (a) a double emulsion method, (b) microfluidic method where the continuous phase flow rate and disperse phase flow rate was 0.1 and 0.01 ml/min, respectively, and (c) microfluidic method where the continuous phase flow rate and disperse phase flow rate was 0.2 and 0.01 ml/min, respectively.

4.3.2 Encapsulation efficiency of Rg_1 in the PPF microspheres

The encapsulation efficiencies of the ginsenoside Rg_1 in the PPF microspheres fabricated using the conventional double emulsion method and microfluidic technique was determined as explained in section 4.2.4. EE of Rg_1 in PPF microspheres fabricated using the microfluidics was quite satisfactory in the range of 73.48 ± 2.31% and 95.35 ± 0.82%, exhibiting a 29.76% increase with increasing the average size of the microspheres. Rg_1-loaded PPF microspheres prepared by the conventional method had a lower EE (78.48 ± 1.64%). In explanation, the entrapment efficiency is affected by the volume of the internal aqueous phase containing ginsenoside Rg_1, vortex speed, internal PVA phase,

www.manaraa.com

and polymer viscosity.[19] However, it seems that the higher entrapment efficiency achieved for the PPF microspheres obtained from the microfluidic approach compared to that from the double emulsion method is due to the more uniform structure. In addition, the mechanism of polymer precipitation is different for Rg_1 encapsulation within the PPF microparticles produced using the microfluidic and double emulsion methods. Fast polymer precipitation on the surface of the dispersed phase can prevent drug loss into the continuous phase and increase the encapsulation efficiency, as less drug diffuses into the continuous phase.[32] The encapsulation efficiency of PPF microspheres prepared using the microfluidics method increases with size since a lower ratio of disperse phase flow rate to continuous phase flow rate was used for the production of larger monodisperse particles, which may result in the fast solidification of microspheres and subsequently higher encapsulation efficiency.[28] Thus, the microsphere size shows a direct effect on the drug release, bioavailability, and the encapsulation efficiency.[23] Encapsulation efficiency is an important factor in drug delivery, especially for valuable and expensive bioactive compounds.[24] The microfluidic method, when the flow rate for the continuous phase and disperse phase were 0.1 and 0.01 ml/min, respectively generated monodisperse Rg_1-loaded PPF microspheres with the narrow size distribution (Figure 4.5b). The encapsulation efficiency of 95.35 ± 0.82% was selected for further analyses as explained in more detail below.

4.3.3 Fourier transform infrared (FTIR) spectroscopy of Rg_1, PPF, and Rg_1-loaded PPF microspheres

To investigate the presence and chemical stability of PPF in the ginsenoside Rg_1-loaded PPF microspheres, the FTIR spectra of Rg_1, pure PPF, and Rg_1-loaded PPF microspheres were measured and are compared in Figure 4.6. In the FTIR spectrum of Rg_1 (Figure 4.6a), three major peaks appear at 3332, 1643, and 1011 cm^{-1}, attributable to O-H, C=C, and C-O stretching bands, respectively. The FTIR spectrum of PPF (Figure 4.6b) exhibits several major characteristic peaks at 1713, 1645, 1250, and 1147 cm^{-1}, attributed to the C=O stretching, C=C stretching, asymmetric C-O-C stretching, and symmetric C-O-C stretching bands, respectively.[8, 25] After ginsenoside Rg_1 was loaded into the PPF, all the PPF peaks are observed in the spectrum of Rg_1-loaded PPF microspheres (Figure

www.manaraa.com

4.6c), confirming the structural stability of PPF during the formation of microspheres. The peaks of ginsenoside Rg_1 are not evident in the spectrum of Rg_1-loaded PPF microspheres, except a weak broad peak at 3332 cm^{-1}, which is attributed to excellent Rg_1 dispersion in the PPF matrix and the resulting low concentration of ginsenoside Rg_1 on the PPF microsphere surface.

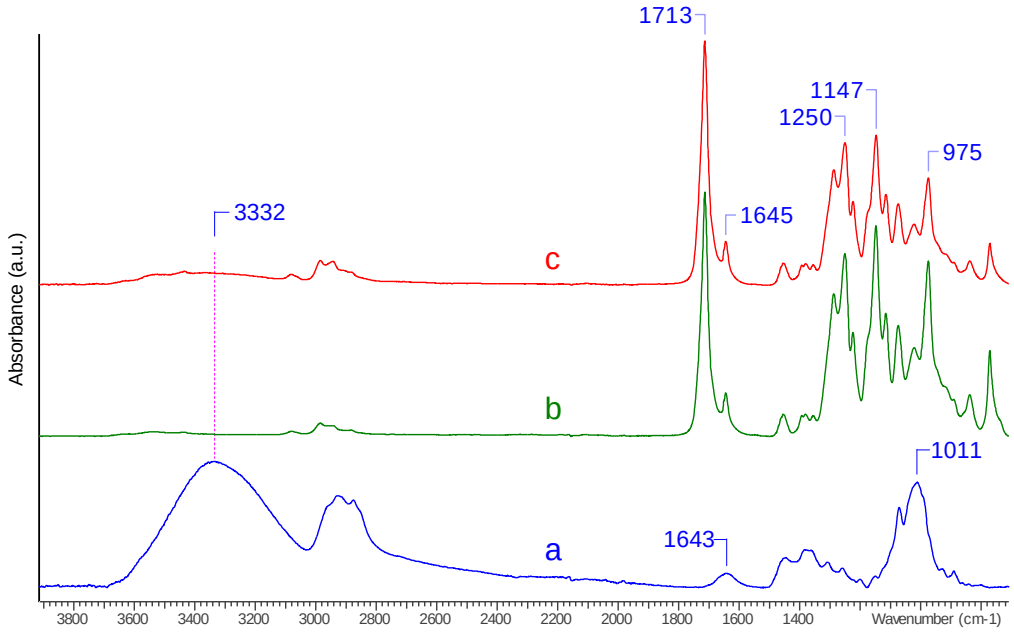

Figure 4.6. FTIR spectra of (a) ginsenoside Rg_1, (b) PPF, and (c) Rg_1-loaded PPF microspheres prepared using microfluidic method.

4.3.4 X-ray diffraction analysis of Rg_1, placebo PPF microspheres, and Rg_1-loaded PPF microspheres

XRD was used to study the physical state of the encapsulated Rg_1 in the PPF microspheres. As evident in the XRD pattern of Rg_1-loaded PPF microspheres fabricated using the microfluidic technique (Figure 4.7d), the crystalline peak at $2\theta = 5°$ indicates the semicrystalline nature of Rg_1 disappeared after encapsulation within the PPF microspheres, which confirms the amorphous state of Rg_1 in the PPF microspheres.[28] This also indicates that Rg_1 is distributed uniformly in the polymer matrix, confirming the FTIR results. Therefore, XRD analysis of the microspheres confirmed that ginsenoside

www.manaraa.com

Rg_1 is dispersed molecularly into the PPF matrix, and that no crystals are present in the Rg_1-loaded matrices.[33]

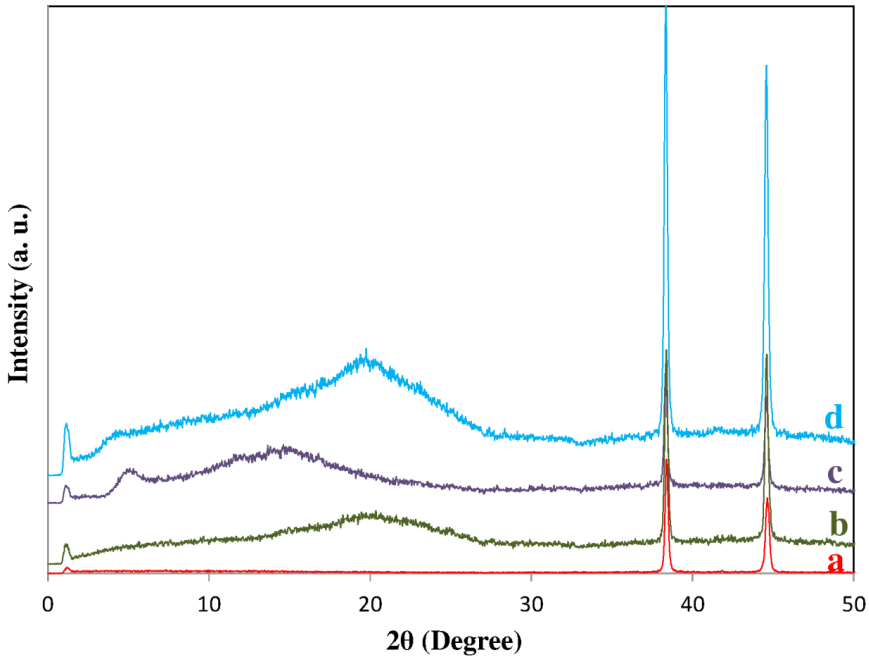

Figure 4.7. XRD patterns of (a) background, (b) placebo PPF microspheres prepared using microfluidic method, (c) ginsenoside Rg_1, and (d) Rg_1-loaded PPF microspheres prepared using microfluidic method.

4.3.5 XANES spectroscopy of Rg_1, PPF, and Rg_1-loaded PPF microspheres

XANES spectroscopy provides additional information about the structure and bonding associated with the absorbing atoms and their immediate surroundings.[34] Thus, we can probe the interaction between the drug carriers and drug molecules by tracking the changes of the electronic structures (XANES spectra) of the drug carriers before and after drug loading.[35] Figure 4.8a displays the C K-edge XANES spectra of the PPF microspheres with/without Rg_1 prepared using the microfluidic technique as well as pure Rg_1 for comparison. The spectrum of the pure PPF microspheres (green curve) is characterized by features at 285.6 ("*a*"), 290.1 ("*d*"), and 294.5 ("*e*") eV. Feature "*a*" and "*e*" are attributed to the C=C π^* and σ^* transitions, while feature "*d*" is assigned to the C=O π^* transition.[36, 37] The spectrum of the pure Rg_1 (blue curve) is a bit more

www.manaraa.com

complicated showing features at 286.9 ("*b*"), 289.1 ("*c*"), 290.1 ("*d*"), and 294.5 ("*e*") eV. Feature "*b*" is proposed to come from the C-O-C bond or C-OH π^* transition.[38] Feature "*d*" is attributed to the C-H* resonance, while the shoulder "*c*" at lower energy is assigned to the C-H* resonance of the carbon not bonded to oxygen.[36] Feature "*e*" corresponds to the C-C σ^* and C-O σ^* resonances.[36] Comparing the XANES spectra of the PPF microspheres with/without Rg_1 molecules showed that in the spectrum of the Rg_1-loaded PPF microspheres (red curve), i) the intensity of feature "*a*" drops off by about 25% compared to that of pure PPF microspheres, ii) feature "*a*" becomes broadened, and iii) a weak shoulder shows up at the lower energy side of feature "*d*". The broadening of feature "*a*" and presence of shoulder "*c*" in the spectrum of the Rg_1-loaded PPF microspheres are due to the contribution from Rg_1 molecules (feature "*b*" and "*c*"), which indicates that Rg_1 molecules were successfully loaded into the PPF microspheres. The decrease of the intensity of feature "*a*" relative to the total edge jump could be due to: i) Rg_1 molecules contributed to the total edge jump and ii) the decrease of the number of carbon-carbon double bonds in the PPF polymer chain after Rg_1 loading. If the Rg_1 molecules were physically loaded or sealed in the PPF microspheres without chemical interaction between each other, the Rg_1 and PPF both contributed to the total edge jump at the C K-edge, and the weight ratio between Rg_1 and PPF would be about 1:3 that resulted in the dropping of the "*a*" intensity by 25%. Figure 4.8b shows the linear combination fitting result of the Rg_1-loaded PPF microspheres (the weight ratio of Rg_1 and PPF is 1:3). The fitting spectrum (black curve) matches well with the experimental one (red curve) except the intensities of feature "*a*" and "*b*". As shown in the inset of Figure 4.8b, the intensity of feature "*a*" in the fitting curve is a bit stronger than that in the experimental one, while feature "*b*" is weaker, which might be due to chemical interaction between the Rg_1 molecules and PPF microspheres. Here we proposed that during the Rg_1 loading process, some of the carbon-carbon double bonds in the PPF broke to form carbon-carbon single bonds, which interacted with the Rg_1 molecules via C-O-C and C-C bonds. After the Rg_1 loading, the decrease of the carbon-carbon double bonds in the PPF and the presence of the C-O-C bond between the Rg_1 and PPF lead to the dropping of feature "*a*" and the rising of feature "*b*", respectively.

www.manaraa.com

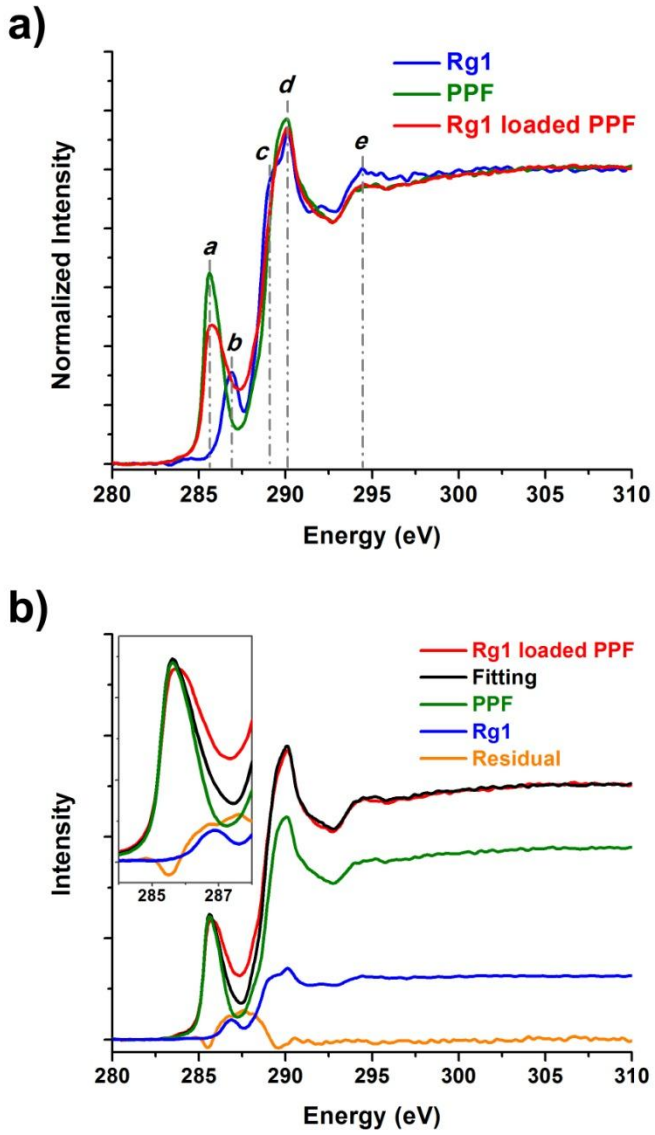

Figure 4.8. (a) C K-edge XANES spectra of pure PPF microspheres, ginsenoside Rg_1, and Rg_1-loaded PPF microspheres prepared using microfluidic method. (b) Linear fitting of the Rg_1-loaded PPF microspheres prepared using microfluidic method. Inset shows the π^* resonance.

4.3.6 Release of ginsenoside Rg_1 from delivery system *in vitro*

We assayed the kinetic profiles of *in vitro* release of ginsenoside Rg_1 from monodisperse

www.manaraa.com

microparticles fabricated using the microfluidic approach and polydisperse microparticles prepared using the conventional double emulsion technique, as shown in Figure 4.9. In general, Rg_1 release behavior for all monodisperse and polydisperse PPF microspheres exhibited a biphasic profile: an initial burst release in the first 2 days followed by a decreased sustained release over a 40-day period. The release profiles show that the total cumulative Rg_1 release from the monodisperse microspheres and conventional polydisperse microspheres are 48.7% and 88%, respectively. In addition, the initial burst release varied from 18.5% to 56.5% for microfluidic microspheres and polydisperse microspheres, respectively. Monodisperse microspheres prepared by the microfluidics device released Rg_1 more slowly than from the conventional polydisperse microspheres. Furthermore, the monodisperse particles revealed a significantly smaller initial burst release than that observed for the polydisperse microspheres. It has been shown the initial burst release of entrapped bioactive agent is affected most by the viscosity of the polymer solution used for the fabrication of microspheres;[19] however, the PPF microspheres for both methods were fabricated using the same batch and viscosity of synthesized polymer. In addition, it is known that the burst release depends on the rapid water penetration into the polymer matrix; therefore, encapsulated molecules that are immediately accessible at the periphery of the microspheres and/or in the aqueous channels inside the microspheres are rapidly released upon contact with the release medium, PBS.[19] The smaller initial burst and slower release kinetics from the conventional microspheres is attributed to homogeneous mixing in the microfluidic device, leading to a more uniform and even drug distribution in the interior of the microparticles, while the conventional microspheres may have drug-rich domains near the surface of the microparticles most likely caused by the inhomogeneous forces involved.[24] The conventional double emulsion method produced a broad size distribution of the particles, particularly a high number of small particles. These will contribute to the larger initial burst release and faster overall kinetics observed in the conventional particles, owing to the larger surface-area-to-volume ratio of the smaller particles.[24] In addition, the large amounts of Rg_1 absorbed at the surface of the microparticles escape easily into PBS solution also resulting in the larger observed initial burst and faster release kinetics.[23] Using the microfluidics approach, PPF scaffolds could be rendered angiogenic by incorporation of

www.manaraa.com

Rg_1-loaded PPF microspheres. It is expected that microsphere incorporation into PPF scaffolds may result in a negligible burst release and a more sustained *in vitro* release over a prolonged period of time.

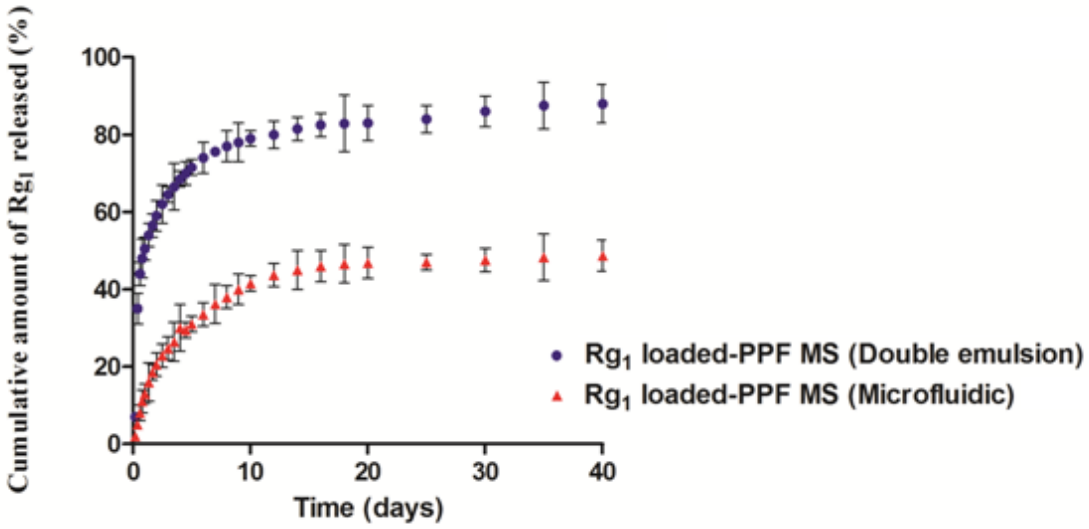

Figure 4.9. Release profiles of ginsenoside Rg_1 from monodisperse PPF microspheres. prepared with microfluidic device and polydisperse PPF microspheres prepared using the conventional double emulsion technique.

4.3.7 Angiogenesis effect/tube formation of HUVEC cell line

Figure 4.10 displays the tube formation of EA.hy926 cell line seeded in a growth factor-reduced Matrigel-coated 96-well plate. This bioassay shows the tube formation in both the absence and presence of ginsenoside Rg_1 at different concentrations before loading and after release from the PPF microspheres prepared using the microfluidic device. After seeding for twelve to eighteen hours in the absence of angiogenic factor, HUVECs cell line formed incomplete and narrow tube-like structures (control sample); however, in the presence of Rg_1 within the dose range of 1-32 µg/ml, elongated and robust capillary-like networks are observed to form, which were organized by a greater number of cells compared with the control indicating the proangiogenesis activity of ginsenoside Rg_1, as shown in Figure 4.10b-g. Based on the obtained results, the functional concentration of Rg_1 was found to be 1 µg/ml, while the optimal concentration is 8 µg/ml, as seen in Figure 4.10o demonstrating that 8 µg/ml of Rg_1 stimulated tube formation by 2-fold over

www.manaraa.com

the control. To study the angiogenesis behavior of ginsenoside Rg_1 after release from the PPF microspheres, the extract liquid in 2 mL of medium from the 19th day to 20th day of release was collected. The concentration of Rg_1 was measured using UV-Vis spectrophotometry, and diluted to different concentrations of 1-32 μg/ml. It was found that tube formation stimulation activity of ginsenoside Rg_1 did not change significantly after release from the delivery carriers. This indicates that the examined PPF microsphere delivery systems did not significantly affect the angiogenic activity of Rg_1. Similarly, ginsenoside Rg_1 released from the PPF microspheres exhibits similar potency towards the formation of networks of honeycomb-like or tube-like structures in the EA.hy926 cell line in a dose-dependent manner, as illustrated in Figure 4.10i-n. These results demonstrate that Rg_1-induced tube formation is related to the dosage. Hence, Rg_1 incorporation into PPF microspheres may result in a gradual *in vitro* release from the PPF composites maintaining local *in vivo* concentrations at angiogenic levels for sufficient time. Therefore, further optimization of the Rg_1 pharmacokinetics is required to obtain a release profile that coincides better with the normal rate of tube and bone formation.[39] In addition, it should be noted that HUVECs' ability to form a network of tubular structures across the surface of a Matrigel substratum is a complex phenomenon which combines elements of attachment, migration, organization, and differentiation. The complex organizational behavior of HUVECs on Matrigel models the type of coordinated activities that are relevant to angiogenesis by endothelial cells. Although the *in vitro* Matrigel model does not represent true angiogenesis, it suggests that Rg_1 is important for many of the activities that are required for vessel formation.[40]

www.manaraa.com

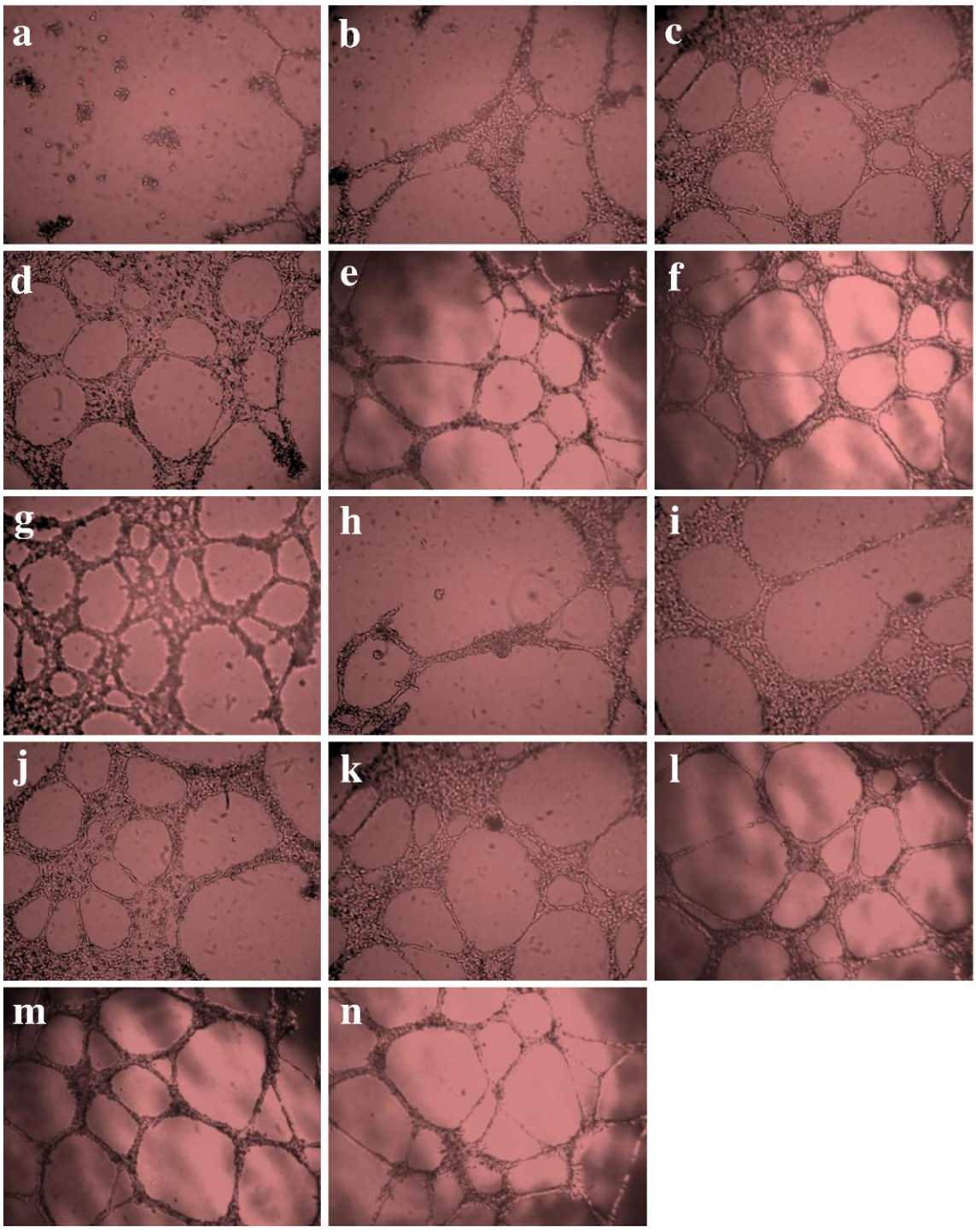

www.manaraa.com

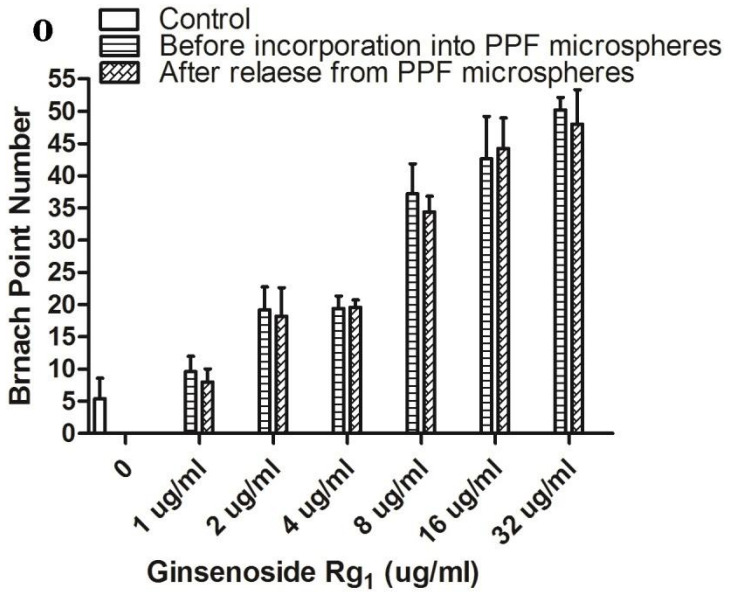

Figure 4.10. Tube formation of HUVECs cell line cultured in different extract-contained media from PPF microspheres.

Effect of ginsenoside Rg_1 (before incorporation into PPF microspheres) on tube formation of EA.hy926 cell line: control (a), 1 μg/ml (b), 2 μg/ml (c), 4 μg/ml (d), 8 μg/ml (e), 16 μg/ml (f), and 32 μg/ml ginsenoside Rg_1 (g), Rg_1-induced angiogenic tube formation of EA.hy926 cell line cultured in media contained extract released from Rg_1 loaded-PPF microspheres for the ninetieth to twentieth day of release at 1 μg/ml (i), 2 μg/ml (j), 4 μg/ml (k), 8 μg/ml (l), 16 μg/ml (m), and 32 μg/ml (n) ginsenoside Rg_1 concentration compared to blank (h), and (p) a dose-dependent increase in the branching points up to 32 μg/ml ginsenoside Rg_1 released from Rg_1-loaded PPF microspheres for the 19th day to 20th day of release.

4.4 Conclusions

In this study, ginsenoside Rg_1 was encapsulated in PPF microspheres comparing a microfluidic and conventional double emulsion method, with the microfluidic method generating microspheres of more uniform size. SEM, FTIR, and XRD analyses were employed to examine the morphology, chemical stability, and physical state of Rg_1 in the microspheres. We also reported the C K-edge XANES study of the PPF microspheres loaded with/without ginsenoside Rg_1. XANES results confirmed that Rg_1 was

www.manaraa.com

successfully loaded in the PPF microspheres and the weight ratio between Rg_1 and PPF is about 1:3. It is proposed that chemical interaction between the Rg_1 and PPF took place via C-O-C and C-C bonds during the Rg_1 loading process. The monodisperse PPF microspheres prepared using the microfluidic method (50-65 μm) exhibited a slower release rate and a smaller burst effect compared to the polydisperse microspheres produced using the double emulsion method (2-45 μm). Furthermore, the ginsenoside Rg_1 released from delivery systems showed tube formation stimulation effect on human umbilical vein cell lines as Rg_1 before loading into the PPF microparticles, which reveales that the microsphere preparation method does not affect the bioactivity of ginsenoside Rg_1 *in vitro*. Monodisperse Rg_1-loaded PPF microspheres could be incorporated to the scaffold formulations to generate Rg_1-releasing scaffolds serving as a synthetic extracellular matrix that would enhance bone regeneration through improved vascularization.

www.manaraa.com

4.5 References

1 Lee K-W, Wang S, Fox BC, Ritman EL, Yaszemski MJ, Lu L. Poly (propylene fumarate) bone tissue engineering scaffold fabrication using stereolithography: effects of resin formulations and laser parameters. Biomacromolecules. 2007;8:1077-1084.

2 Chen G, Ushida T, Tateishi T. Scaffold design for tissue engineering. Macromolecular Bioscience. 2002;2:67-77.

3 Hedberg EL, Shih CK, Lemoine JJ, Timmer MD, K Liebschner MA, Jansen JA, Mikos AG. *In vitro* degradation of porous poly (propylene fumarate)/poly (dl-lactic-co-glycolic acid) composite scaffolds. Biomaterials. 2005;26:3215-3225.

4 Thomson R, Wake M, Yaszemski M, Mikos A. Biodegradable polymer scaffolds to regenerate organs. Biopolymers Ii: Springer; 1995. p. 245-274.

5 Liao E, Yaszemski M, Krebsbach P, Hollister S. Tissue-engineered cartilage constructs using composite hyaluronic acid/collagen I hydrogels and designed poly (propylene fumarate) scaffolds. Tissue engineering. 2007;13:537-550.

6 Vehof JW, Fisher JP, Dean D, van der Waerden JP, Spauwen PH, Mikos AG, Jansen JA. Bone formation in transforming growth factor β-1-coated porous poly (propylene fumarate) scaffolds. Journal of biomedical materials research. 2002;60:241-251.

7 Lee K-W, Wang S, Yaszemski MJ, Lu L. Physical properties and cellular responses to crosslinkable poly (propylene fumarate)/hydroxyapatite nanocomposites. Biomaterials. 2008;29:2839-2848.

8 Shung AK, Timmer MD, Jo S, Engel PS, Mikos AG. Kinetics of poly (propylene fumarate) synthesis by step polymerization of diethyl fumarate and propylene glycol using zinc chloride as a catalyst. Journal of Biomaterials Science, Polymer Edition. 2002;13:95-108.

9 Payne RG, McGonigle JS, Yaszemski MJ, Yasko AW, Mikos AG. Development of an injectable, *in situ* crosslinkable, degradable polymeric carrier for osteogenic cell populations. Part 3. Proliferation and differentiation of encapsulated marrow stromal osteoblasts cultured on crosslinking poly (propylene fumarate). Biomaterials. 2002;23:4381-4387.

10 Lee K-W, Wang S, Lu L, Jabbari E, Currier BL, Yaszemski MJ. Fabrication and characterization of poly (propylene fumarate) scaffolds with controlled pore structures using 3-dimensional printing and injection molding. Tissue engineering. 2006;12:2801-2811.

11 Kleinheinz J, Stratmann U, Joos U, Wiesmann H-P. VEGF-activated angiogenesis during bone regeneration. Journal of oral and maxillofacial surgery. 2005;63:1310-1316.

www.manaraa.com

12 Kaigler D, Wang Z, Horger K, Mooney DJ, Krebsbach PH. VEGF scaffolds enhance angiogenesis and bone regeneration in irradiated osseous defects. Journal of Bone and Mineral Research. 2006;21:735-744.

13 Villars F, Bordenave L, Bareille R, Amedee J. Effect of human endothelial cells on human bone marrow stromal cell phenotype: role of VEGF? Journal of cellular biochemistry. 2000;79:672-685.

14 Leung KW, Cheng Y-K, Mak NK, Chan KK, David Fan T, Wong RN. Signaling pathway of ginsenoside-Rg_1 leading to nitric oxide production in endothelial cells. FEBS letters. 2006;580:3211-3216.

15 Leung KW, Pon YL, Wong RN, Wong AS. Ginsenoside-Rg_1 induces vascular endothelial growth factor expression through the glucocorticoid receptor-related phosphatidylinositol 3-kinase/Akt and β-catenin/T-cell factor-dependent pathway in human endothelial cells. Journal of Biological Chemistry. 2006;281:36280-36288.

16 Chiellini F, Piras AM, Errico C, Chiellini E. Micro/nanostructured polymeric systems for biomedical and pharmaceutical applications. Nanomedicine. 2008;3:367-393.

17 Lee J, Lee KY. Injectable microsphere/hydrogel combination systems for localized protein delivery. Macromolecular Bioscience. 2009;9:671-676.

18 Kempen DH, Lu L, Kim C, Zhu X, Dhert WJ, Currier BL, Yaszemski MJ. Controlled drug release from a novel injectable biodegradable microsphere/scaffold composite based on poly (propylene fumarate). Journal of Biomedical Materials Research Part A. 2006;77:103-111.

19 Kempen DH, Lu L, Zhu X, Kim C, Jabbari E, Dhert WJ, Currier BL, Yaszemski MJ. Development of biodegradable poly (propylene fumarate)/poly (lactic-co-glycolic acid) blend microspheres. II. Controlled drug release and microsphere degradation. Journal of Biomedical Materials Research Part A. 2004;70:293-302.

20 Kempen DH, Lu L, Zhu X, Kim C, Jabbari E, Dhert WJ, Currier BL, Yaszemski MJ. Development of biodegradable poly (propylene fumarate)/poly (lactic-co-glycolic acid) blend microspheres. I. Preparation and characterization. Journal of Biomedical Materials Research Part A. 2004;70:283-292.

21 Okushima S, Nisisako T, Torii T, Higuchi T. Controlled production of monodisperse double emulsions by two-step droplet breakup in microfluidic devices. Langmuir. 2004;20:9905-9908.

22 Zhang H, Tumarkin E, Peerani R, Nie Z, Sullan RMA, Walker GC, Kumacheva E. Microfluidic production of biopolymer microcapsules with controlled morphology. Journal of the american chemical society. 2006;128:12205-12210.

www.manaraa.com

23 He T, Liang Q, Zhang K, Mu X, Luo T, Wang Y, Luo G. A modified microfluidic chip for fabrication of paclitaxel-loaded poly (l-lactic acid) microspheres. Microfluidics and Nanofluidics. 2011;10:1289-1298.

24 Xu Q, Hashimoto M, Dang TT, Hoare T, Kohane DS, Whitesides GM, Langer R, Anderson DG. Preparation of monodisperse biodegradable polymer microparticles using a microfluidic flow-focusing device for controlled drug delivery. Small. 2009;5:1575-1581.

25 Peter SJ, Suggs LJ, Yaszemski MJ, Engel PS, Mikos AG. Synthesis of poly (propylene fumarate) by acylation of propylene glycol in the presence of a proton scavenger. Journal of Biomaterials Science, Polymer Edition. 1999;10:363-373.

26 Salarian M, Xu WZ, Biesinger MC, Charpentier PA. Synthesis and characterization of novel TiO_2-poly(propylene fumarate) nanocomposites for bone cementation. Journal of Materials Chemistry B. 2014;2:5145-5156.

27 Nisisako T, Torii T, Higuchi T. Droplet formation in a microchannel network. Lab on a Chip. 2002;2:24-26.

28 Samimi R, Salarian M, Xu WZ, Lui EM, Charpentier PA. Encapsulation of Acetyl Ginsenoside Rb_1 within Monodisperse Poly (dl-lactide-co-glycolide) Microspheres Using a Microfluidic Device. Industrial & Engineering Chemistry Research. 2014;53:11333-11344.

29 Lee J, Tan CY, Lee S-K, Kim Y-H, Lee KY. Controlled delivery of heat shock protein using an injectable microsphere/hydrogel combination system for the treatment of myocardial infarction. Journal of Controlled Release. 2009;137:196-202.

30 Yu L-C, Chen S-C, Chang W-C, Huang Y-C, Lin KM, Lai P-H, Sung H-W. Stability of angiogenic agents, ginsenoside Rg_1 and Re, isolated from Panax ginseng: *In vitro* and *in vivo* studies. International journal of pharmaceutics. 2007;328:168-176.

31 Chang C-H, Liao T-C, Hsu Y-M, Fang H-W, Chen C-C, Lin F-H. A poly (propylene fumarate)–Calcium phosphate based angiogenic injectable bone cement for femoral head osteonecrosis. Biomaterials. 2010;31:4048-4055.

32 Yeo Y, Park K. Control of encapsulation efficiency and initial burst in polymeric microparticle systems. Archives of pharmacal research. 2004;27:1-12.

33 Kajjari PB, Manjeshwar LS, Aminabhavi TM. Semi-interpenetrating polymer network hydrogel blend microspheres of gelatin and hydroxyethyl cellulose for controlled release of theophylline. Industrial & Engineering Chemistry Research. 2011;50:7833-7840.

34 Sham T. Nanoparticles and nanowires: synchrotron spectroscopy studies. International Journal of Nanotechnology. 2008;5:1194-1246.

www.manaraa.com

35 Guo X, Wu J, Yiu Y-M, Hu Y, Zhu Y-J, Sham T-K. Drug–nanocarrier interaction—tracking the local structure of calcium silicate upon ibuprofen loading with X-ray absorption near edge structure (XANES). Physical Chemistry Chemical Physics. 2013;15:15033-15040.

36 Kikuma J, Tonner B. XANES spectra of a variety of widely used organic polymers at the C K-edge. Journal of electron spectroscopy and related phenomena. 1996;82:53-60.

37 Dhez O, Ade H, Urquhart S. Calibrated NEXAFS spectra of some common polymers. Journal of electron spectroscopy and related phenomena. 2003;128:85-96.

38 Chuang C-H, Wang Y-F, Shao Y-C, Yeh Y-C, Wang D-Y, Chen C-W, Chiou J, Ray SC, Pong W, Zhang L. The Effect of Thermal Reduction on the Photoluminescence and Electronic Structures of Graphene Oxides. Scientific reports. 2014;4.

39 Kempen DH, Kruyt MC, Lu L, Wilson CE, Florschutz AV, Creemers LB, Yaszemski MJ, Dhert WJ. Effect of autologous bone marrow stromal cell seeding and bone morphogenetic protein-2 delivery on ectopic bone formation in a microsphere/poly (propylene fumarate) composite. Tissue Engineering Part A. 2008;15:587-594.

40 Liang H-C, Chen C-T, Chang Y, Huang Y-C, Chen S-C, Sung H-W. Loading of a novel angiogenic agent, ginsenoside Rg_1 in an acellular biological tissue for tissue regeneration. Tissue engineering. 2005;11:835-846.

www.manaraa.com

Chapter 5

5 Hydroxapatite-TiO_2-based Nanocomposites Synthesized in Supercritical CO_2 for Bone Tissue Engineering: Physical and Mechanical Properties

Abstract

Calcium phosphate-based nanocomposites offer a unique solution towards producing scaffolds for orthopedic and dental implants. However, despite attractive bioactivity and biocompatibility, hydroxyapatite (HAp) has been limited in heavy load-bearing applications due to its intrinsic low mechanical strength. In order to improve the mechanical properties of HAp, in this work HAp nonaplates were grown from the surface of one-dimensional titania nanorod structures by combining a co-precipitation and sol-gel methodology using supercritical fluid processing with carbon dioxide ($scCO_2$). The effect of metal alkoxide concentration (1.1-1.5 mol/L), reaction temperature (60-80 °C), and pressure (6000-8000 psi) on the morphology, crystallinity, and surface area of the resulting nanostructured composites was examined using scanning electron microscopy, transmission electron microscopy, X-ray diffraction (XRD) analysis, and Brunauer-Emmet-Teller method. Chemical composition of the products was characterized using Fourier transform infrared (FTIR), X-ray photoelectron spectroscopy (XPS), and X-ray absorption near-edge structures (XANES) analyses. HAp nanoplates and HAp-TiO_2 nanocomposites were homogenously mixed within poly(ε-caprolactone) (PCL) to develop scaffolds with enhanced physical and mechanical properties for bone regeneration. Mechanical behavior analysis demonstrated that Young's and flexural modulus of PCL/HAp-TiO_2 composites were substantially higher than PCL/HAp composites. Therefore, this new synthesis methodology in $scCO_2$ holds promise for bone tissue engineering with improved mechanical properties.

www.manaraa.com

5.1 Introduction

Hydroxyapatite ($Ca_{10}(PO_4)_6(OH)_2$, HAp) nanoparticles have attracted great interest, as their chemical and crystallographic structure is similar to the mineral phase of human hard tissues, bone and teeth.[1] HAp has shown excellent biocompatibility, bioactivity, and high osteo-conductivity. Thus, it has been extensively used in dental and medical applications such as reconstructive and prosthetic materials for bone and teeth.[1-3] However, the principal limitation in the clinical use of pure HAp as a load bearing implant is its intrinsic brittleness and poor mechanical properties in the presence of body fluids and under local loading.[4, 5] Generally, the size and morphology of the HAp particles have a direct influence on its ability to reinforce materials.[6] Mechanical properties of these HAp-based materials can potentially be improved by dispersing into them one dimensional nanostructures including nanorods, nanofibers, or nanotubes.[7, 8] It was previously shown that the morphology and size of HAp particles could be controlled by the presence of cetyltrimethylammonium bromide (CTAB) and polyethylene glycol (PEG) under hydrothermal conditions.[9, 10] Nevertheless, it is very challenging to prepare HAp nanogeometries, as HAp nanoparticles tend to agglomerate.[5]

On the other hand, immobilization of a biocompatible metal/metal oxide, such as Al_2O_3, ZrO_2, SiO_2, and TiO_2 on the surface of the hydroxyapatite will enhance the mechanical properties of HAp along with enhancing cellular responses and biocompatibility.[11, 12] Among these HAp-based composites, HAp-TiO_2 composites have attracted considerable attention due to the combined advantages of both materials. Namely TiO_2 is capable of enhancing osteoblast adhesion[13] and inducing cell growth[14] by forming a chemical bond with the living tissue as well as the bioactivity of the HAp.

These composite materials are suggested to demonstrate improved mechanical and physical properties compared to pure HAp ceramics. Therefore, HAp-TiO_2 composite materials have recently been indicated for load-bearing biomedical applications.[15, 16] In addition, HAp-TiO_2 composites are able to decompose both bacteria and organic materials, hence being beneficial in antibacterial applications.[17]

www.manaraa.com

HAp-TiO_2 composites have been prepared by different methods such as sol-gel,[18, 19] hydrothermal,[20] combined gravity/hydrothermal processing,[5] electrospinning method,[16] microwave-assisted co-precipitation process,[11, 21] and so on. However, obtaining a crystalline powder in most of these methods requires costly heat treatments at high temperatures or for long reaction periods. Besides, they are not environmentally friendly, and suffer scale-up problems.[11] Consequently, a more efficient synthetic methodology has been explored to prepare HAp-TiO_2 composites. Previously, direct sol-gel reactions in $scCO_2$ have attracted much attention for synthesizing oxide nanomaterials of unique morphologies.[22, 23] Recently, the Charpentier group introduced a one-step sol-gel method to prepare TiO_2 nanofibers and ZrO_2-modified TiO_2 nanotubes where $scCO_2$ was used as the functional solvent for both self-assembly and as the drying agent.[24, 25] This method provides several advantages to tailoring the nanomorphology by "tuning" the supercritical fluids temperature and/or pressure.[24, 26] Moreover, any unreacted starting materials can be safely removed from the synthesized products by supercritical fluid extraction (SFE) during the cleaning process, maintaining the porous nanostructure of the product while providing clean products suitable for biomedical applications.[25, 26]

The aim of this study was to develop a new synthetic procedure for the synthesis of HAp-TiO_2 nanocomposites by combining co-precipitation and sol-gel method in $scCO_2$. The nanosized HAp-TiO_2 particles are examined as a reinforcing phase in polycaprolactone (PCL) matrix. PCL is a biocompatible and bioresorbable polyester used in numerous medical and drug delivery applications.[27, 28] The degradation kinetics and preservation of the mechanical properties make PCL an excellent candidate as a temporary joint spacer in total joint prostheses.[29] It was found that Young's and flexural modulus of PCL/HAp-TiO_2 composites are significantly higher than PCL/HAp composites confirmed by uniaxial tensile and flexural testings. In addition, X-ray absorption near-edge structures (XANES) spectroscopy that probes the local structure and bonding of the absorbing atoms by monitoring the absorption coefficient above the absorption edge using tunable X-rays from a synchrotron light source and provides information on oxidation states, coordination, and symmetry of the system was applied to study the composition of the HAp-TiO_2 nanoparticles, showing that the weight ratio between

www.manaraa.com

anatase TiO_2 and HAp is about 1:1.6. These nanosized PCL/HAp-TiO_2 composites are encouraging for the preparation of scaffolds for next generation bone tissue engineering applications.

5.2 Experimental details

5.2.1 Materials

Calcium nitrate tetrahydrate ($Ca(NO_3)_2.4H_2O$), diammonium hydrogen phosphate ($(NH_4)_2HPO_4$), cetyltrimethylammonium bromide (CTAB), and polyethylene glycol PEG 400 were obtained from Sigma-Aldrich, Canada. All chemicals were of analytical grade or higher and used as received. Titanium isopropoxide (TIP, 99.999%) trace metals basis, glacial acetic acid (>99.7%), ammonium hydroxide (NH_4OH, 30%), dichloromethane (DCM, 99.5%), anhydrous ethanol (EtOH), and polycaprolactone (PCL) (MW 80,000 g/mol) were purchased from Sigma-Aldrich, Canada and used as received.

5.2.2 Characterization

The morphologies of the samples were examined using scanning electron microscopy (SEM, Hitachi S-4500) and transmission electron microscopy (TEM, JEOL 2010F) with a 200 keV Schottky field emission microscope (TEM/STEM). For SEM imaging, samples were prepared by applying the powder directly to a carbon adhesive tape. Samples were then coated with an ultrathin layer of gold to reduce charging problems. For TEM analysis, the powdered samples were dispersed in methanol by sonication for 1 min, and then placed on a copper grid covered with holey carbon film, and dried by normal evaporation. The bulk composition and elemental analysis of the HAp-TiO_2 powders was analyzed using energy-dispersive Quartz XOne x-ray spectroscopy (EDX) attached to a Hitachi S-4500 field emission SEM on three fields of view (n=3). Structural analysis of the powders was performed using an Inel Powder Diffractometer. The instrument was equipped with a Cu-X-ray radiation Tube, an Inel XRG3000 generator and an Inel CPS 120 detector. The diffraction pattern data was processed with the IMAD

www.manaraa.com

program and the MATCH Software, which was used for phase identification from powder diffraction data. ICDD PDF4+ database was used to search for reference patterns.

The thermogravimetric analysis (TGA) was carried out to study the thermal decomposition behavior of the HAp and HAp-TiO_2 nanocomposites. TGA analysis of the synthesized nanostructures was performed using a thermogravimetric analyzer, TA Instrument (TA-Q500), at a heating rate of 10 °C/min from room temperature to 1200 °C under flowing air. X-ray photoelectron spectroscopy (XPS) analyses were carried out with a Kratos Axis Ultra spectrometer using a monochromatic Al Kα source (15mA, 14kV). Samples were mounted on a non-conductive double-sided adhesive tape. The Kratos charge neutralizer system was used on all specimens. Survey scan analyses were carried out with an analysis area of 300 x 700 microns and a pass energy of 160 eV. Spectra have been charge corrected to the main line of the carbon 1s spectrum set to 284.8 eV. Spectra were analyzed using CasaXPS software (version 2.3.14).

Synchrotron measurements were carried out at the high-resolution spherical grating monochromator (SGM) beamline at the Canadian Light Source (CLS), the University of Saskatchewan. The samples were mounted on conventional carbon tapes with an angle of 20° facing toward the photon beam. XANES spectra were recorded in total electron yield (TEY) that was detected with the specimen current. All XANES spectra were normalized to the incident photon flux collected on a refreshed Au grid.

The FTIR spectra of the samples were collected using a Bruker IFS 55 FTIR instrument with an attached MCT detector. Specimens were prepared by mixing 4 wt % of each sample with potassium bromide (KBr) and then pressing into a pellet. The spectra were recorded within the range of 400-4000 cm^{-1} with a resolution of 4 cm^{-1} over 32 scans. The specific surface areas and the average pores size of the powders were determined via Brunauer-Emmet-Teller method and Barret-Joyner-Halenda (BJH) analysis of BET isotherms using Tristar II 3020 (Micromeritics Instrument Corporation). All the samples were degassed at 150 °C for 12 h.

Mechanical properties of PCL/HAp-TiO_2 and PCL/HAp composites were determined using an Instron 5943 universal testing machine (Instron, Canton, MA) equipped with a

www.manaraa.com

500 N (tension) load cell. For tensile testing, dogbone specimens with overall length of 60 mm and width of grip section of 10 mm were prepared by slicing the PCL/HAp and PCL/HAp-TiO_2 films and adding to a stainless steel mold. The mold was heated at 100 °C for 30 min and heat-pressed at 100 °C and 670 N for 2 min. Prepared specimens were soaked in deionized water at 37 °C for 24 h prior to testing. Stress-strain relationships were obtained from the load and displacement data. The Young's modulus was determined by calculating the slope of the linear portion of the stress-strain curve, and the tensile strength was defined as the maximum stress achieved. For each group, 5 independent specimens (n=5) were tested in tension at a crosshead speed of 10 mm/min. Flexural strength and flexural modulus of the nanocomposites were determined in accordance with ASTM D790M-92 using a dynamic mechanical analyzer, DMA Q800 (TA instruments). Flexural testing samples, rectangular bar specimens (n=5) (50 mm × 25 mm × 2 mm), were prepared using the stainless steel mold heat-pressed following the same procedure as tensile testing specimens. Prepared specimens were soaked in deionized water at 37 °C for 24 h prior to testing, and placed on a three-point bending apparatus with two supports spanning 40 mm from each other and loaded at the cross-head speed of 10 mm/min to the center of each specimen until failure. In an approach similar to that of tensile testing, flexural modulus was calculated as the slope of the initial linear region of the stress-strain curve, while flexural fracture strength was determined as the maximum applied stress prior to failure.

5.2.3 Preparation of materials

5.2.3.1 *Preparation of HAp nanoparticles using a combined co-precipitation and sol-gel method*

The reactant molar ratio of Ca^{2+}/PO_4^{3-} was kept at 1.67 (stoichiometric ratio of HAp). The general procedure is as follows: first, $(NH_4)_2HPO_4$ (1.078 g, 0.008 mol) and CTAB (2.083 g, 0.0056 mole) were dissolved in 33.3 ml of deionized water. The solution was stirred for 30 min with a magnetic stirrer, then the pH value was adjusted to 4.5 by adding pure acetic acid. After this, $Ca(NO_3)_2.4H_2O$ (3.228 g, 0.0135 mol) was dissolved in 46.67 ml of deionized water and 6.67 ml of PEG 400 was simultaneously added to the

www.manaraa.com

solution under constant stirring for 20 min. Then, the mixed solution of $Ca(NO_3)_2 \cdot 4H_2O$ and PEG 400 was added to the latter dropwise under continuous magnetic stirring in air. The pH of the solution was then adjusted to 9 using ammonia. The final milky-white suspension was rigorously stirred at room temperature for 6 h. The resulting white precipitates were separated from the suspension by centrifuging, washed 3X with ethanol to remove the residual CTAB and PEG 400 and denoted as the HAp precursor (Figure 5.1). To synthesize the HAp nanoplates in $scCO_2$, HAp precursor (3 g) was dispersed in ethanol at the ratio of 1:1 by weight while vigorously stirring, and placed in a 10 mL stainless steel view cell reactor, followed by the addition of CO_2 using a high pressure syringe pump (Isco 260D). The schematic diagram of the experimental setup can be found in Sui et al.[23] The temperature and pressure in the view cell were controlled to a range from 60 to 80 °C and 6000 psi as the optimized experimental conditions. The precursor was stirred for one day using a magnetic stirrer with TFE stir bar. Stirring was stopped after 24 h, while 4-5 days of aging were required for complete reaction. After aging, the formed gel was washed continuously using CO_2 at a rate of approximately 0.5 mL/min, followed by controlled venting at 0.5 mL/min to prevent collapse of the solid network. The as-prepared powder was kept in a vacuum oven at 80 °C to remove moisture.

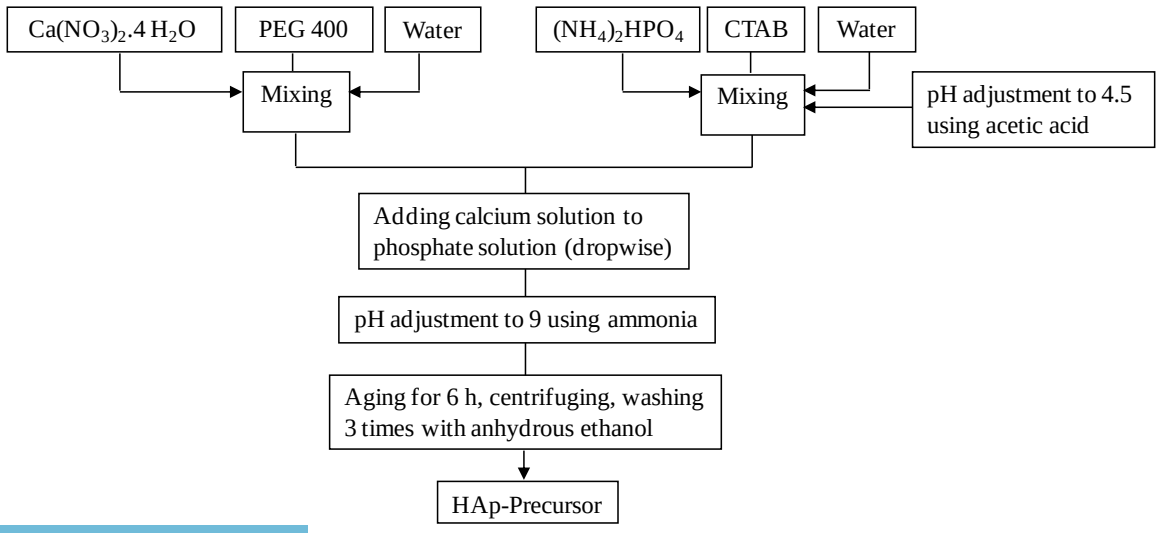

www.manaraa.com

Figure 5.1. Schematic representation of the preparation of HAp precursor.

5.2.3.2 *Preparation of HAp-TiO_2 nanocomposites using a combined co-precipitation and sol-gel method*

In a typical experiment, the HAp precursor (1.5 g), prepared following the explained procedure in section 3.3.1 was dispersed in ethanol (1.5 g) and placed in a 10 mL high pressure view cell followed by quick addition of titanium isopropoxide (1 g) and acetic acid (4 g) and heated/pressurized with CO_2 to the desired temperature and pressure. A magnetic stirrer with TFE stir bar was used for mixing the reaction mixture. The mixture of HAp precursor, titanium isopropoxide, and acetic acid was dispersed in supercritical CO_2 at the studied temperature 80 °C and pressure range from 6000 to 8000 psi. The reaction was kept under continuous stirring for 24 h, and 5-6 days of aging were required for complete reaction, as shown in Figure 5.2. After aging, the formed gel was washed with CO_2 followed by controlled venting at 0.5 mL/min. After CO_2 extraction and venting, the resulting powders were subjected to further drying and calcination at 500 °C in air for 2 h using a heating rate of 10 °C/min and a cooling rate of 0.5 °C/min to room temperature.

For comparison of XANES study, TiO_2 nanoparticles were synthesized following the procedure presented in Salarian et al.,[30] and calcined at 450 °C and 750 °C.

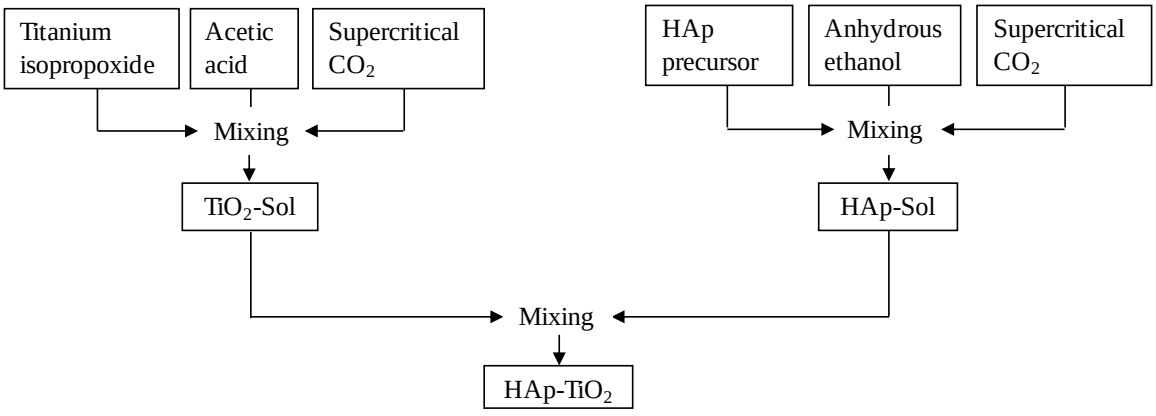

Figure 5.2. Schematic representation of sol-gel process for producing HAp-TiO_2 composites.

www.manaraa.com

5.2.3.3 *Preparation of HAp-TiO_2 nanocomposites using hydrothermal technique*

Similar to the synthesis of HAp precursor, $(NH_4)_2HPO_4$ (1.213 g, 0.009 mol) and CTAB (2.343 g, 0.0063 mol) were dissolved in 37.5 ml of deionized water, and the solution was stirred for 30 min with a magnetic stirrer followed by adjusting the pH value to 4.5 using acetic acid. After that, $Ca(NO_3)_2 \cdot 4H_2O$ (3.632 g, 0.0152 mol) was dissolved in 52.5 ml of deionized water and 7.5 ml of PEG 400 was simultaneously added to the solution while stirring for 20 min. Then, the $Ca(NO_3)_2 \cdot 4H_2O$+PEG 400 solution was added to the $(NH_4)_2HPO_4$+CTAB solution dropwise with constant stirring. Simultaneously, TIP (1 g) was mixed with acetic acid (6 g), and added dropwise to the reaction media (phosphate solution). Ammonia was used to adjust the solution pH to 11. The final suspension was transferred to a 125 ml stainless steel autoclave; then hydrothermally treated at 200 °C for 24 h. After reaction, any precipitates were separated from the suspension by centrifugation at 5000 rpm for 10 min, washed 3X with ethanol, then freeze-dried to yield the product (white powder).

5.2.3.4 *Preparation of PCL/HAp-TiO_2 and PCL/HAp composite*

In order to produce PCL/HAp composites, HAp powders synthesized in $scCO_2$ were added to dichloromethane (DCM) and then stirred for 15 min, followed by sonication for 5 min. PCL was then added to the HAp/DCM suspension to produce a PCL/HAp slurry containing the following ratios PCL:HAp (w/w): 90:10, 80:20, and 70:30. The PCL/HAp slurry was cast in a glass dish, and the solvent evaporated in a fume hood. Finally, the resulting PCL/HAp films were heat-pressed at 100 °C and 670 N for 2 min. PCL/HAp-TiO_2 specimens were prepared following the same procedure using HAp-TiO_2 powders synthesized by combined co-precipitation and sol-gel method and hydrothermal treatment.

5.3 Results and Discussion

5.3.1 SEM and TEM characterization of the as-synthesized HAp and calcined HAp-TiO_2 composites powders

The experimental conditions and characterization results for the as-synthesized HAp and

www.manaraa.com

calcined HAp-TiO_2 composites powders are provided in Table 5.1.

Table 5.1. Synthesis conditions of HAp and HAp-TiO_2 nanostructures in $scCO_2$ and characterization results (morphology and BET surface area).

	Temperature [°C]	**Pressure [psi]**	**$C_{0\,(TIP)}$ [mol l^{-1}]**	**(AcOH/TIP) weight ratio**	**BET [m^2 g^{-1}]**	**Morphology**
TiO_2	60	6000	1.1	4	111	Nanofiber-Nanotube
HAp-1	60	6000	-	-	60	Nanoplate
HAp-2	80	6000	-	-	72	Nanoplate
HAp-TiO_2-1	80	6000	1.1	4	100	Nanoplate-Thick sheet type structure
HAp-TiO_2-2	80	6000	1.5	4	170	Nanoplate on the surface of Nanorods
HAp-TiO_2-3	80	8000	1.5	4	108	Nanoplate-Nanorods
HAp-TiO_2-h	Hydrothermal treatment at 200 °C for 24 hours				98	Oblong-shaped

SEM micrographs of the synthesized materials (Figure 5.3(a-f)) and TEM images of HAp-TiO_2-2 and HAp-TiO_2-h nanocomposite (Figure 5.3g&h) show that the HAp and the HAp-TiO_2 composites powders were composed of various nanostructures. SEM image of the TiO_2 nanoparticles calcined at 450 °C are shown in Figure 5.3a indicating the formation of tube-like and fiber-like structure. More detailed information on the experimental procedure of these TiO_2 nanoparticles are presented in Salarian et al.[30] Figure 5.3b&c show the plate-like particles of samples HAp-1 (150-250 nm in width) and HAp-2 (40-100 nm in width), synthesized in $ScCO_2$ using a system pressure of 6000 psi

www.manaraa.com

at 60 °C and at 80 °C, respectively. In general, we found slight changes in the morphology and dimensions of the particulates when adjusting the reaction temperature from 60 to 80 °C, although the higher studied reaction temperature (80 °C) gave nanoplates with smaller dimensions and higher surface areas. SEM analysis of the composite samples revealed that the initial concentration of TIP had a significant influence on the morphology of the synthesized nanocomposites. Typically, at 80 °C and 6000 psi with initial concentration of 1.1 mol l^{-1} TIP (HAp-TiO_2-1), HAp nanoplates with 50-200 nm width and TiO_2 particles having a thick sheet-type structure with 200 nm width and 1-2 μm length were obtained (Figure 5.3d). At higher TIP concentration (1.5 mol/l), HAp nanoplates were formed on the surface of well-separated TiO_2 nanorods with a diameter of about 50-300 nm and lengths from 1 to 4 μm, as seen in the SEM and TEM images of HAp-TiO_2-2 given in Figure 3.3 e&g. The effect of the reaction pressure on the morphology of the nanocomposites was studied by varying the pressure from 6000 to 8000 psi, while keeping the temperature at 80 °C and the initial TIP concentration of 1.5 mol l^{-1}. SEM analysis of the HAp-TiO_2-3 (prepared at 8000 psi) revealed that the $scCO_2$ pressure did not have a significant effect on the morphology of the synthesized particulates (data not shown here). On the other hand, using the hydrothermal technique resulted in the formation of oblong-shaped particles, as shown in Figure 5.3f&h.

www.manaraa.com

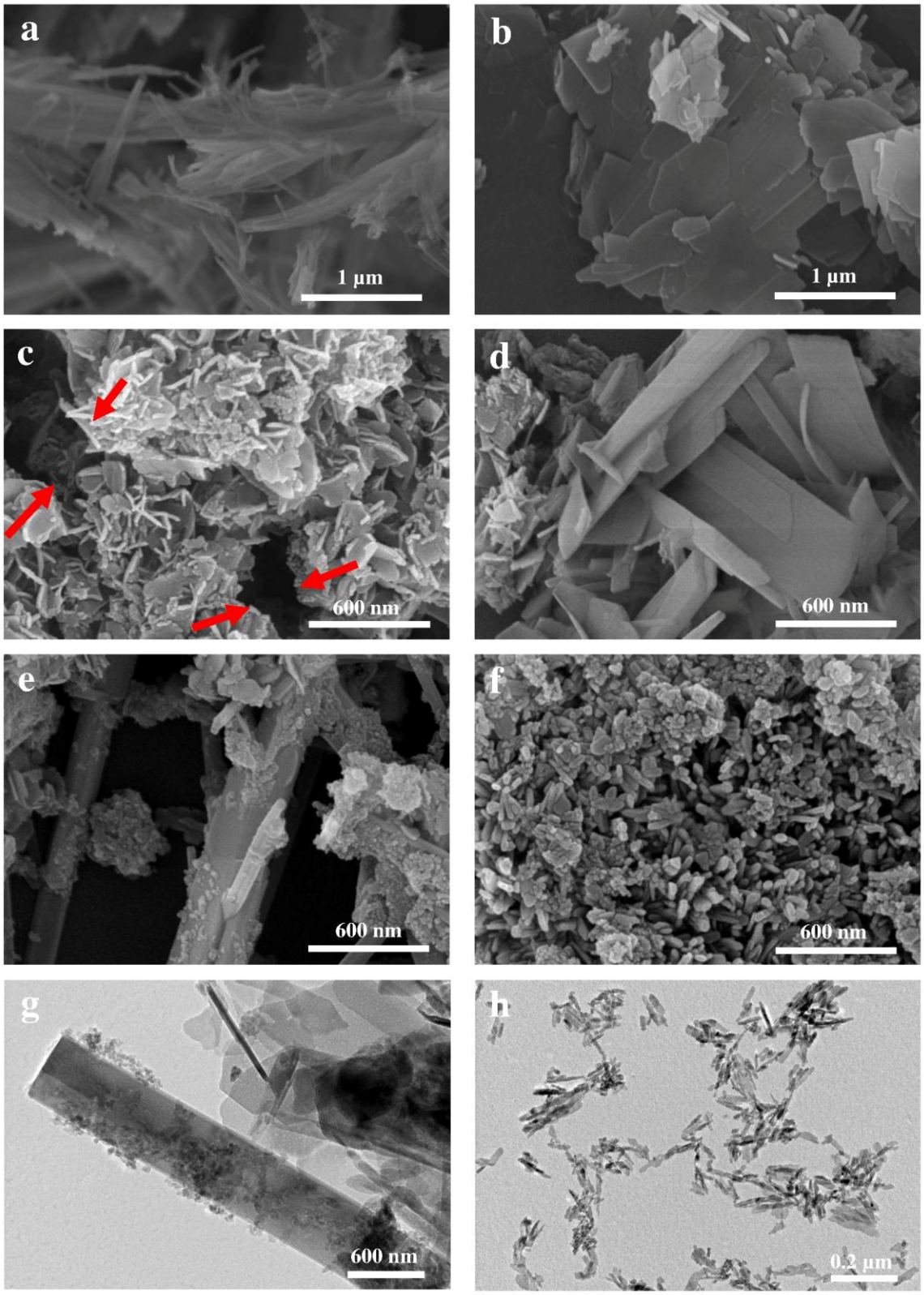

www.manaraa.com

Figure 5.3. SEM images of the (a) TiO_2 nanotubes calcined at 450 °C, (b) as-prepared HAp-1 nanoplates, (c) as-prepared HAp-2 nanoplates, (d) HAp-TiO_2-1 nanocomposites calcined at 500 °C, (e) HAp-TiO_2-2 nanocomposites calcined at 500 °C, and (f) HAp-TiO_2-h nanocomposites and TEM images of (g) HAp-TiO_2-2 nanocomposites calcined at 500 °C and (h) HAp-TiO_2-h nanocomposites. Arrows in Figure 5.3c indicate the voids between aggregates of plate-like HAp secondary particles.

5.3.2 EDS analysis of HAp and HAp-TiO_2 nanocomposites

To provide additional information on elemental analysis for the synthesized HAp-TiO_2 nanocomposites, energy-dispersive spectroscopy (EDS) was used to map Ca, P, Ti, and O. EDS is a widely utilized tool for bulk elemental analysis of samples where the X-rays are generated in a region about 2 μm in depth. Figure 5.4 and Figure 5.5 clearly demonstrate the presence of Ca, P, Ti, and O in the nanocomposites. From the EDS elemental mapping of HAp-TiO_2-2 nanocomposites (Figure 5.4), the rod like morphology shows the presence of Ti, the major elemental component of TiO_2, in the composites (Figure 5.4c). It can also be seen that Ca (Figure 5.4e) and P (Figure 5.4d), found exclusively in HAp, are uniformly distributed on the surface of the TiO_2 rods. This further confirms that the nanoplates are HAp grown on the surface of TiO_2 rods.

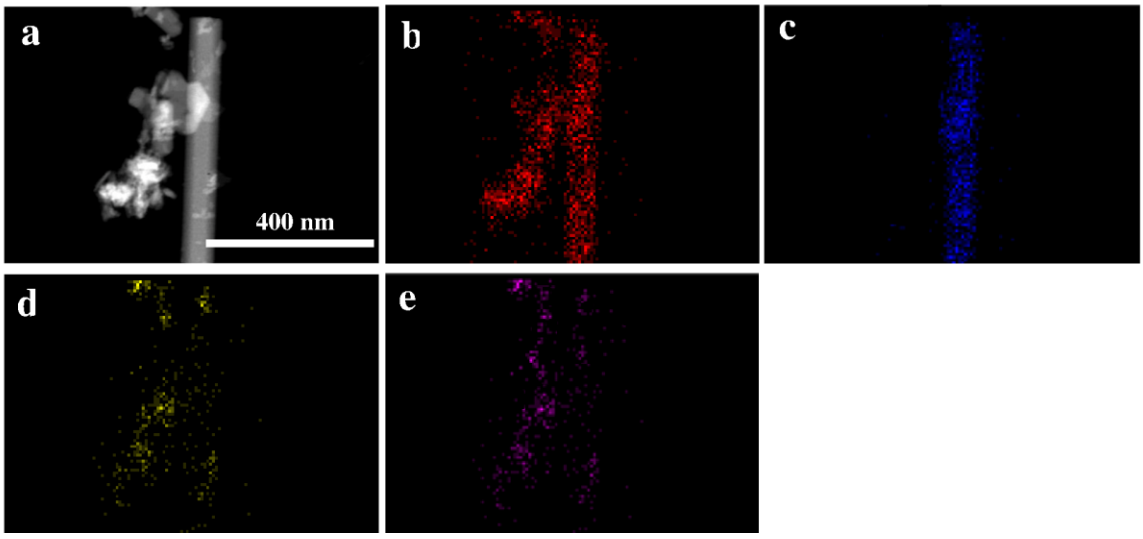

Figure 5.4. EDS elemental mapping of HAp-TiO_2-2 nanocomposites: (a) selected area on the sample, (b) O mapping, (c) Ti mapping, (d) P mapping, and (e) Ca mapping.

www.manaraa.com

EDX elemental mapping of HAp-TiO_2-h nanocomposites demonstrates a relatively homogeneous distribution of Ti (Figure 5.5c), P (Figure 5.5d), and Ca (Figure 5.5e) throughout the composite material. Thus, it can also be concluded that the oblong-shaped particles of TiO_2 and HAp are uniformly and homogeneously distributed within the synthesized nanocomposites.

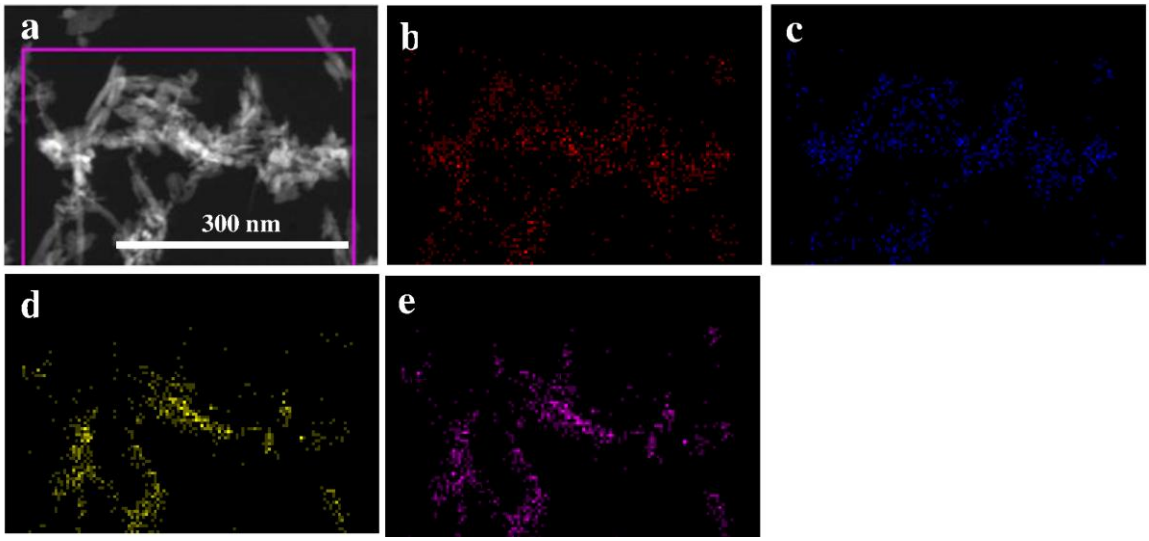

Figure 5.5. EDS elemental mapping of HAp-TiO_2-h nanocomposites: (a) selected area on the sample, (b) O mapping, (c) Ti mapping, (d) P mapping, and (e) Ca mapping.

The EDX spectra for HAp-2 and HAp-TiO_2-2 are shown in Figure 5.6. The investigation confirms the existence of Ca, P, O, and C elements for HAp-2 (Figure 5.6a) and Ca, P, O, Ti, and C elements in the synthesized HAp-TiO_2-2 nanocomposites (Figure 5.6b). Calcium to phosphorus (Ca/P) atomic ratio of HAp-1 and HAp-2 powders (Table 5.2) indicates a predominately stoichiometric HAp crystal (Ca/P≈1.67). In addition, there was no significant difference among the Ca/P ratios of the HAp-TiO_2 nanocomposites synthesized at different conditions (reaction temperature, reaction pressure, and initial concentration of TIP) and HAp-TiO_2-h nanocomposites, exhibiting a lowered Ca/P atomic ratio, likely reflecting higher PO_4^{3-} content.

www.manaraa.com

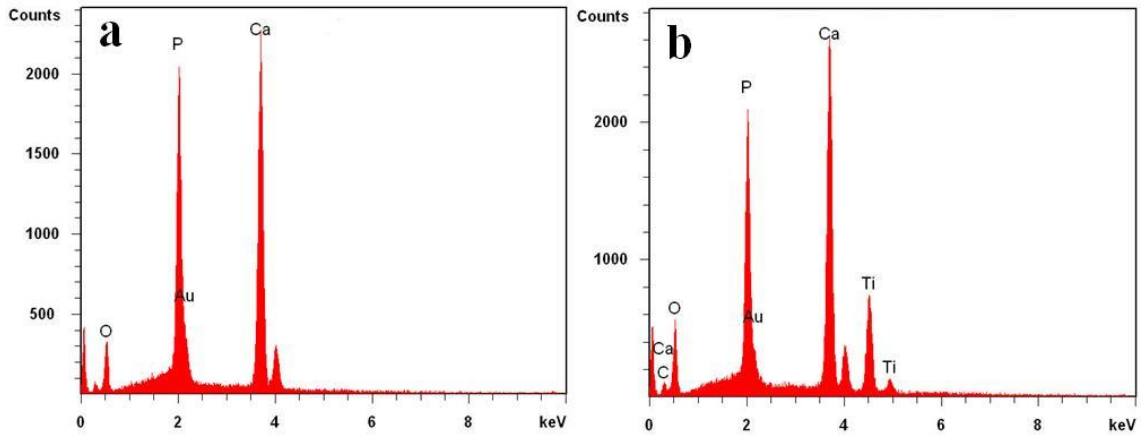

Figure 5.6. EDX spectra of the (a) HAp-2 and (b) HAp-TiO_2-2 nanocomposites.

Table 5.2. Ca/P atomic ratio of HAp powders and HAp-TiO_2 nanocomposites.

	Atomic %			
	Ca	P	Ca/P	Ti
HAp-1	21.9 ± 1.2	13.45 ± 1.7	1.63 ± 0.06	-
HAp-2	24.7 ± 2.3	14.97 ± 1.3	1.65 ± 0.06	-
HAp-TiO_2-1	27.36 ± 1.8	17.2 ± 1.6	1.59 ± 0.04	5.8 ± 1.2
HAp-TiO_2-2	27.6 ± 1.9	17.81 ± 1.3	1.53 ± 0.02	7.8 ± 1.1
HAp-TiO_2-3	25.08 ± 2.2	16.5 ± 1.8	1.52 ± 0.05	5.9 ± 0.08
HAp-TiO_2-h	21.85 ± 1.4	14.64 ± 0.9	1.49 ± 0.02	4.88 ± 0.06

5.3.3 XRD analysis of HAp and HAp-TiO_2 nanocomposites

Figure 5.7 shows the XRD patterns for the HAp-2 and HAp-TiO_2-2 and HAp-TiO_2-h nanocomposites in the 2θ range of 10-70°. In the XRD pattern of HAp-2 (Figure 5.7a), all the diffraction peaks correspond to hexagonal HAp according to JCPDS: 09-432.[5] No

www.manaraa.com

impurities are observed in the pattern, indicating pure HAp. In Figure 5.7b&c (for HAp-TiO_2 nanocomposites), the XRD patterns show all the diffraction peaks for HAp, along with new intensive peaks at $2\theta \approx 25.2°$, 37.7°, 53.8°, and 55° (shown by filled triangles) which are the prominent characteristic peaks of anatase TiO_2 assigned to the diffraction of (101), (004), (105), and (211) planes of TiO_2 anatase phase, respectively, confirming the incorporation of titania into the HAp matrix. This perfectly coincides with the anatase TiO_2 JCPDS card data (file No: 21-1272). Meanwhile, the peak at 47.9° is consistent with (213) Bragg reflection of HAp and (200) plane of TiO_2 anatase.[5, 21, 31] From the XRD patterns, it can be concluded that the unique HAp-TiO_2 nanocomposites maintain HAp crystal phase without phase transformation. Under the examined experimental conditions, the HAp precursor is stable, with TIP precursors grown to form anatase TiO_2 rod-like crystals. For the composite samples it can also be observed that the intensity of the TiO_2 peaks increases with the increase of the TiO_2 content, while the intensity of the HAp peaks decreases, as distinguishable in the XRD pattern of HAp-TiO_2-2 nanocomposites shown in Figure 4b compared to the HAp-TiO_2-h nanocomposite (Figure 5.7c).

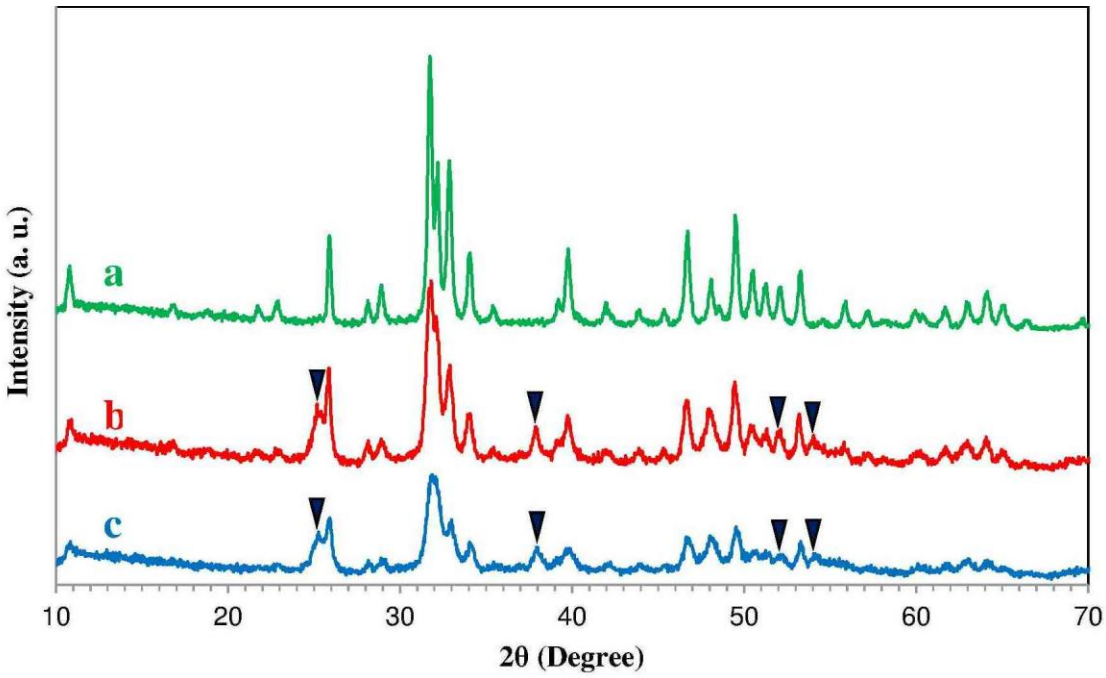

www.manaraa.com

Figure 5.7. XRD patterns of the (a) HAp-2, (b) HAp-TiO_2-2, and (c) HAp-TiO_2-h nanocomposites. In Figure 5.7b&c, filled triangles are representing the prominent characteristic peaks of anatase TiO_2.

5.3.4 FTIR spectroscopy of HAp and HAp-TiO_2 nanocomposites

The synthesized HAp and HAp-TiO_2 nanocomposites were also analyzed by means of FTIR. The FTIR spectra of HAp-2 nanoplates and HAp-TiO_2-2 and HAp-TiO_2-h nanocomposites are displayed in Figure 5.8. Several characteristic peaks of HAp are present in all the three spectra at 3570, 1095, 1034, 962, 633, 602, and 565 cm^{-1}. The peaks at 3570 and 633 cm^{-1} are attributed to the stretching and libration bands originating from the OH^- ion, respectively while the characteristic bands of PO_4^{3-} ion appear at 1095 and 1034 (υ_3), 962 (υ_1), 602 and 565 cm^{-1} (υ_4).[32-34] The well-preserved characteristic peaks of HAp in the spectra of HAp-TiO_2 nanocomposites suggest no significant structural change or transformation of HAp during the formation of the HAp-TiO_2 nanocomposites. This is fairly difficult to attain by using other synthesis methods, confirming the superior temperature control provided by the proposed synthesis method for HAp-TiO_2 nanocomposites. The broad peaks at 3429 and 1635 cm^{-1} in Figure 3.8 a are attributable to the O-H stretching and bending modes of the surface-absorbed water, respectively. These peaks became more evident in the spectra of the synthesized HAp-TiO_2 nanocomposites (Figure 5.8b&c), maybe also attributable to the structural hydroxyl group in the nano TiO_2.[35] In comparison to the spectrum of HAp (Figure 5.8a), there is an extra broad peak in the region of 600-800 cm^{-1} in the spectra of HAp-TiO_2 nanocomposites (Figure 5.8b&c), with the spectrum of HAp-TiO_2-2 (Figure 5.8b) being more evident. This broad peak may be due to the Ti-O-Ti band of TiO_2 as revealed by XRD.[36] Hence, these FTIR results confirmed the presence of TiO_2 with intact HAp in the synthesized HAp-TiO_2 nanocomposites.

www.manaraa.com

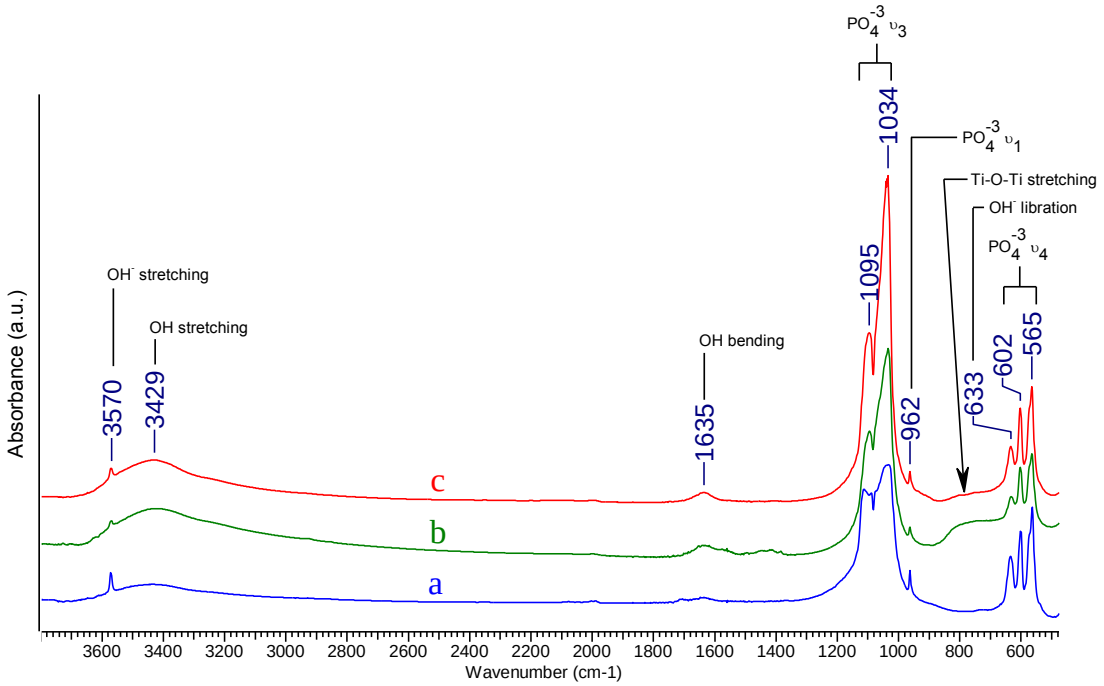

Figure 5.8. Fourier transform infrared (FTIR) spectroscopy of the (a) HAp-2, (b) HAp-TiO_2-2, and (c) HAp-TiO_2-h nanocomposites.

5.3.5 BET analysis of HAp and HAp-TiO_2 nanocomposites synthesized in supercritical CO_2

The N_2 adsorption-desorption isotherms of the pure HAp-2 and HAp-TiO_2-2 nanocomposites are plotted in Figure 5.9a&b, respectively. Both isotherms correspond to type IV isotherms (IUPAC classification) with a capillary condensation step above 0.4 P/P0, which is typical of mesoporous structures.[37, 38] According to the IUPAC classification, the isotherms have a type H3 hysteresis loop with the continuous nitrogen uptake at very high relative pressure that is associated with aggregates of plate-like HAp particles giving rise to slit-shaped pores.[39] The HAp-TiO_2 nanocomposites show significantly higher specific surface area, close to 170 m^2/g with very homogeneous mesopores that are clearly distinguished from the macropores as confirmed by its N_2 physisorption isotherm (Figure 5.9b). The adsorption in the low relative pressure region is a consequence of adsorption in micropores. The first hysteresis loop in the P/P0 range of 0.4-0.6 corresponds to the small size mesopores generated from the void space between the HAp crystallites.[39] Moreover, it exhibits another distinguished steep

www.manaraa.com

increase in the adsorption starting at P/P0 of 0.8. This nitrogen uptake at very high relative pressure corresponds to the formation of macropores that start filling only at high P/P0, close to 1.0. The observed macroporosity can be referred to the voids between agglomerate of plate-like HAp primary particles, voids between the secondary particles.[40] Pure HAp-2 exhibits surface area of about 72 m^2/g, and compared with HAp-TiO_2 nanocomposites it showed a wide distribution of the pores and larger average pore diameter as shown in Figure 5.9a. The capillary condensation step is much pronounced and shifted to higher relative pressures, 0.6-0.8, for pure HAp with respect to HAp-TiO_2 composite, which reveals the dominance of larger mesopores.[37] The SEM micrographs of pure HAp, Figure 5.3c, show aggregates of porous secondary particles. Compared with HAp-TiO_2 composite, the aggregates are larger, 0.3-0.8 μm, indicating the presence of larger and less homogeneous macropores. Therefore, it is suggested that in the case of HAp-TiO_2 nanocomposite, the HAp agglomerates forming the slit like pores tend to diminish in population and size. Also, the volume of the intercrystallite HAp space is reduced, so it could be concluded that the mesopore size of HAp is altered upon formation of TiO_2. Farhangi and Charpentier synthesized TiO_2 nanowires on the graphene sheets in $scCO_2$, reporting similar results.[41]

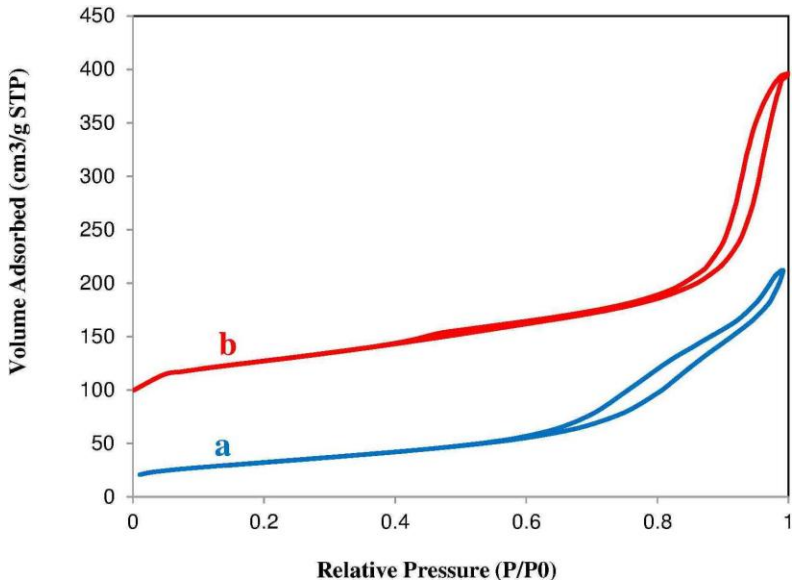

Figure 5.9. N_2 adsorption/desorption isotherm of the (a) HAp-2 and (b) HAp-TiO_2-2 nanocomposites.

www.manaraa.com

5.3.6 XPS measurements of HAp and HAp-TiO_2 nanocomposites synthesized in supercritical CO_2

During the A chemical analysis of the HAp and HAp-TiO_2 samples was performed using XPS, and the core level spectra obtained for the samples of HAp-2 and HAp-TiO_2-2 are depicted in Figure 5.10. As illustrated in the survey scans (Figure 5.10a&e), the only elements detected on the surface are Ca, P, O, and C for HAp-2 and Ca, P, O, Ti, and C for HAp-TiO_2-2 nanocomposites. The respective atomic percentages of those elements are given in Table 5.3. No contaminant element other than carbon was detected. The carbon concentration of 11.3 and 11.9% observed in HAp-2 and HAp-TiO_2-2 composites, respectively, is typical for organic contamination levels on clean surfaces.[18] This contamination could be resulted from the chemisorption of CO_2 molecules from the atmosphere and from the reaction under $ScCO_2$, unreacted acetic acid, and washing with $ScCO_2$. In the recorded spectrum for HAp-2, the high resolution XPS scan of the Ca 2p region (Figure 5.10b) could be resolved into two peaks for Ca 2p1/2 and Ca 2p3/2 at binding energies of 350.80 eV and 347.28 eV, respectively, which are related to hydroxyapatite. In the high resolution P 2p XPS scan of HAp (Figure 5.10c), two peaks for P 2p1/2 and P 2p3/2 are observed at 134.99 eV and 133.15 eV, respectively, which correspond to P in hydroxyapatite. Figure 5.10d shows the core level spectrum of O 1s, and the peaks at binding energies of 532.93 eV and 531.12 eV are attributed to the adsorbed water in hydroxyapatite crystal and phosphate group, respectively.[11] The calculated Ca/O and Ca/P ratios for the HAp-2 are 0.34 and 1.62, respectively, which are very close to the theoretical values of 0.38 and 1.67 for HAp. The high resolution XPS record of Ca 2p region of HAp-TiO_2 (Figure 5.10f) shows peaks for Ca 2p1/2 and Ca 2p3/2 at bonding energies of 350.99 eV and 347.44 eV, respectively, and that of P 2p represents two peaks for P 2p1/2 and P 2p3/2 at 134.12 eV and 133.28 eV, respectively (Figure 5.10g). These peak positions coincide well with the Ca and P in hydroxyapatite, as explained earlier, and only the negligible difference in binding energies of Ca 2p and P 2p core levels indicates the formation of HAp with similar stoichiometries in both HAp-2 and HAp-TiO_2-2 nanocomposite. The O 1s XPS spectrum (Figure 5.10h) could be deconvoluted into three distinct peaks indicating the presence of multiple O species on the surface.[42] The sub-peak at binding energy of 529.59 eV is assigned to the lattice

www.manaraa.com

oxygen atoms TiO_2 (Ti-O bonds), while the sub-peak peak at 533.36 corresponds to adsorbed water in HAp crystal, and the other peak at 531.41 eV is due to contribution of OH^- groups on the surface, phosphate group, and/or defective oxide sites. In Figure 5.10, the core level spectrum of Ti 2p could be resolved into two spin-orbit pairs of 2p3/2 and 2p1/2 with binding energies of 458.35 eV and 464.02 eV, respectively, which are attributed to Ti in the 4+ state.[43] Therefore, the Ti detected in TiO_2-HAp nanocomposites is only the oxide (TiO_2) derived from the TIP hydrolyzed in the synthesis procedure. These XPS results confirm the formation of hydroxyapatite and titania in the HAp-TiO_2 nanocomposites, and also indicate that the HAp-TiO_2 nanocomposite is stable under the reaction conditions. The calculated Ca/O and Ca/P ratios for the HAp-TiO_2-2 composite are 0.3 and 1.43, respectively. The obtained Ca/O and Ca/P ratios can be considered close to the theoretical ones, as the XPS information is mediated on the analyzed area constituted by TiO_2 and HAp.[18] Consequently, due to the matrix effect, the intensity and the resolution of the Ca 2p and P 2p signals in both HAp-2 and HAp-TiO_2-2 composite samples are lower than the ones detected for the same elements in stoichiometric HAp powder.

Table 5.3. Atomic percentage of the elements detected in the HAp-2 and HAp-TiO_2-2 samples.

	Atomic %				
	Ca	P	O	C	Ti
HAp-2	19.3	11.9	57.5	11.3	-
TiO_2-HAp-2	15.2	10.6	57.9	11.9	4.5
			TiO_2 / 6.72	**HAp, OH** / 51.18	

Compared to the theoretical value for Ca/O ratio, 0.38, the calculated Ca/O ratio for the HAp-TiO_2-2 composite corresponds to the oxygen excess that could be attributed to the

www.manaraa.com

presence of OH groups on the surface. It is reported that the hydroxyl groups, such as Ti-OH, remain in the sol-gel prepared materials promoting the osteointegration process [18]. Therefore, from the XPS results it could be suggested that the prepared HAp-TiO_2 composites may exhibit enhanced bioactive properties. In order to confirm this hypothesis, a study of *in vitro* biocompatibility of the synthesized nanocomposites is planned as the next stage for this work.

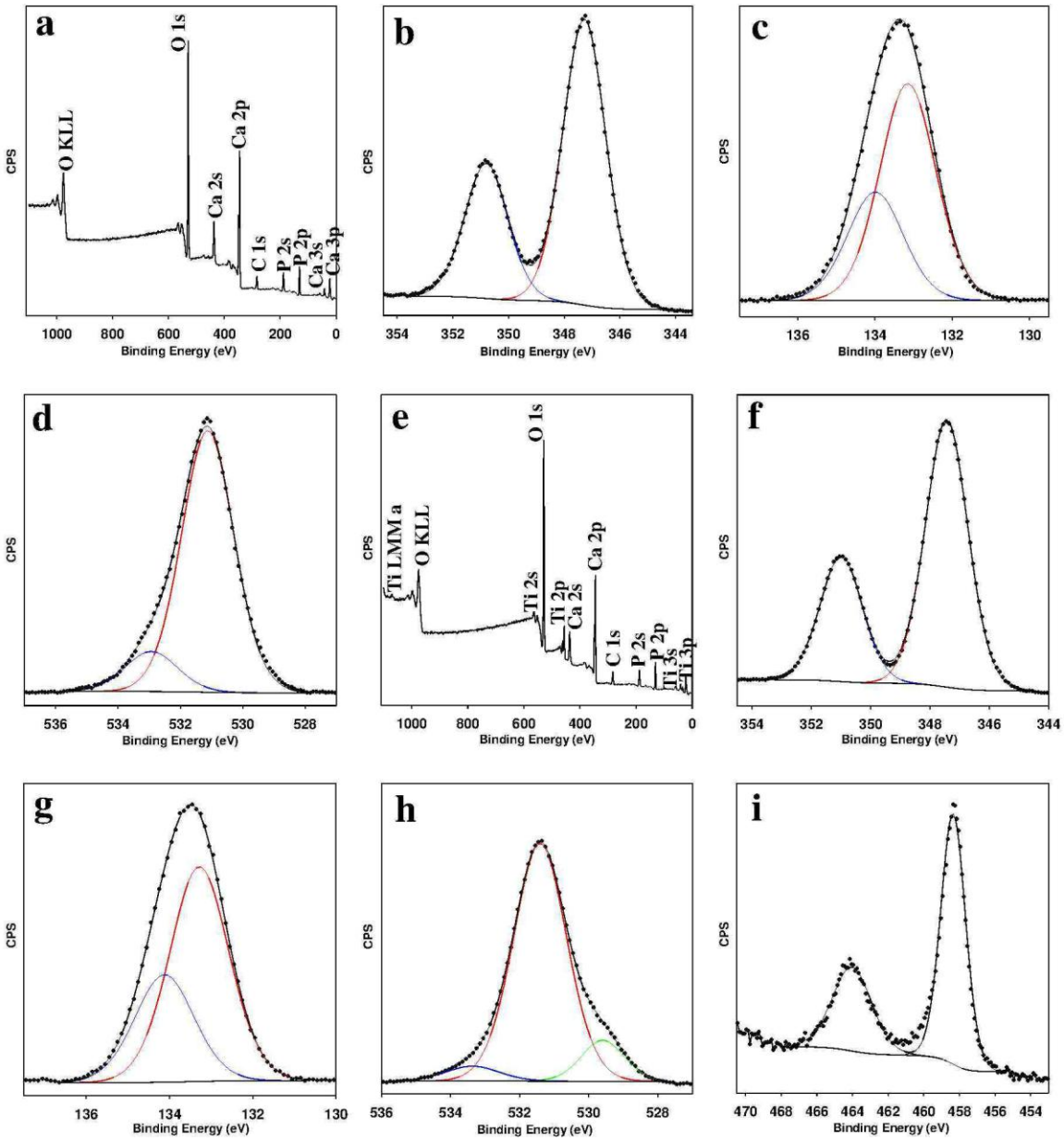

www.manaraa.com

Figure 5.10. (a) XPS survey spectrum of the HAp-2 and core level spectra of (b) Ca 2p, (c) P 2p, and (d) O 1s recorded from the HAp-2 and (e) XPS survey spectrum of the HAp-TiO_2-2 and core level spectra of (f) Ca 2p, (g) P 2p, (h) O 1s, and (i) Ti 2p recorded from the HAp-TiO_2-2.

5.3.7 XANES spectroscopies of TiO_2, HAp, and HAp-TiO_2 nanocomposites synthesized in supercritical CO_2

Figure 5.11 shows the Ti $L_{3,2}$-edge XANES of the HAp-TiO_2-2 nanocomposites in comparison with TiO_2 nanoparticles synthesized in supercritical CO_2 following the procedure presented in Salarian et al.[30] after calcination at 450 °C and 750 °C as standard samples. X-ray diffraction studies of the TiO_2 nanoparticles showed that the as-prepared materials transferred from the amorphous to anatase phase during heat treatment at 450 °C, while after calcination at 750 °C the transformation from anatase to rutile occurs (data not shown here). Characteristic features of TiO_2 can be observed that arise from the transitions of Ti 2p electrons to unoccupied 3d electronic states. From the XANES spectra of TiO_2 standard samples, the peaks in the spectra can be understood as due to the crystal field splitting of the d orbitals into t_{2g} and e_g under O_h symmetry followed by local distortion resulting in a local symmetry of D_{2d} and D_{2h} for anatase (TiO_2 nanoparticles calcined at 450 °C) and rutile (TiO_2 nanoparticles calcined at 750 °C), respectively. It can be seen that the most significant difference is the intensity ratio of peak *a* and *b*, i.e. *a* is more intense than *b* in anatase (Figure 5.11a), but in rutile (Figure 5.11b) this is reversed. The lowering of the O_h symmetry to D_{2d} and D_{2h} leads to the $2p \rightarrow e_g$ transition further splitting into peak *a* and *b* at the L_3-edge. The e_g state is more sensitive to the variation in symmetry; and thus, anatase and rutile phases can be tracked by the relative ratio of peaks *a* and *b*.[44, 45] The spectrum of the HAp-TiO_2-2 nanocomposites (Figure 5.11c) shows well-resolved features of the anatase phase, as can be immediately identified by the intensity ratio between *a* and *b*. It indicates that the TiO_2 in the nanocomposites is of anatase phase, which is consistent with the XRD results.

www.manaraa.com

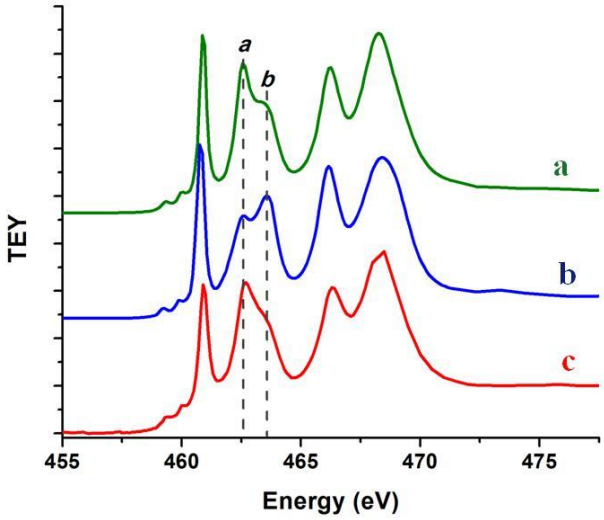

Figure 5.11. Ti $L_{3,2}$-edge XANES spectra of the (a) TiO_2 nanoparticles calcined at 450 °C, (b) TiO_2 nanoparticles calcined at 750 °C, and (c) HAp-TiO_2-2 nanocomposite.

Figure 5.12 shows the Ca $L_{3,2}$-edge XANES spectra of the HAp-TiO_2-2 nanocomposites and HAp-2 powders. Sharp peaks at 351.4 and 354.7 eV are observed, which come from the transitions of $2p_{3/2}$ and $2p_{1/2}$ electrons to the empty 3d state of Ca^{2+} ion that yields this spin-orbit doublet. The XANES spectrum of HAp-TiO_2-2 nanocomposites (Figure 5.12b) shows the same features to that of HAp-2 (Figure 5.12a), indicating that HAp was formed in the sample. Ca $L_{3,2}$-edge XANES results agree with the XRD results.

www.manaraa.com

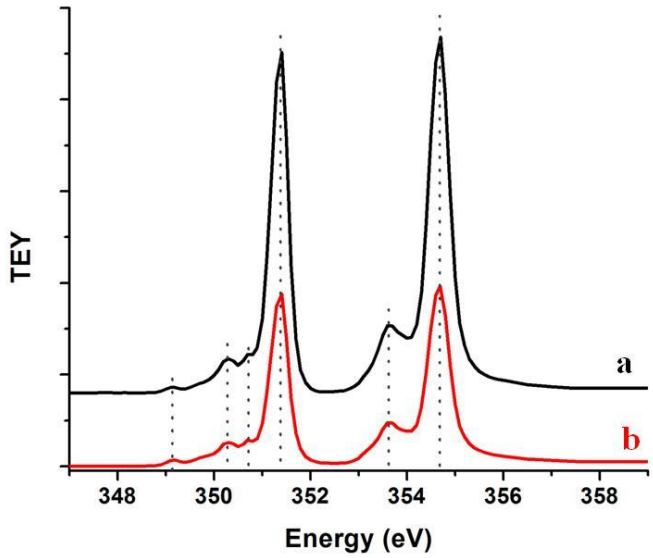

Figure 5.12. Ca $L_{3,2}$-edge XANES spectra of the (a) HAp and (b) HAp-TiO_2-2 nanocomposite powders.

Figure 5.13(I) shows the O K-edge XANES spectra of the HAp-TiO_2-2 nanocomposites in comparison with HAp-2, anatase, and rutile TiO_2. The peaks are from the transitions of O 1s to 2p (for TiO_2, O 2p states are hybridized with Ti 3d states). It can be seen that the spectrum of the HAp-TiO_2-2 nanocomposites (Figure 5.13(I) b) shows the features of both anatase TiO_2 and HAp (e.g.: peaks *a* and *c* are from anatase TiO_2, and peaks *b*, *d*, and *e* are from HAp). It agrees well with the Ti $L_{3,2}$-edge and Ca $L_{3,2}$-edge XANES results, confirming that the prepared sample contains both anatase TiO_2 and HAp. Since the edge jump of the XANES spectrum is proportional to the quantities of the sample, the compositional fractions of the HAp-TiO_2-2 nanocomposites can be obtained by fitting a linear combination of the spectra of their components to that of the composites. Figure 5.13(II) displays the linear fitting results of the HAp-TiO_2-2 nanocomposites. The fitting curve (red dash-dotted curve) is in good agreement with the experimental data (black solid curve), illustrating that the weight ratio between anatase TiO_2 and HAp is about 1:1.6. This also implies that the nanocomposite is uniform in the area being probedwhich are essentially at the same retention times as that of the reference sample.

www.manaraa.com

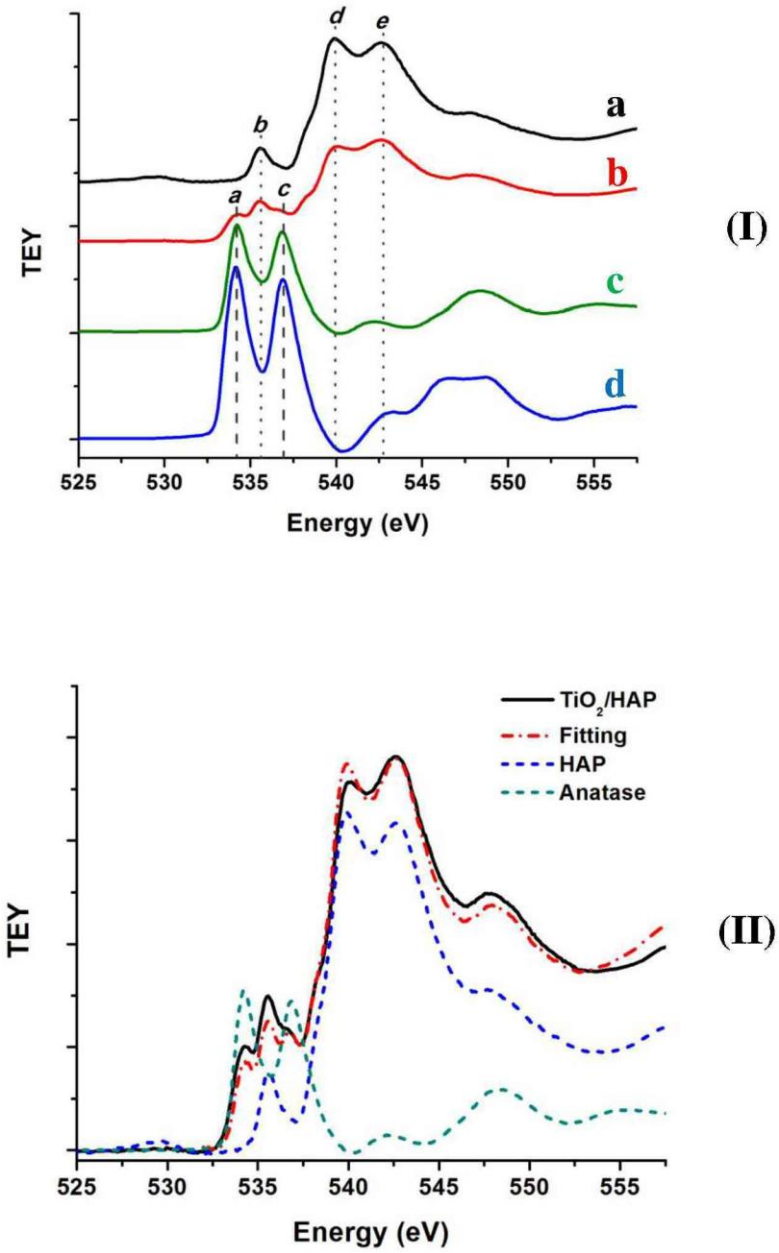

Figure 5.13. (I) O K-edge XANES spectra of the (b) HAp-TiO_2-2 nanocomposites in comparison with (b) HAp-2, (c) TiO_2 nanoparticles calcined at 450 °C, and (d) TiO_2 nanoparticles calcined at 750 °C. **(II)** O K-edge linear fitting of the HAp-TiO_2-2 nanocomposites.

5.3.8 TGA of HAp and HAp-TiO_2 nanocomposites

The thermal analysis of the HAp-2 powder and HAp-TiO_2-2 and HAp-TiO_2-h nanocomposites was performed under flowing air from room temperature to 1200 °C by

www.manaraa.com

TGA, as illustrated in Figure 5.14. The TGA curve of pure HAp is divided into four stages based on heating in air, as illustrated in Figure 5.14a. The first stage from room temperature to 240 °C corresponds to the evaporation of the physically absorbed water of the product. The second stage is from 240 to 440 °C, which is attributed to the combustion and carbonization of organic substance such as CTAB and unreacted acetic acid. The third stage from 440 to 550 °C is caused by the decomposition of residual organic materials. The forth stage took place between 550-1100 °C with a peak at 800 °C, which is due to the partial decomposition of HAp to low-temperature phase of tricalcium phosphate (β-TCP). It has been reported that HAp is likely to decompose at 800-900 °C in air and 950 °C in vacuum,[46, 47] and the following chemical reaction is proposed:

$$Ca_{10}(PO_4)_6(OH)_2 = CaO + 3Ca_3(PO_4)_2 + H_2O\ (g) \quad (1)$$

For TiO_2-HAp nanocomposites, the increase in peak area of the peak at 800 °C as compared to pure HAp is due to both the partial dissociation of HAp to TCP as well as the conversion of anatase TiO_2 to the rutile phase of TiO_2 crystal, as the transformation from anatase to rutile occurs at temperatures between 400 and 1000 °C.[12] Moreover, it has been reported that the reaction between HAp and TiO_2 is feasible and expected to happen at the temperature above ~750 °C, and β-TCP and $CaTiO_3$ are formed.[47] The related chemical reaction is as follows:

$$Ca_{10}(PO_4)_6(OH)_2 + TiO_2 = 3Ca_3(PO_4)_2 + CaTiO_3 + H_2O\ (g) \quad (2)$$

There is another possibility of formation of TCP through the direct dissociation of HAp, as it can dissociate to Ca-orthophosphate and TCP by the following reaction:

$$Ca_{10}(PO_4)_6(OH)_2 = 2Ca_3(PO_4)_2 + Ca_4O(PO_4)_2 + H_2O\ (g) \quad (3)$$

And the Ca-orthophosphate formed as a result of reaction (3) subsequently reacts with TiO_2 leading to the formation of TCP and $CaTiO_3$.[47] The suggested reaction could be:

$$Ca_4O(PO_4)_2 + TiO_2 = CaTiO_3 + Ca_3(PO_4)_2 \quad (4)$$

From the above discussion, the weight changes in this region should therefore be correlated with TiO_2 phase transformation and TCP and $CaTiO_3$ formation (Eq. 2, 3, and

www.manaraa.com

4). Since TCP formation is widely reported in all the HAp-TiO_2 compositions at or above 900 °C, it is highly likely that the weight loss must be due to TCP formation by reaction (Eq. 2), while $CaTiO_3$ formation does not produce recordable weight change. In any case, the $CaTiO_3$ formation can be described by two possible reactions (Eq. 2, 4). So, it could be concluded that the presence of the titania modifies the thermal behavior with respect to the pure HAp.

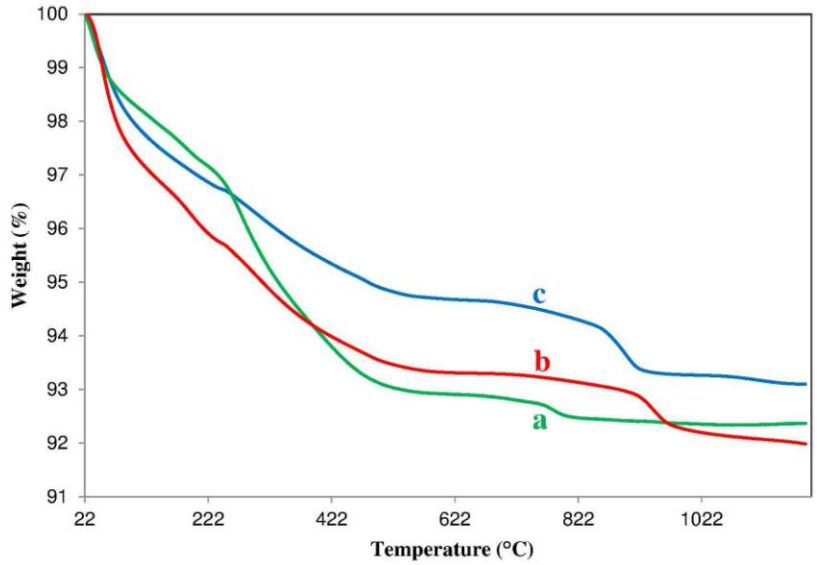

Figure 5.14. TGA spectrum of (a) HAp-2, (b) HAp-TiO_2-2 nanocomposites, and (c) HAp-TiO_2-h nanocomposites.

5.3.9 Mechanical properties of PCL/HAp and PCL/HAp-TiO_2 composites

The Young's modulus and tensile strength of PCL/HAp and PCL/HAp-TiO_2 composites comprising 0-30% (w/w) HAp and HAp-TiO_2 synthesized by the combined co-precipitation and sol-gel method and hydrothermal process were investigated. An exponential increase in the Young's modulus of PCL/HAp-2 and PCL/HAp-TiO_2-2 was observed with the increase in HAp-2 and HAp-TiO_2-2 concentrations, respectively. For example, the 20% (w/w) HAp-TiO_2-2 added composite possesses the highest Young's modulus with more than a 4-fold increase from 155.2 MPa for PCL alone to 665.5 MPa. Therefore, it could be concluded that the growth of titania nanorods followed by HAp deposition on the surface of the TiO_2 nanorods in supercritical CO_2 highly influences the

www.manaraa.com

mechanical properties of reinforced composites. Moreover, the ultimate tensile strength showed little variation between examined material groups, while a noticeable trend was observed with respect to loading concentration. It was shown that the tensile strength of PCL/HAp decreased from 9.3 for unfilled PCL to 6.47 MPa for PCL/HAp with increasing the amount of filler, HAp-2, to 30%. In other words, the greater HAp-2 content results in an increase in the brittle nature of the composites. On the contrary, an exponential increase in the tensile strength of PCL/HAp-TiO_2 composites to 11.97 and 15.76 MPa for specimens containing 10-20% (w/w) HAp-TiO_2 occurred. On the other hand, compared to PCL/HAp-TiO_2-h composite specimen containing 20% (w/w) HAp-TiO_2-h, PCL/HAp-TiO_2-2 composite clearly exhibits higher modulus and higher maximum tensile strength. The strengthening effects observed for PCL/HAp-TiO_2-2 composite over the PCL/HAp-TiO_2-h composition were concluded to be due to the morphology, size and, the preferred orientation. The comparison of the mechanical properties of our resulting nanocomposites to the work of others is complicated by the different measurement techniques utilized, although compared to cortical and cancellous bone, the tensile strength of our PCL/HAp-TiO_2-2 composites is considered to be sufficient enough to preserve their structure and mechanical integrity for predictable times, even under load-bearing conditions.

In addition, flexural modulus and flexural strength values of composites reflect its resistance to flexural loading which is a combination of tension and compression forces. Similarly, dramatic reinforcements in the flexural properties (FS and FM) were achieved for PCL/HAp-TiO_2-2 composites, as evident in Table 5.4. PCL/HAp-TiO_2-2 composite formulation containing 20 wt% HAp-TiO_2-2 exhibited a roughly 3-fold increase in flexural modulus and 2-fold increase in flexural strength compared to blank PCL. This extraordinary mechanical reinforcement provided by PCL/HAp-TiO_2-2 composites exceeded the enhancements observed with PCL/HAp-2 composites, indicating the importance of mechanical coupling between the TiO_2 nanorods and the PCL matrix.

The SEM micrographs of the fracture surfaces of the PCL/HAp-TiO_2 nanocomposite loaded with 20 wt% HAp-TiO_2 are shown in Figure 5.15. It can be seen that the nanocomposite loaded with 20 wt% HAp-TiO_2 exhibited a rough surface with partially

www.manaraa.com

broken or pulled out TiO_2 rod like structures on their surface, shown by the arrows in Figure 5.15b. This nanorod "pull out" effect may significantly increase the work of fracture due to interfacial friction between the TiO_2 nanorods and matrix resulting from the high surface area of the nanorods and the strong interfacial shear strength between the TiO_2 nanorods and PCL matrix. Moreover, it is clear from Figure 5.15b and d that there is a strong adhesion between the HAp-TiO_2 and PCL matrix, as these partially pulled out TiO_2 nanorods take part in bridging the crack during propagation and bridge the cracks in the matrix, seen in Figure 5.15c. Conversely, the unfilled PCL matrix displays a very smooth fracture plane with the cracks propagating without any hindrance (data not shown here).

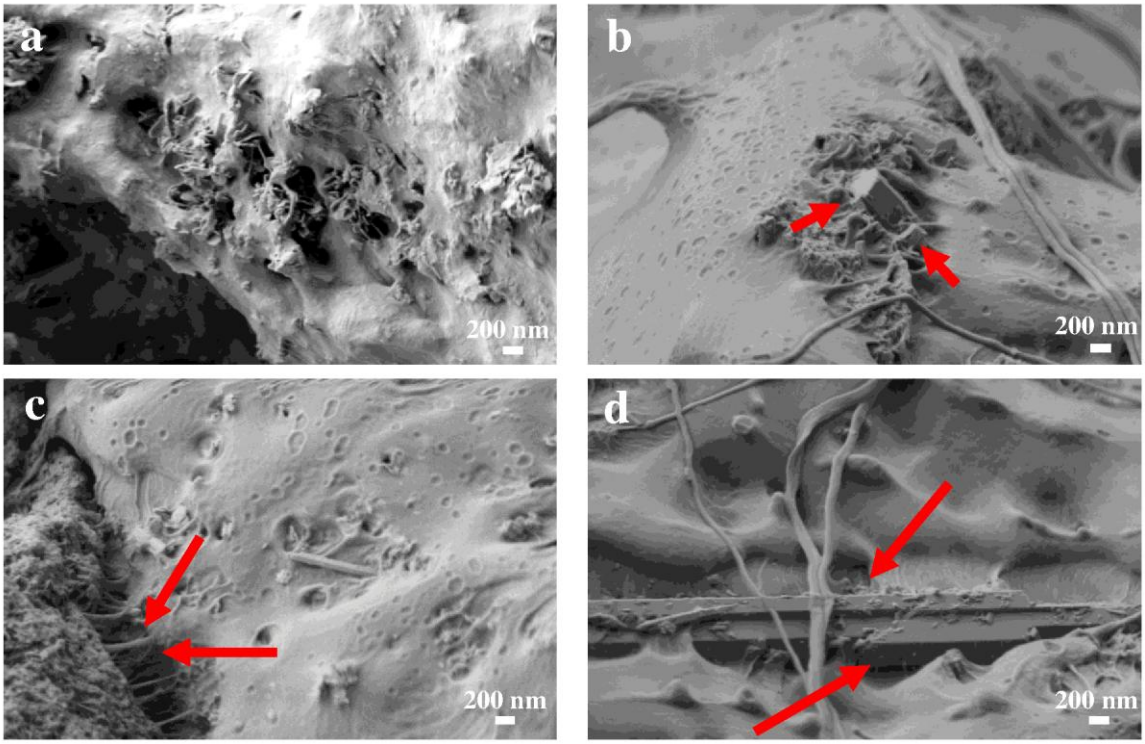

Figure 5.15. SEM images of the fracture surfaces of (a) PCL/HAp and (b-d) PCL/HAp-TiO_2 containing 20 wt% HAp and HAp-TiO_2, respectively. Short arrows indicate nanorods pullout and the long arrows indicate crack bridging by the TiO_2 nanorods.

Table 5.4. Mechanical Properties of PCL/HAp and PCL/HAp-TiO_2 composites.

www.manaraa.com

	PCL:HAp-TiO_2- 2 (w/w)	PCL: HAp-TiO_2- h (w/w)	Young's modulus (MPa)	Tensile strength (MPa)	Flexural modulus (MPa)	Flexural strength (MPa)
100:0	-	-	155.2 ± 24.5	9.3 ± 2.9	247 ± 28.5	13.2 ± 1.6
90:10	-	-	379.6 ± 16.1	10.9 ± 2.5	551 ± 16.8	16.3 ± 0.3
80:20	-	-	352.8 ± 16.3	7.1 ± 0.9	485.8 ± 23.6	16.6 ± 2.2
70:30	-	-	238.2 ± 11.5	6.47 ± 1.4	425 ± 32.7	11.4 ± 0.6
-	90:10	-	355.2 ± 13.2	11.97 ± 3.6	744.6 ± 25.8	18.23 ± 2.62
-	80:20	-	665.5 ± 24.6	15.76 ± 0.9	716.3 ± 14.6	26.5 ± 0.7
-	70:30	-	467 ± 6	11.51 ± 1.9	512 ± 24.3	17.4 ± 0.9
-	-	100:20	241.8± 25.6	6.24 ± 1.9	423.6 ± 35.4	10.8 ± 1.7

5.4 Conclusions

A novel combined co-precipitation and sol-gel method in the green solvent, supercritical carbon dioxide ($scCO_2$), was successfully applied to derive an innovative HAp-titania bioceramic with excellent chemical and structural uniformity. PCL/HAp-TiO_2 composites with significantly improved physical and mechanical properties suitable for tissue engineering was designed as described above. Our results showed that the morphology of the HAp-TiO_2 composites could be tailored by changing the initial concentration of TIP and the reaction temperature. The formed HAp-TiO_2 nanocomposites with a higher surface area and greater thermal stability compared to HAp nanoparticles are particularly attractive as reinforcing fillers for biodegradable synthetic

www.manaraa.com

polymers. With a loading of 20% (w/w) TiO_2-HAp, the obtained nanocomposites exhibited a tensile modulus of 665.5 MPa, which is more than a 4-fold increase compared to blank polymer. The presented work suggests that PCL/HAp-TiO_2 nanocomposites may be synthesized to match the mechanical properties of bone, and thus demonstrates the potential for their use in orthopedic and dental implant materials.

www.manaraa.com

5.5 References

1 Jevtic M, Mitric M, Skapin S, Jancar B, Ignjatovic N, Uskokovic D. Crystal structure of hydroxyapatite nanorods synthesized by sonochemical homogeneous precipitation. Crystal Growth and Design. 2008;8:2217-2222.

2 Sun Y, Guo G, Tao D, Wang Z. Reverse microemulsion-directed synthesis of hydroxyapatite nanoparticles under hydrothermal conditions. Journal of Physics and Chemistry of Solids. 2007;68:373-377.

3 Wang Y, Zhang S, Wei K, Zhao N, Chen J, Wang X. Hydrothermal synthesis of hydroxyapatite nanopowders using cationic surfactant as a template. Materials Letters. 2006;60:1484-1487.

4 Xiao X, Liu R, Zheng Y. Characterization of hydroxyapatite/titania composite coatings codeposited by a hydrothermal–electrochemical method on titanium. Surface and Coatings Technology. 2006;200:4406-4413.

5 Joseph Nathanael A, Mangalaraj D, Chen PC, Ponpandian N. Mechanical and photocatalytic properties of hydroxyapatite/titania nanocomposites prepared by combined high gravity and hydrothermal process. Composites Science and Technology. 2010;70:419-426.

6 Costa DO, Dixon SJ, Rizkalla AS. One-and Three-Dimensional Growth of Hydroxyapatite Nanowires during Sol–Gel–Hydrothermal Synthesis. ACS applied materials & interfaces. 2012;4:1490-1499.

7 Lin K, Chang J, Cheng R, Ruan M. Hydrothermal microemulsion synthesis of stoichiometric single crystal hydroxyapatite nanorods with mono-dispersion and narrow-size distribution. Materials Letters. 2007;61:1683-1687.

8 Liu Y, Hou D, Wang G. A simple wet chemical synthesis and characterization of hydroxyapatite nanorods. Materials chemistry and physics. 2004;86:69-73.

9 Salarian M, Solati-Hashjin M, Shafiei SS, Goudarzi A, Salarian R, Nemati A. Surfactant-assisted synthesis and characterization of hydroxyapatite nanorods under hydrothermal conditions. Materials Science-Poland. 2009;27:961-971.

10 Salarian M, Solati-Hashjin M, Shafiei SS, Salarian R, Nemati ZA. Template-directed hydrothermal synthesis of dandelion-like hydroxyapatite in the presence of cetyltrimethylammonium bromide and polyethylene glycol. Ceramics International. 2009;35:2563-2569.

11 Pushpakanth S, Srinivasan B, Sreedhar B, Sastry T. An *in situ* approach to prepare nanorods of titania–hydroxyapatite (TiO_2–HAp) nanocomposite by microwave hydrothermal technique. Materials chemistry and physics. 2008;107:492-498.

www.manaraa.com

12 Fidancevska E, Ruseska G, Bossert J, Lin Y-M, Boccaccini AR. Fabrication and characterization of porous bioceramic composites based on hydroxyapatite and titania. Materials chemistry and physics. 2007;103:95-100.

13 Sato M, Aslani A, Sambito MA, Kalkhoran NM, Slamovich EB, Webster TJ. Nanocrystalline hydroxyapatite/titania coatings on titanium improves osteoblast adhesion. Journal of Biomedical Materials Research Part A. 2008;84:265-272.

14 Kim HW, Kim HE, Salih V, Knowles JC. Hydroxyapatite and titania sol–gel composite coatings on titanium for hard tissue implants; mechanical and *in vitro* biological performance. Journal of Biomedical Materials Research Part B: Applied Biomaterials. 2005;72:1-8.

15 Oktar F. Hydroxyapatite–TiO_2 composites. Materials Letters. 2006;60:2207-2210.

16 Kim HM, Chae WP, Chang KW, Chun S, Kim S, Jeong Y, Kang IK. Composite nanofiber mats consisting of hydroxyapatite and titania for biomedical applications. Journal of Biomedical Materials Research Part B: Applied Biomaterials. 2010;94:380-387.

17 Wakamura M. Photocatalysis by calcium hydroxyapatite modified with Ti (IV). Fujitsu Sci Tech J. 2005;41:181-190.

18 Milella E, Cosentino F, Licciulli A, Massaro C. Preparation and characterisation of titania/hydroxyapatite composite coatings obtained by sol–gel process. Biomaterials. 2001;22:1425-1431.

19 Im K-H, Lee S-B, Kim K-M, Lee Y-K. Improvement of bonding strength to titanium surface by sol–gel derived hybrid coating of hydroxyapatite and titania by sol–gel process. Surface and Coatings Technology. 2007;202:1135-1138.

20 Anmin H, Tong L, Ming L, Chengkang C, Huiqin L, Dali M. Preparation of nanocrystals hydroxyapatite/TiO_2 compound by hydrothermal treatment. Applied Catalysis B: Environmental. 2006;63:41-44.

21 Siddharthan A, Kumar T, Seshadri S. *In situ* composite coating of titania–hydroxyapatite on commercially pure titanium by microwave processing. Surface and Coatings Technology. 2010;204:1755-1763.

22 Pai RA, Humayun R, Schulberg MT, Sengupta A, Sun J-N, Watkins JJ. Mesoporous silicates prepared using preorganized templates in supercritical fluids. Science. 2004;303:507-510.

23 Sui R, Rizkalla AS, Charpentier PA. Formation of titania nanofibers: A direct sol-gel route in supercritical CO_2. Langmuir. 2005;21:6150-6153.

www.manaraa.com

24 Lucky RA, Charpentier PA. A One-Step Approach to the Synthesis of ZrO_2-Modified TiO_2 Nanotubes in Supercritical Carbon Dioxide. Advanced Materials. 2008;20:1755-1759.

25 Lucky R, Charpentier P. A thermal study on the structural changes of bimetallic ZrO_2-modified TiO_2 nanotubes synthesized using supercritical CO_2. Nanotechnology. 2009;20:195601.

26 Lucky RA, Charpentier PA. N-doped ZrO_2/TiO_2 bimetallic materials synthesized in supercritical CO_2: Morphology and photocatalytic activity. Applied catalysis B, Environmental. 2010;96:516-523.

27 Allo BA, Rizkalla AS, Mequanint K. Hydroxyapatite formation on sol–gel derived poly (ε-caprolactone)/bioactive glass hybrid biomaterials. ACS applied materials & interfaces. 2012;4:3148-3156.

28 Allo BA, Rizkalla AS, Mequanint K. Synthesis and electrospinning of ε-polycaprolactone-bioactive glass hybrid biomaterials via a sol− gel process. Langmuir. 2010;26:18340-18348.

29 Allo BA, Lin S, Mequanint K, Rizkalla AS. Role of Bioactive 3D Hybrid Fibrous Scaffolds on Mechanical Behavior and Spatiotemporal Osteoblast Gene Expression. ACS applied materials & interfaces. 2013;5:7574-7583.

30 Salarian M, Xu WZ, Biesinger MC, Charpentier PA. Synthesis and characterization of novel TiO_2-poly(propylene fumarate) nanocomposites for bone cementation. Journal of Materials Chemistry B. 2014.

31 Kuroda K, Shidu H, Ichino R, Okido M. Formation of titania/hydroxyapatite composite films by pulse electrolysis. Materials transactions. 2007;48:322-327.

32 Fowler B. Infrared studies of apatites. I. Vibrational assignments for calcium, strontium, and barium hydroxyapatites utilizing isotopic substitution. Inorganic chemistry. 1974;13:194-207.

33 Park E, Condrate Sr RA, Lee D. Infrared spectral investigation of plasma spray coated hydroxyapatite. Materials Letters. 1998;36:38-43.

34 Rapacz-Kmita A, Ślósarczyk A, Paszkiewicz Z, Paluszkiewicz C. Phase stability of hydroxyapatite–zirconia (HAp–ZrO_2) composites for bone replacement. Journal of molecular structure. 2004;704:333-340.

35 Soler-Illia GdA, Louis A, Sanchez C. Synthesis and characterization of mesostructured titania-based materials through evaporation-induced self-assembly. Chemistry of Materials. 2002;14:750-759.

www.manaraa.com

36 L. Mohan DD, M. Geetha, T.S.N. Sankara Narayanan, R. Asokamani,. Electrophoretic deposition of nanocomposite (HAp+TiO_2) on titanium alloy for biomedical applications. Ceramics International. 2012;38:3435–3443.

37 Tsoncheva T, Ivanova L, Paneva D, Mitov I, Minchev C, Fröba M. Cobalt and iron oxide modified mesoporous zirconia: Preparation, characterization and catalytic behaviour in methanol conversion. Microporous and Mesoporous Materials. 2009;120:389-396.

38 Sing KS. Reporting physisorption data for gas/solid systems with special reference to the determination of surface area and porosity (Recommendations 1984). Pure and applied chemistry. 1985;57:603-619.

39 Giannakopoulou T, Todorova N, Romanos G, Vaimakis T, Dillert R, Bahnemann D, Trapalis C. Composite hydroxyapatite/TiO2 materials for photocatalytic oxidation of NOx. Materials Science and Engineering: B. 2012;177:1046-1052.

40 Khaleel A, Al-Mansouri S. Meso-macroporous γ-alumina by template-free sol–gel synthesis: The effect of the solvent and acid catalyst on the microstructure and textural properties. Colloids and Surfaces A: Physicochemical and Engineering Aspects. 2010;369:272-280.

41 Farhangi N, Chowdhury RR, Medina-Gonzalez Y, Ray MB, Charpentier PA. Visible light active Fe doped TiO_2 nanowires grown on graphene using supercritical CO2. Applied Catalysis B: Environmental. 2011;110:25-32.

42 Abbasi S, Bayati M, Golestani-Fard F, Rezaei H, Zargar H, Samanipour F, Shoaei-Rad V. Micro arc oxidized HAp–TiO_2 nanostructured hybrid layers-part I: Effect of voltage and growth time. Applied Surface Science. 2011;257:5944-5949.

43 Golestani-Fard F, Bayati M, Zargar H, Abbasi S, Rezaei H. MAO-preparation of nanocrystalline hydroxyapatite–titania composite films: Formation stages and effect of the growth time. Materials Research Bulletin. 2011;46:2422-2426.

44 de Groot FMF, Figueiredo MO, Basto MJ, Abbate M, Petersen H, Fuggle JC. 2p X-ray absorption of titanium in minerals. Physics and Chemistry of Minerals. 1992;19:140-147.

45 Liu L, Chan J, Sham T-K. Calcination-induced phase transformation and accompanying optical luminescence of TiO_2 nanotubes: An X-ray absorption near-edge structures and X-ray excited optical luminescence study. The Journal of Physical Chemistry C. 2010;114:21353-21359.

46 Cannillo V, Lusvarghi L, Sola A. Production and characterization of plasma-sprayed TiO_2–hydroxyapatite functionally graded coatings. Journal of the European Ceramic Society. 2008;28:2161-2169.

www.manaraa.com

47 Nath S, Tripathi R, Basu B. Understanding phase stability, microstructure development and biocompatibility in calcium phosphate–titania composites, synthesized from hydroxyapatite and titanium powder mix. Materials Science and Engineering: C. 2009;29:97-107.

www.manaraa.com

Chapter 6

6 Conclusions and Recommendations

6.1 Conclusions

The need for biodegradable polymer composite materials for bone regeneration is increasing due to the aging of our population as well as the increase of traumatologic injuries and necrosis-related bone resorption. Therefore, superior synthetic orthopaedic materials and techniques are required for clinical practice. In orthopaedics, the demand for synthetic bone cement materials can be fulfilled by using composite structures, as it is possible to mimic better the structures of living materials, like bone, cartilage or teeth using these composites. Polymer composites are combinations of two or more components, usually containing an inorganic phase and a polymer phase that are essentially insoluble in one another. Polymers have typically lower modulus and deformation resistance than the inorganic phase, although provide processability to the system. Thus, attempts are made to adjust the mechanical properties of polymeric materials to approximate those of bone, using a composite structure.

The mechanical performance of any kind of nanocomposite reflects the interaction between the various phases. If there is adhesion between the two phases either chemical or physical, even at low strains, stress transfer can take place across the interface, which allows the filler to share the stress and provide a reinforcing effect. The successful reinforcement of poly(propylene fumarate) matrix by nanostructured titania fibers shows that the incorporation of one-dimensional nanomaterials is a promising technique for augmenting the mechanical properties of PPF-based bone cements. A novel functionalizing technique using the ring opening reaction of maleic anhydride was

www.manaraa.com

applied to PPF in order to establish chemical adhesion between the nanofillers and organic polymer matrix. The major outcomes from these studies include:

(1) TiO_2 nanofibers up to a certain limit of loading exhibit homogenous dispersion in the functionalized polymeric continuous phase.

(2) Reinforcement using TiO_2 nanofibers is a promising technique only when there is a homogenous distribution of the nanomaterials to provide strong adhesion with the continuous phase.

(3) The obtained reinforcing effect of the TiO_2 nanofibers is attributed mainly to the strong interfacial chemical adhesion between the TiO_2 nanofibers and the functionalized PPF matrix.

It is very important for an orthopaedic surgeon to be able to easily monitor and evaluate the healing and loosening processes to differentiate between bone, bone cement, and osteolysis. Incorporation of TiO_2 nanofibers into a cement formulation will not provide sufficient radiopacity to the PPF matrix at the optimum level of loading, which seems to be a major limitation for the potential application of the nanocomposites as bone cement materials. In an attempt to address this limitation, this study demonstrated a novel pathway to develop an alternative radiopacifier for PPF-based bone cements which also acts as a reinforcing agent. The modification of the titania nanotubes was performed through a novel sol-gel reaction in supercritical CO_2.

(1) TiO_2 nanofibes were successfully modified with radiopaque Sr^{2+} component using a sol-gel methodology in supercritical CO_2.

(2) This process offers several advantages over conventional sol-gel processes including: producing well-defined nanostructure, very good dispersion, high conversions, high surface areas, simple operating procedure, e.g. one-pot synthesis, mild operating conditions, e.g. 60 °C and 6000 psi, and environmental benignness.

(3) Nanostructured Sr-doped TiO_2 material was incorporated into the PPF-based bone cement formulations as reinforcing fillers presenting a homogeneous dispersion of the nanomaterials with strong chemical adhesion with the matrix while keeping the radiopacity of the cement intact.

Blood vessels are an important component of bone formation and maintenance, and the bone tissue differentiation is related to the local presence of blood vessels. The local

www.manaraa.com

release of a pro-angiogenic mediator leads to more intensive angiogenesis in the necrotic defect area, and thus improves osteogenesis and bone regeneration. Therefore, novel ginsenoside Rg_1-releasing PPF microspheres were fabricated using both a conventional double emulsion and a microfluidic method.

(1) The microfluidic approach produced more uniform sized microspheres (50-65 μm) compared to the more polydisperse microspheres prepared the W/O/W emulsion method (2-45 μm).

(2) The monodisperse microspheres produced by the microfluidic method were found to exhibit a slower release rate and a smaller burst effect than the polydisperse microspheres formed by the double emulsion method.

(3) The PPF microspheres obtained from the microfluidic approach demonstrated higher encapsulation efficiencies, which is a very important factor in drug delivery, especially for valuable and expensive bioactive compounds.

(4) Rg_1-induced tube formation is related to the dosage, and tube formation stimulation activity of ginsenoside Rg_1 did not change significantly before and after release from the PPF microspheres.

(5) Monodisperse microspheres generated by microfluidic devices are believed to enhance drug release kinetics, reproducibility, and bioavailability. Therefore, the monodisperse Rg_1-loaded PPF microspheres are expected to significantly increase blood vessel density and vascular perfusion in necrotic defects and increased bone formation.

In addition, immobilization of the biocompatible TiO_2 on the surface of the hydroxyapatite will enhance the mechanical properties of HAp along with enhancing cellular responses and biocompatibility. A novel combined co-precipitation and sol-gel methodology using supercritical fluid processing with carbon dioxide ($scCO_2$) was proposed to improve the mechanical properties of hydroxyapatite with HAp nonoplates grown from the surface of one-dimensional TiO_2 nanorods. Then, a novel polymer/ceramic composite network of poly(ε-caprolactone) (PCL) and HAp-TiO_2 with improved mechanical properties was developed for bone regeneration and bone tissue engineering applications. The rationale for the design of the nanocomposite consists of synthetic polymer, PCL, in combination with nanoscale synthetic HAp-TiO_2 was based, in part, on the natural nanocomposite structure of bone tissue.

www.manaraa.com

(1) The particle diameter and length, morphology, and BET surface area of the HAp-TiO_2 composite materials was tunable by adjusting the metal alkoxide concentration, reaction temperature, and pressure.

(2) Morphologies of the HAp-TiO_2 compound varied from nanoplate-thick sheet type structure to Nanoplate-Nanorods.

(3) HAp-TiO_2 nanocomposites were homogenously mixed within poly(ε-caprolactone) (PCL) to develop scaffolds with enhanced physical and mechanical properties for bone regeneration.

(4) The significant increase in the Young's and flexural modulus observed for PCL/HAp-TiO_2 composite over the PCL/HAp composition were concluded to be due to the morphology, size and, the preferred orientation. Due to the small diameters and large aspect ratios of TiO_2 nanorods (large surface area), an intimate interface with the polymer matrix is formed, and the intrinsic properties of the HAp-TiO_2 fillers contribute to an increase in the mechanical strength and stiffness of composites. In addition, there is a strong adhesion between the HAp-TiO_2 and PCL matrix, and partially pulled out TiO_2 nanorods will impart the bridging of the crack during propagation and bridge the cracks in the PCL matrix.

6.2 Recommendations

The intended use of nanocomposite materials described in this thesis will be to provide temporary mechanical strength and conditions for new bone growth into a skeletal region deficient in trabecular bone of femoral head as well as tissue engineering which offers a promising alternative to conventional therapies by potentially enabling the regeneration of normal native tissues.

The following recommendations will be useful in the future investigations of this study:

i) N-Vinyl pyrrolidone (NVP) is normally used as a crosslinking reagent in PPF-based formulations, but any unreacted NVP after *in situ* polymerization is of concern on account of its toxicity. In addition, even if titania is an established biocompatible material, nanomaterials are well known to exhibit completely

www.manaraa.com

different characteristics at their nanodimensions, often being more toxic. This is attributed to their larger surface area, enhanced chemical reactivity, and easier penetration into cells. Therefore, the PPF-based polymer networks using NVP as a crosslinking reagent and reinforced with TiO_2 nanofibers needs to be evaluated in terms of cell adhesion, proliferation, and cytotoxicity in a rat model system. In addition, the *in vitro* growth of osteoblast onto the reinforced cement composites and in vivo biocompatibility should be explored.

ii) The synthesis part of the composite biomaterials or composite-Rg_1 construct should degrade in a controlled fashion into nontoxic molecules that the body can metabolize or excrete and then allow the usual process of remodeling to optimize the mechanical properties of the newly formed bone. It has been reported that the poly(vinyl pyrrolidone) (PVP) crosslinks in the crosslinked PPF networks might be non-degradable. Thus, the degradation reaction of the PPF-based polymer networks and TiO_2-PPF-based bone cement composite networks needs to be studied, and the degradation products should be isolated and characterized by instrumental analysis (^1H and ^{13}C NMR).

iii) The sol-gel methodology using supercritical fluid processing with carbon dioxide ($scCO_2$) to modify the titania nanofibers with strontium atom needs to be optimized in terms of concentration of strontium atom in the nanofibers. In addition, the effect of synthesis conditions including metal alkoxide concentration, reaction temperature, and pressure on the morphology, crystallinity, and chemical and physical state of modified nanofibers need to be studied by HRTEM, XPS and XRD.

iv) Functionalization reaction of PPF with maleic anhydride (MA) needs to be optimized. The extent of functionalization could be adjusted by varying the pH of the reaction medium.

v) An injectable, *in situ* polymerizable, biodegradable poly(propylene fumarate) (PPF) scaffold with embedded ginsenoside Rg_1-delivering PPF microspheres should be developed for bone regeneration. Then, the performance of the ginsenoside Rg_1-releasing scaffold is evaluated by observing *in vitro* cell differentiation of pre-osteoblast and in vivo bone formation in a rat model system

www.manaraa.com

of irradiated osseous defects compromised in their vasculature as well as the tube formation of human umbilical vein endothelial cells (HUVEC) to examine the angiogenesis behavior of the PPF-based Rg_1 delivery systems. In addition, the release profiles *in vitro* should be measured to monitor how the fabricated microsphere-containing scaffold could gradually releases agniogenic modulator.

www.manaraa.com

Appendices

Appendix A. Calibration curve of Rg_1

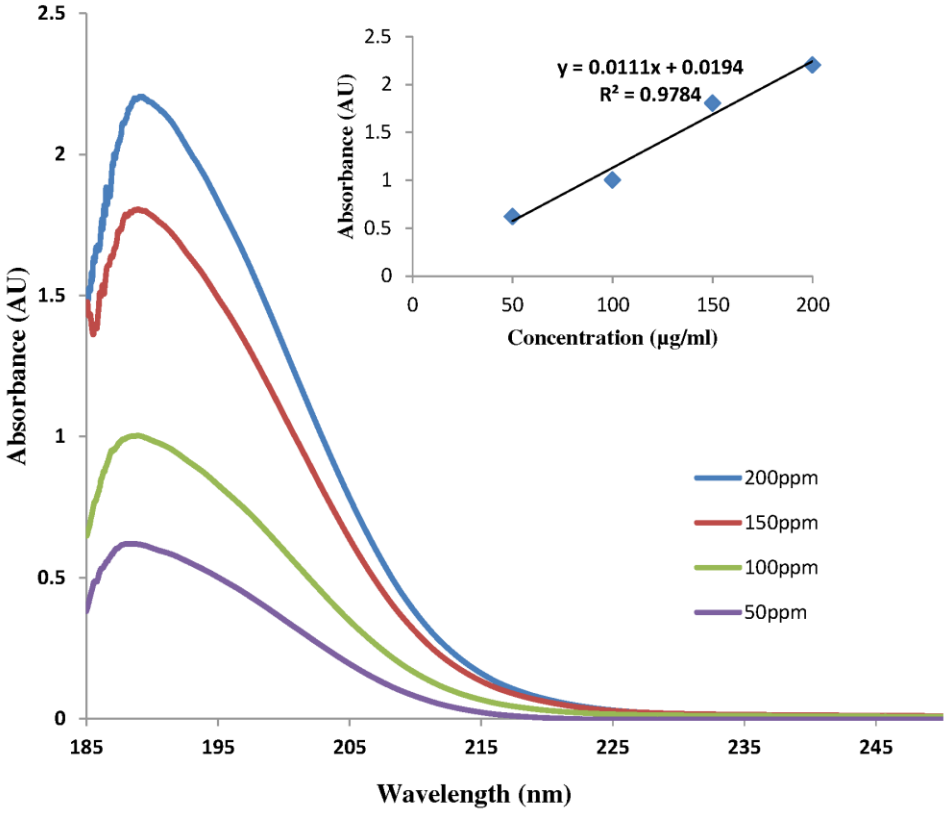

www.manaraa.com

Appendix B. Copyright releases.

B.1 ELSEVIER LICENSE TERMS AND CONDITIONS

This is a License Agreement between Mehrnaz Salarian ("You") and Elsevier ("Elsevier") provided by Copyright Clearance Center ("CCC"). The license consists of your order details, the terms and conditions provided by Elsevier, and the payment terms and conditions. All payments must be made in full to CCC. For payment instructions, please see information listed at the bottom of this form.

Supplier:	Elsevier Limited The Boulevard,Langford Lane Kidlington,Oxford,OX5 1GB,UK
Registered Company Number:	1982084
Customer name:	Mehrnaz Salarian
License number:	3502611401385
License date:	Nov 05, 2014
Licensed content publisher:	Elsevier
Licensed content publication:	Bone
Licensed content title:	Unique alignment and texture of biological apatite crystallites in typical calcified tissues analyzed by microbeam x-ray diffractometer system
Licensed content author:	T Nakano,K Kaibara,Y Tabata,N Nagata, S Enomoto,E Marukawa,Y Umakoshi
Licensed content date:	October 2002
Licensed content volume number:	31
Licensed content issue number:	4
Number of pages:	9
Start Page:	479
End Page:	487
Type of Use:	reuse in a thesis/dissertation
Portion:	figures/tables/illustrations
Number of figures/tables/ illustrations:	1
Format:	electronic
Are you the author of this Elsevier article?	No
Will you be translating?	No
Title of your thesis/dissertation:	A NEW GENERATION OF POLYMER/CERAMIC COMPOSITE BIOMATERIALS FOR BONE REGENERATION
Expected completion date:	Dec 2014
Estimated size (number of pages):	220
Elsevier VAT number:	GB 494 6272 12
Permissions price:	0.00 USD

www.manaraa.com

VAT/Local Sales Tax:	0.00 USD / 0.00 GBP
Total:	0.00 USD

B.2 ELSEVIER LICENSE TERMS AND CONDITIONS

This is a License Agreement between Mehrnaz Salarian ("You") and Elsevier ("Elsevier") provided by Copyright Clearance Center ("CCC"). The license consists of your order details, the terms and conditions provided by Elsevier, and the payment terms and conditions. All payments must be made in full to CCC. For payment instructions, please see information listed at the bottom of this form.

Supplier:	Elsevier Limited The Boulevard,Langford Lane Kidlington,Oxford,OX5 1GB,UK
Registered Company Number:	1982084
Customer name:	Mehrnaz Salarian
License number:	3502620882612
License date:	Nov 05, 2014
Licensed content publisher:	Elsevier
Licensed content publication:	Journal of Solid State Chemistry
Licensed content title:	Crystal Structure of Calcium-Deficient Carbonated Hydroxyapatite. Thermal Decomposition
Licensed content author:	T.I. Ivanova,O.V. Frank-Kamenetskaya,A.B. Kol'tsov,V.L. Ugolkov
Licensed content date:	September 2001
Licensed content volume number:	160
Licensed content issue number:	2
Number of pages:	10
Start Page:	340
End Page:	349
Type of Use:	reuse in a thesis/dissertation
Intended publisher of new work:	other
Portion:	figures/tables/illustrations
Number of figures/tables/ illustrations:	1
Format:	electronic
Are you the author of this Elsevier article?	No
Will you be translating?	No
Title of your thesis/dissertation:	A NEW GENERATION OF POLYMER/CERAMIC COMPOSITE BIOMATERIALS FOR BONE REGENERATION
Expected completion date:	Dec 2014
Estimated size (number of pages):	220
Elsevier VAT number:	GB 494 6272 12

www.manaraa.com

Permissions price:	0.00 USD
VAT/Local Sales Tax:	0.00 USD / 0.00 GBP
Total:	0.00 USD

B.3 WOLTERS KLUWER HEALTH LICENSE TERMS AND CONDITIONS

This is a License Agreement between Mehrnaz Salarian ("You") and Wolters Kluwer Health ("Wolters Kluwer Health") provided by Copyright Clearance Center ("CCC"). The license consists of your order details, the terms and conditions provided by Wolters Kluwer Health, and the payment terms and conditions. All payments must be made in full to CCC. For payment instructions, please see information listed at the bottom of this form.

License number:	3502680233196
License date:	Nov 05, 2014
Licensed content publisher	Wolters Kluwer Health
Licensed content publication	Current Orthopaedic Practice
Licensed content title	Cementation for Femoral Head Osteonecrosis: A Preliminary Clinic Study.
Licensed content author	Mark Wood, Cathy McDowell, and Scott Kelley
Licensed content date	Jan 1, 2003
Volume Number	412
Type of Use	Dissertation/Thesis
Requestor type	Individual
Portion	Figures/table/illustration
Number of figures/tables/ illustrations	1
Figures/tables/illustrations used	Fig 2A–B
Author of this Wolters Kluwer article	No
Title of your thesis / dissertation	A NEW GENERATION OF POLYMER/CERAMIC COMPOSITE BIOMATERIALS FOR BONE REGENERATION
Expected completion date	Dec 2014
Estimated size(pages)	220
Billing Type	Invoice
Total	0.00 CAD

www.manaraa.com

B.4 AMERICAN CHEMICAL SOCIETY LICENSE TERMS AND CONDITIONS

Title: *In Vitro* Cytotoxicity of Injectable and Biodegradable Poly(propylene fumarate)-Based Networks: Unreacted Macromers, Cross-Linked Networks, and Degradation Products

Author: Mark D. Timmer, Heungsoo Shin, R. Adam Horch, et al

Publication: Biomacromolecules

Publisher: American Chemical Society

Date: Jul 1, 2003

Copyright © 2003, American Chemical Society

PERMISSION/LICENSE IS GRANTED FOR YOUR ORDER AT NO CHARGE

This type of permission/license, instead of the standard Terms & Conditions, is sent to you because no fee is being charged for your order. Please note the following:

Permission is granted for your request in both print and electronic formats, and translations.

If figures and/or tables were requested, they may be adapted or used in part.

Please print this page for your records and send a copy of it to your publisher/graduate school.

Appropriate credit for the requested material should be given as follows: "Reprinted (adapted) with permission from (COMPLETE REFERENCE CITATION). Copyright (YEAR) American Chemical Society." Insert appropriate information in place of the capitalized words.

One-time permission is granted only for the use specified in your request. No additional uses are granted (such as derivative works or other editions). For any other uses, please submit a new request.

If credit is given to another source for the material you requested, permission must be obtained from that source.

www.manaraa.com

B.5 AMERICAN CHEMICAL SOCIETY LICENSE TERMS AND CONDITIONS

Title: Characterization of the Cross-Linked Structure of Fumarate-Based Degradable Polymer Networks

Author: Mark D. Timmer, Seongbong Jo, Chuanyue Wang, et al

Publication: Macromolecules

Publisher: American Chemical Society

Date: May 1, 2002

Copyright © 2002, American Chemical Society

PERMISSION/LICENSE IS GRANTED FOR YOUR ORDER AT NO CHARGE

This type of permission/license, instead of the standard Terms & Conditions, is sent to you because no fee is being charged for your order. Please note the following:

Permission is granted for your request in both print and electronic formats, and translations.

If figures and/or tables were requested, they may be adapted or used in part.

Please print this page for your records and send a copy of it to your publisher/graduate school.

Appropriate credit for the requested material should be given as follows: "Reprinted (adapted) with permission from (COMPLETE REFERENCE CITATION). Copyright (YEAR) American Chemical Society." Insert appropriate information in place of the capitalized words.

One-time permission is granted only for the use specified in your request. No additional uses are granted (such as derivative works or other editions). For any other uses, please submit a new request.

If credit is given to another source for the material you requested, permission must be obtained from that source.

www.manaraa.com

B.6 AMERICAN CHEMICAL SOCIETY LICENSE TERMS AND CONDITIONS

Title: Hydroxyapatite–TiO2-based Nanocomposites Synthesized in Supercritical CO2 for Bone Tissue Engineering: Physical and Mechanical Properties

Author: Mehrnaz Salarian, William Z. Xu, Zhiqiang Wang, et al

Publication: Applied Materials

Publisher: American Chemical Society

Date: Oct 1, 2014

Copyright © 2014, American Chemical Society

PERMISSION/LICENSE IS GRANTED FOR YOUR ORDER AT NO CHARGE

This type of permission/license, instead of the standard Terms & Conditions, is sent to you because no fee is being charged for your order. Please note the following:

Permission is granted for your request in both print and electronic formats, and translations.

If figures and/or tables were requested, they may be adapted or used in part.

Please print this page for your records and send a copy of it to your publisher/graduate school.

Appropriate credit for the requested material should be given as follows: "Reprinted (adapted) with permission from (COMPLETE REFERENCE CITATION). Copyright (YEAR) American Chemical Society." Insert appropriate information in place of the capitalized words.

One-time permission is granted only for the use specified in your request. No additional uses are granted (such as derivative works or other editions). For any other uses, please submit a new request.

www.manaraa.com

Curriculum Vitae

Name:	Mehrnaz Salarian
Post-secondary Education and Degrees:	Islamic Azad University 1999-2003 B.Sc. (Materials-Ceramic Engineering) Islamic Azad University 2005-2008 M.Sc. (Materials-Ceramic Engineering) The University of Western Ontario London, Ontario, Canada 2009-2014 Ph.D. (Biomedical Engineering)
Related Work Experience:	Teaching and Research Assistant The University of Western Ontario 2009-2014

Publications and Conferences:

Mehrnaz Salarian, William Z. Xu, Mark Biesinger, Paul A. Charpentier, Synthesis and Characterization of Novel TiO_2-poly(propylene fumarate) Nanocomposites for Bone Cementation, Journal of Materials Chemistry B 2 (2014) 5145–5156.

Mehrnaz Salarian, William Z. Xu, Zhiqiang Wang, Tsun-Kong Sham, Paul A. Charpentier, Hydroxapatite-TiO_2-based Nanocomposites Synthesized in Supercritical CO_2 for Bone Tissue Engineering: Physical and Mechanical Properties, ACS Applied Materials & Interfaces 6 (19) (2014) 16918–16931.

Mehrnaz Salarian, William Z. Xu, Richard Bohay, Edmund M.K Lui, Paul A. Charpentier, Delivery of an Angiogenic Mediator for Bone Regeneration in a Radiopaque Sr-doped TiO_2/poly(propylene fumarate) Based Bone Cement (In preparation).

Mehrnaz Salarian, Raziye Samimi, William Z. Xu, Zhiqiang Wang, Tsun-Kong Sham, Edmund M.K Lui, Paul A. Charpentier, Design and Preparation of monodisperse PPF Microspheres Encapsulating a Pro-angiogenic Mediator, Ginsenoside Rg_1, using a Microfluidic Device (In preparation).

www.manaraa.com

Raziye Samimi, Mehrnaz Salarian, Paul A. Charpentier, Encapsulation of acetyl ginsenoside Rb_1 within PLGA microspheres using microfluidic technique, Industrial & Engineering Chemistry Research53 (28) (2014) 11333–11344.

Mehrnaz Salarian, Raziye Samimi, Paul A. Charpentier, Preparing Nanorods of Titania-Hydroxyapatite Composites Using a Surfactant-Assisted Hydrothermal Method for Orthopedic Applications, 2013 AIChE Annual Meeting, San Francisco, CA, USA.

Mehrnaz Salarian, Raziye Samimi, Paul A. Charpentier, Synthesis and Characterization of Ginsenoside Rg_1-loaded PPF Microspheres for Controlled Drug Release in Bone Cement, 24th Canadian Materials science Conference, London, ON (2012 CMSC).

Raziye Samimi, Mehrnaz Salarian, Kazi Farida Akhter, Paul A. Charpentier, Edmund Lui, Preparation of Polymeric Micro-Nano-Spheres Using a Microfluidic Approach for Delivery of Nutraeuticals, 2012 AIChE Annual Meeting, Pittsburgh, PA, USA.

Mehrnaz Salarian, Paul A. Charpentier, Mehrnaz Salarian, Kazi Farida Akhter, Sepideh Rezvani, Edmond Lui, Synthesis and Characterization of Polymer Microspheres for Biomedical and Nutraceutical Release, 61st Canadian Chemical Engineering Conference, London, ON (2011 CSChE).

Paul A. Charpentier, Chike Azike, Raziye Samimi, Mehrnaz Salarian, Kazi Farida Akhter, Edmond Lui, Drug Delivery of Ginsenosides and Polysacharides From North American Ginseng: Immunomodulatory and Angiogenesis Effects, AIChE 2013 Annual Meeting, San Francisco, CA, USA.

Raziye Samimi, Qasem Alsharari, Mehrnaz Salarian, Paul A. Charpentier, Supercritical Fluid Extraction and Chromatography of Bioactive Nutraceuticals, AIChE 2013 Annual Meeting, San Francisco, CA, USA.

Raziye Samimi, Mehrnaz Salarian, Kazi Farida Akhter, Paul A. Charpentier, Edmund Lui, Preparation of Polymeric Micro-Nano-Spheres using a Microfluidic Approach for Delivery of Nutracuticals, AIChE 2012 Annual Meeting, Pittsburg, PA, USA.

Raziye Samimi, Mehrnaz Salarian, Paul A. Charpentier, Edmund Lui, Controlled Release of North American Ginseng extracts Encapsulated within Microsphere/Hydrogel Combination System, Cultivating Natural Bioactives International Conference, London, ON (2012).

Mehrnaz Salarian, Mehran Solati-Hashjin, Seyedeh Sara Shafiei, Reza Salarian, Ziarat Ali Nemati, Template-Directed Hydrothermal Synthesis of Dandelion-Like Hydroxyapatite in the Presence of Cetyltrimethylammonium Bromide and Polyethylene Glycol, Ceramics International 35(7) (2009) 2563–2569

Mehrnaz Salarian, Mehran Solati-Hashjin, Seyedeh Sara Shafiei, Azadeh Goudarzi, Reza Salarian, Ali Nemati, Surfactant-Assisted Synthesis and Characterization of

www.manaraa.com

Hydroxyapatite Nanorods under Hydrothermal Conditions, Materials Science-Poland 27 (4/1) (2009) 961–971.

Mehrnaz Salarian, Mehran Solati-Hashjin, Azadeh Goudarzi, Seyedeh Sara Shafiei, Reza Salarian, Ziarat Ali Nemati, Effect of Surfactant in Formation of Hydroxyapatite Nano-rods in Hydrothermal Conditions, Iranian Journal of Pharmaceutical Sciences (IJPS) 4(2) (2008) 157–162.

Mehrnaz Salarian, Mehran Solati-Hashjin, Seyedeh Sara Shafiei, Ali Nemati, Reza Salarian, Effect of Hydrothermal Temperature on the Composition and Morphology of Surfactant-Assisted Hydrothermally Synthesized Hydroxyapatite Nano Particles, Sharif Journal of Science and Technology, Transaction on Materials Science & Engineering 47 (2009) 69–75.

Seyedeh Sara Shafiei, Mehran Solati-Hashjin, Mehrnaz Salarian, Synthesis, Characterization and Evaluation of Drug Release from Mg/Al-LDH Nanobiohybrid, Amirkabir Journal of Science and Technology, 20 (70-A) (2009) 37–43.

Seyedeh Sara Shafiei, Mehran Solati-Hashjin, Mehrnaz Salarian, Evaluation of Structure, Thermal Property and Drug Release of Nano Structure Clay (Layered Double Hydroxide) Containing Ibuprofen, Iranian Journal of Biomedical Engineering 3 (2) (2009) 119–126.

www.manaraa.com